Parameterizing the impact of fjord circulation on the ocean forcing of melting ice sheets

Adam Stanway

Pembroke College

University of Oxford

A thesis submitted for the degree of

Doctor of Philosophy

Trinity 2022

After time adrift among open stars, along tides of light and through shoals of dust, I will return to where I began

- Tali'Zorah nar Rayya

Some part of a mistake is always correct

- Savielly Tartakower

Acknowledgements

I would like to thank my supervisors; Andrew Wells, Helen Johnson and Jeff Ridley, for their incredible insights, expertise and patience throughout this project. In particular, the support that Andrew and Helen have provided in the lowest moments – both work-related and otherwise – has played a huge part in allowing me to pull the research together.

The last few years have been the most challenging of my life. I have relied so much on my close family; mum, dad, Emily and Katie (and Paddy!), who are always there to pick me back up again, and to whom I am always so grateful. Thanks to the Swan and Pillow; Chris, Glenn, Isabelle, Mantas and Thomas. I'm not sure I'd have survived Oxford without you.

Thanks to the University of Oxford; the Atmospheric, Oceanic and Planetary Physics Department, Pembroke College, Merton College, the Oxford DTP in Environmental Research, and the University as a whole. The flexibility and support that I have been given over the last two years in particular are greatly appreciated. I would also like to thank my funding bodies, the Natural Environment Research Council and the Met Office.

Abstract

Freshwater flux from the melting of the Greenland Ice Sheet (GrIS) accounts for 15% of the observed rise in global-mean sea level since 1993, with the rate of mass loss expected to increase as ocean temperatures rise. Exchanges of heat and freshwater between the GrIS and the ocean are mediated by circulation in proglacial fjords, ubiquitous around the coast of Greenland. Fjord circulation occurs on length scales which are too small to be resolved in contemporary Earth system models, representing a fundamental limitation in the ability of these models to form accurate long-term predictions of global climate. To include ice-ocean interaction mediated by fjord circulation, a sub-grid scale parameterization scheme is required. Here we take the first steps towards developing such a scheme, exploring and characterising several first-order controls on circulation within fjords.

This thesis develops theoretical understanding of fjord circulation in a regime dominated by the injection of subglacial discharge at the grounding line. We employ computational modelling of idealised fjords and develop scaling laws for the vertical structure of the flow when averaged across the width of the fjord. We produce a dynamically motivated prediction of cross-fjord velocities at the ice face, which is used to predict submarine melt rates across the entire glacial terminus. These theoretical developments are used as the basis for a simple multi-layered box-model parameterization of fjord circulation in an estuarine regime, which is tested under a range of forcing conditions. Finally, we investigate the impact of bathymetric sills on plume-driven circulation. Within fjords with shallow sills, the stratification differs significantly from that of the neighbouring ocean outside of the sill, and submarine melt rates are reduced relative to sill-less fjords given a realistic ocean stratification. The work in this thesis could be used as the basis for a sub-grid scale parameterization scheme, with the potential to be extended to include additional geophysical processes in the future.

Contents

1 Introduction and literature review

1.1 Overview

With an estimated volume of 2.9 million km^3 (Bamber et al. 2001), the Greenland Ice Sheet (GrIS) is the second largest ice sheet in the world – behind the Antarctic Ice Sheet – with highly variable mass loss both spatially and temporally (Bartholomaus et al. 2016). Studies of the long-term stability of the ice sheet suggest that the GrIS is more sensitive to global mean temperature increases than previously thought. In one study, the warming threshold allowing transition to a completely ice-free state was found to be just 1.6 °C above pre-industrial global-mean temperatures (Robinson et al. 2012). Freshwater flux from the melting of the GrIS is thought to have accounted for 15% of the observed rise in global mean sea level between 1993 and 2018 (WCRP Global Sea Level Budget Group 2018), with a significant proportion of this associated with increased freshwater flux from marine-terminating glaciers within coastal fjords (Straneo et al. 2013).

It has been suggested that increased ocean temperatures have triggered the retreat of Greenland's outlet glaciers (Straneo et al. 2013), with the melting of submarine glacier termini leading to an acceleration of inland regions of the ice sheet (Holland et al. 2008). Indeed, mass loss from the GrIS has been increasing since the mid-1990s (Broeke et al. 2016), and since 1995 the ice sheet has experienced an

unprecedented increase in runoff from surface melt that exceeds any other period during the last century (Fettweis et al. 2017), with this increase in runoff also coinciding with an increase in submarine discharge (Rignot et al. 2008; Fettweis et al. 2017). This ice sheet mass loss contributes to a cumulative freshening anomaly close to areas critical for the oceanic overturning circulation in the subpolar North Atlantic, and has been increasing monotonically since 1995 (Bamber et al. 2012). Further implications for the structure and stability of large scale ocean currents have been suggested; an increase in freshwater flux (FWF) into the ocean in this region has been shown to change water properties in the Labrador Sea (Yang et al. 2016), and potentially influence the strength of the Atlantic Meridional Overturning Circulation (AMOC) via suppression of the formation of North Atlantic Deep Water (Rahmstorf et al. 2015; Böning et al. 2016).

It has recently been suggested that AMOC variability is more closely linked with changes in water properties east of Greenland, rather than within the Labrador Sea (Lozier et al. 2019). Nevertheless, GrIS melt may still be an important factor in controlling the properties of water in this region. Studies have shown that increased FWF also has an impact on the local marine ecosystem (Rysgaard et al. 2003), glacier dynamics (Seale et al. 2011), and atmospheric temperatures (Smith et al. 2009). As such, increased FWF could have significant repercussions for both local and global climate. Understanding the controls on changes in FWF is of vital importance in making accurate predictions of future climate.

The coupling between the Greenland Ice Sheet and the wider ocean occurs via a network of long, narrow, strongly stratified coastal fjords (e.g. see Figure 1.1), too small to be directly resolved in global ocean models. This is in contrast to the more widely studied Antarctic case, where the ice sheet is generally in direct contact with the ocean through vast, floating ice shelves (e.g. Alley et al. 2015). As such, current global ocean models (such as NEMO, the Nucleus for European Modelling of the Ocean, https://www.nemo-ocean.eu/) do not include the impact of ocean heat supplied to the Greenland Ice Sheet, with climate models relying solely on simulations of the atmospheric contribution to the loss of GrIS mass, or having

some spatially distributed freshwater input which is not modified by the state of the ocean itself. This represents a fundamental limitation in the ability of these models to form accurate predictions of both the response of the GrIS to climate change and the effect of the resulting freshwater flux on the global ocean and climate, generating significant uncertainty in long term projections (Church et al. 2013; Fox-Kemper et al. 2021). Therefore, understanding the ice-ocean interaction and circulation in these fjords is of key importance, particularly given that the heat content of the North Atlantic ocean is predicted to continue to rise (Hoegh-Guldberg et al. 2014).

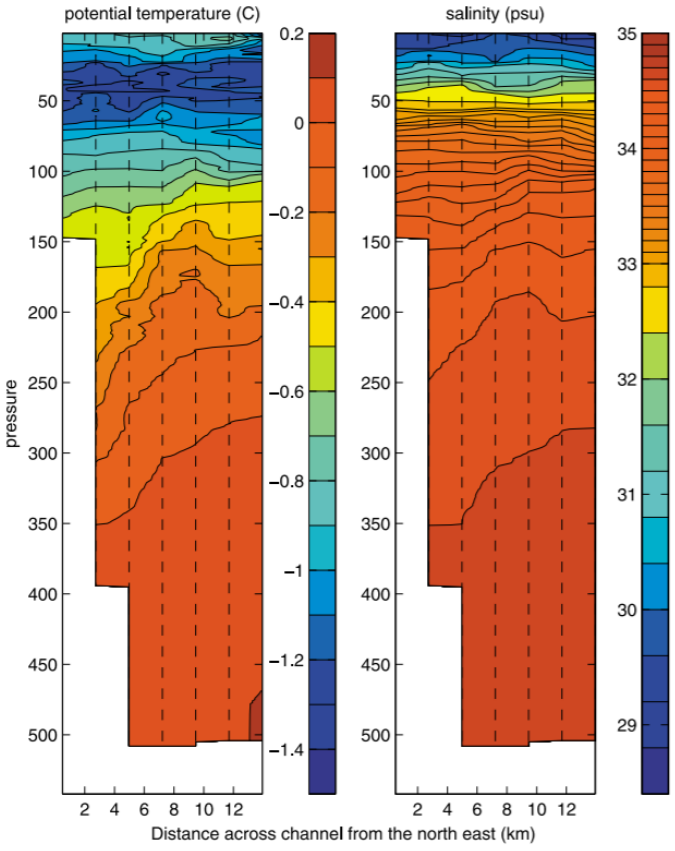

Figure 1.1: Cross-fjord sections of potential temperature and salinity across Petermann Fjord in 2009, measured via CTD (a conductivity, temperature and depth probe). Figure from Johnson et al. 2011.

Observational data from within fjords is sparse (Straneo et al. 2013; Straneo et al. 2015). This is firstly due to practical difficulties associated with measuring close to glacial termini or below the ice mélange (a mixture of sea ice and calved icebergs often extending tens of kilometres into the fjord from the glacial terminus). Secondly, significant observational campaigns only began relatively recently, in response to an increased awareness of the effect of warming oceans on the GrIS (Straneo et al. 2015; Fenty et al. 2016). Notably, only a few observational datasets are capable of constraining temporal variability for a single fjord (e.g. Mortensen et al. 2011;

Jackson et al. 2016). Oceanographic sections within several of Greenland's major fjords reveal a vertical structure echoing the coastal stratification in temperature and salinity (Figure 1.1). Within the fjord, relatively cold and fresh Polar Water (PW) sits above a warm, saline layer of Atlantic Water (AW), with glacially modified waters near to the surface and intruding at the Polar-Atlantic Water interface. Observations close to the ice face (e.g. Mankoff et al. 2016) have also suggested that intrusions of warm, saline fluid into the surface layers of fjord waters could occur as a result of buoyant glacial plume-driven flows.

Modelling efforts and laboratory studies are beginning to provide insight into individual physical processes of potential relevance within fjords (e.g. see review in Straneo et al. 2015). However, there exists no systematic investigation of how the relevance of each of these physical processes varies between fjords and thus no accurate way of incorporating a complete GrIS-ocean coupling scheme into global-scale climate models. Global ocean models currently operate at resolutions too coarse to resolve ice-ocean interaction on length scales typical of coastal fjords. Therefore, a parameterization scheme is required to incorporate the relevant physics, representing the sub-grid scale processes in terms of physical variables that can be resolved in such models. In this thesis, we develop understanding of the physics necessary to build such a parameterization scheme and build and test a simple box model upon which a parameterization scheme within Earth system models could be based. In the next section (§1.2), we review current literature regarding processes of relevance to fjord circulation in more detail. Next (§1.3), we discuss the current state of ice-ocean interaction in Earth system models. Finally, in §1.4 we provide a more detailed overview of the aims of this thesis.

1.2 Fjord circulation

Previous studies have often taken a reductionist approach in trying to understand the flow within fjords, considering key driving processes of the circulation in isolation (e.g. katabatic winds in Spall et al. 2017). This approach, combined with limited observational campaigns, is beginning to improve understanding of the impact of ocean heat content on ice sheet melt.

Fjord circulation is controlled by a variety of processes, as illustrated in Figure 1.2 and discussed in §1.2.1.1 – 1.2.1.5. Briefly, discharge of buoyant, fresh meltwater into the fjord via surface runoff, subglacial discharge (due to atmospherically forced melt), and submarine melt (due to the fluxes of oceanic heat and salt to the ice face) drive a strongly stratified estuarine circulation, with relatively fresh outflow at or near the surface and a return flow at depth. Often, some intrusion of meltwater is observed at the interface between lower saline and upper fresh layers (Jackson et al. 2016). Katabatic wind events, strong along-fjord winds blowing down glaciers and out to sea, occur on the order of 10 times per winter. This reinforces the estuarine circulation with a large transfer of along-fjord momentum to water in the surface layer (Spall et al. 2017). Sea ice and icebergs, however, impede this transfer of momentum from winds into the surface layer, in addition to providing sources and sinks of fresh- and saltwater via iceberg melt and brine rejection in the formation of sea ice. This ice mélange often extends tens of kilometres from the glacial terminus (Sutherland et al. 2014). Frequent barrier wind events on the shelf drive baroclinic exchange flows at the fjord mouth forming the intermediary circulation, as shown in both observations (e.g. Jackson et al. 2014; Jackson et al. 2016) and models (e.g. Fraser et al. 2018).

The bathymetry, geometry, and dimensions of the fjord affect the circulation response of fjord waters to forcing processes, and their typical ranges are discussed in §1.2.2. This includes whether the glacier terminates in a (typical) steep calving front (e.g. Helheim Glacier, Straneo et al. 2010; Jakobshavn Glacier, Gladish et al. 2015), or a more uncommon floating ice shelf (e.g. Petermann Glacier, Johnson et al. 2011; 79N Glacier, Blau et al. 2021). Bottom topography, particularly the

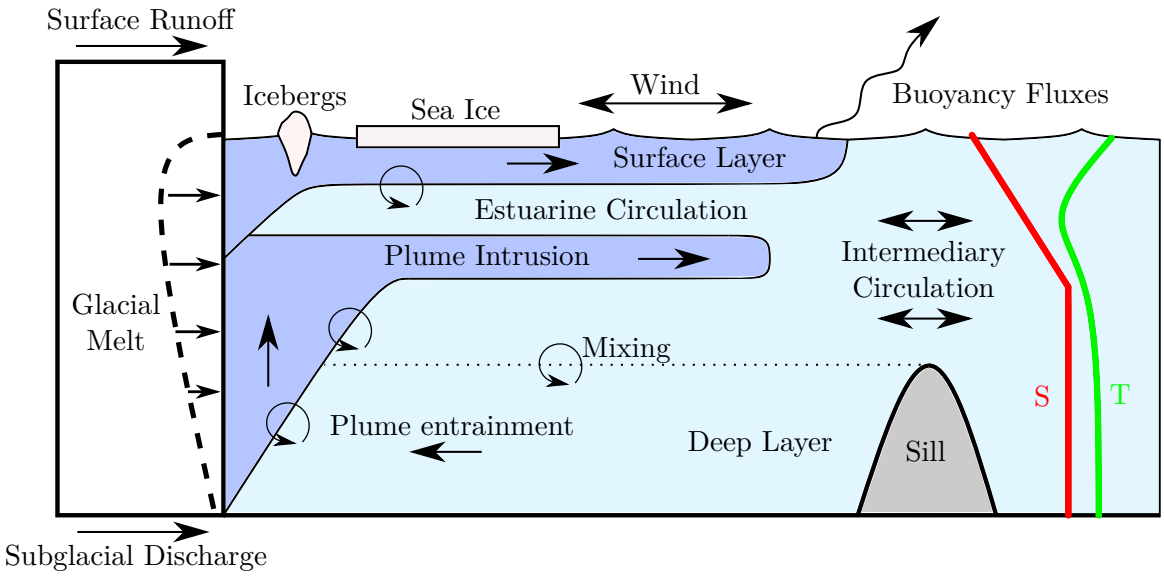

Figure 1.2: Some key processes impacting fjord circulation. We discuss plume-driven circulation in §1.2.1.1 and §1.2.1.2, and intermediary circulation in §1.2.1.3. The impact of katabatic wind events are discussed in §1.2.1.4, and sea ice and icebergs in §1.2.1.5. Processes and features not shown here include shelf winds (which drive the intermediary circulation), and iceberg melt injecting freshwater throughout a range of fjord depths.

depth of the sill at the fjord mouth and the depth of the glacial grounding line, has an impact on the transportation of heat to the glacial terminus by controlling the properties of coastal waters able to enter the fjord. This potentially restricts the inflow of warm, dense Atlantic water at depth, and controls the formation and residence time of deep waters within the fjord.

Recent studies, such as Jackson et al. 2018, have begun to explore idealised models in parameter spaces covering both narrow 'slab-like' fjords – in which coastally forced depressions in the pycnocline behave analogously to standing waves in the fjord – and wide, rotationally influenced fjords – where coastal waves propagate as Kelvin waves into and around the fjord. Interestingly, combining the stratification strengths, flow velocities and fjord widths for all fjords for which data is available, Jackson et al. 2018 find a ratio of fjord width to Rossby radius of deformation R_d of around 1 (Table 1.1), where $R_d = c/f$, f is the Coriolis parameter and c is the baroclinic gravity-wave phase speed. One might expect fjord geometry to be controlled entirely by glaciological dynamics, given the nature of

Fjord	W/R_d	Source
Sermilik Fjord	0.6 [0.6, 1.5]	Sutherland et al. 2014
Petermann Fjord	2.0 [1.5, 2.3]	Johnson et al. 2011
Kangerdlugssuaq Fjord	1.0 [0.7, 1.3]	Inall et al. 2014
Ilulisat Icefjord	0.8 [0.5, 1.2]	Gladish et al. 2015
Rink Fjord	1.1 [0.9, 1.8]	Bartholomaus et al. 2016
Store Fjord	0.9 [0.8, 1.6]	Chauché et al. 2014
Godthåbsfjord	0.7 [0.5, 0.9]	Mortensen et al. 2011
Kangerlussuup Sermia	1.2 [0.9, 1.4]	Bartholomaus et al. 2016

Table 1.1: Ratios of fjord widths W to the first baroclinic Rossby radii R_d (showing the mean, minimum and maximum values) for a variety of Greenlandic proglacial fjords (Jackson et al. 2018).

the formation of fjords, whilst the ocean stratification is set by far-field and shelf conditions. Hence, this observation is rather curious, and unexplained as of yet.

1.2.1 Processes driving circulation within fjords

1.2.1.1 Buoyant subglacial discharge plumes

Freshwater from atmospherically induced surface melt over inland regions of the Greenland Ice Sheet can penetrate through the ice and form channelised conduits. At the grounding line of marine-terminating glaciers, these subglacial conduits act as a source of buoyant freshwater, which rises up the ice face and generates a vigorous discharge plume. Plume theory describes the evolution of fluid from a source with a given density, as it rises through an ambient fluid of a different density (Priestley et al. 1955; Morton et al. 1956). As the source fluid rises, ambient fluid is entrained into the resultant plume, changing the density and volume (and therefore buoyancy) of water within the plume towards the ambient conditions.

This entrainment process is strongly turbulent and difficult to describe fully analytically. However, a key simplifying insight developed by Morton et al. (1956) parameterizes this turbulent entrainment in terms of a single constant 'entrainment parameter' α, using dimensional arguments to relate the vertical velocities within the plume w to the horizontal velocity of ambient fluid entrained into the plume at each depth u_H, such that $u_H = \alpha w$. This simplification allowed for the computational

prediction of the evolution of fluid from a source of buoyancy within ambient fluid with an arbitrary vertical density profile, and the development of analytic solutions where the ambient fluid has uniform density, both of which compare well to laboratory experiments for axisymmetric plumes. It has been shown (Morton et al. 1956) that plumes rise continuously through ambient layers of constant density, but can outflow at a level of neutral buoyancy in a stratified ambient fluid.

This formulation of buoyant plume theory has been subsequently adapted for a variety of both source and ambient conditions. Of primary relevance to fjord circulation are theories which apply buoyant plume theory to a localised source of freshwater at the base of a vertical ice front, leading to the formation of a half-conical plume, with density controlled by both the salinity and temperature of the source and the ambient fluid. Alternatively, a distributed source at the grounding line forms a line plume, with slightly modified dynamics (e.g. Jenkins 2011). Slater et al. (2016) modified the equations of Morton et al. (1956) for a half-conical plume and investigated the impact of a plume of this form as it rises in contact with a vertical ice face, leading to the development of a coupled system of equations which relate conservation of buoyancy, momentum, heat and salt in the plume to the melting of ice where the plume is in contact with the ice face. They then derive dimensional scalings for the local melt rate $\dot{m}(z)$ as a function of subglacial discharge, for ambient stratifications of either constant or linearly varying density. Equations for the variation of volume, momentum, heat and salt with depth within the plume are given in turn by:

$$\frac{\partial}{\partial z}\left(\frac{\pi}{2}b^2 w\right) = \pi\alpha b w + 2b\dot{m}, \tag{1.1a}$$

$$\frac{\partial}{\partial z}\left(\frac{\pi}{2}b^2 w^2\right) = \frac{\pi}{2}b^2 g' - 2C_d b w^2, \tag{1.1b}$$

$$\frac{\partial}{\partial z}\left(\frac{\pi}{2}b^2 w T\right) = \pi\alpha b w T_a + 2b\dot{m}T_b - 2C_d^{1/2}\Gamma_T b w(T - T_b), \tag{1.1c}$$

$$\frac{\partial}{\partial z}\left(\frac{\pi}{2}b^2 w S\right) = \pi\alpha b w S_a + 2b\dot{m}S_b - 2C_d^{1/2}\Gamma_S b w(S - S_b), \tag{1.1d}$$

where b is the plume radius, w the plume vertical velocity, T plume temperature and S plume salinity. Properties with subscript a refer to ambient fluid properties,

subscript b refer to properties within the ice-ocean boundary layer, $g' = g(\rho_a - \rho)/\bar{\rho}$ is the reduced gravity of the plume, ρ is the density within the plume, $\bar{\rho}$ is a reference density, C_d is a drag coefficient between the plume and ice, $\Gamma_{T,S}$ are heat and salt transfer coefficients, and $\dot{m}$ is the melt rate of the ice in contact with the plume (see Figure 1.3).

The relationship between the melt rate and the plume properties can be characterised in several ways. The formulation we use in this thesis is that of the 'three-equation formulation' (Holland et al. 1999), which considers a boundary layer between the plume and ice, with the melt rate given by the solution of three equations:

$$\dot{m}\left[c_i(T_b - T_i) + L\right] = c_w C_d^{1/2} \Gamma_T w (T - T_b), \tag{1.2a}$$

$$\dot{m} S_b = C_d^{1/2} \Gamma_S w (S - S_b), \tag{1.2b}$$

$$T_b = \lambda_1 S_b + \lambda_2 + \lambda_3 z, \tag{1.2c}$$

where λ_1 is the variation of the freezing point of the ice with salinity, λ_2 a constant offset, λ_3 is the variation of freezing point with depth, c_i is the heat capacity of ice, c_w the heat capacity of water, and T_i the ice temperature. Equation 1.2a describes conservation of energy, with sensible and latent heat needed to warm and melt ice at a rate given by the parameterized heat flux on the right-hand side. Equation 1.2b describes the salt balance in the ice-ocean boundary layer, in the presence of a freshwater flux due to melting or freezing of the ice. Equation 1.2c equates the ice-ocean boundary layer temperature to the freezing point of ice given a salinity S_b within the boundary layer, at depth z.

Numerical simulation has begun to develop understanding of the impact of turbulent plumes on the submarine melt rates of marine-terminating glaciers. For example, Xu et al. (2012) uses high-resolution computational modelling (with horizontal and vertical resolutions $\mathcal{O}(10\,\mathrm{m})$) of a vertical marine-terminating ice face to predict melt rates given a localised source of freshwater at the grounding line generating a buoyant plume. They employ a two-dimensional model (with no

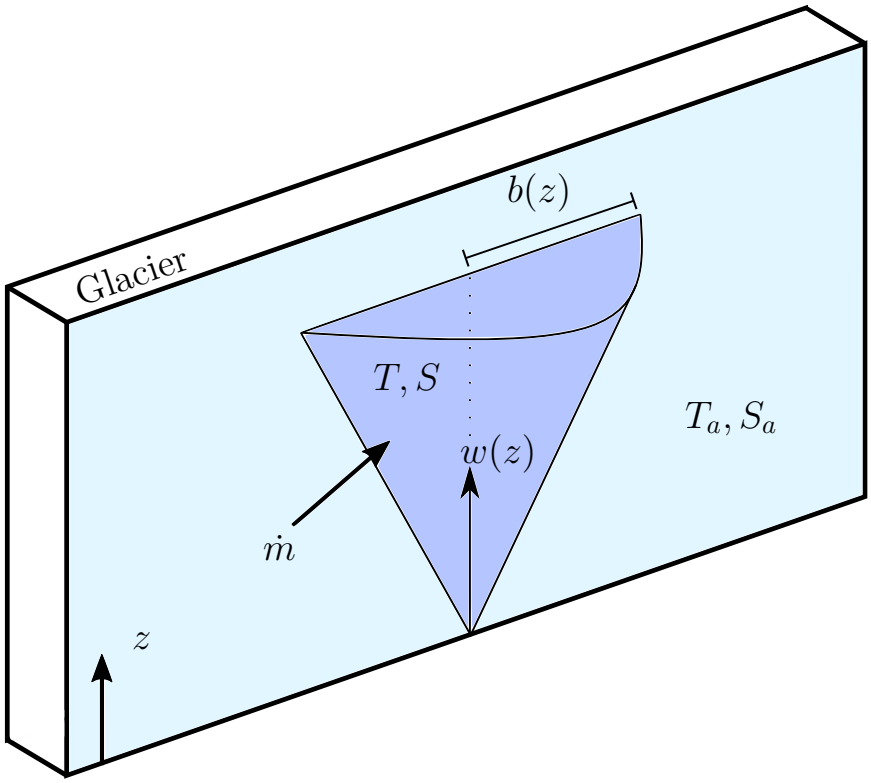

Figure 1.3: Schematic of half-conical subglacial-discharge-driven plumes of relevance to circulation within Greenland's fjords. The plume rises with vertical velocity $w(z)$, radius $b(z)$, temperature $T(z)$ and salinity $S(z)$ in ambient fjord water with temperature $T_a(z)$ and salinity $S_a(z)$. The strong vertical velocity within the plume generates large melt rates $\dot{m}(z)$ where it is in contact with the ice.

variability in the across-ice direction) and find a sublinear relationship between the subglacial discharge flux and glacial melt rate, along with a linear relationship between melt rate and ocean thermal forcing, given ambient ocean conditions taken from real-world observational data (Store Glacier). Kimura et al. (2014) also employ high-resolution computational modelling for unstratified ambient ocean conditions, with a three-dimensional domain allowing for across-ice variations. They find that the increase in vertical velocity within the plume with distance from the plume source causes a corresponding increase in melt rates with height above the grounding line.

Modelling approaches of this type are of great utility in the development of understanding of the impact of discharge plumes on the melt rates of glacial termini around Greenland. In particular, the ability to cover a range of parameter space is of great importance to the development of a parameterization scheme describing

all marine-terminating glaciers around Greenland. However, the scale separation between an ice face with geophysically relevant dimensions, and the turbulent length scales involved in the plume dynamics, mean that both Xu et al. (2012) and Kimura et al. (2014) still require the use of sub-grid scale parameterizations to describe mixing and turbulent heat transfer processes, with the value of several of the relevant parameters (such as heat and salt turbulent transfer coefficients) poorly constrained. Further, the direct, high-resolution simulation of ice-ocean interactions is extremely computationally intensive. As such, a sub-grid scale parameterization scheme for use within Earth system models must represent a significant simplification to even these simulations.

The impact of subglacial-discharge-driven plumes has also been investigated through laboratory experiments. For example, Cenedese et al. (2016) investigates the melting driven by the injection of buoyant freshwater at the base of a vertical block of ice in contact with ambient water consisting of two layers of differing densities. Neglecting rotation, they find good agreement with previous theoretical and computational modelling studies in regards to the relationship between increased freshwater flux at the source, and melting of the ice. Furthermore, they find that in a stratified ambient fluid, the plume can intrude in the subsurface as well as at the free surface, consistent with previous theoretical and modelling studies, as well as observations of marine-terminating glacial termini. The observed flow structures and melt rates suggest that for non-negligible subglacial discharge, the system is in a turbulent convection-driven melting regime. However, it is unclear whether there is full dynamical similarity between laboratory-scale experiments and real marine-terminating glacier systems, particularly with regards to the Reynolds and Rossby numbers achievable in lab studies of this type.

Limited direct observation of marine-terminating glaciers has also begun to provide insight into the impact of subglacial discharge on the submarine melting of tidewater glaciers, and the flow structures generated by sources of buoyant freshwater at the glacial grounding line. Observation of fjord waters at distances greater than 500 m from glacial termini is more common. However, properties

of water collected at this distance from the ice reflect the sum of both subglacial discharge and submarine melting, as well as other fjord scale processes, such that the precise dynamics of subglacial discharge plumes themselves is often difficult to infer.

Mankoff et al. (2016) presents in-situ measurements of salinity, temperature, and velocity profiles close to the glacial terminus of Saqqarliup Sermia, in Sarqardleq Fjord, western Greenland. Using measurements collected by conductivity, temperature and depth probe and acoustic Doppler current profilers, as well as aerial photography, they find the properties of a subglacial discharge plume rising at the glacial terminus agree well with theoretical predictions. In particular, the plume radius is found to increase from a narrow source $\mathcal{O}(10\,\mathrm{m})$ to $\mathcal{O}(300\,\mathrm{m})$ as it rises up the ice face. They estimate that the total volume flux of the plume outflow is around 1 order of magnitude larger than the subglacial discharge injected at the grounding line, and suggest that submarine meltwater fluxes are around 2 orders of magnitude smaller than the subglacial discharge. They also find that the total freshwater input into the fjord due to submarine melt is significantly larger than that predicted by buoyant plume theory alone. This suggests that submarine melting across the ice face away from the plume is a significant source of freshwater. Similarly, Jackson et al. (2020) presents observational data from LeConte Glacier, Alaska, which suggests that the ambient submarine melt across the ice face is substantially higher than that predicted by buoyant plume theory alone. This highlights the importance of characterization of submarine melt rates away from the plume to develop accurate predictions of the total freshwater flux due to melting at the glacial terminus.

More frequently than direct measurements, subglacial discharge plumes are observed in aerial photography as a result of the influence of plume outflow on ice and sediment at the surface. Interestingly, it has been suggested that the surface emergence of subglacial discharge plumes may occur less frequently as surface melt over inland regions of the ice sheet increases, despite the increased buoyancy flux into fjords at the glacial grounding line. De Andrés et al. (2020) combines oceanographic observations and scaling arguments from plume theory to show that although there is predicted to be increased meltwater driving subglacial

plumes, the corresponding increase in surface runoff increases the strength of the stratification near to the surface. As the stratification within fjords controls the level of neutral buoyancy and so the depth at which horizontal outflow occurs, this means that it is possible for record melt years to counter-intuitively prevent the surface emergence of plumes, where years of weaker melt may allow plumes to penetrate all the way to the surface. This highlights the importance of representation of the full stratification in temperature and salinity within fjords when conducting further theoretical and modelling studies.

1.2.1.2 Buoyancy-driven estuarine circulation

The discharge of freshwater into fjords and estuaries (both with and without marine-terminating glaciers) generates a large-scale overturning circulation, with a surface outflow and a return flow at depth (Straneo et al. 2010). In fjords without glaciers, estuarine circulation is driven by the injection of freshwater in the surface layer, due to runoff from land. Mixing of ambient water in the surface layer due to winds and other processes, combined with mass conservation, generate a balancing inflow in the subsurface layers (Farmer et al. 1983; Stigebrandt 2012). This picture is modified in the case of a proglacial fjord, where freshwater is not only injected at the surface, but also at depth. In this case, subglacial discharge provides a flux of freshwater at the glacial grounding line, together with submarine melt of the glacial terminus across the entire face. This generates buoyant plumes which entrain warm subsurface waters, increasing the melt rate at the ice face (Jenkins 2011; Slater et al. 2016; Magorrian et al. 2016).

Figure 1.4 details the buoyancy-driven estuarine component of fjord circulation for the case of a marine-terminating glacier. The strong stratification within Greenland's fjords may generate two overturning cells, with outflow occurring both at the surface and at mid-depth if the discharge-driven buoyant plume reaches neutral buoyancy below the surface.

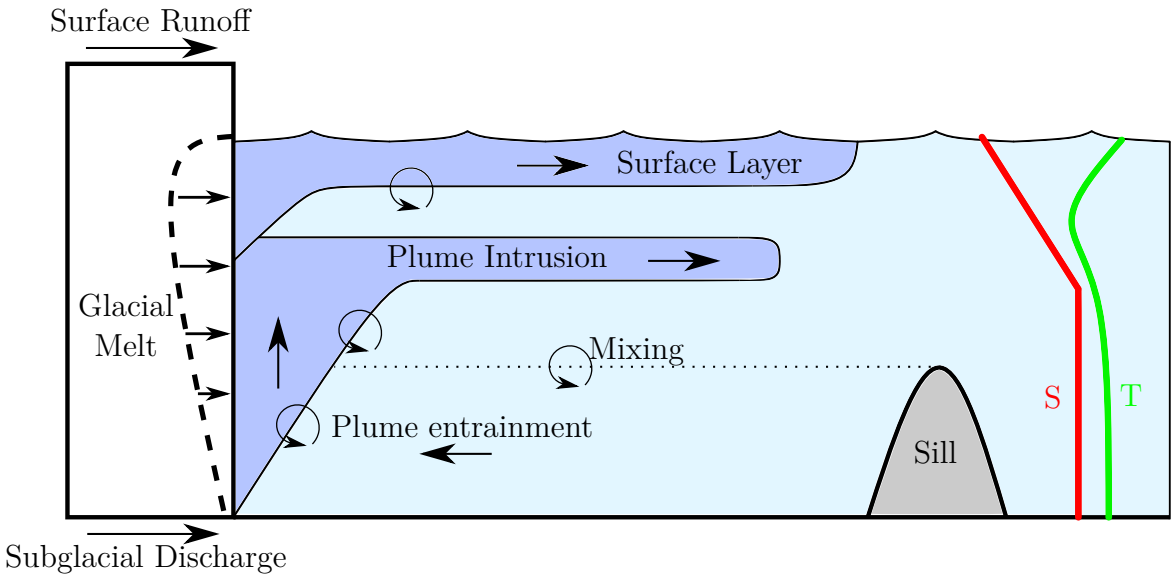

Figure 1.4: Simplified picture of buoyancy-driven estuarine circulation in a fjord with a marine-terminating glacier. Subglacial discharge, surface runoff and glacial melt inject buoyant freshwater, generating buoyant plumes at the ice face and a fjord scale overturning circulation, with an outflow at the surface and an inflow at depth. In highly stratified estuaries, such as Greenland's proglacial fjords, plume water intrusions at mid-depth are commonly observed. Outflows at the ocean surface can also be driven by melt above the plume intrusion depth, or the injection of freshwater at the ocean surface due to runoff from the surface of the ice sheet.

Several parameterizations for estuarine circulation exist, with varying degrees of applicability to Greenland's proglacial fjords (Straneo et al. 2015).

Knudsen relation (see Knudsen, 1900; MacCready and Geyer, 2010)

The Knudsen relation for estuarine circulation assumes a two-layer, steady state system with a volume flux of freshwater Q_f entering one closed end of an estuary (see Figure 1.5), and uses the conservation of volume and salt to calculate the volume transport of the upper layer Q_e^{kn} and return flow in the lower layer Q_2:

$$Q_e^{kn} = Q_f + Q_2, \qquad S_1 Q_e^{kn} - S_2 Q_2 = 0,$$

$$\implies Q_e^{kn} = Q_f \left(\frac{S_2}{\Delta S} \right), \tag{1.3}$$

where S_2 is the salinity of the lower layer and $\Delta S = S_2 - S_1$.

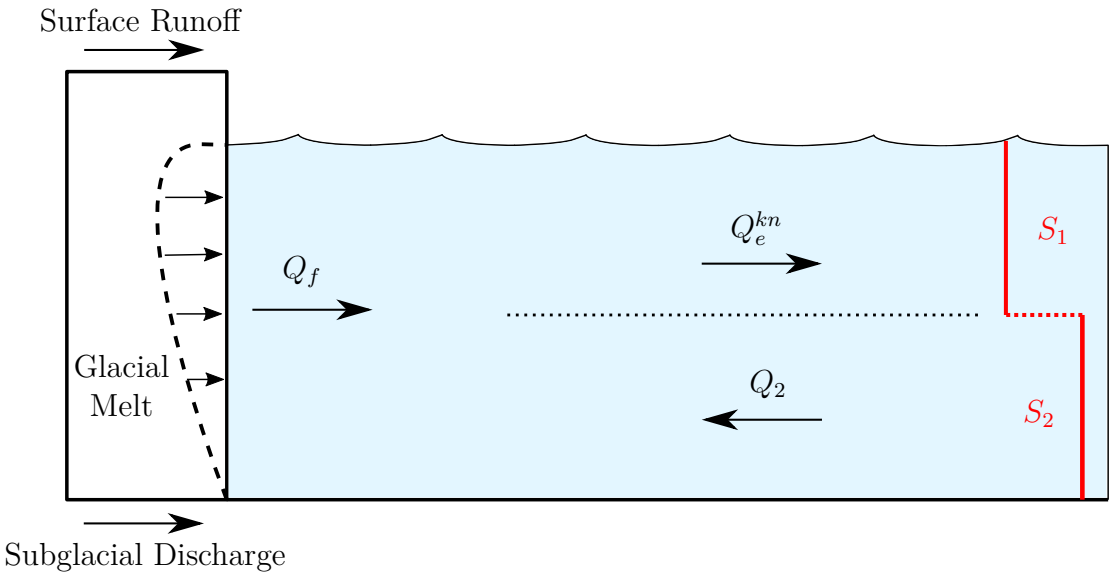

Figure 1.5: Diagram showing the configuration considered in Knudsen (1900), which approximates continuously varying stratification as a two-layer flow with salinity S_1 and S_2 in the surface and lower layers respectively.

The assumptions of steady state and 2 layers are often violated in Greenland's fjords. Firstly, plume intrusions at mid-depth in a continuously varying stratification mean that the estuarine circulation can have 3 or more layers. Also, the high temporal variability in glacial melt rate, as well as the influence of other processes in setting the circulation, mean that Greenland's proglacial fjords often cannot be modelled as steady state, given the time-varying storage of heat and salt within the fjord. Furthermore, the Knudsen relation does not take into account any potential inhibition of return flows at depth due to the presence of a bathymetric sill. It also neglects the potential impacts of vertical stratification in temperature (although salinity variations dominate in setting the differences in density in typical proglacial fjord settings). Considering the above, we conclude that this parameterization may be of only limited relevance to Greenlandic fjords (Straneo et al. 2015), although it does provide a conceptual framework from which to build a more complex estuarine parameterization.

Motyka et al., 2003

Motyka et al. (2003) derived a steady-state model for estuarine circulation in an

Alaskan proglacial fjord. This model assumes that the surface freshwater flux is small compared to that from subglacial discharge and submarine melt, and that the stratification can be described as a single deep ambient fjord water mass with an overlying freshwater layer due to glacial melt. Conservation of mass and salt for this model can be written as in the Knudsen equations. Motyka et al. (2003) further included conservation of heat, assuming that the system is in steady state, and that the only heat sources and sinks are due to submarine melting with volume flux Q_{sm} and subglacial discharge with volume flux Q_{sg}:

$$\rho_1 C_1 Q_e^M \theta_1 = \rho_1 C_2 Q_2 \theta_2 + \rho_{fw} C_{fw} Q_{sg} \theta_{sg} + Q_{sm} L,$$

where Q_e^M is the Motyka estuarine volume flux, C denotes the specific heat capacity of each layer, θ the potential temperature and L the latent heat of fusion for water. Subscripts 1 and 2 refer to the upper layer and lower layer respectively, 'fw' refers to freshwater, 'sg' to subglacial discharge and 'sm' to submarine melt. This theory may be useful in some settings. However, it does not account for the strongly stratified water column typical of Greenland's fjords, potentially giving rise to multiple distinct layers. As mentioned previously, steady state approximations are also frequently violated within Greenland's fjords.

On the whole, buoyancy-driven estuarine circulation within Greenland's proglacial fjords is not well understood. Stratification profiles vary significantly between Greenlandic fjords (Straneo et al. 2015), as do fjord dimensions (Carroll et al. 2017), winds (Straneo et al. 2013), and the sensitivity to the distribution of freshwater input at the ice face (Cowton et al. 2015). This means that previous theoretical parameterizations developed for other settings require non-trivial modification. Modelling efforts are beginning to provide insight into the estuarine contribution to fjord scale circulation (e.g. Carroll et al. 2017). However, only a limited fraction of the parameter space has been explored and so no generalised theory has been developed.

1.2.1.3 Intermediary circulation

A further fjord scale circulation regime, known as 'intermediary circulation' (Stigebrandt 1990), is driven by density gradients between the fjord and the coastal shelf region. This type of flow is common in deep fjords (Klinck et al. 1981), characteristically generating strongly sheared baroclinic flows, and potentially rapid flushing and renewal of fjord waters relative to any other processes (Fraser et al. 2018). The largest drivers of these fjord-shelf density gradients are the along-coast barrier wind events common to much of Greenland's coastline (Straneo et al. 2010). For southeastern Greenland in particular, shelf winds are typically northeasterly (e.g. Broeke et al. 1996), such that Ekman transport during wind events is directed into the coastal fjords.

Wind-driven intermediary circulation is comprised of two main stages (Figure 1.6). Firstly, along-shelf wind events depress the pycnocline between the Atlantic Water and Polar Water on the coast, adjacent to the fjord mouth. The resultant horizontal density gradient forces water into the fjord at the surface, along with direct Ekman-driven transport through the fjord mouth. An outflow at depth is necessary such that the water level within the fjord does not increase by several meters, with any sea surface height gradients between the fjord and the coast generating a barotropic flow out of the fjord, consistent with observations (Straneo et al. 2010). After the wind event ceases, the pycnocline displacement on the coast relaxes, and so is now raised with respect to its new depth within the fjord, resulting in a density gradient in the opposite direction. Now, warm Atlantic Water in the lower layer is drawn towards the glacial terminus, causing a large increase in the amount of heat supplied to the ice face. Fraser et al. (2018) find that the heat flux approximately doubled during barrier wind events in their simulations of Kangerdlussuaq Fjord. In wider fjords, it has been suggested that barrier wind signals propagate into the fjord as coastally trapped Kelvin waves (Jackson et al. 2018; Fraser et al. 2018).

There remains some uncertainty with regards to the ability of waters driven into the fjord to reach the glacial terminus, and thus influence the rate of ice

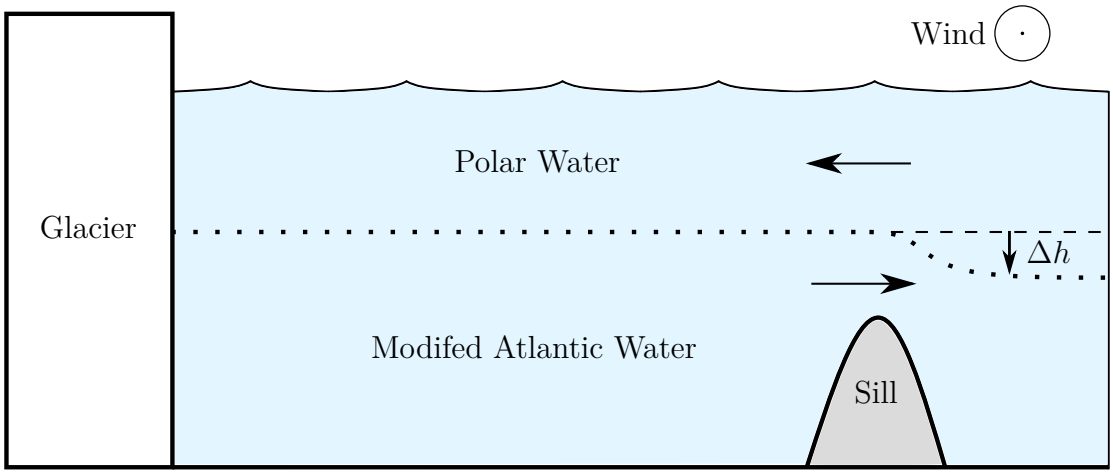

Figure 1.6: Schematic illustrating the generation of intermediary circulation by barrier wind events on the shelf outside of a fjord. Depression of the pycnocline on the coast by Ekman pumping during the wind event generates a density gradient driving water into the fjord at the surface, with an outflow at depth. Once the wind event ends, the coastal pycnocline relaxes and sets up an opposing density gradient between the fjord and the shelf region, driving fjord water out in the surface layer and bringing in warm modified Atlantic water at depth.

ablation directly. For example, Cowton et al. (2015) simulated the effect of barrier winds by varying the stratification at the mouth of an idealised model configuration motivated by Kangerdlussuaq Fjord. They found that whilst wind-driven intermediary circulation is effective at transporting coastal water into the fjord, this water does not travel sufficiently far into the fjord to significantly affect glacial melt. Straneo et al. (2010) point out that shelf-driven baroclinic flows have a far shorter flushing timescale for the renewal of fjord waters than any other drivers of large-scale circulation. This suggests that, even if water driven into the fjord by intermediary circulation does not directly increase the heat transported to the ice face over a typical barrier wind event timescale, this process nevertheless provides a rapid and direct pathway for large scale changes in water properties on the coast to propagate into the fjord.

To develop a simple formula that quantifies the mean intermediary circulation due to fjord-shelf density gradients, Stigebrandt et al. (1990) fitted outputs for

a variety of fjord widths, mouth cross-sectional areas, and sill depths from the simple box model described in Stigebrandt (1990), finding an expression for the mean volume exchange between the shelf and the fjord:

$$Q = \beta \left(\frac{H_s B_m A_f g \Delta M}{\rho_0} \right)^{1/2}. \tag{1.4}$$

Here, H_s is the sill depth, B_m is the smaller of either the fjord mouth width or the local internal Rossby radius of deformation, A_f is the surface area of the fjord and β is a dimensionless fitting parameter, estimated to be 1.7×10^{-3} for the setting they consider. ΔM is the standard deviation of the mass of water above sill depth up to the mean sea surface, per unit area:

$$\Delta M = \int_{H_s}^{H} \sigma_\rho(z) dz, \tag{1.5}$$

where σ_ρ is the standard deviation of density and H is the mean sea surface height. For the Norwegian fjord systems considered by Stigebrandt et al. (1990), this formula gives a volume flux an order of magnitude larger than the estuarine circulation in these fjords. This is consistent with observations in several Norwegian and Greenlandic fjords (Straneo et al. 2010; Jackson et al. 2014; Jackson et al. 2018).

A second, simpler theory developed by Arneborg et al. (2004) and Stigebrandt (2012), applies to narrow, two-layer fjords for which rotational effects are negligible. In this case, the pycnocline heaves uniformly throughout the fjord. For these 'slab model' settings, the upper layer volume flux at the mouth is simply given by:

$$Q = -A_f \frac{\partial \eta}{\partial t}, \tag{1.6}$$

where A_f is the surface area of the fjord, and η is the vertical displacement of the pycnocline.

Previous studies suggest that the exchange fluxes driven by intermediary circulation are large relative to that resulting from other processes discussed in this chapter. Spall et al. (2017) compare the volume flux due to along-fjord katabatic wind events (see §1.2.1.4) in their model simulations with previous observations

of along-fjord and along-shelf wind-driven exchange flows in Sermilik Fjord, east Greenland. Two datasets are used to investigate the along-fjord and along-shelf wind forcing. Firstly, a weather station on the southeast coast of the fjord provides an estimate of the local wind forcing within the fjord (Oltmanns et al. 2014). Secondly, along-shelf winds are taken from ERA-Interim reanalysis data, which has been shown to accurately capture winds along the southeast coast of Greenland (Harden et al. 2011). Model outputs show that over the course of one katabatic wind event, $2.4 \times 10^{10}\,\mathrm{m}^3$ is exchanged between the fjord and shelf. Previous work has shown that the shelf-driven flows in Sermilik drive a typical exchange of $8.5 \times 10^{10}\,\mathrm{m}^3$ over one event (Straneo et al. 2010), 3.5 times larger than the katabatic exchange. Furthermore, shelf wind events occur around 16 times per winter; twice as often as katabatic wind events in Sermilik fjord (Jackson et al. 2014), suggesting that shelf-driven flows may be the dominant method of exchange in some proglacial fjords around Greenland's coastline.

Straneo et al. (2010) used observational data to compare flushing rates for Sermilik Fjord via estuarine circulation and shelf-driven exchange flows. They collected temperature and salinity profiles together with bathymetric and current data, within and just offshore of Sermilik Fjord during two surveys in July and September 2008. Between the two observational campaigns, the mean temperature of the upper 400 m layer of water increased from 0.5 °C to 2 °C. Generating this temperature change through surface forcing would require a surface heat flux in excess of $470\,\mathrm{Wm}^{-2}$. As this is far greater than atmospheric measurements alone can explain, they conclude that this must have been due to the rapid advection of warm shelf waters into the fjord. Over this period, the magnitude of the estuarine circulation and the resulting flushing time is estimated from the observed stratification time series. Assuming that the circulation is limited to the upper 300 m, the shortest estimated estuarine flushing time is $\sim$ 2 years, far too long to explain the observed warming.

Both observational campaigns were conducted during or immediately after significant along-shelf wind events. If the observed velocities were sustained,

the upper 300 m of the fjord would be renewed within four days, representing a significantly faster renewal rate than estuarine circulation alone. The time-averaged effect of the flow generated by these wind events is less clear. Although the summer measurements from moorings within the fjord are too short to establish statistical significance, records of pressure, temperature, and salinity from a third mooring over an eight-month period suggest that anomalies in all three fields are significantly correlated with along-shore wind events. Thus, they conclude that along-shore wind events control the renewal rate of waters in Sermilik Fjord and cause the fjord to rapidly track changes on the shelf.

The literature on shelf-forced renewal of fjord waters is primarily site-specific, with little work undertaken towards developing a generalised theory of this driver of fjord circulation, or towards understanding the relative importance of the driving processes discussed in this section. It is clear (e.g. Jackson et al. 2014; Jackson et al. 2018) that the propagation of disturbances in the coastal pycnocline into fjords differs between 'narrow' and 'wide' fjord cases with respect to the Rossby radius of deformation. Several studies have investigated the role of shelf forcing in the absence of rotational effects using 2D models (e.g. Gladish et al. 2015) and including cross-fjord variations via 3D models (Cowton et al. 2015; Carroll et al. 2017; Spall et al. 2017). Recent studies suggest that the flow structure may be fully three-dimensional, with significant cross-fjord gradients in velocity (e.g. Sutherland et al. 2014).

1.2.1.4 Katabatic wind events

The effects of wind events acting along a stratified estuary have been widely studied, the physical principles being relevant to any long body of water (including rivers, sounds, and some lakes). Of key importance in understanding along-fjord, wind-driven flow in proglacial fjords on the coast of Greenland is the theoretical exploration of Farmer (1976). Neglecting variations in the cross-fjord direction, Farmer (1976) studies a 2D linear model of a 2-layer, infinitely long, stably stratified estuary in the presence of a wind that is potentially time-varying. Further neglecting rotational effects, Farmer (1976) derives expressions for the volume transport of water due to

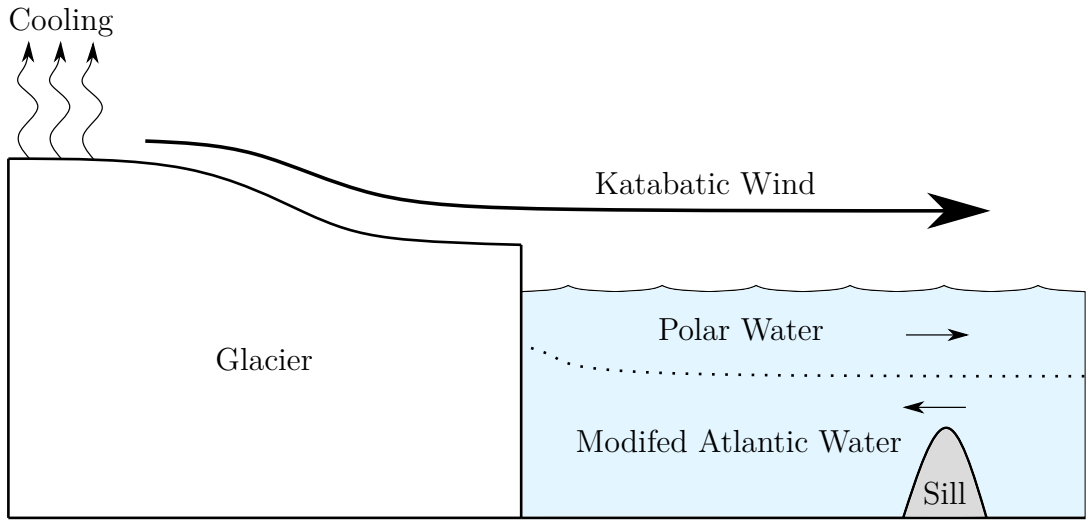

Figure 1.7: Schematic diagram of katabatic wind events. Cool, dense air formed over the ice sheet accelerates down glacial slopes and injects along-fjord momentum into the surface layer of fjord waters.

baroclinic modes excited by the winds, as well as the deviations of the interface of the two layers from equilibrium. These oceanographic responses are of great importance for freshwater transport in Greenland's fjords, where intense katabatic winds form due to cold air descending down glaciers and into fjord valleys (Figure 1.7).

Farmer (1976) starts from the linearised shallow water equations, considering a 2-layer estuary. The volume transport in each layer (where primed quantities refer to the surface layer, and double-primed to the lower layer) is defined as:

$$U' = \int_0^{h'} u' dz, \qquad U'' = \int_{-h''}^{0} u'' dz$$

with u', u'' and h', h'' the velocities and depths of each layer (such that the full depth $h = h' + h''$), and the interface between layers at $z = 0$ (z increasing upwards). A change of variables allows us to see the barotropic and baroclinic modes more clearly:

$$U_1 = U' + U'', \; U_2 = \frac{h''}{h} U' - \frac{h'}{h} U'',$$

$$T_1 = \tau_1 - \tau_3, \; T_2 = \frac{h''}{h} (\tau_1 - \tau_2) - \frac{h'}{h} (\tau_2 - \tau_3) . \tag{1.7}$$

Here, τ_1, τ_2 and τ_3 are the kinematic stress at the free surface, layer interface and bottom, respectively. U_1 is the depth-integrated barotropic transport, and U_2 is the

corresponding baroclinic transport, approximated to lowest order in $\frac{\Delta\rho}{\rho''}$, where ρ'' is the density in the lower layer and $\Delta\rho$ is the density difference between layers. Farmer (1976) then forms a forced wave equation which separates the two modes:

$$\frac{\partial^2 U_i}{\partial t^2} = c_i^2 \frac{\partial^2 U_i}{\partial x^2} + \frac{\partial T_i}{\partial t}, \tag{1.8}$$

where $c_1 = (gh)^{1/2}$ is the surface gravity wave speed, $c_2 = \left(\frac{g\Delta\rho h' h''}{\rho'' h}\right)^{1/2}$ is the baroclinic gravity wave speed and g is the full acceleration due to gravity. The flow response to instantaneously imposed wind represents the sum of counter propagating baroclinic wave responses within the fjord.

Spall et al. (2017) applies this theoretical framework to the case of katabatic wind events in a fjord, in the limit of negligible internal friction. They consider a model configuration whereby a constant, spatially uniform along-fjord wind provides a surface stress of $1.5\,\mathrm{Nm}^{-2}$ for 3 days, with fjord waters consisting of 2 layers, with a lower layer of salinity $S_2 = 32.5$ PSU and upper layer with salinity $S_1 = 31$ PSU. The model is initially at rest, with no sources or sinks of freshwater. Spall et al. (2017) investigates the volume flux of low salinity water (defined as water with salinity S <31.5 PSU) ejected at the fjord mouth, $x = d$. If the barotropic component of the flow is negligible, then the velocity of the upper, low salinity layer is $U(d,t)/h'$, to good approximation. This gives a transport that initially increases linearly in magnitude, until a baroclinic wave has propagated the entire length of the fjord (in a time $t_m = d/c_2$ for a fjord of length d). From $t = d/c_2$ to $2d/c_2$, the magnitude linearly decreases as the pressure gradient set up between the fjord and coastal region goes to zero. After $t = 2d/c_2$, the net transport remains at zero until the along-fjord winds stop, at which point the pressure gradient which previously balanced the wind stress now sets up a return flow in the opposite direction, with a surface inflow and outflow at depth.

It should be noted that theory of Farmer (1976) explicitly neglects rotational effects, whereas the model domain of Spall et al. (2017) is set on an f-plane, with a constant Coriolis parameter $f_0 = 1.2 \times 10^{-4}\,\mathrm{s}^{-1}$. Furthermore, the theory of Farmer (1976) is derived for the case of an infinitely long channel with winds in

the region $x \in [0, d]$, whilst the simulation of Spall et al. (2017) has a periodic coastal region for $x \geq d$. Despite these differences, Spall et al. (2017) shows a close correspondence between theory and model results. This may be due to the fact that, in both cases, the controlling flow velocity is the baroclinic wave speed $c_2 = \left(\frac{g\Delta\rho h' h''}{\rho'' h}\right)^{1/2}$. In the rotationally influenced case, this is the speed at which Kelvin waves travel; identical to the gravity wave speed in the absence of rotation in the Farmer theory (Vallis 2006). The close correspondence between theory and model output despite these differences, however, is remarkable.

1.2.1.5 Sea ice, icebergs, and ice front calving events

Greenlandic fjords typically contain significant floating ice, in the form of sea ice formed when surface water within the fjord freezes as heat is lost to the atmosphere and icebergs which periodically calve from glacial termini. In particular, fjords often contain a dense iceberg and sea ice mélange extending on the order of tens of kilometres from the ice face. The presence of ice in both forms has implications for both the stratification within the fjord, as fresh meltwater can modify the salinity of surface water throughout the fjord, and the circulation response within the fjord as driven by other processes discussed here.

Modification of the ambient stratification in the fjord due to the melting of icebergs or sea ice can have implications for the depth at which subglacial discharge plumes reach neutral buoyancy, and thus the structure of the resultant estuarine circulation. Indeed, freshwater from the melting of discharged icebergs can form a significant fraction of the total freshwater budget of some fjords (Jackson et al. 2016). The surface area available for melting of sea ice and icebergs is potentially an order of magnitude or more larger than that of the ice face, providing a freshwater flux comparable in magnitude to subglacial discharge (Sulak et al. 2017), in some cases accounting for up to 95% of the total heat used for ice melt within fjords (Davison et al. 2020). Previous studies suggest that 68-78% of iceberg melt enters the fjord at depths greater than 20 m (Moon et al. 2018), with up to 100% of this

freshwater remaining at depth. Thus, the melting of icebergs and sea ice is a key control on the stratification within fjords even at depth.

The presence of sea ice and icebergs can also impact the transfer of momentum from katabatic winds into the surface fjord water. Sea ice can act as a surface cap, sheltering fjord waters from the wind and thus preventing a fjord-scale circulation response from developing (e.g. Spall et al. 2017). Icebergs, on the other hand, frequently have keel depths approaching hundreds of metres. Thus, sufficiently strong katabatic wind events which act on the exposed section of these deep icebergs can act as mechanisms to stir a significant fraction of the top hundred metres of the fjord water (Sutherland et al. 2014). Furthermore, the injection of iceberg meltwater itself can drive an estuarine circulation within the fjords, with implications for the transport of heat towards the ice face (Davison et al. 2020).

The controls on iceberg calving rates and the eventual transformation of icebergs and sea ice into fresh meltwater within the fjord is not well understood. Prediction and modelling of fjords including a realistic treatment of iceberg generation at the ice face and residence times within the fjord would require significant investigation, with work in this direction beginning to make some progress. Therefore, whilst we note that physically motivated treatment of icebergs and sea ice within fjords is likely to be crucial to the development of a parameterization scheme, we leave this process for future work.

1.2.2 Fjord geometry, bathymetry, and flow response

1.2.2.1 Fjord geometry

Before the mid-2010s, studies of fjord circulation primarily focused on data collection and analysis at specific sites around Greenland. In recent years, however, more work has been undertaken with the aim of developing a generalised picture of fjord circulation, applicable to all fjords along Greenland's coastline. Previous studies of Scandinavian fjords (Arneborg et al. 2004; Stigebrandt 2012) assume that fjord dynamics more closely resemble the 'slab model', whereby the pycnocline heaves uniformly across the width of the fjord. For this model to be accurate, fluctuations

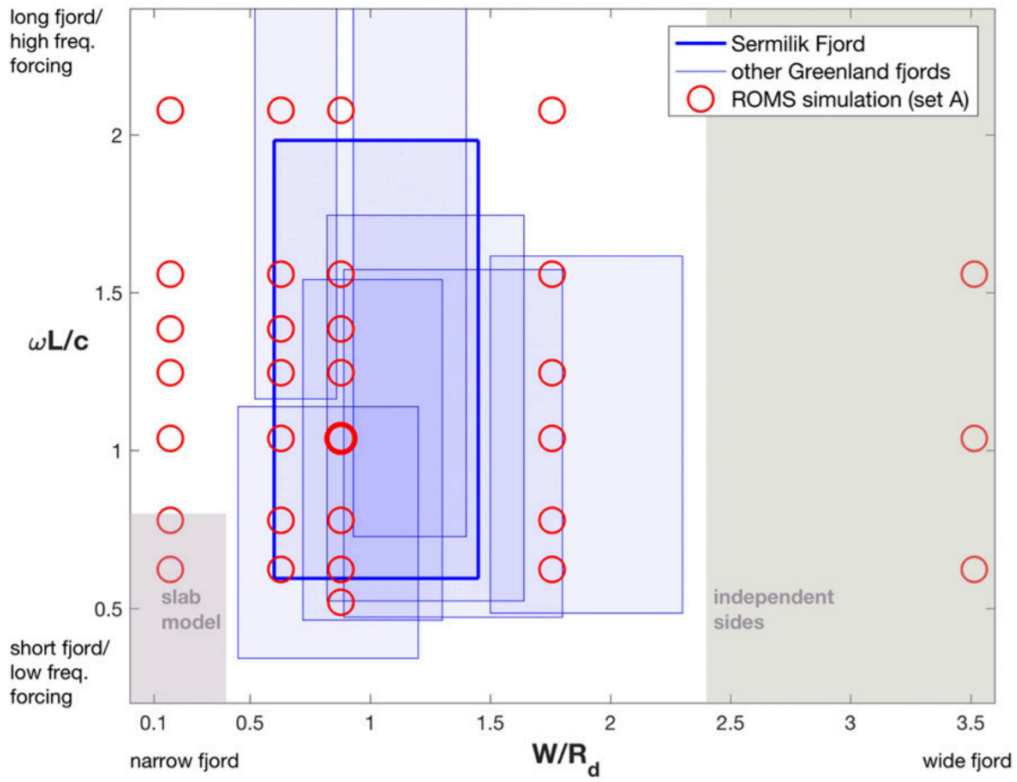

Figure 1.8: Parameter space considered in Jackson et al. (2018). $\omega L/c$ is the along-fjord adjustment timescale L/c divided by the forcing period $1/\omega$, for a fjord of length L. W/R_d is the ratio of fjord widths W to Rossby radius of deformation R_d. Circles represent parameter values employed in the simulations considered by Jackson et al. (2018). The slab model from e.g. Arneborg et al. (2004) is represented in the lower left corner. Wide fjords with effectively independent flow on each side (Inall et al. 2015) are on the right. The Greenlandic fjords from table 1 are shown in blue. Figure from Jackson et al. (2018).

in properties on the shelf must propagate through the fjord on a timescale much shorter than the period of the fluctuations themselves. These fjords are also required to be narrow in comparison to the Rossby radius R_d, such that fluctuations within the fjord have no cross-fjord gradients (Figure 1.8).

Other studies have been conducted into fjords several times wider than the Rossby radius, where rotational effects become greatly important in setting the structure of the fjord circulation (e.g. Inall et al. 2015; Fraser et al. 2018). However, observational efforts have shown that many (if not all) of Greenland's proglacial fjords have widths and density stratifications such that the ratio of characteristic fjord width to R_d is $\mathcal{O}(1)$ (Figure 1.8 and Table 1.1). This intermediate regime

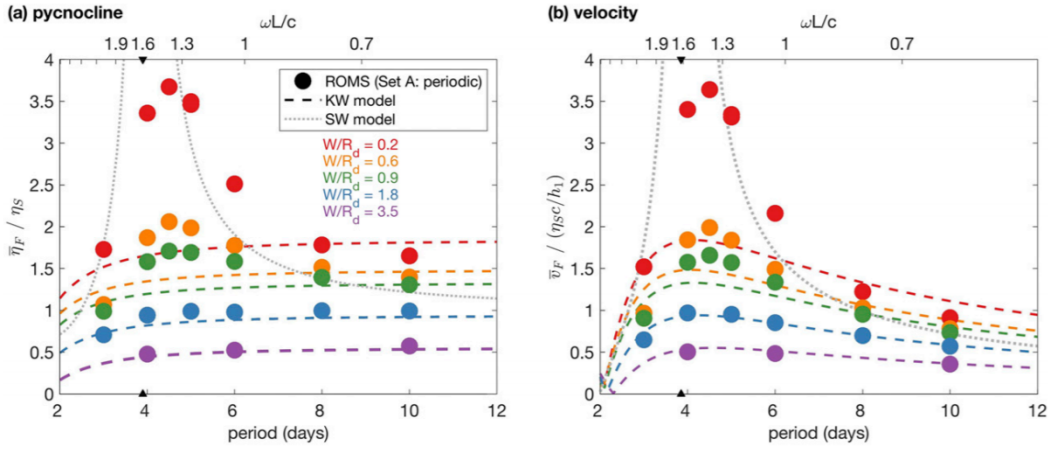

Figure 1.9: Two diagnostics of the fjord circulation response to coastal wind events. (a) Amplitude of the average pycnocline fluctuation in the inner fjord at a point $3L/4$ away from the mouth $\bar{\eta_F}$, normalized by the amplitude of the shelf wave η_S. (b) Amplitude of the average velocity in the upper layer at the fjord mouth scaled by $\eta_S c/h_1$, with the phase speed of oscillations on the shelf $c = 1.1\text{ms}^{-1}$ and h_1 the upper layer thickness. Circles represent model configurations, where colour indicated W/R_d. Dashed lines are the theoretical Kelvin wave response. The dotted line is the standing wave response. Figure from Jackson et al. 2018.

remains relatively unexplored. Understanding this region of parameter space is crucial to developing a physically relevant generalised picture of circulation within Greenland's proglacial fjords.

Jackson et al. (2018) investigated an idealised model of fjord circulation due to wind-driven intermediary circulation in fjords where the ratio of width W to Rossy radius of deformation R_d is $\mathcal{O}(1)$, comparing results to both the 2D standing wave slab model, and the fully 3D case, where waves propagate as coastally trapped Kelvin waves (see Jackson et al. 2018, Fig. 3 for a schematic of each model). They found that the flow response is highly dependent on the precise value of W/R_d, based upon several metrics (Figure 1.9). For $W/R_d \gtrsim 1.8$, the flow response effectively matches the pure Kelvin wave response, suggesting a fully 3D flow structure within the fjord. The other limit ($W/R_d \lesssim 0.2$) effectively displays purely 2D behaviour.

The model simulations with $W/R_d = 0.6,\ 0.9$ lie in the intermediate region between these two regimes. The metrics in Figure 1.9 show some amplification near the standing wave resonant frequency. However, the response generally falls

closer to the Kelvin wave solution. Importantly, even when the fjord width is half the deformation radius the cross-fjord structure still provides a significant control on the flow, with a resonant amplification far smaller than the corresponding slab model case. This is supported by the work of Sutherland et al. (2014), who used GPS-tracked icebergs in Sermilik fjord, where $W/R_d \sim 0.8$, to show that surface outflows generally display behaviour consistent with rotational steering. Hence, for much of the typical range of parameter space inhabited by Greenland's fjords, the flow structure may be fundamentally three-dimensional.

1.2.2.2 Influence of bathymetric sills

Many proglacial fjords have bathymetric sills at or near the mouth, which modify the flow response to forcing (Straneo et al. 2012). These sills usually represent the historical furthest extent of the glacier; rocks and sediment carried along by the flow of ice are deposited over time, forming a raised mound stretching across the width of the fjord. The precise effect of these sills on the transport of heat to the GrIS is not fully understood, not least because the number and depth of sills varies between fjords. Typically, sills in Greenland's fjords are sufficiently deep for both the AW and PW layers to exchange between the fjord and shelf outside. This is in contrast to assumptions made in most fjord theories that the sill is shallow enough to entirely block exchange in the lower layer (Straneo et al. 2015).

Observations of the lifting of isopycnals within Godthåbsfjord, southwestern Greenland, reveal the presence of an intermittent dense inflow over a subglacial sill acting as a primary control on the renewal rate of water below sill depth (Mortensen et al. 2011). This concept is supported by observations of dissolved oxygen in water below sill depth in Petermann Fjord in northwestern Greenland (Johnson et al. 2011). Here, it is found that water below sill depth but above the glacial grounding line is the oldest in the fjord (i.e. this water has the longest flushing timescale).

In the absence of a buoyancy-driven circulation, Spall et al. (2017) extended the treatment of along-fjord katabatic wind events to settings with various sill depths, investigating the impact on the upper layer outflow. The sill height above the bottom

was varied from 100 m to 350 m, with the latter corresponding to a sill at the same depth as the interface between layers. They found that, for moderate sill heights, the exchange is close to that predicted by the Farmer theory discussed previously. However, for sill heights greater than 75% of the lower layer, the volume exchange rapidly decreases. In this case, an overturning circulation begins to develop within the fjord to balance the surface outflow, due to the restriction of inflow at depth.

Filling box models

Theoretical work on the fluid dynamics of filling box models, initially developed for the design of building ventilation (e.g. Worster et al. 1983 and Kaye et al. 2004), may provide some insight into the flow structure of waters below sill depth in the presence of a subglacial-discharge-driven buoyant plume. The most relevant of these models consider a stratified fluid in a ventilated box, with a point source of buoyancy generating a half-axisymmetric plume at one side of the domain and a ventilating gap on the opposing side of the domain (see Figure 1.10). The volume flux into the plume due to entrainment below the vent generates a weak downwelling through the interior of the box to conserve mass. Kaye et al. (2004) find that the steady-state flow through the ventilating gap is proportional to the ratio of timescales T_d/T_f, where T_d is the time taken for a ventilated box to drain of buoyant fluid through the ventilating gap, and T_f is the time taken for fluid from a buoyant plume to fill a closed box.

However, their configuration relies on a second ventilating gap below the first to prevent an overturning exchange through a single gap, and so their result is untested in fjord-like configurations. The fjord water renewal rate may impact the deep fjord temperature and glacial melt rate, with magnitude varying significantly between fjords, and is potentially dependent on the depth of the glacial grounding line relative to the sill depth, although this requires further study. Filling box models of this sort do not include the effects of rotation on the flow configuration through the vent, which is likely to impact the validity of this approach for fjords with widths approaching the Rossby radius of deformation.

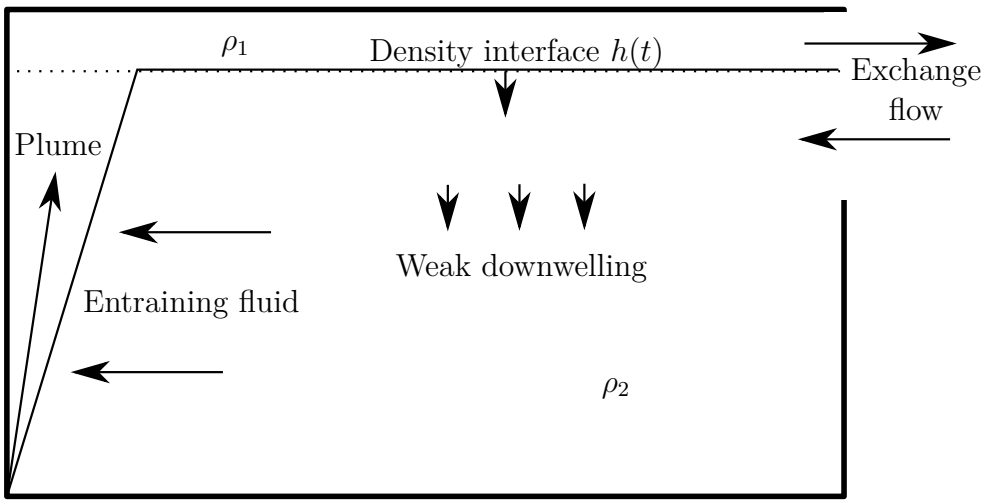

Figure 1.10: Schematic diagram of a ventilated filling box model driven by a buoyant plume, of potential relevance to renewal rates of fjord waters for silled fjords.

Hydraulic control theory

Of more relevance to flow in silled fjords is previous work on hydraulic control theory for multi-layered flows in geophysical settings. Hydraulic models are based upon the shallow water equations or similar reduced-gravity models, and typically make several simplifying assumptions. They treat the stratification as a series of discrete, homogeneous layers (see Figure 1.11). The hydraulics of single-layer flows beneath or above a passive layer are well studied. Two- or more layer flows introduce complexity into the description of allowed flow states and behaviours, given that each layer – and the interaction between layers – contributes to setting the overall flow state (Stommel et al. 1953). Armi (1986) formulated the internal hydraulics of non-rotating, two-layer flows in a channel of rectangular cross-section in terms of the internal Froude number (a dimensionless number essentially characterising the ratio of kinetic to potential energy) of each layer, and produced graphical solutions in Froude number space for the possible flow states. Broadly, these flow states are often characterised as combinations of shallow layers with high flow velocities, and deep layers with low flow velocities. The model of Armi (1986) neglected several physical processes and scenarios which have since been studied. For example, time-dependent forcing (e.g. Helfrich 1995), more complex stratifications

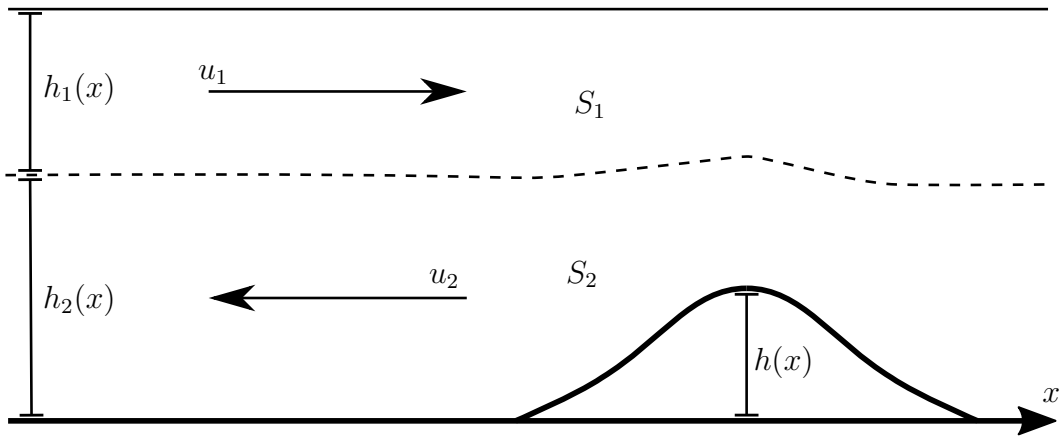

Figure 1.11: Schematic diagram of a two-layer exchange flow over a bathymetric sill with a rigid lid (e.g. Armi 1986). S_i denotes the salinity, h_i the thickness, and u_i the velocity of layer i, with $h(x)$ the bathymetry.

(e.g. Smeed 2000), and rotation (e.g. Dalziel 1991). Selected studies and their assumptions are outlined in Table 1.2.

The graphical approach of Armi (1986) was extended by Dalziel (1991), who used a functional approach based on that of Gill (1977). In both treatments, the flow is assumed to be hydrostatic, inviscid and steady, most frequently with a rigid lid, although some treatments consider a free uppermost surface. For example, under the Boussinesq approximation and considering cross-fjord velocities to be negligible, the along-fjord momentum equation in each layer for a three-layer model with layers $i = 1,\ 2,\ 3$ (where i increases downward) is:

$$\begin{aligned}
i = 1, \qquad & \frac{\partial}{\partial x}\left(\frac{1}{2}u_1^2 + \frac{p_0}{\bar{\rho}} + \frac{g}{\bar{\rho}}\rho_1 z_T\right) = 0, \\
i = 2, \qquad & \frac{\partial}{\partial x}\left(\frac{1}{2}u_2^2 + \frac{p_0}{\bar{\rho}} + \frac{g}{\bar{\rho}}\left[\rho_1 h_1 + \rho_2(z_T - h_1)\right]\right) = 0, \\
i = 3, \qquad & \frac{\partial}{\partial x}\left(\frac{1}{2}u_3^2 + \frac{p_0}{\bar{\rho}} + \frac{g}{\bar{\rho}}\left[\rho_1 h_1 + \rho_2 h_2 + \rho_3(z_T - h_1 - h_2)\right]\right) = 0,
\end{aligned} \tag{1.9}$$

where p_0 is the pressure at the surface, $\bar{\rho}$ is the reference density, ρ_i is the density, h_i the thickness and u_i the along-channel velocity in layer i, and $z_T(x)$ is the total depth.

$$\frac{\partial \boldsymbol{J}}{\partial x} = 0. \tag{1.10}$$

Source	Layers	Key Assumptions
Armi 1986	2	Rectangular channel cross-section, no rotation
Timmermans et al. 2005	2	Rectangular channel cross-section, with rotation
Bormans et al. 1989	2	Non-rectangular cross-section, no rotation, includes dissipation
Dalziel 1991	2	Rectangular cross-section, with rotation
Helfrich 1995	2	Time dependent forcing, rectangular cross-section, no rotation
Laanearu et al. 2007	2	No rotation, quadratic channel cross-section
Hogg 1983	3	With rotation, unidirectional flow
Engqvist 1996	3	With rotation, exchange flow, zero flux middle layer
Smeed 2000	3	No rotation, exchange flow
Killworth 1992	Continuous	Continuously stratified unidirectional flow over a sill, with rotation

Table 1.2: Selected previous studies of hydraulic multi-layer flows in silled channels, and their specific assumptions and settings.

These momentum equations are combined with equations linking velocity u_i and layer thickness h_i in each layer. In the non-rotating case, this is simply an expression of volume conservation, with the volume flux $Q_i = u_i h_i$ in each layer. With rotation, the most practical choice is the across-fjord momentum equation in each layer, which introduces the Coriolis parameter:

$$f u_i = -\frac{1}{\bar{\rho}} \frac{\partial p_i}{\partial y} \tag{1.11}$$

with p_i the hydrostatic pressure in each layer. It is important to note that a consequence of rotation in channel flow is the development of cross-channel gradients in the layer thicknesses, such that h_i is a function of both along- and cross-channel position.

Integrating Equation 1.9 with respect to x, taking the difference between consecutive layers, and combining with either the expression for continuity in each layer (in the non-rotating case), or the cross-fjord momentum equation (in the

rotating case) leads to $i-1$ equations, which together form a functional $\boldsymbol{J}=0$. The continuous tracing of roots of this functional through a constriction is necessary for a given flow state to be possible. That is, flow state solutions satisfy

Using the chain rule, this can be rewritten in terms of the layer thicknesses h_i and channel geometry (with b the channel width and h the depth):

$$\boldsymbol{K}\begin{pmatrix}\frac{\partial h_2}{\partial x}\\ \\ \frac{\partial h_3}{\partial x}\\ \vdots\\ \frac{\partial h_i}{\partial x}\end{pmatrix}=\boldsymbol{L}\begin{pmatrix}\frac{\partial b}{\partial x}\\ \\ \frac{\partial h}{\partial x}\end{pmatrix}, \tag{1.12}$$

where

$$\boldsymbol{K}=\begin{pmatrix}\frac{\partial \mathcal{J}_1}{\partial h_2} & \cdots & \frac{\partial \mathcal{J}_1}{\partial h_i}\\ \vdots & & \vdots\\ \frac{\partial \mathcal{J}_{i-1}}{\partial h_2} & \cdots & \frac{\partial \mathcal{J}_{i-1}}{\partial h_i}\end{pmatrix},\ \text{and}\ \boldsymbol{L}=\begin{pmatrix}\frac{\partial \mathcal{J}_1}{\partial b} & \frac{\partial \mathcal{J}_1}{\partial h}\\ \vdots & \vdots\\ \frac{\partial \mathcal{J}_{i-1}}{\partial b} & \frac{\partial \mathcal{J}_{i-1}}{\partial h}\end{pmatrix}. \tag{1.13}$$

Note that the rigid lid assumption means that for i layers, there are $i-1$ independent layer thicknesses h_i. For a channel of constant width ($\partial b/\partial x=0$), at the crest of any sill in the bathymetry (where $\partial h/\partial x=0$), Equation 1.12 shows that either all $\partial h_i/\partial x=0$ simultaneously, or $\det \boldsymbol{K}=0$. The latter condition corresponds to the flow at the sill becoming critical (transitioning from sub- to supercritical flow) relative to an internal wave mode in one or more layers. Thus, a key result is that unless the flow in one or more layers is critical, the layer thicknesses are symmetrical about the top of the sill. Otherwise, the different solution branches to $\boldsymbol{J}$ can be shown to meet at points which satisfy $\det \boldsymbol{K}=0$ (Gill 1977; Dalziel 1991).

1.2.3 Summary

In general, the circulation within Greenland's proglacial fjords is driven by a combination of several processes. Buoyancy-driven flow, due to freshwater influx at the glacial terminus, drives a fjord-scale overturning circulation with a fresh outflow within a stratified surface layer. Along-fjord katabatic wind events can also

drive a similar vertical flow structure to the estuarine circulation, with a significant percentage of the relatively fresh surface layer ejected from the fjord during each wind event. Shelf winds and mixing drive baroclinic exchange flows between fjord and shelf, which have been shown to dominate the renewal of fjord waters on short timescales, although the mean seasonal effect averaged over multiple cycles remains less clear. Sea ice and icebergs can both drive circulation, and modify the fjord response to other driving processes. The relative importance of these processes varies over the course of the year as atmospheric and oceanic properties change, and between specific fjords due to differing geometries and bathymetries. However, the first-order controls on the variation between fjord settings are not well understood.

The lack of sustained observations within a representative ensemble of Greenland's proglacial fjords represents a key limitation in developing understanding of GrIS melt. Current observational studies are from a modest number of sites. A generalised picture of how circulation varies between fjords has not been developed. Perhaps the most progress in this regard has been made towards understanding the 'intermediary circulation', although even here there is no theory spanning all of the relevant parameter space. Theory relevant to the estuarine circulation is typically based upon heat and salt conservation arguments, and there is little explicit treatment of the actual flow dynamics. However, idealised models and some simple theoretical developments show good correspondence with observational data for specific fjords, suggesting that these models may be useful tools in developing a generalised theory.

Studies of the shelf-driven intermediary circulation require precise knowledge of the background water properties within the fjord, with the intermediary circulation itself recovered as a residual about the mean state. This requires observations not only of water within the fjord but also on the coastal shelf. Furthermore, estuarine circulation typically includes outflow at the interface between the PW and AW layers, potentially affecting the intermediary volume flux, which is driven by changes in the depth of this interface.

Bathymetric sills have the potential to modify the impact of forcing processes on the stratification within the fjord, by restricting the range of depths over which inflow and outflow can occur. This has implications for the exchange of heat and salt between the fjord and the wider ocean, and for glacial melt rates as a result. Previous studies of multi-layer exchange flow over sills typically use hydraulic models based on shallow-water equations. However, no previous study is directly applicable to subglacial-discharge-driven estuarine circulation within fjords, which requires an as yet uninvestigated combination of approximations and assumptions. Specifically, fjords are most accurately described using a 3-layer model with outflow in the middle layer, inflow in the lower layer, and volume fluxes and layer thicknesses in the fjord upstream of the sill set by plume dynamics, including the influence of rotation.

1.3 Ice-ocean interaction in current generation Earth system models

Both the Greenland and Antarctic Ice Sheets play a major role in determining the current and future state of the global Earth system. Ice sheets are subject to many interactions and feedbacks with atmospheric, oceanic, radiative, and solid earth processes (see Fyke et al. (2018) for an overview). The realistic representation of ice sheets within coupled climate models is key to the accurate prediction of future global climate and sea level, on timescales of decades to centuries.

The interaction between the Antarctic Ice Sheet and the ocean is more easily represented within Earth system models, due to larger spatial scales and the absence of ubiquitous fjord-like topographic constrictions, although some exist (e.g. Lundesgaard et al. 2019). In the UKESM (UK Earth System Model) GO6 and GO7 configurations (Kuhlbrodt et al. 2018; Storkey et al. 2018), for example, ocean temperatures and salinities are used to calculate melt at the marine-terminating ice sheet margins. Either the ocean properties are extended into Antarctic ice shelf cavities and basal melt rates calculated directly (GO7 configuration), or the ice shelf cavities are assumed closed (GO6 configuration), with either treatment

allowing for the inclusion of ocean forced melting in the ice sheet component of the model (Storkey et al. 2018).

The impact of fjord circulation on the exchange of heat and freshwater between the GrIS and the wider ocean is a key and as yet unrepresented process in most, if not all, Earth system models. Some previous work has developed a simple understanding of the relationship between glacial melt rates and drivers of fjord circulation (e.g. Slater et al. 2019). However, no attempt has been made to represent the impact of fjord circulation itself on glacial melt. Currently, the resolution of standard global models used for long-term climate projection is such that all glaciers at Greenland's margins are treated as land-terminating, with freshwater due to melt calculated from the ice-atmosphere component and injected into the surface ocean some grid cells away from the coastline. There is no marine boundary condition for the GrIS (Smith et al. 2021). The lack of a fjord circulation parameterization allowing for more physical interaction of the GrIS with the ocean represents a key limitation in the ability of current-generation Earth system models to predict the future evolution of both the Greenland Ice Sheet and, by extension, the wider climate system.

Previous work in this area has focused on the development of high (and variable) resolution adaptive mesh fjord models, able to capture the bathymetry and forcings within Greenland's fjords directly, with the initial aim of inclusion in regional or global-scale climate models (e.g. Kopera et al. 2018). However, the complexity of fully representing and computing the range of possible flow forcing conditions with accurate bathymetry for the $\mathcal{O}(300)$ fjords around Greenland's coastline means that this approach quickly becomes computationally prohibitive.

Any parameterization scheme intended to provide a coupling between the ice sheet and ocean components of an Earth system model must fulfil two functions. The ice sheet component requires both the projection of ocean conditions to the ice face, modified by fjord circulation and other relevant processes, as well as some treatment of the impact of circulation within the fjord itself, in order to calculate the melt rates at glacial termini. The ocean component requires information on the amount and spatial distribution of meltwater, both due to atmospheric melt, and

the melt driven by ocean forcing and fjord circulation. In general, this will result in a vertically distributed exchange flow between the ice sheet, fjord, and wider ocean. Future work should include the addition of some representation of iceberg calving, although little simple characterization of this process currently exists.

1.4 Project Aims

Modelling of water velocities and properties near to the ice is of key importance to the prediction of melt rates at marine-terminating glaciers around Greenland's coastline, with implications for predictions of ice sheet stability, and global climate. Several processes are thought to contribute to setting the flow structure within fjords. These processes modify the heat and salt exchanges with the wider ocean, and control submarine melt rates at glacial termini as a result. Inclusion of the ocean forced melting of marine-terminating glaciers around Greenland's coastline within Earth system models requires representation of these processes in the form of a sub-grid scale parameterization scheme. In recent years, a number of studies have begun to increase understanding of various processes which control circulation within Greenland's proglacial fjords and submarine melt rates of marine-terminating glaciers. However, many questions remain, and quantitative understanding of these processes must be built before a parameterization scheme can be developed.

In this thesis, we develop simple theoretical understanding of fjord circulation in a subglacial-discharge-driven estuarine regime, and take the first steps in the development of a sub-grid scale parameterization scheme in the form of a multi-layered box model.

In Chapter 2, we investigate fjord circulation in a subglacial-discharge-driven regime, for fjords without bathymetric sills. We employ computational modelling of idealised fjords to explore the fjord scale circulation and glacial melt rates over a geophysically relevant range of fjord widths and subglacial discharge fluxes. We build on previous theoretical scalings from plume theory to develop understanding of the vertical structure of along-fjord flow, and develop a phenomenological representation

of cross-fjord flow at the glacial terminus to predict the spatial pattern of melt across the entire ice face.

In Chapter 3, we develop a simple box-model parameterization of ice-ocean interaction as a result of subglacial-discharge-driven circulation in Greenland's proglacial fjords. This is in the form of a multi-layered box model, with parameterized exchange rates between the ice face and the wider ocean based on the theoretical developments in Chapter 2. The scheme is relatively simple and flexible, such that future refinements and additions can be made as understanding of the relevant physical processes develops.

In Chapter 4, we investigate the impact of bathymetric sills on the circulation within Greenland's proglacial fjords. We again employ computational modelling of idealised fjords, to build understanding of the effect of bathymetric sills on the exchange of heat and salt between the fjord and the wider ocean. This is intended to lay the groundwork for the inclusion of bathymetric sills into the box-model parameterization developed in Chapter 3, via modification of the theoretical arguments developed in Chapter 2. Then, in Chapter 5 we summarise and discuss potential avenues for future work.

2

Scalings for subglacial-discharge-driven circulation in Greenland's proglacial fjords

2.1 Introduction

Chapter 1 emphasised the importance of characterising circulation within Greenland's proglacial fjords in order to develop accurate predictions of glacial melt rates at the ice face. In particular, it would be of great utility to develop simple, physically-based scaling arguments which capture the leading order impact of changes to geophysically relevant parameters, and could form the basis of a parameterization scheme.

In this chapter, we develop theoretical understanding of fjord scale circulation in a subglacial-discharge-driven regime, focussing on fjords without an appreciable sill. We employ computational modelling of idealised fjords to explore the flow structure and resultant glacial melt rates over a geophysically relevant range of subglacial discharge fluxes and fjord widths. In particular, we focus on horizontally integrated vertical profiles of properties at the fjord mouth, as these could be usefully parameterized as a coupling between global-scale ice and ocean models. The cross-fjord averages of along-fjord velocities are found to remain the same along the length of the fjord, leading to the development of scaling laws based on plume theory to describe the flow at the fjord mouth. At the ice face, cross-fjord velocities driven by

the plume and resulting fjord-scale circulation are found to provide a strong control on melt rates. We develop theoretical arguments predicting cross-fjord velocities at the ice face, using this to predict the resultant spatial melt pattern across the ice, given only the subglacial discharge flux, fjord width, and ambient fjord stratification.

2.2 Idealised fjord model

To develop theoretical insight, we consider a suite of numerical experiments in an idealized fjord domain. For simplicity, we restrict the simulations to fjords with rectangular cross sections, and aim to characterise the flow structures which occur across a geophysically relevant range of parameter space. The full computational model configuration is described in §2.2.1. We discuss the parameter space spanned by our simulations in §2.2.2.

2.2.1 Computational model setup

We use the Massachusetts Institute of Technology general circulation model (MITgcm), described in Marshall et al. (1997) and Adcroft et al. (2004). For our purposes, it solves the Navier-Stokes equation (see Appendix A2.1) under the Boussinesq approximation and including the Coriolis force, on an Arakawa C-grid. The model domain is set on an f-plane, with a constant Coriolis parameter $f = 1.4 \times 10^{-4}\,\mathrm{s}^{-1}$, consistent with a Greenlandic fjord at a latitude $\sim 75\,^{\circ}\mathrm{N}$. Sub-grid scale horizontal viscosity is parameterised by the Smagorinsky scheme and vertical viscosity is parameterized using the K-Profile Parameterization (KPP) scheme (Large et al. 1994). Unless otherwise stated, the model has horizontal resolution of 500 m and 20 vertical levels with 15 grid cells of 10 m vertical extent to resolve the strongly stratified surface layer, and 5 grid cells of 70 m in the more weakly stratified lower layer, such that the total fjord depth $D = 500\,\mathrm{m}$. We run the MITgcm in a simple 'long channel' domain configuration, with a sheer vertical ice cliff at one end, vertical, straight, adiabatic sidewalls, and an open boundary with restoring sponge region at the other end (Figure 2.1). The open boundary is constrained to have a uniform

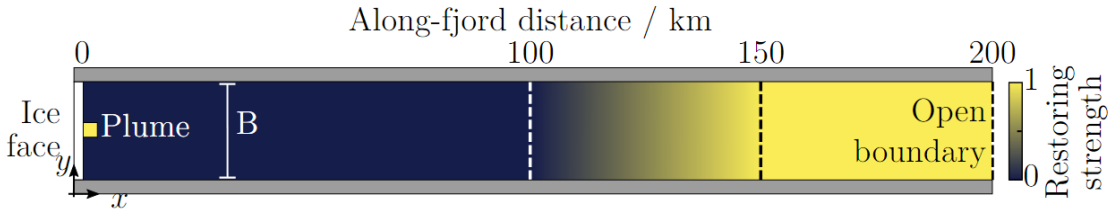

Figure 2.1: Plan view of the MITgcm model configuration. A subglacial discharge plume is parameterized using the ICEPLUME package (Cowton et al. 2015), adjacent to a thermodynamically active ice face at $x = 0$. The fjord is bounded by impermeable walls at $y = \pm B/2$ for a fjord of width B. To prevent waves from reflecting off the open boundary and back into the fjord itself, the salinity and temperature are restored to the initial ambient stratification in the second half of the domain. Between 100 km and 150 km the restoring strength increases linearly, reaching a constant maximum value between 150 km and 200 km.

barotropic velocity, conserving total mass in the domain by balancing the incoming volume flux of freshwater at the ice face.

In the full geophysical setting, the injection of buoyant freshwater at depth, either through submarine melt or as a direct subglacial discharge flux Q_{sg}, generates strongly non-hydrostatic and turbulent flow (e.g. Xu et al. 2012). To directly resolve these processes in MITgcm would require prohibitively high resolutions and short timesteps when coupled to fjord scale circulation. Hence, we model this non-hydrostatic flow using the 'ICEPLUME' parameterization (Cowton et al. 2015). ICEPLUME solves the ordinary differential equations for a buoyant meltwater plume fed by subglacial discharge at the grounding line and rising up the ice face, and then exchanges heat, salt, and mass with neighbouring ocean grid cells (see Equation 1.1a–Equation 1.1d), solving for the plume salinity, temperature, velocity and radius at each depth. The vertical level at which the plume is predicted to terminate then acts as a volume source into the ocean domain. Grid cells below this depth level – in which the plume entrains ambient water – behave as sinks. Turbulent plumes are primarily comprised of entrained ambient fluid after a short distance from the initial freshwater source. Outside of the plume, the ice face at $x = 0$ is thermodynamically active, with melt rates calculated via the 'three equation formulation' (Equation 1.2a–Equation 1.2c, except with the vertical velocity of the plume w replaced by the the magnitude of the velocity tangential to the ice face)

and a background velocity of $0.01\,\mathrm{ms}^{-1}$ unless otherwise stated (see Cowton et al. 2015 for further details of the thermodynamic implementation).

To mitigate the reflection of waves from the open boundary, a sponge region in the outer half of the domain relaxes salinity and temperature to the initial ambient stratification as illustrated in Figure 2.1. We choose the restoring timescale to be the approximate time taken for the plume outflow to travel the length of the sponge region, which differs for each value of subglacial discharge and fjord width. This timescale ranges from 1×10^6 to 1×10^7 seconds, inversely proportional to subglacial discharge which varies from $Q_{sg} = 50 - 1500\,\mathrm{m}^3\,\mathrm{s}^{-1}$. We increase the restoring strength linearly from $x = 100\,\mathrm{km}$ to $x = 150\,\mathrm{km}$ such that the sponge region does not reflect waves back towards the ice face.

2.2.2 Parameter space

Greenland's fjords are typically $\sim 100\,\mathrm{km}$ long, $\sim 10\,\mathrm{km}$ wide and $\lesssim 1\,\mathrm{km}$. Recent work has made some progress in quantifying the dimensions of all fjords around Greenland's coastline (Slater et al. 2022). The parameter space covering all possible fjord dimensions, shapes, and forcing conditions is vast and multidimensional, requiring an impractical number of model configurations to represent all possible combinations of parameter values. To build a picture of the first-order controls on fjord circulation, we therefore restrict the number of parameters under consideration, focusing on a number of easily characterised cases. We initially restrict the parameter space to fjord width and subglacial discharge flux, with no sill, and other fjord dimensions and conditions held constant.

Buoyant melt plumes driven by subglacial discharge are primarily a summertime phenomenon. Freshwater from atmospherically induced melting over inland regions of the ice sheet drains towards the ice sheet margins and into proglacial fjords. This occurs both as runoff at the surface, and via a network of drainage channels beneath the glacier itself, created when surface meltwater drains down through crevasses in the ice (e.g. Hewitt 2011). Water flow beneath the ice can be distributed, or channelized. However, subglacial drainage channels can be shown to have a lower

water pressure for increased fluid volume flux, whilst distributed flow has larger water pressure (Hewitt 2011). This results in subglacial channels drawing in water from the surrounding distributed flow. Hewitt (2011) derives a length scale for the spacing of these subglacial drainage channels of $\sim 10\,\mathrm{km}$ around the margins of Greenland's ice sheet, meaning that proglacial fjords would typically be expected to be fed by only one or two drainage channels. Thus, the base model configuration we consider has one single, central discharge plume. Here, we consider half-conical discharge plumes only, with the line plume case left for future work.

Typical estimates of summer subglacial discharge fluxes into Greenland's proglacial fjords are $\lesssim 750\,\mathrm{m^3\,s^{-1}}$ (Straneo et al. 2013). In non-summer months, freshwater fluxes are not distinguishable from zero (Jackson et al. 2016). The exchange flow which develops in summer months allows the inference of freshwater flux as a residual. Jackson et al. (2016), find a maximum freshwater flux into Sermilik fjord of approximately $1500\,\mathrm{m^3\,s^{-1}}$ over the course of a year. This includes the contribution of melting icebergs, surface runoff, and submarine melting of the glacial terminus, as well as the subglacial discharge flux itself, and hence is a guide for the upper bound. To span this range we apply steady subglacial discharge fluxes of 50, 225, 400, 750, and $1500\,\mathrm{m^3\,s^{-1}}$, with each simulation allowed to run out to steady state. Building understanding of the steady-state response is an important first step towards understanding the more complex transient response to such time-dependent forcing.

Typically, the summertime stratification within Greenland's fjords consists of a cool, fresh Polar Water layer overlying a warm, more saline layer of modified Atlantic Water (Straneo et al. 2012). The Polar Water layer is strongly stratified, with a large vertical salinity gradient. The modified Atlantic Water layer, on the other hand, has a weak salinity gradient and is therefore of approximately constant density. In winter months the mixed layer is much deeper, leading to a stratification more accurately described by two layers of constant density with a pycnocline between them. However, there is thought to be negligible subglacial discharge during winter months, due to the reduced surface melt over the inland regions of the ice sheet. Thus, we consider fjords with ambient stratifications consisting of

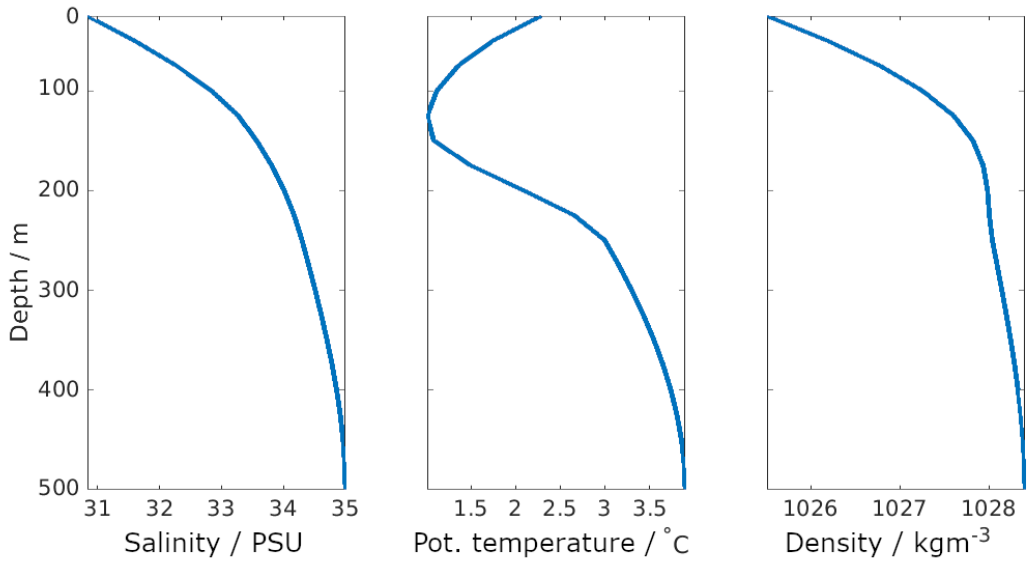

Figure 2.2: Initial ambient profiles in salinity, potential temperature and density for the 'baseline' fjord configuration, based on summertime observations for Sermilik fjord, eastern Greenland (Straneo et al. 2010). Note that salinity variations are the primary control on the density stratification.

either the realistic profile illustrated in Figure 2.2, or an idealised stratification with a similar deep, well-mixed layer, underlying a layer with linear stratification.

In a typical summertime Greenlandic fjord setting, the 1st baroclinic Rossby radius $R_d \sim 10\,\text{km}$ (Straneo et al. 2013). This provides some initial indication of the range of fjord widths which may be interesting to investigate, and provides a key dynamical length scale. We consider 'narrow' fjords with widths smaller than R_d, and 'wide' fjords with widths larger than R_d, anticipating the latter to be more strongly influenced by Coriolis effects. As discussed in Chapter 1, Jackson et al. (2016) shows that the ratio of fjord width to Rossby radius is approximately 1, for a range of Greenlandic fjords, with extremal values of ~ 0.5 and ~ 2. To investigate a representative sample of fjord widths above and below R_d, we therefore consider fjords with widths of 3, 6, 9, 12, and 24 km.

To restrict the size of the parameter space, we keep the fjord length and depth constant. Fjord length may be of relevance in controlling the allowed wavelengths of any resonant modes which may be excited by the subglacial discharge, and also in setting the timescale over which signals propagate between the fjord mouth

and the ice face. However, we initially consider steady-state conditions, which should mitigate the impact of wave-like behaviour and removes the dependence on propagation timescale.

Fjord depth itself in a case with flat bathymetry is of less relevance to the behaviour of a buoyant plume than the stratification, provided the fjord is deep enough for the plume to 'forget' the initial conditions at the source (Slater et al. 2016). Hence, we vary stratification profiles with fjord depth kept constant, but expect the results to extend straightforwardly to cases of different fjord depth.

2.3 Results

To guide theoretical developments, it is crucial to develop insight into the flow structures and behaviour exhibited by fjord circulation across a geophysically relevant range of parameter space. In this section, we discuss the 3-dimensional flow structures in the MITgcm model output. As previously discussed, the horizontal resolution of ocean model components of Earth system models is such that each fjord is likely to be influenced by a single column of ocean model grid cells only, with no horizontal resolution in the ocean forcing. Furthermore, any parameterization scheme must represent the amount, and vertical distribution, of freshwater from the ice sheet as it enters the ocean. As such, we focus particularly on the along-fjord component in MITgcm simulation outputs.

2.3.1 Fjord circulation overview

Figure 2.3 and Figure 2.4 show the 3-month time-mean along-fjord velocity in model simulations with subglacial discharge $Q_{sg} = 400,\ 1500\,\mathrm{m^3 s^{-1}}$, for narrow (3 km wide) and wide (24 km wide) fjords, respectively. Time-averaging is performed after a 3-month spin-up period. In all cases the simulation is initialised with the realistic stratification from Figure 2.2. The observed velocity structures are consistent with expectations in terms of both the vertical and horizontal shear which develops in each simulation across our parameter space. The injection of buoyant freshwater from a point source at the glacial grounding line drives large vertical velocities in

the plume, with freshwater rising up the ice face and entraining a significant volume of ambient fluid as it does so, generating horizontal flow towards the plume at depth. In a stably stratified layer, the plume density can often reach the same value as the ambient density at some depth level, at which point the plume outflows horizontally (in reality this is after some overshoot as a result of the residual momentum of plume water as it reaches this level of neutral buoyancy, although this is not resolved in the ICEPLUME parameterization). Alternatively, the plume rises buoyantly all the way to the surface, where it outflows. As such, plumes drive a vertical overturning flow towards the ice face at depth, and away from the ice in the outflow layer. Broadly, the outflow occurs in the subsurface for weak subglacial discharge, whilst the plume can penetrate to the surface for large subglacial discharge.

We determine the baroclinic Rossby radius of deformation via $R_d = NH_1/f$, where N is the buoyancy frequency in the stratified upper layer, H_1 is the upper layer thickness and f is the Coriolis parameter. For fjord widths much smaller than this deformation radius ($\sim 10\,\mathrm{km}$), the structure is primarily that of a vertical overturning circulation, with inflow at depth and outflow where plume modified water reaches its level of neutral buoyancy in the surface layer. In the narrowest case considered (Figure 2.3), there is a relatively small cross-fjord variation in the magnitudes and depth ranges of the inflow and outflow velocities, with enhanced outflow on the left-hand boundary looking into the fjord, and the depth at which the flow direction reverses 10 m lower on the left-hand boundary than the right. The spatial pattern of along-fjord velocity with depth and cross-fjord distance remains broadly the same along the fjord, after an initial adjustment where the peak outflow velocity migrates to the left of the fjord (looking into the fjord) on the order of one deformation radius from the ice face. At the fjord mouth, the peak inflow occurs on the right-hand boundary (looking into the fjord).

For fjords much wider than the deformation radius, significant cross-fjord structure develops at the fjord mouth with both inflow and outflow at the level of neutral buoyancy of the plume (Figure 2.4). The outflow at the plume neutral buoyancy level is confined to the left-hand boundary, looking into the fjord, with a

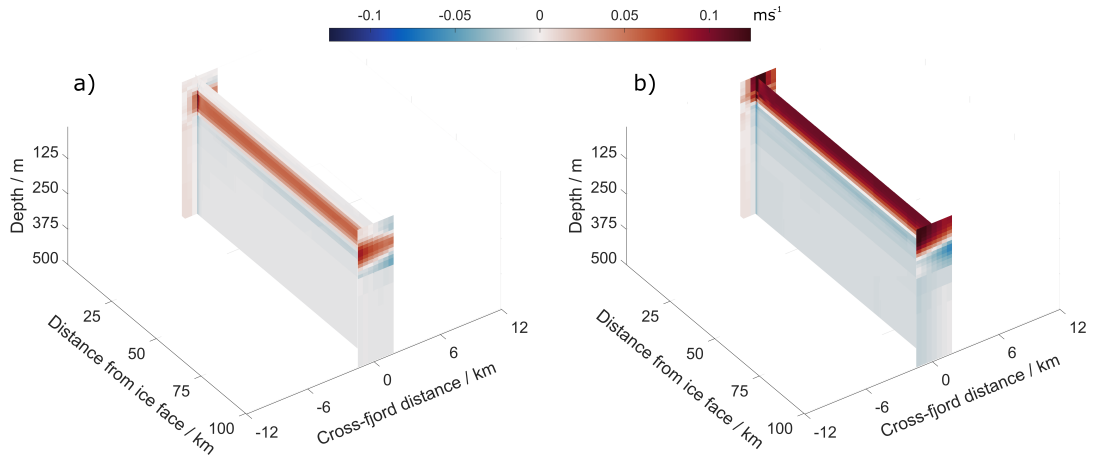

Figure 2.3: 3-month time-averaged along-fjord velocity ($\mathrm{m\,s^{-1}}$) for a narrow fjord of width 3 km, driven by a single plume with subglacial discharge flux of $400\,\mathrm{m^3\,s^{-1}}$ (left) and $1500\,\mathrm{m^3\,s^{-1}}$ (right), from MITgcm simulation output. Red denotes velocities away from the ice face. Slices show along-fjord velocity at the ice face, fjord mouth, and along the fjord centreline.

strong boundary current type structure. Furthermore, variation can be seen in the along-fjord direction; when the distance from the ice face is comparable to the fjord width, there is flow away from the ice face on the right-hand boundary (looking towards the ice face) across the full depth, with a layer of strong outflow close to the surface. On the left-hand boundary a curious structure develops. There are two flow reversals with depth, with a thin layer of outflow between two inflowing layers. This along-fjord velocity structure suggests the presence of an anticyclone close to the ice face. We discuss this further in §2.3.3. At the fjord mouth, a horizontally and vertically sheared flow develops, with outflow on the left-hand boundary and inflow on the right close to the surface. A weaker reversal of this horizontal structure forms at depth, with inflow on the left-hand boundary and outflow on the right.

Intermediate fjord widths show a gradual transition between these two extremal velocity structures, with increased cross-fjord structure as the fjord width increases relative to the deformation radius. This cross-fjord structure suggests that developing a simple characterization of the flow at the fjord mouth may require a full 3-dimensional treatment. However, we find that there is little vertical motion within the interior of the fjord, with upwelling occurring primarily via the plume

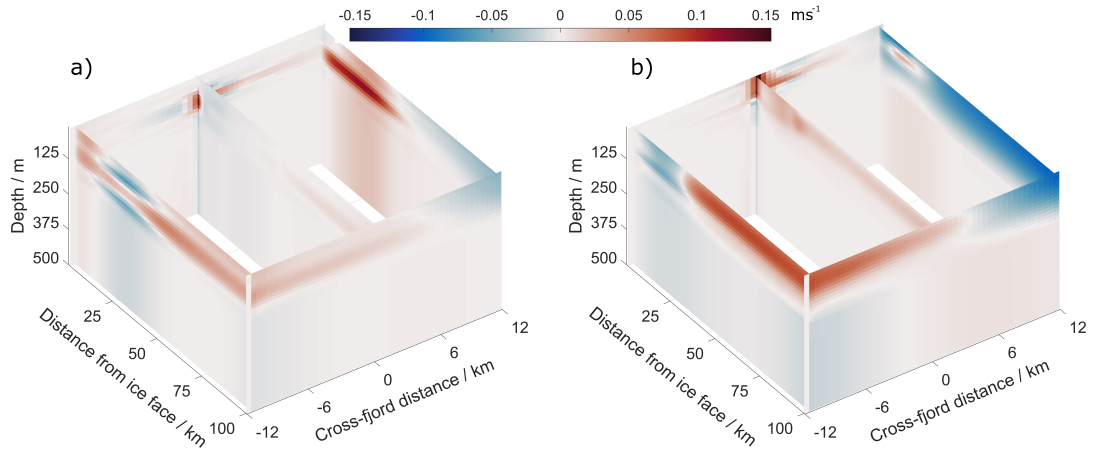

Figure 2.4: 3-month time-averaged along-fjord velocity ($\mathrm{m\,s^{-1}}$) for a wide fjord of width 24 km, driven by a single plume with subglacial discharge flux of $400\,\mathrm{m^3\,s^{-1}}$ (left) and $1500\,\mathrm{m^3\,s^{-1}}$ (right), from MITgcm simulation output. Slices show along-fjord velocity at the ice face, fjord mouth (inner edge of the sponge region), and along the fjord sidewalls and centreline.

at the ice face. Thus vertical profiles of cross-fjord-integrated volume transport do not depend on fjord width, as discussed below.

2.3.2 Vertical structure

2.3.2.1 Model output - realistic stratification

Understanding and describing the vertical distribution of ice- and fjord-modified waters is of key importance in the development of a parameterization scheme, as commonly used global ocean simulations have horizontal resolutions larger than the typical fjord width, but non-trivial vertical resolution over the fjord depth. As such, we investigate the cross-fjord-integrated, along-fjord velocity profiles in MITgcm simulation output over a range of subglacial discharge and fjord width.

Figure 2.5 shows the 3-month time-averaged, cross-fjord-integrated, along-fjord velocities plotted for a range of subglacial discharge fluxes, and for the narrowest and widest fjord cases. Profiles are taken at the ice face, and the fjord mouth. Averages are taken after a 3-month spin-up period. In steady state, the vertical velocity structure set up by the subglacial discharge is very similar at the ice face and the fjord mouth, with a slight broadening of the vertical extent of the outflow by

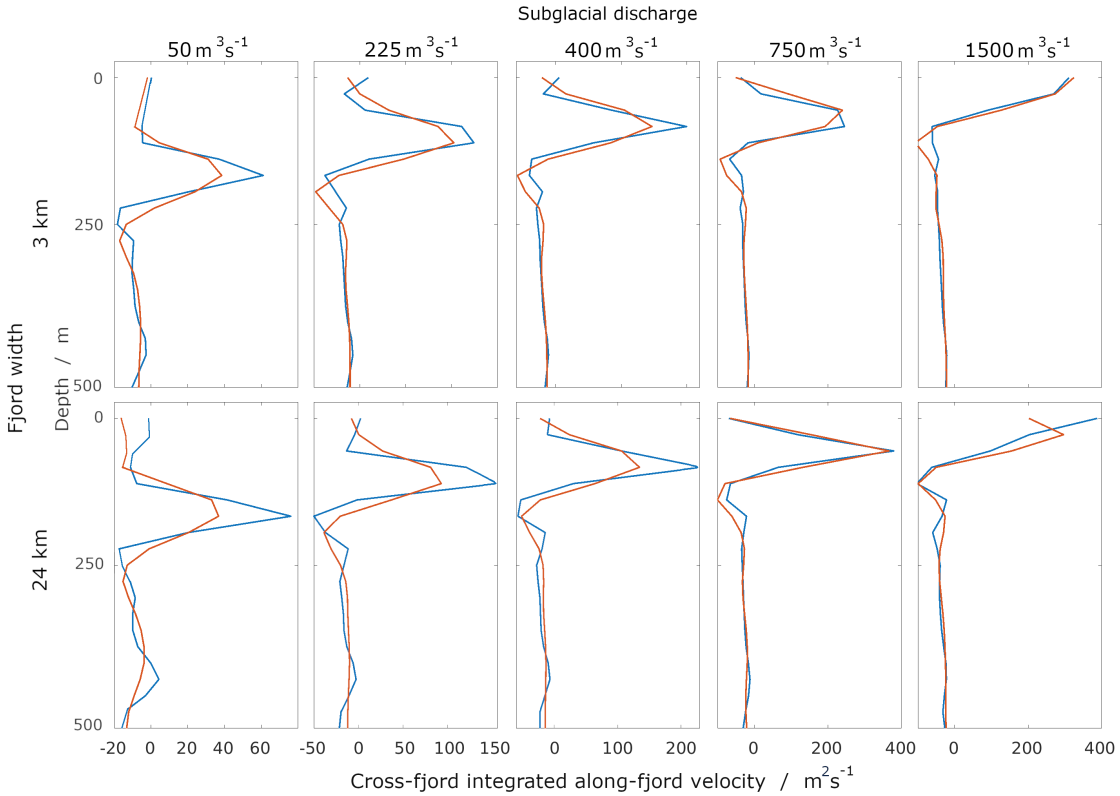

Figure 2.5: 3-month time-averaged cross-fjord integrated along-fjord velocities at the ice face (blue) and at the fjord mouth (red) for fjord widths of 3 km (top row) and 24 km (bottom row). From left to right, $Q_{sg} = 50,\ 225,\ 400,\ 750$ and $1500\,\mathrm{m^3\,s^{-1}}$.

the time it reaches the fjord mouth. Furthermore, the profiles remain very similar in magnitude and structure between these extremal fjord widths, with differences between the narrow 3 km fjord (upper row in Figure 2.5) and wide 24 km fjord (lower row) more pronounced at the ice face than at the mouth. Peak outflow depth, magnitude, and vertical extent at the fjord mouth (red lines) are approximately the same for all fjord widths with equivalent subglacial discharge, as is the magnitude and structure in the inflow region at depth. Despite the influence of fjord width on the horizontal structure of the flow seen in Figure 2.3 and Figure 2.4, the fjord width has a relatively small impact on the vertical profile of horizontally-averaged along-fjord velocity in Figure 2.5, and the corresponding mass flux. In all cases, we see that the intrusion depth decreases as subglacial discharge strength increases.

In a cross-fjord-integrated sense, the dynamics are dominated by that of the buoyant plume, which sets the inflow and outflow depths and volume fluxes,

independently of the width of the fjord. An asymmetry between magnitudes of inflow and outflow is required to satisfy the constraints set by the plume. Stratification in the surface layer confines the outflow, which remains at the same depth along the entire length of the fjord.

In summary, considering typical horizontal resolutions of global-scale climate models of the sort that a fjord circulation parameterization would target, the fjord width has negligible impact on the vertical structure of freshwater fluxes that an ocean model would take as an input at a coastal grid cell. Furthermore, the vertical structure of cross-fjord integrated along-fjord velocities remains broadly constant along the entire length of the fjord, suggesting that predictions for the vertical structure based on plume theory at the ice face remain applicable at the fjord mouth.

2.3.2.2 Scalings for the vertical structure of along-fjord velocities

We now develop theoretical scaling laws to predict the plume intrusion dynamics. Scaling laws from plume theory (e.g. Morton et al. 1956; Slater et al. 2016) are most well developed for cases of constant, or linearly varying density in the ambient fluid, but not for their combination. For simplicity in the theoretical scalings that follow, we consider the overall stratification within the fjord as a layer of constant density lying below a layer of linearly varying density. This is a fairly good approximation for summer months (see Figure 2.2), when the subglacial discharge volume flux is non-trivial and the plume intrudes within the upper region of stronger stratification. Recall that the entrainment of ambient waters into the plume generates a vertical volume flux far larger than the initial injection of freshwater into the fjord, and plume properties a short vertical distance from the source are dominated by the buoyancy of the mixture of entrained fluid and source freshwater, rather than by the initial conditions for the plume (Slater et al. 2016).

Previous studies have investigated the relationship between subglacial discharge, stratification, and plume height-of-rise, in the context of subglacial discharge plumes within Greenland's proglacial fjords. De Andrés et al. (2020) use a combination of

observational data and numerical ice sheet and plume modelling to fit a simple power-law relationship. Here, we instead propose a dynamically motivated theoretical model derived from plume theory which accounts for the properties in both the lower, unstratified layer and the upper, stratified layer. We produce a scaling for the height-of-rise of the plume purely in terms of the initial conditions of the plume and the ambient fjord stratification, without any additional fitting parameters.

We exploit previous scaling laws from Slater et al. (2016) in each layer, and combine these with overall salt and volume flux constraints for the subglacial discharge and inflow/outflow from the plume, to predict the plume outflow depth at the fjord mouth. A key addition to the previous approaches is that we explicitly use a global salt flux constraint, balancing the total fluxes into and out of the plume. Whilst this is implicit in the original plume equations, we found it useful to explicitly constrain the scalings for flow and intrusion in the upper stratified layer which are approximations to the true solution.

The plume vertical velocity, radius, volume and buoyancy fluxes are found analytically in the lower layer of constant ambient density. Then, as this lower-layer plume reaches the interface with the upper layer, the properties are used as initial conditions for the plume in the stratified surface layer. We consider a half-conical volume encompassing the plume, split into two at the layer interface (Figure 2.6). In a stratified layer, the plume rises through layers of decreasing density, carrying entrained water from lower in the water column. The plume can hence reach a level of neutral buoyancy, where the plume density matches the ambient fluid density. In the case of constant ambient density, the buoyancy flux is constant in the vertical within the plume, and the plume rises to the top of this layer, with buoyancy flux at the surface of this layer equal to that at the source.

The plume outflow is considered to occur about one depth level only - the level of neutral buoyancy. We assume that density depends only on salinity at leading order, and thus the outflow occurs with a single salinity for each value of Q_{sg}. We further assume that the ambient density remains unchanged by the plume itself, given that the volume of injected freshwater resident in the fjord at

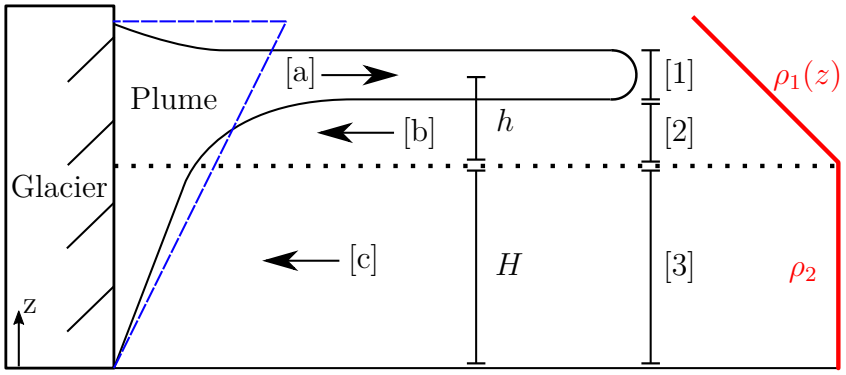

Figure 2.6: Schematic of the plume outflow (a) and inflow depths (b,c). Regions 1 to 3 are described in the text. Blue dashed line denotes a control volume encompassing the plume. The piecewise linear approximation to the density stratification is illustrated in red, with linearly varying density $\rho_1(z)$ in the upper layer and constant density ρ_2 in the lower layer.

any time remains a small fraction of the volume of the fjord. Below the level of neutral buoyancy the plume entrains ambient water, generating a horizontal inflow which renews the water with ambient properties.

For a plume with a finite height-of-rise in the surface layer h, we have three regions of interest, listed here moving down from the surface (see Figure 2.6):

[1] - Outflow around the level of neutral density $z = h + H$, where H is the lower layer thickness and h the height of rise of the plume above this layer.

[2] - Inflow below the level of neutral buoyancy, but still in the stratified upper layer, with salinity and density $S_1(z)$ and $\rho_1(z)$, respectively.

[3] - Inflow in the lower layer, with constant salinity S_2 and density ρ_2.

Our argument proceeds by estimating the salt fluxes in different regions of the plume, to calculate the net balance. Neglecting the comparatively small flux of melt water at the plume-ice interface, conservation of salt in the half-conical plume is given by (Morton et al. 1956):

$$\frac{d}{dz}\left[\frac{\pi}{2}b^2 w S_p\right] = \pi u_H b S_a, \tag{2.1}$$

with $u_H(z) = \alpha w(z)$ the horizontal velocity of fluid entraining into the plume, $w(z)$ the vertical velocity of the plume, α is the plume entrainment parameter, $b(z)$ the plume radius, $S_p(z)$ the salinity in the plume, and $S_a(z)$ the ambient salinity. Vertically integrating over the full plume height and noting that the plume salinity must equal the ambient salinity S_1 at the plume outflow depth $z = H + h$ for the plume outflow to be at neutral density, this yields:

$$S_1 Q_{out} - S_0 Q_{sg} = \int_0^{H+h} \pi u_H b S_a \, \mathrm{d}z. \tag{2.2}$$

Here $S_0 = S_p(z = 0) = 0$ is the salinity of subglacial discharge and Q_{out} is the total volume flux outflowing at the level of neutral buoyancy. Thus, the salt flux out of the plume is equal to the salt flux into the plume due to entrainment, with the height-of-rise of the plume constrained to occur at a depth which ensures that this is the case. The volume flux in the plume outflow satisfies

$$Q_{out} = Q_{in} + Q_{sg} \tag{2.3}$$

where Q_{in} is the total entraining volume flux for a half-conical plume, given by

$$Q_{in} = \int_0^{h+H} \pi b(z) u_H(z) \mathrm{d}z. \tag{2.4}$$

By considering each of the layers 1 to 3 in Figure 2.6 in turn, we determine the salt flux between the plume and fjord waters in each layer in terms of Q_{sg} and the ambient density profile, using scaling laws developed by Slater et al. (2016).

Lower Layer

In the lower layer of constant ambient density (layer 3 in Figure 2.6), the plume equations have analytic solutions for w and b as a function of z and the ambient stratification (see Slater et al. 2016):

$$w(z) = \frac{5}{6\alpha} \left(\frac{9\alpha Q_{sg} g'_0}{5\pi} \right)^{1/3} (z + z_0)^{-1/3}, \qquad b(z) = \frac{6}{5} \alpha (z + z_0), \tag{2.5}$$

where

$$z_0 = \frac{5}{6\alpha}\left(\frac{32\alpha Q_{sg}^2}{5\pi^2 g_0'}\right)^{1/5}, \tag{2.6}$$

and g_0' is the reduced gravity of the plume at the source. Using these scalings, the volume flux entrained into the plume in the lower layer is

$$Q_{in,lower} = \int_0^H \pi b u_H \mathrm{d}z = \frac{3\pi\alpha H_0^{5/3}}{5}\left(\frac{9\alpha g_0'}{5\pi}\right)^{1/3} Q_{sg}^{1/3}, \tag{2.7}$$

where $H_0^{5/3} = (H + z_0)^{5/3} - z_0^{5/3}$ and we have used the standard entrainment hypothesis $u_H = \alpha w$. As the salinity and density are constant in this layer, the entrained salt flux is

$$F_{S,in,lower} = \rho_2 S_2 \frac{3\pi\alpha H_0^{5/3}}{5}\left(\frac{9\alpha g_0'}{5\pi}\right)^{1/3} Q_{sg}^{1/3}. \tag{2.8}$$

Upper Layer

Slater et al. (2016) give further scalings for plume properties in a linearly stratified layer, based upon Morton et al. (1956) and Turner (1973). For an ideal plume with negligible mass or momentum flux at the source, the plume height-of-rise in the surface layer $h \sim L$, where $L = \Gamma_1 (Q_{sg} g_0')^{1/4} N^{-3/4}$, N is the buoyancy frequency in the surface layer, and Γ_1 is a dimensionless $\mathcal{O}(1)$ constant.

In our case, the initial mass and momentum fluxes may be non-trivial at the bottom of the surface layer and thus Γ_1 may differ in numerical value from that determined in Slater et al. (2016), but should remain $\mathcal{O}(1)$. Dimensionally, we expect $w \sim (Q_{sg} g_0')^{1/4} N^{1/4} f_w(z/L) \equiv \bar{w} f_w(z/L)$ and $b \sim (Q_{sg} g_0')^{1/4} N^{-3/4} f_b(z/L) \equiv \bar{b} f_b(z/L)$, for shape functions f_w and f_b. In general, w and b have some z dependence in the surface layer, described by the shape factors f_w and f_b. The magnitudes of w and b, however, are accounted for by the dimensional prefactors, with the shape factors $\mathcal{O}(1)$. Thus, we neglect the detailed structure of the shape factors for simplicity, and instead approximate $w(z)b(z) \approx \Gamma_2 \bar{w}\bar{b}$ in this layer. This approximation captures the leading scalings with Q_{sg}, g_0 and N, but could modestly impact the numerical prefactors arising from integrating the plume velocity and

radius in the upper layer in the calculations below. However, we ultimately find that the leading order scaling for h is independent of Γ_2 and hence this approximation should not have a significant impact on the final results. The volume flux into the plume in the surface layer, below the plume outflow depth (layer [2]), is therefore given by

$$Q_{in,upper} = \int_H^{h+H} \pi b u_H \mathrm{d}z \approx \Gamma_2 \pi \alpha \bar{w} \bar{b} h, \tag{2.9}$$

where we have applied the entrainment law $u_H = \alpha w$. The incoming salt flux in the upper layer is:

$$F_{S,in,upper} = \int_H^{h+H} \pi \alpha S_a(z) \rho_a(z) b(z) w(z) \ \mathrm{d}z \approx \pi \alpha \Gamma_2 \bar{w} \bar{b} h \rho_2 S_2 \left(1 - \frac{h \Delta S}{2 H_1 S_2}\right), \tag{2.10}$$

where we have assumed that $bw \sim \Gamma_2 \bar{b}\bar{w}$ is constant, have neglected the $\mathcal{O}(0.1\%)$ variation of $\rho_a(z)$ consistent with the Boussinesq approximation, and approximate $S_a(z) = S_2 - \Delta S(z - H)/H_1$ with H_1 the surface layer depth and ΔS the change in salinity between the top and bottom of the surface layer. The salinity at the outflow depth is given by $S(h) = S_2 - h\Delta S/H_1$.

We can now write the total salt flux into the full plume purely as a function of Q_{sg} and the properties of the ambient water. At the plume outflow layer (layer [1]), the salt flux out of the plume is determined by the outflow volume flux given by the sum of the entrained fluxes (Equation 2.7 and Equation 2.9) and subglacial discharge, multiplied by the salinity at which this outflow occurs. This yields

$$F_{S,out} \approx \rho_2 S_1 \left(\Gamma_2 \pi \alpha \bar{w} \bar{b} h + \frac{3 \pi \alpha H_0^{5/3}}{5} \left(\frac{9 \alpha g_0'}{5\pi}\right)^{1/3} Q_{sg}^{1/3} + Q_{sg}\right). \tag{2.11}$$

Combining the individual salt fluxes in each of the layers 1 through 3, the total salt flux between the plume and the fjord is given by $F_{S,plume} = F_{S,out} - F_{S,in,lower} - F_{S,in,upper}$. Using Equation 2.8, Equation 2.10 and Equation 2.11, one can show that

$$F_{S,plume} = -\frac{\pi \alpha \rho_2 h \Delta S}{2 H_1} \left(\Gamma_2 \bar{w} \bar{b} h + \frac{6 H_0^{5/3}}{5} \left(\frac{9 \alpha g_0'}{5\pi}\right)^{1/3} Q_{sg}^{1/3}\right) + \rho_2 S_1 Q_{sg}. \tag{2.12}$$

These salt fluxes into and out of the plume must sum to zero (so that $F_{S,plume} = 0$). Combining this constraint with Equation 2.12 yields a quadratic equation for h, with solution

$$h = -\frac{A_1 + Q_{sg}}{A_2} \pm \left(\frac{(A_1 + Q_{sg})^2}{A_2^2} + \frac{2S_2 H_1 Q_{sg}}{\Delta S A_2} \right)^{1/2}, \tag{2.13}$$

where $A_1 = Q_{in,lower}$ is the entrained volume flux in the lower layer from Equation 2.7 and $A_2 = Q_{in,upper}/h$ the entrained flux per unit height in the upper layer from Equation 2.9. The negative root yields negative h, which is unphysical, and hence we take the positive root. For our range of parameter space, numerical evaluation (for Γ_2 of $\mathcal{O}(1)$) reveals that

$$\frac{2S_2 Q_{sg} H_1}{\Delta S A_2} << \frac{(A_1 + Q_{sg})^2}{A_2^2}.$$

The negative root yields an unphysical, negative intrusion depth. Thus, taking the positive root in Equation 2.13, and Taylor expanding, we find:

$$h = -\frac{A_1 + Q_{sg}}{A_2} + \frac{A_1 + Q_{sg}}{A_2} + \frac{S_2 H_1 Q_{sg}}{\Delta S (A_1 + Q_{sg})} - \frac{1}{2} \left(\frac{S_2 H_1 Q_{sg}}{\Delta S (A_1 + Q_{sg})} \right)^2 + ...$$

Over the range of subglacial discharge we consider, the entrained volume flux in the lower layer A_1 (Equation 2.7) dominates with $A_1 >> Q_{sg}$. Hence, to first order in $Q_{sg}/(A_1 + Q_{sg}) \approx Q_{sg}/A_1$, this yields

$$h \approx \frac{S_2 H_1 Q_{sg}}{\Delta S \left(A_1 + Q_{sg}\right)} \approx \frac{S_2 H_1 Q_{sg}}{\Delta S A_1}. \tag{2.14}$$

Equation 2.14 can be written in terms of the stratification and subglacial discharge using Equation 2.7 as

$$h \approx \frac{5 S_2 H_1}{3\pi\alpha H_0^{5/3} \Delta S} \left(\frac{9\alpha g_0'}{5\pi} \right)^{-1/3} Q_{sg}^{2/3}. \tag{2.15}$$

The unknown dimensionless scale factors Γ_1 and Γ_2 drop out, and the final expression for plume height-of-rise is in terms of known physical quantities from the ambient stratification, the subglacial discharge flux, and the entrainment constant α. This

scaling breaks down where the plume reaches the ocean surface. Setting $h = H_1$ for outflow at the surface, Equation 2.15 provides an estimate for the subglacial discharge at which the plume would be expected to reach the surface.

We compare Equation 2.15 for the depth at which the plume terminates to the depth of the peak outflow at the fjord mouth from MITgcm model results initialised with realistic ambient stratification. Markers in Figure 2.7 shows the depth of the largest cross-fjord-integrated outflow velocity, for the full range of subglacial discharge fluxes and fjord widths. The colour scale shows the cross-fjord-integrated velocity structure for a 6 km wide fjord. Comparison with the theoretical scaling (blue line) is encouraging, particularly since Equation 2.15 contains no unknown fitting parameters, and h is here determined entirely in terms of known quantities. Whilst the entrainment coefficient α could be used as a tuning parameter in principle for comparison to observations, we here use $\alpha = 0.2$ for consistency with the MITgcm ICEPLUME model. The scaling shows reasonable agreement over the full range of subglacial discharge flux. The scaling slightly overestimates the outflow depth in the lowest subglacial discharge case, where the weak density gradient in the lower layer (which was neglected in developing Equation 2.15) is sufficient to cause the plume to outflow below the surface layer in the piecewise linear density profile. However, the overestimate remains reasonably small (~ 10 m). As shown in Figure 2.7, the predicted outflow depth remains well within the depth range of the outflow layer over the entire range of subglacial discharge.

Once the plume outflow approaches the surface, the scaling breaks down, and the peak outflow depth in Figure 2.7 shows larger variance with fjord width, with little systematic pattern. For example, the peak outflow for the 6 km and 24 km wide fjords occur at the same depth for $Q_{sg} = 1250\,\mathrm{m^3\,s^{-1}}$. These values nevertheless lie within the depth range over which outflow occurs for the reference fjord width of 6 km. In a linearly stratified layer, a characteristic length scale over which the ambient stratification becomes important is given by $L = \Gamma_1 (Q_{sg} g'_0)^{1/4} N^{-3/4}$. We expect that the outflow layer thickness Δh scales with L. Given that for a plume rising in a layer of constant density the vertical buoyancy flux $(Q_{sg} g'_0)^{1/4}$ is constant,

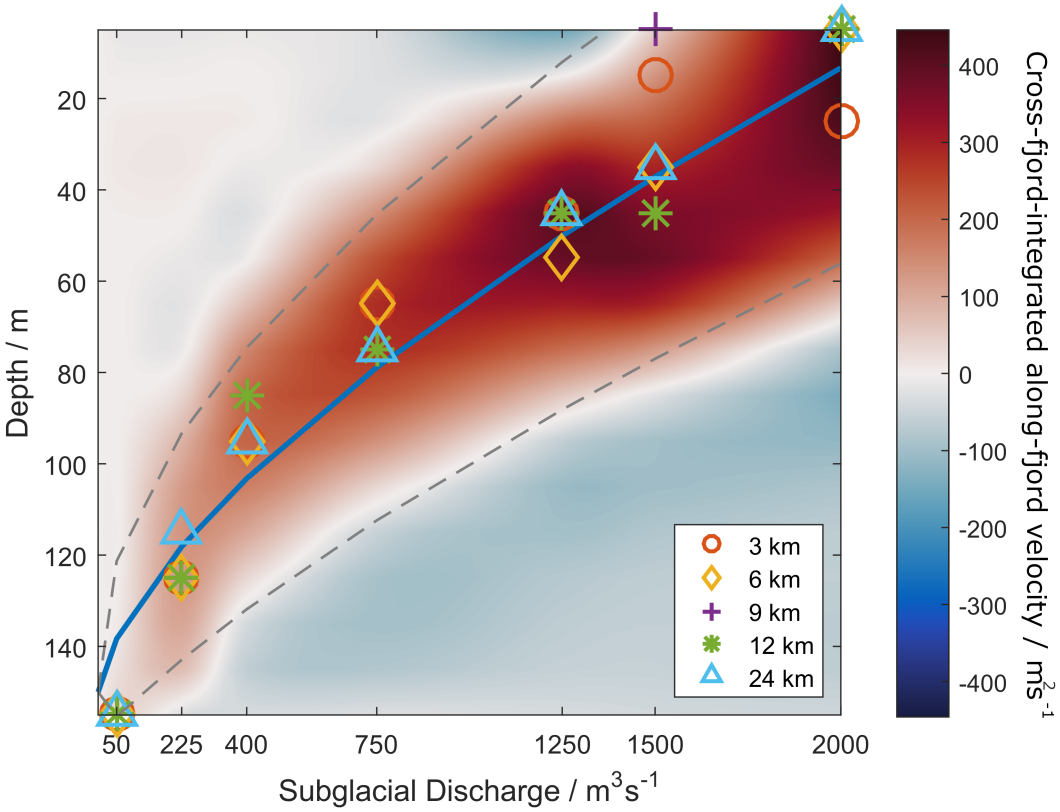

Figure 2.7: *Colour*: Model output for cross-fjord-integrated along-fjord velocity in the surface layer at the fjord mouth over a range of subglacial discharge flux plotted for a 6 km wide fjord with realistic ambient stratification. Colour is interpolated between data points at the labelled values of subglacial discharge. *Solid line*: Outflow depth using the prediction for h as a function of Q_{sg} from Equation 2.15. *Markers*: Depth of peak outflow velocity at the fjord mouth from simulation output, using the ambient stratification profiles of Figure 2.2, varying subglacial discharge flux and for different fjord widths indicated by the legend. *Dashed lines*: Outflow layer thickness prediction $\Delta h = (Q_{sg} g_0')^{1/4} N^{-3/4}$ assuming the peak outflow depth occurs in the middle of the outflow.

at the level of neutral buoyancy this is approximately given by the buoyancy flux at the source (where we are neglecting changes in buoyancy due to entrainment in the stratified layer), with g_0' the reduced gravity in the plume at the grounding line. Setting $\Delta h = L$ with $\Gamma_1 = 1$ yields

$$\Delta h = (Q_{sg} g_0')^{1/4} N^{-3/4}. \tag{2.16}$$

This yields $35 \lesssim \Delta h \lesssim 85$ m over our range of subglacial discharge. Plotting these values and comparing to model output in Figure 2.7, this is a reasonable

approximation to the outflow layer thickness in model output. We employ this scaling for Δh in subsequent calculations in this chapter.

An alternative approach to estimate the outflow layer thickness considers the outflow as a boundary current in the fjord. The plume outflow generates a buoyancy anomaly with reduced gravity $g' \sim N^2 \Delta h$. For wide fjords, geostrophic balance in the along-fjord velocity means that $fu \sim g' \partial h / \partial y \sim g' \Delta h / R_d$, where $R_d \sim \sqrt{g' \Delta h}/f$ is the deformation radius. Thus, the characteristic boundary current velocity is $u \sim c \sim (g' \Delta h)^{1/2}$. The boundary current volume flux Q is given by scalings for the total outflow volume flux of the plume. For wide channels, boundary currents have characteristic widths 'R' of the Rossby radius of deformation. For fjords narrower than this length scale, this characteristic width is simply the fjord width $R \sim B$. Therefore, we have $Q = u \Delta h R = \Delta h^2 N R$, split into narrow and wide fjord cases, with R the smaller of the fjord width B or deformation radius R_d. Therefore, $\Delta h = (Q/NB)^{1/2},\ (Qf/N^2)^{1/3}$ for narrow and wide fjords, respectively. This approach yields $\Delta h \sim$ 100-200 m over the range of fjord widths and subglacial discharge. This is similar in magnitude to that predicted using the first method, if slightly larger by a factor of $\mathcal{O}(1)$.

The depth range over which freshwater is injected into the ocean component of global-scale Earth system models is of key interest. Where the plume outflow depth is predicted to lie within half of the corresponding outflow layer thickness Δh from the surface for a given subglacial discharge, one sensible approximation may be to consider the outflow as a uniform layer between the ocean surface at $z = 0$ and $z = -\Delta h$ for all higher values of Q_{sg}.

2.3.2.3 Comparison with alternative realistic stratifications

In order to test the scaling further, we consider the impact on plume outflow depth of modifications to the initial realistic ambient stratification. First, we consider ambient stratification with a surface layer salinity gradient twice that of the initial case. This is achieved firstly by calculating a linear approximation to the initial realistic stratification, then scaling the salinity difference between consecutive grid

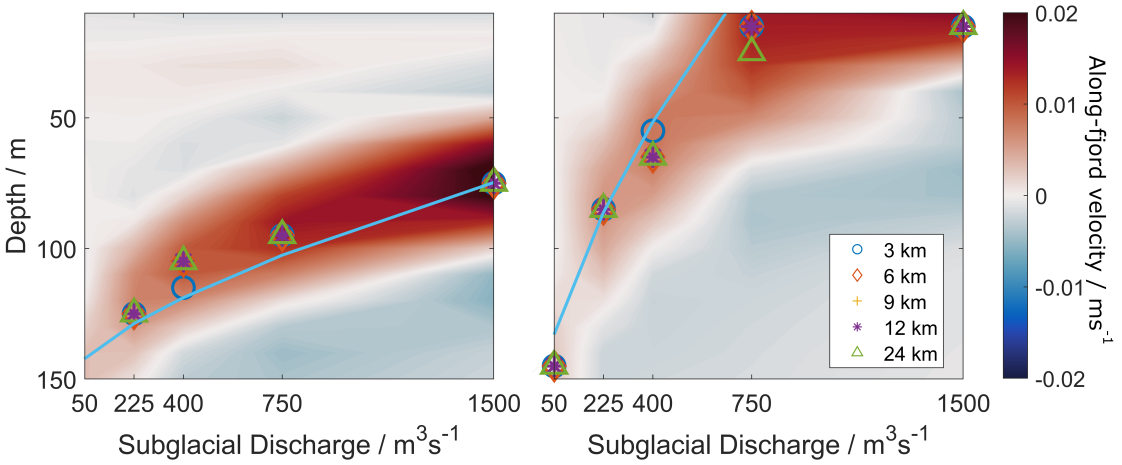

Figure 2.8: Plume outflow depth versus subglacial discharge for two alternative stratifications. *Left:* Surface layer salinity gradient twice that of the initial realistic stratification. *Right:* Surface layer salinity gradient half that of the initial realistic stratification. *Blue line:* Outflow depth prediction using the prediction for h (Equation 2.15). *Markers:* Peak outflow depth at the fjord mouth from numerical simulations. *Colour:* Cross-fjord mean along-fjord velocity at the fjord mouth (ms^{-1}) from MITgcm simulation output for a 12 km wide fjord (blue is towards the ice face, red away).

cells to produce a nonlinear salinity profile with approximated linear gradient either double or half that of the initial profile. The lower layer salinity remains the same, and the salinity gradient in the surface layer is doubled (such that the salinity at the ocean surface is reduced compared to the previous stratification). This would be a significant change in a geophysical context, with a strongly stratified upper layer. Figure 2.8 (left panel) shows that the scaling performs well for this strongly stratified case, over the full range of subglacial discharge and without any parameter tuning. The plume outflow occurs well below the ocean surface for all values of subglacial discharge considered, such that there is expected to be little impact of interactions with the surface.

We also consider a case with weak ambient stratification in the surface layer, with salinity gradient halved relative to the initial profile of Figure 2.2, such that the plume would be expected to reach the surface for lower values of subglacial discharge flux. Figure 2.8 (right panel) shows that Equation 2.15 qualitatively captures this behaviour. The scaling again captures the dependence of the plume height-of-rise on subglacial discharge. For high subglacial discharge, the scaling predicts an intrusion

depth above $z = 0$. As previously discussed, for a parameterization scheme, one simple method to account for the finite fjord depth in this case may be to consider the plume outflow as occurring in a layer of thickness Δh at the surface (at $z = 0$), where the scaling of Equation 2.15 predicts that the plume terminates above $z = -\Delta h/2$.

2.3.3 Horizontal structure

Typical ice models used in global-scale Earth system models have horizontal resolution small enough that the ice face could contain several grid cells in the cross-fjord direction. Thus, building a picture of the cross-fjord variations in melt rates at the ice face is an important step on the way to a parameterization of the impacts of fjord circulation.

In a modelling study of subglacial-discharge-driven circulation in Greenland's fjords, Carroll et al. (2017) found that an anticyclonic recirculation cell develops close to the ice face at the plume outflow depth, which periodically sheds due to baroclinic instability. This is consistent with previous studies of horizontal flow in the vicinity of plumes in the open ocean, such as turbulent megaplumes which occur as a result of hydrothermal vents or oil spills at the ocean bed (e.g. Woods et al. 1999). Typically, these plumes are found to form an anticyclonically rotating, geostrophically balanced bolus at the level of neutral buoyancy, with characteristic horizontal extent of the Rossby radius of deformation R_d (e.g. Woods et al. 1999). This recirculation is also consistent with anticyclonic circulation due to upwelling in estuaries and bays more generally (e.g. Fujiwara et al. 1997).

The existence of these recirculation structures within Greenlandic fjords generates cross-fjord flow at the ice, which can drive increased melting across the entire ice face in response to a localised subglacial plume (Slater et al. 2018), with implications for glacier terminus position and ice sheet stability as a whole (e.g. Mankoff et al. 2016; Jackson et al. 2020). In this section, we develop a phenomenological theory for the horizontal circulation at the plume outflow depth, which is then used to provide a prediction of the spatial pattern of melt across the entire ice face in §2.3.4.2.

2.3.3.1 Phenomenological theory

In order to investigate the cross-fjord velocity at the ice face, we develop theory guided by the phenomenology observed in MITgcm simulation output, as well as previous studies of open ocean plumes (e.g. Speer et al. 1995), and subglacial-discharge-driven circulation in fjords, which also display recirculation in the near-ice region (Carroll et al. 2017). Cross-fjord velocities at the plume outflow depth at the ice are set both by the plume outflow directly, and by the circulation response induced in the fjord. Therefore, we develop a simple prediction of the strength and structure of a recirculation region close to the ice and use this to predict the cross-fjord velocities across the entire ice face. We consider a localised volume source from the plume and determine the circulation as these waters advect away from the ice. We aim to develop an *ad hoc*, physically motivated conceptual model which captures key features, rather than a formal approximation of the full governing equations.

To reproduce the observed outflowing boundary current structure in the outflow for wider fjords, we introduce a dividing streamline across the fjord (Figure 2.9) at $x = l$, which partially encloses the plume outflow region, before turning into an outflowing boundary current. For simplicity, we assume that the relative vorticity of the fluid is constant within the partially enclosed region. This is motivated by the conservation of potential vorticity $(f + \omega)/\Delta h$ for a layer of thickness Δh and relative vorticity ω (c.f. Vallis 2006), along with a simplifying assumption of constant layer thickness for the outflow from the plume. Further, we assume that the outflow in the boundary current is horizontally uniform across horizontal extent b, balancing the volume input into the fjord by the plume at this depth level. For the parameters determining the position of the dividing streamline at $x = l$ and the boundary current width b, we set $b = l \sim R$, where the geophysically relevant length scale R for the flow is taken to be the smaller of the Rossby radius of deformation in the surface layer, or the fjord width. If the flow is incompressible with negligible vertical motion, this allows the definition of a 2D streamfunction ψ such that the along-fjord velocity component $u = -\partial\psi/\partial y$ and the cross-fjord component

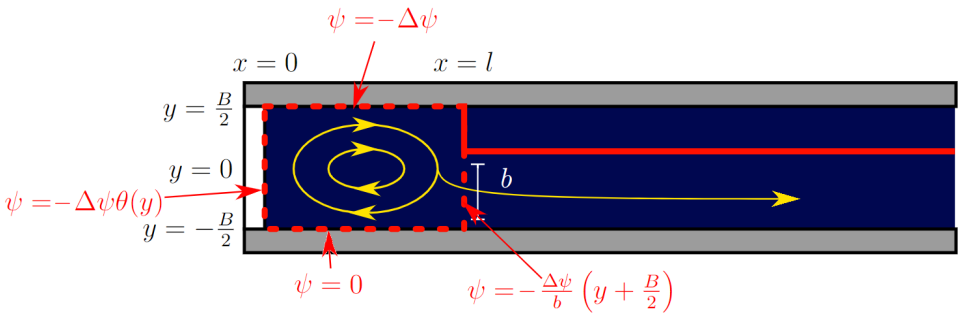

Figure 2.9: Schematic of fjord circulation in the 2D plane at the plume outflow depth. We define a streamfunction in this region (boundary values in red, dashed) which produces a phenomenologically motivated flow pattern in the fjord (yellow). A dividing streamline is introduced at $x = l$ to qualitatively recover the recirculation seen in model output (red, solid). This leads to a boundary current of width b propagating along the right-hand boundary, looking away from the ice (i.e. the lower boundary). Here, $\Delta\psi$ is a constant depending on the outgoing volume flux, and θ is the Heaviside step function. Boundary conditions on ψ are labelled in red.

$v = \partial\psi/\partial x$. Therefore, with a constant relative vorticity $\omega = (\nabla \times \underline{u}) \cdot \hat{\underline{k}}$, with $\hat{\underline{k}}$ the vertical unit vector, we can write a Poisson equation for the streamfunction:

$$\nabla^2\psi = \omega, \tag{2.17}$$

within this region. The boundary conditions for ψ must satisfy no normal flow at the lateral boundaries at $y = \pm B/2$, with the along-fjord velocity a delta function at the ice face to specify the volume flux due to the plume, and constant across the outflow region at $x = l$, with no flow across the dividing streamline. To account for the volume flux and inhomogeneous solution, we split the solution for ψ such that:

$$\psi = -\frac{\Delta\psi}{B}\left(y + \frac{B}{2}\right) + \frac{\omega}{2}\left(y^2 - \frac{B^2}{4}\right) + \psi', \tag{2.18}$$

where $\nabla^2\psi' = 0$, and $\Delta\psi$ is a constant depending on the outgoing volume flux. The first term accounts for the volume flux from the plume, the second is a particular integral associated with the vorticity of plume modified water, and ψ' satisfies a homogeneous partial differential equation and homogeneous boundary conditions, allowing the use of Fourier methods. The boundary conditions for ψ (illustrated in Figure 2.9) are

$$\psi(0,y) = -\Delta\psi\ \theta(y), \tag{2.19}$$

$$\psi(l, -B/2 < y < -B/2 + b) = -\frac{\Delta\psi}{b}\left(y + \frac{B}{2}\right), \tag{2.20}$$

$$\psi(l, y > -B/2 + b) = -\Delta\psi, \tag{2.21}$$

$$\psi\left(x, -B/2\right) = 0, \tag{2.22}$$

$$\psi\left(x, B/2\right) = -\Delta\psi, \tag{2.23}$$

with the corresponding boundary conditions on ψ' therefore given by

$$\psi'(0,y) = -\Delta\psi\ \theta(y) + \frac{\Delta\psi}{B}\left(y + \frac{B}{2}\right) - \frac{\omega}{2}\left(y^2 - \frac{B^2}{4}\right), \tag{2.24}$$

$$\psi'(l, -B/2 < y < -B/2 + b) = -\frac{\Delta\psi}{b}\left(y + \frac{B}{2}\right) + \frac{\Delta\psi}{B}\left(y + \frac{B}{2}\right) - \frac{\omega}{2}\left(y^2 - \frac{B^2}{4}\right), \tag{2.25}$$

$$\psi'(l, y > -B/2 + b) = -\Delta\psi + \frac{\Delta\psi}{B}\left(y + \frac{B}{2}\right) - \frac{\omega}{2}\left(y^2 - \frac{B^2}{4}\right), \tag{2.26}$$

$$\psi'\left(x, -B/2\right) = 0, \tag{2.27}$$

$$\psi'\left(x, B/2\right) = 0, \tag{2.28}$$

with $\theta(y)$ the Heaviside step function, such that $\theta(y) = 0$ for $y < 0$ and $\theta(y) = 1$ for $y > 0$. We can solve $\nabla^2\psi' = 0$ subject to these boundary conditions using standard separation of variables and Fourier series methods. After some calculation, we find that the full solution for $\psi'(x,y)$ is given by

$$\begin{aligned}\psi' = \sum_{n=1}^{\infty}\Bigg[&\left(A_n e^{\frac{2\pi n x}{B}} + B_n e^{-\frac{2\pi n x}{B}}\right)\sin\frac{2\pi n y}{B} \\ &+ \left(\alpha_n e^{\frac{(2n-1)\pi x}{B}} + \beta_n e^{-\frac{(2n-1)\pi x}{B}}\right)\cos\frac{(2n-1)\pi y}{B}\Bigg],\end{aligned} \tag{2.29}$$

where the coefficients $A_n,\ B_n,\ \alpha_n$, and β_n depend on $\Delta\psi,\ \omega,\ b,\ l$ and B, with the full forms given in Appendix A2.2.

The value of $\Delta\psi$ is found from scalings for the total volume flux of the plume outflow and layer thickness. If the outflow layer is distributed uniformly in the vertical over a depth Δh then $\Delta\psi = Q_{out}/\Delta h$. However, the outflow layer has some

vertical structure or shape factor, which influences the value of the peak cross-fjord velocity. For example, assuming that the outflow layer is of constant velocity with no vertical structure predicts a peak outflow velocity half that of an outflow layer with a roughly triangular 'peaked' structure, as is seen in the MITgcm model output (Figure 2.5). As we are considering the peak outflow velocity, and as a triangular shape factor more closely resembles model output, the value of $\Delta\psi$ is modified such that at the peak outflow depth $\Delta\psi = 2Q_{out}/\Delta h$, with the factor of 2 accounting for the triangular shape factor in converting from volume flux to velocity.

To determine a value for the relative vorticity ω at the plume outflow depth *a priori*, we consider a fluid parcel entering the plume at the glacier grounding line and consider the change in vorticity experienced by this parcel as it rises. We start from the vorticity equation for an inviscid, incompressible fluid and neglect the horizontal components of vorticity, to find the change in the vertical component of the vorticity due to vortex stretching within the plume:

$$\frac{D\underline{\omega}}{Dt} = (\underline{\omega} \cdot \nabla)\,\underline{u}, \tag{2.30}$$

where $\underline{\omega} \approx \omega_a \hat{\underline{k}}$ and the absolute vorticity $\omega_a = f + \omega = f + (\nabla \times \underline{u}) \cdot \hat{\underline{k}}$ for vertical unit vector $\hat{\underline{k}}$. In a Lagrangian frame following the parcel as it rises in the plume, taking only the z component of Equation 2.30, this yields

$$\frac{1}{\omega_a}\frac{\partial \omega_a}{\partial z} = \frac{1}{u_z}\frac{\partial u_z}{\partial z}, \tag{2.31}$$

where we here relabel the vertical velocity in the plume $u_z(z)$ for distinguishability (elsewhere in this thesis we use w to refer to vertical velocity unless otherwise stated). In the uniform lower layer, we use the vertical velocity from Equation 2.5. In the stratified surface layer, no analytic solution of this form exists. In the stratified layer, we assume that $u_z(z)$ is approximately constant below the level of neutral buoyancy. Thus, there is no vortex stretching in this layer, and the vorticity of the outflow is that of the plume at the layer interface. Assuming that the fluid parcels enter the plume with zero relative vorticity, and neglecting the impact on vorticity of the deceleration of fluid parcels above the level of neutral buoyancy, we have that

$$\int_f^{\omega_a} \frac{1}{\omega_a'} \mathrm{d}\omega_a' = \int_0^{H+h} \frac{1}{u_z} \frac{\partial u_z}{\partial z} \mathrm{d}z \equiv \int_0^{H} \frac{1}{u_z} \frac{\partial u_z}{\partial z} \mathrm{d}z, \tag{2.32}$$

At the outflow depth and using Equation 2.5, we obtain

$$\omega_a(H+h) = \frac{f z_0^{1/3}}{(H+z_0)^{1/3}},$$

$$\implies \omega(H+h) = \frac{f z_0^{1/3}}{(H+z_0)^{1/3}} - f. \tag{2.33}$$

Due to the dependence of z_0 on subglacial discharge, this leads to a prediction for the relative vorticity of the outflow which increases with Q_{sg}. Over our parameter range, ω varies from $\sim -0.95f$ to $\sim -0.75f$. Taking these values for ω, we use Equation 2.18 and Equation 2.29 to predict cross-fjord velocities at the plume outflow depth and compare to MITgcm simulation output in §2.3.3.3.

2.3.3.2 Alternative approach

Alternatively, it may be possible to derive a prediction for the horizontal flow field in the outflow layer by relaxing the assumption that the outflow layer thickness is constant in the horizontal, and instead employing a reduced gravity quasi-geostrophic approach which conserves potential vorticity. The potential vorticity q for the outflow layer is

$$q = \frac{f + \nabla \times \underline{u}}{\Delta h}, \tag{2.34}$$

where $\Delta h(x, y)$ is the outflow layer thickness.

If we again assume negligible vertical velocities, we can relate the horizontal velocity field $\underline{u} = (u, v)$ to a streamfunction ψ via $u = -\partial\psi/\partial y$ and $v = \partial\psi/\partial x$. Furthermore, assuming that the along-fjord velocity u is in geostrophic balance, we have that $fu = -g'\partial\Delta h/\partial y$, with g' the reduced gravity of the outflow layer. Thus, we can relate the relative vorticity term in Equation 2.34 to the thickness of the outflow layer. This leads to an inhomogeneous modified Helmholtz equation in outflow layer thickness of the form

$$\frac{g'\nabla^2(\Delta h)}{f} - \frac{q\Delta h}{f} + 1 = 0. \tag{2.35}$$

Solutions to this equation are significantly more complex than those to Equation 2.17, and are beyond the scope of this thesis (see, e.g., Antipov et al. 2005 for a relevant treatment). We also note that our phenomenological theory generalises more simply to the inflow layer, below the plume outflow layer. However, it can be seen that a natural Rossby radius of deformation arises, with $R_d \sim (g'\Delta h/f)^{1/2}$, where this length scale is explicitly imposed in the treatment of Equation 2.17. Thus, the use of Equation 2.35 is an interesting line of future inquiry with regards to improvements on the treatment developed in §2.3.3.1. Throughout this thesis, however, we instead employ the solution in Equation 2.18 to generate predictions for the cross-fjord velocities at the ice face.

2.3.3.3 Model output

At the ice face, the influence of the discharge plume is clearly visible in cross-fjord velocity profiles (Figure 2.10). The direct influence of the plume is visible close to (but not precisely at) the centreline of the ice face in each panel, where the cross-fjord velocity sharply peaks, with strong velocities away from the plume over the outflow depth range. The cross-fjord velocity shows increased outflow towards the right-hand side of the plume, at the peak outflow depth. This structure is observed for every combination of parameter values. Note that at the very centreline the cross-fjord velocities drop to zero as a result of symmetry of the outflow from the plume.

Above the outflow (dashed lines, Figure 2.10) for $Q_{sg} = 50 - 750\,\mathrm{m^3\,s^{-1}}$, the cross-fjord velocities display interesting structure. Broadly, for wide fjords the flow is weakly away from the plume location across the entire ice face, mirroring the structure in the outflow below (e.g. Figure 2.10, purple dashed lines). However, there is some variation across combinations of subglacial discharge and fjord width for $B = 3 - 12\,\mathrm{km}$. In these cases, the flow is weakly left to right across the entire width of the fjord for $Q_{sg} = 50\,\mathrm{m^3\,s^{-1}}$ (e.g. Figure 2.10, orange dashed line), and right to left for other values of subglacial discharge (e.g. Figure 2.10, green dashed

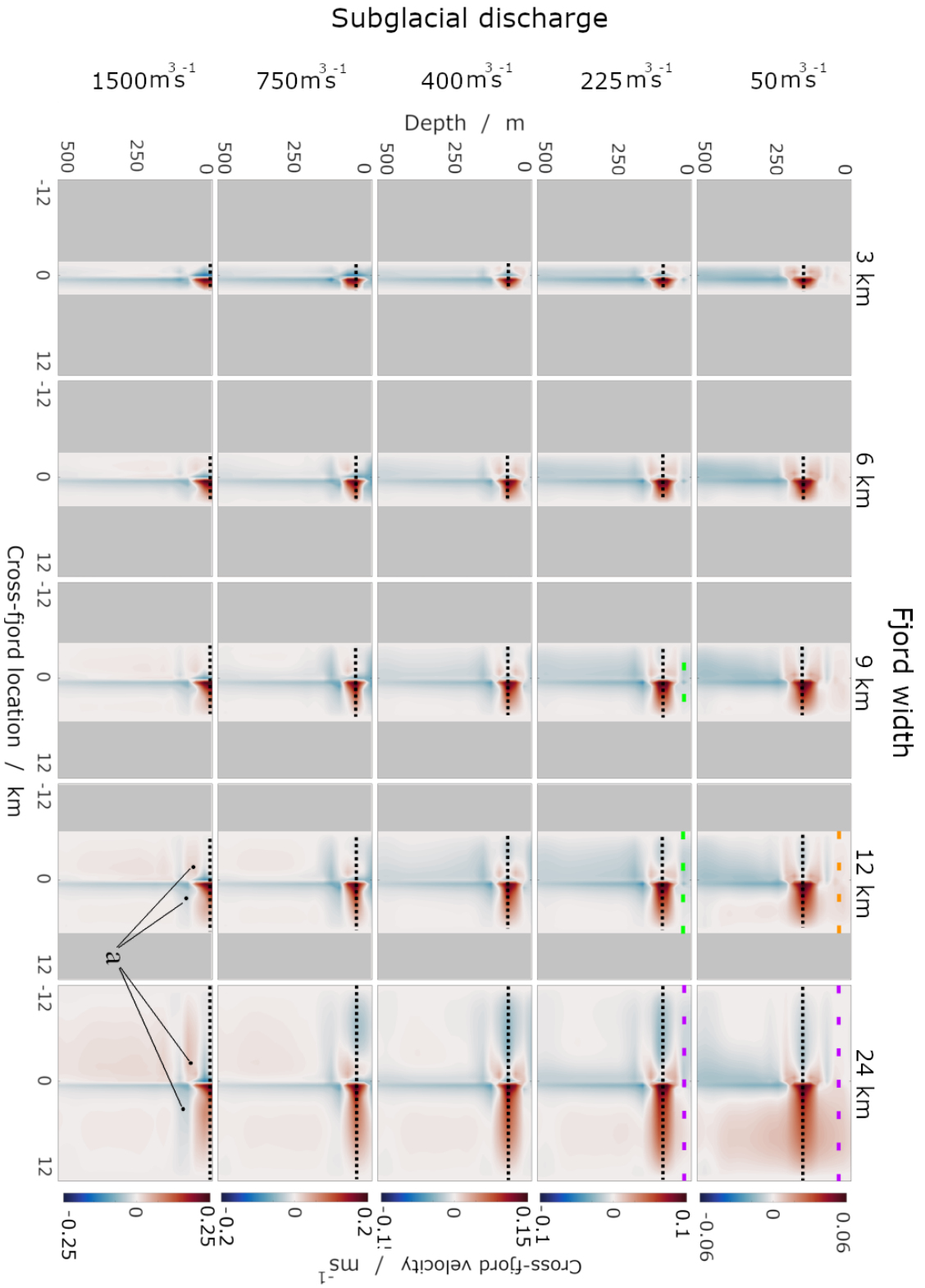

Figure 2.10: Cross-fjord velocity (colour scale) and depth of peak outflow velocity (dotted line) at the ice face averaged over 2 months, after a 1-month spin-up period. Red indicates velocities to the right (looking towards the ice face) and blue to the left. The subglacial discharge and fjord width for each simulation is indicated at the start of each row and column. Orange, green and purple dashed lines, and points labelled 'a' are described in the text.

lines). Furthermore, where the plume reaches the surface ($Q_{sg} = 1500\,\mathrm{m^3\,s^{-1}}$) and for fjords with widths $B \geq 9\,\mathrm{km}$, a layer of flow can be seen below the plume outflow with the opposing sign (e.g. Figure 2.10, points labelled a). Possibly, the injection of mass by the plume at the outflow depth generates sufficient along-fjord variation in isopycnals to generate a cross-fjord flow above and below the plume outflow. However, the variation in direction of the flow above the outflow with B and Q_{sg} is unexplained as of yet.

Below the outflow depth, there is significant variability in the cross-fjord velocity structure between simulations. For all combinations of subglacial discharge from $Q_{sg} = 50 - 750\,\mathrm{m^3\,s^{-1}}$ and fjord widths from $B = 3 - 12\,\mathrm{km}$, the flow at depth is leftwards, with a peak in magnitude close to the centreline due to the radial flow direction induced by the plume here. This is reminiscent of the two-layer structure discussed in Fujiwara et al. (1997), where cyclonic circulation is induced in the lower layer by spatially uniform upwelling between the two layers, although this effect is unlikely to explain the observed structure here as upwelling occurs only within the plume in our setting. For very wide fjords $B = 24\,\mathrm{km}$, the flow displays more variation in direction. For low subglacial discharge in simulations of 24 km wide fjords, the flow at depth is seemingly away from the plume across most of the ice face, whereas for high subglacial discharge the flow is towards the plume. Furthermore, for all fjord widths at high subglacial discharge, the cross-fjord flow is (weakly) towards the plume at depth.

These results highlight the complexity of the near-ice flow structures driven by the plume. Understanding and characterization of the mechanisms generating the variability in cross-fjord flow structure below and above (where applicable) the plume outflow layer is left for future work. However, we investigate the flow structure at the plume outflow depth below.

Investigating the horizontal velocity in a horizontal plane taken at the peak outflow depth of the plume provides insight into the cross-fjord flow within the estuarine outflow layer driven by the plume (Figure 2.11). Performing a time mean over one month, two weeks after model initialization to avoid effects of model spin

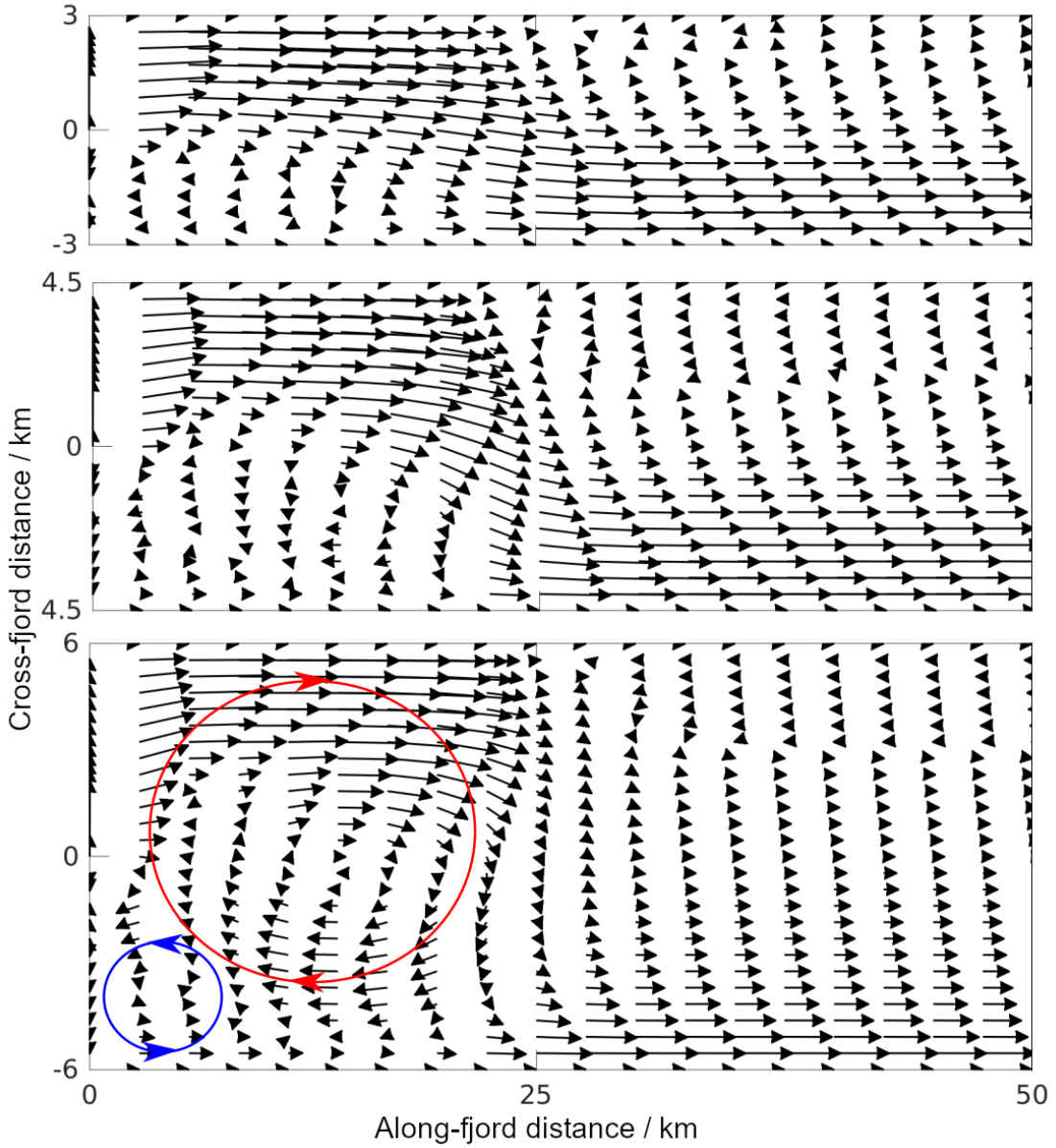

Figure 2.11: Quiver plots illustrating time-mean horizontal components of velocity at the plume outflow depth, from model simulation outputs for fjord widths B of a) 6 km, b) 9 km and c) 12 km. Average is over one month, two weeks after model initialization. Along-fjord distance is considered away from the ice face. All panels show outputs from model configurations with subglacial discharge flux $Q_{sg} = 750\,\mathrm{m^3\,s^{-1}}$. Horizontal anticyclonic recirculation develops next to the ice face as fjord width increases (see red arrows, 12 km case), with a small secondary cyclonic recirculation in the lower left corner (blue arrows, 12 km case).

up, a strong anticyclonic recirculation region is visible at plume outflow depth. Rotationally influenced flow across the ice is of sufficient magnitude to slow or even reverse any opposing radially spreading flow driven by the plume (Figure 2.11). For all but the narrowest fjords, the recirculation region extends to a distance roughly two deformation radii away from the ice face, after which the flow settles into a boundary current structure, with an intensified outflow along the right-hand fjord wall (looking out of the fjord). Investigation of the time-dependent flow suggests that the region of anticyclonic recirculation does periodically shed away from the ice face and travel down-fjord, consistent with Carroll et al. (2017). This shedding typically occurs 3-4 months after model initialization.

There is some evidence that in addition to the anticyclonic recirculation, which extends across the full width of the fjord, there is a small cyclone at the plume outflow depth which sits in the left-hand corner of the fjord (looking towards the ice face) during periods prior to eddy shedding (lower left corners in each panel of Figure 2.11). This feature is reminiscent of Moffatt eddies (Moffatt 1964), which are counter-rotating secondary vortices generated in corners of cavities by a larger vortex. Moffatt eddies increase in intensity as the Reynolds number of the flow Re is increased. Indeed, the cyclone sits in the expected corner for a secondary eddy of this type for moderate $Re \sim 400$ (e.g. Biswas et al. 2016). Furthermore, model configurations with rounded corners show reduced evidence of this counter-rotating flow, although there is difficulty in directly comparing cross-fjord velocity profiles at the ice in the two cases (sharp vs. rounded corners). We later see that the magnitude of the flow velocity in this region is similar to the theoretical prediction, even though the sign is reversed, and so the impact on cross-fjord velocity-driven melt rates should be small. More detailed study of this secondary vortex is left to future work.

We compare cross-fjord velocity v calculated from Equation 2.18, to velocities at plume outflow depth in the MITgcm model simulations, across the range of subglacial discharge flux and fjord width. The horizontal resolution of the MITgcm simulation is 500 m, and velocities are calculated on an Arakawa C-grid. Therefore, for fair comparison between cross-fjord velocities from the theory of §2.3.3.1 and

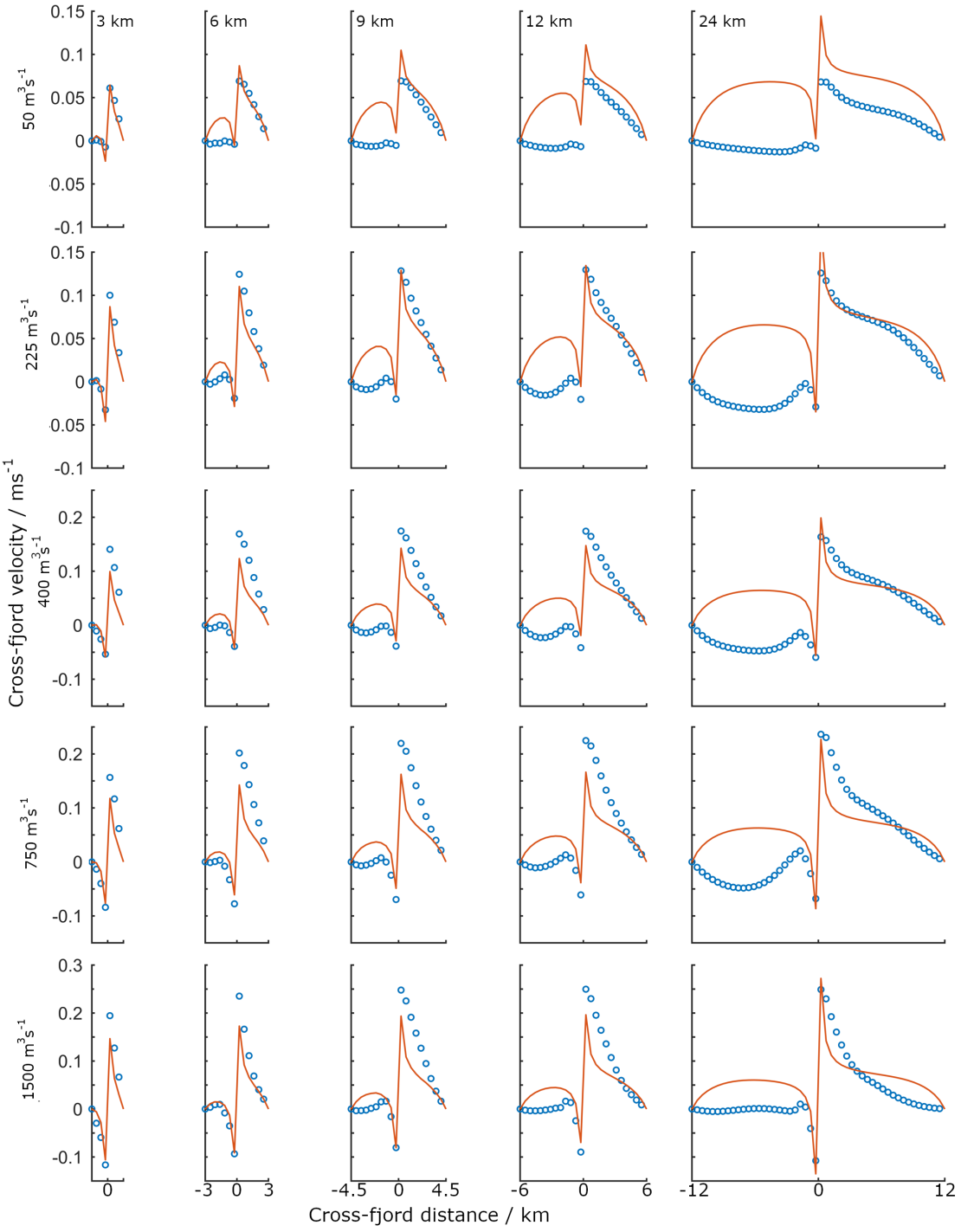

Figure 2.12: Cross-fjord velocity at the plume outflow depth, as a function of cross-fjord distance y for different values of subglacial discharge flux and fjord width, using Equation 2.18 (red lines) and taken from MITgcm model output (blue circles). From top to bottom (rows), $Q_{sg} = 50,\ 225,\ 400,\ 750,\ 1500\,\mathrm{m^3 s^{-1}}$. From left to right (columns), fjord width $B = 3,\ 6,\ 9,\ 12,\ 24\,\mathrm{km}$.

MITgcm simulation, we take the cross-fjord velocity 250 m from the ice face in the theoretical prediction. Figure 2.12 shows that, for most parameter values, the theory is a reasonable approximation to the cross-fjord velocity profiles at plume outflow depth in the MITgcm model to the right of the fjord centreline. However, the theory does not capture the sign reversal on the left of the fjord centreline which is present for many combinations of fjord width and subglacial discharge flux. In narrow fjords, there is reasonable agreement across the entire ice face in both sign and magnitude of the cross-fjord flow. In wider cases, the magnitude of the peak velocities and the velocities on the right-hand side of the ice face ($y > 0$, looking towards the ice) match fairly well in all but the lowest subglacial discharge case, where the theory nevertheless remains within a factor of 2 of MITgcm model output. The theory does not capture the sign reversal on the left-hand side of the ice in wider fjords. Furthermore, the magnitude of the velocities on this side of the ice is slightly overestimated, which will have an impact on the resultant melt rate predictions.

For the lowest subglacial discharge flux, the theory is largely inaccurate in the widest case. Primarily, this seems to be a result of a large overestimation of the recirculation strength, which appears as a half-wavelength cosine structure in the theoretical curve. Furthermore, MITgcm output shows significant time-dependent behaviour close to the ice face in wider fjords, most notably the 24 km cases, with long periods of slow vortex growth ($\sim$ 2-3 months) interspersed with vortex shedding, which we cannot capture with a simple steady flow prediction such as Equation 2.18. Developing a simple velocity scaling which captures this time-dependent behaviour would add significant complication. Potentially, increased understanding of the time dependence of vortex shedding could be built into a time-dependent $l(t)$, as the vortex sheds and fluid of constant relative vorticity ω spreads from the plume outflow. However, as a first approximation to the cross-fjord velocity at the plume outflow depth, Equation 2.18 provides reasonable predictions for the time-averaged case, over most of the parameter space.

2.3.4 Glacial melt rates

Having developed scalings for the cross-fjord velocities in contact with the ice, we now proceed to calculate the melt of ice across the glacial terminus. This melt occurs as a result of both the cross-fjord velocities due to the fjord circulation, as well as strong vertical velocities within the plume itself. In this section, we first apply scaling laws developed in Slater et al. (2016) for the melt of ice in direct contact with the plume, considering the two-layer stratification typical of Greenlandic fjords. Next, we use the cross-fjord velocity predictions developed in §2.3.3 to generate a prediction for the spatial pattern of melt across the entire ice face.

2.3.4.1 Ice in contact with the plume

Strong melting of ice in direct contact with the plume occurs due to the large vertical velocities driven by the buoyancy forces, which remain unaffected by fjord width. Slater et al. (2016) derive dimensional scalings for the melt rate of ice in contact with a point source plume, in both unstratified and linearly stratified ambient water. We test the ability of these scalings to recreate ice melt rates predicted by the ICEPLUME package for the realistic stratification of Figure 2.2, considering the typical two-layer stratification in Greenland's fjords as having uniform ambient density and temperature in the lower layer and linearly varying density in the surface layer. We also assume constant temperature in the surface layer (although different to that in the lower layer), which is not the case in Greenland's fjords. Slater et al. (2016) suggest that a scaling for the melt rate of ice in contact with a plume in a layer with varying salinity and temperature is not generally possible. Therefore, we employ this approximation in order to make progress and provide some initial estimate of melt rates. In this section, we take the mean temperature in the upper layer to be the mean over $H < z < H + h$ in Figure 2.2, with h given by Equation 2.15.

In an unstratified layer, Slater et al. (2016) show that the total melt in the plume can be written

$$\dot{M}_{unstrat.} = \int_0^H 2b\dot{m}\ \mathrm{d}z = A_1 \left[1 + A_2 \left(T_a - T_0\right)\right] Q_{sg}^{1/3} H^{5/3}, \tag{2.36}$$

with $A_1 = 4.05 \times 10^{-6}$ $\mathrm{m^{1/3}s^{-2/3}}$ and $A_2 = 0.75$ $(^\circ\mathrm{C})^{-1}$ determined by fitting melt rates predicted by the plume model and the three-equation formulation for the melt rate (Slater et al. 2016), T_0 the temperature of the incoming subglacial discharge and T_a the constant ambient temperature of the lower layer. In a stratified layer of thickness H_1, they find that the melt rate scales, on dimensional grounds, as $\dot{M}_{strat.} \propto Q_{sg}^{1/2} N^{-1/2} {g'_0}^{1/2} h$ if the plume does not reach the surface (case [1]), or a similar expression if the plume reaches the surface (case [2]).

Noting that the buoyancy flux is constant in the unstratified lower layer (Morton et al. 1956), we can write an approximate total melt rate of ice in contact with the plume across both layers by summing the contribution in each layer:

$$\dot{M} = \begin{cases} A_1 \left[1 + A_2 \left(T_a - T_0\right)\right] Q_{sg}^{1/3} H^{5/3} + A_3 T_u Q_{sg}^{1/2} N^{-1/2} {g'_0}^{1/2} h & \text{in case [1]}, \\ A_1 \left[1 + A_2 \left(T_a - T_0\right)\right] Q_{sg}^{1/3} H^{5/3} + A_4 T_u Q_{sg}^{1/2} N^{-1/2} {g'_0}^{1/2} H_1 & \text{in case [2]}, \end{cases} \tag{2.37}$$

where A_3 and A_4 are unknown constants, $T_a = 3.5\,^\circ\mathrm{C}$ is the mean ambient lower layer temperature and T_u is the mean ambient upper layer temperature below the plume outflow depth. The temperature of the incoming subglacial discharge T_0 is set to zero.

There is potential ambiguity in interpreting the value of h which corresponds to the plume having reached the surface, given the finite thickness of the outflow layer. In one interpretation, the plume may be considered to have reached the surface when the top of the outflow is at the surface (i.e. when $h \geq H_1 - \Delta h/2$). Alternatively, the plume may be considered to have reached the surface only when $h \geq H_1$. Under the latter interpretation, there is a range of outflow depths for which $H_1 - \Delta h/2 < h < H_1$, where there is positive along-fjord velocity at the ocean surface, but the plume is still considered to terminate in the subsurface. Using the second interpretation leads to conditions where the plume is considered to terminate in the subsurface over the full range of subglacial discharge considered in our MITgcm simulations (such that only case [1] is applicable), whilst the first interpretation suggests that the plume reaches the surface at around $Q_{sg} = 750\,\mathrm{m^3 s^{-1}}$.

Figure 2.13 shows nonlinear fits of the two cases in Equation 2.37 for the 9 km wide fjord, using the previous values of A_1 and A_2 from Slater et al. (2016). In

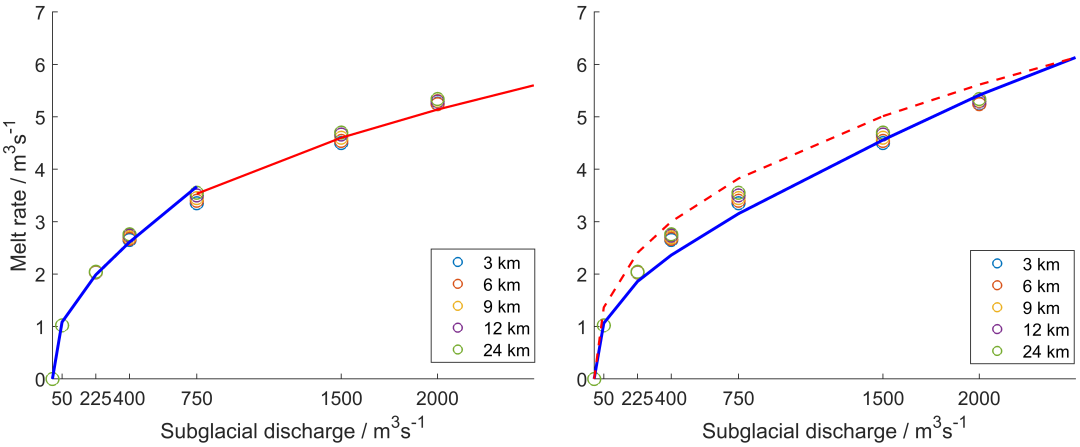

Figure 2.13: Freshwater flux due to melting of ice in direct contact with the plume, for varying subglacial discharge flux, and fjord width.
Left: Fitting each case individually in Equation 2.37 (allowing $A_3 \neq A_4$) considering the plume to have reached the surface when $h \geq H_1 - \Delta h/2$. *Solid blue line*: nonlinear fit using A_3 as a free variable in case [1], where the plume does not reach the surface. *Solid red line*: Fit in case [2] where the plume approaches the surface, using A_4 as a free variable.
Right: Considering the plume to have reached the surface only when $h > H_1$ and constraining continuity in Equation 2.37 by enforcing $A_3 = A_4$. *Solid blue line*: nonlinear fit using A_3 as a free parameter. *Dashed red line*: predicted melt in case [2] constraining $A_3 = A_4$, using A_3 from the fit in case [1]. As the plume does not reach the surface in this interpretation, only case [1] is valid over the range of simulation output considered here.

all cases, the predicted freshwater flux into the fjord due to melting of ice in direct contact with the plume is negligible compared to the subglacial discharge driving the plume, across the full range of Q_{sg}, consistent with observations (e.g. Mankoff et al. 2016). Under the interpretation that the plume reaches the surface for $h \geq H_1 - \Delta h/2$, we fit case [1] using model data for $Q_{sg} = 50,\ 225,\ 400$, and $750\,\mathrm{m^3 s^{-1}}$ (Figure 2.13, left). Averaging over output for all fjord widths at each value of subglacial discharge yields a best fit value of $A_3 = 2.3 \times 10^{-4}\,(^\circ\mathrm{C})^{-1}$. The fit in case [2] uses model output for $Q_{sg} = 750 - 2000\,\mathrm{m^3 s^{-1}}$, producing a best fit value of $A_4 = 9.3 \times 10^{-5}\,(^\circ\mathrm{C})^{-1}$. Figure 2.13 shows that the fits approximate the melt rates well. Typically, the values of A_3 and A_4 are constrained to be equal, such that the melt rate $\dot{M}$ is continuous as the plume reaches the surface. Here, however, this constraint leads to an overestimation of the melt rate over the range of parameter space where the plume is predicted to reach the surface, such that

the red line in Figure 2.13 would be higher than MITgcm simulation output by $\sim 2\,\mathrm{m}^3\,\mathrm{s}^{-1}$ over this range of subglacial discharge.

Alternatively, we now consider the plume to have reached the surface only for $h > H_1$. Under this interpretation, the plume does not reach the surface in any of our simulation outputs. We therefore fit case [1] using the full range of subglacial discharge with A_3 as the only free parameter, leading to a best fit value of $A_3 = 1.21 \times 10^{-4}\,(^\circ\mathrm{C})^{-1}$. Here, the prediction of Equation 2.37 is reasonably close to simulation output across the full range of parameter space (Figure 2.13, right), although the fit is not as close as that under the previous interpretation of plume height-of-rise. A more complex approximation considering the mean temperature over the of the upper layer T_u as the mean over the range of depths through which the plume rises, rather than the full mean over H_1, will modify the dependence of Equation 2.37 on Q_{sg}. This provides a potential avenue to extend the predictions here, although this still falls short of a scaling accounting for the full ambient stratification in T and S.

2.3.4.2 Fjord circulation driven melt

Prediction of the melt rates driven by the horizontal fjord scale circulation requires some prediction of cross-fjord velocities across the entire ice face. Equation 2.18 provides an approximation to the cross-fjord velocities at the peak outflow depth of the plume. However, as shown in Figure 2.10, this velocity is not uniform with depth in the outflow layer, and a different structure is present over depths where the plume is entraining. Guided by the profiles in along-fjord velocity in Figure 2.5, within the outflow layer we consider the vertical structure of the outflow to be a piecewise linear or triangular shape $\zeta(z)$. Where the plume terminates in the subsurface, we consider the outflow to have vertical extent Δh from the scaling of Equation 2.16. Where the plume is predicted to terminate within $\Delta h/2$ of the ocean surface by Equation 2.15, we modify the shape factor $\zeta(z)$. We choose to retain the same peak velocity and volume flux as in an equivalent case in which interaction

with the surface is neglected, but allow for a non-zero velocity at the ocean surface, as well as changes to the outflow layer thickness, to simulate surface interaction.

To retain the same depth-integrated volume flux when applying the shape factor to the predicted velocities at plume outflow depth, the area enclosed by $\zeta(z)$ for the case that the plume reaches the surface (i.e. Figure 2.14, right, solid red line) must match the equivalent area for a shape factor which is triangular and symmetric about $z = h$ that ignores the interaction with the surface (Figure 2.14, right, dashed blue line). Assuming that the value of the shape factor at the predicted outflow depth ζ_p is equal and that the gradient in the shape factor between the peak depth and the surface remains the same in the two cases, equating the areas enclosed by the dashed blue and solid red shape factors allows a new outflow layer thickness Δh_n to be calculated geometrically in terms of Δh and h. This leads to a quadratic expression for the new layer thickness

$$\Delta h_n(\epsilon) = \Delta h + \epsilon \left(\frac{2\epsilon}{\Delta h} - 1 \right).$$

where $\epsilon = D - h - H$ is the distance of the plume height-of-rise from the surface. This leads to a prediction for the outflow layer thickness $\Delta h_n(\epsilon)$ which is equal to the original layer thickness Δh where $\epsilon = 0, \Delta h/2$, and has a minimum $\Delta h_n(\Delta h/4) = \Delta h - \Delta h/8$. Thus, this construction allows for the extension of the triangular shape factor to cases where the plume reaches the surface, conserving both vertically-integrated volume flux and peak velocity.

The prediction for the spatial pattern of melt at the ice face is split into 4 areas (see Figure 2.15). Between the outflow layer and the surface (purple), the velocity of fjord water is given by a uniform small background velocity $u_{bg} = 0.001\,\mathrm{m\,s^{-1}}$, accounting for unresolved fine-scale turbulent mixing as a result of buoyant meltwater flow or background waves. In this section, MITgcm simulations use the same background velocity in the ICEPLUME parameterization, for a fairer comparison. In the outflow layer, the cross-fjord velocity is calculated via the streamfunction method developed in §2.3.3, assuming the formation of an anticyclonic vortex at the plume outflow depth. Below the plume outflow layer, we assume a solution

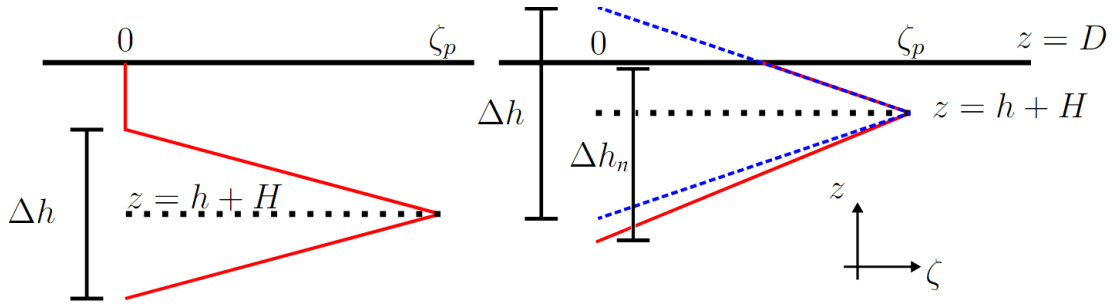

Figure 2.14: Schematic of the plume outflow shape factor $\zeta(z)$ (solid red line) below the ocean surface (solid black line). *Left:* Where the plume is predicted to terminate at least $\Delta h/2$ below the surface, $\zeta(z)$ is triangular. *Right:* Where the plume is predicted to terminate within $\Delta h/2$ of the surface, $\zeta(z) = \zeta_b$ is non-zero at the ocean surface, $\zeta(z)$ is no longer symmetrical about $z = h + H$, but retains the outflow velocity at $z = h$ and layer thickness Δh from scalings. The blue dashed line shows an equivalent triangular structure, symmetrical about $z = h + H$, with identical vertical extent Δh.

of the same form as Equation 2.18, with two key differences. Firstly, we set the rotational terms to zero (i.e. $\omega = 0$ in this layer). Secondly, we assume no vertical structure, and choose $\Delta\psi = Q_{in}/h_{in}$, where Q_{in} is given by the sum of Equation 2.7 and Equation 2.9, and $h_{in} = h + H - \Delta h/2$, to reflect the fact that the plume acts as a volume sink in the horizontal over this range of depths. In principle, one could calculate the plume entrainment at each depth independently. This would yield the same depth-averaged velocity, and hence the same depth-averaged melt if the temperature T was uniform in the vertical. Therefore, this approximation neglects terms on the order of $\int(u-\bar{u})(T-\bar{T})\,\mathrm{d}z$, where overbars denote the vertical average over the range of depths where the plume is entraining ambient fluid, with the benefit of improved computational efficiency. Combining the solution for cross-fjord velocity at depth with the combination of cross-fjord velocity and shape factor in the outflow layer, we reproduce a full 2D reconstruction of the melt rate across the entire ice face in Figure 2.15. Where the plume is in direct contact with the ice, there are enhanced melt rates due to the large vertical velocities within the plume, and we employ Equation 2.37 for the additional contribution.

To convert the predicted velocities at the ice face to melt rates, we employ the 'three-equation formulation' (Holland et al. 1999, Equation 1.2a - Equation 1.2c) for energy and salt conservation along with salinity (and depth) dependent freezing

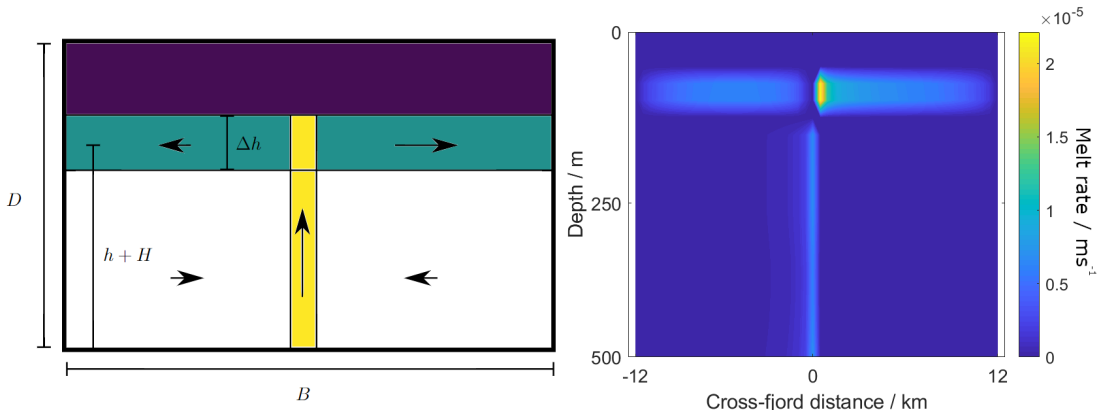

Figure 2.15: *Left*: Schematic of the predicted flow structure at the ice face, with four regions in which the velocity (and melt) is calculated separately. Purple: stagnant layer above the plume outflow where the velocity is taken to be a small background velocity u_{bg} in calculation of the melt rate. Green: outflow layer, using the velocity structure prediction from §2.3.3. Yellow: sum of the ice melt due to direct contact with the vertical velocities within the plume (Equation 2.37), and the melt due to the horizontal component of velocity. White: inflow dominated by the convergent plume signal, with negligible rotational component. Arrows illustrate the flow direction in each section.
Right: Spatial pattern of melt (ms^{-1}) resulting from the predictions for horizontal fjord circulation only (i.e. without the melt of ice in direct contact with the plume) for fjord width $B = 24\,\mathrm{km}$, subglacial discharge $750\,\mathrm{m}^3\mathrm{s}^{-1}$, depth $D = 500\,\mathrm{m}$ and the stratification shown in Figure 2.2.

temperature, and the stratification profile of Figure 2.2. Given the typical resolution of ice sheet components of Earth system models, depth-integrated melt rates across the ice face are of primary interest. Figure 2.16 compares the predicted vertically-integrated melt rates to MITgcm simulation output, over a range of fjord widths and subglacial discharge, again taking cross-fjord velocities 250 m from the ice in the theoretical prediction of §2.3.3.1 for the cross-fjord velocities at the plume outflow depth. The melt rate parameterization in the model here uses a background velocity of $u_{bg} = 0.001\,\mathrm{ms}^{-1}$: if ice grid cells are adjacent to ocean grid cells with a velocity smaller than u_{bg}, then we instead use the value of u_{bg} to calculate the melt rate. Similarly, in regions predicted by theory to have a cross-fjord velocity smaller than u_{bg}, we instead set the velocity to u_{bg} before the calculation of the melt rate.

For comparison to our theoretical prediction, simulation output is averaged over the third week after model initialization. This allows 2 weeks of spin up, and then a 1-week average, motivated by geophysically relevant timescales over which subglacial

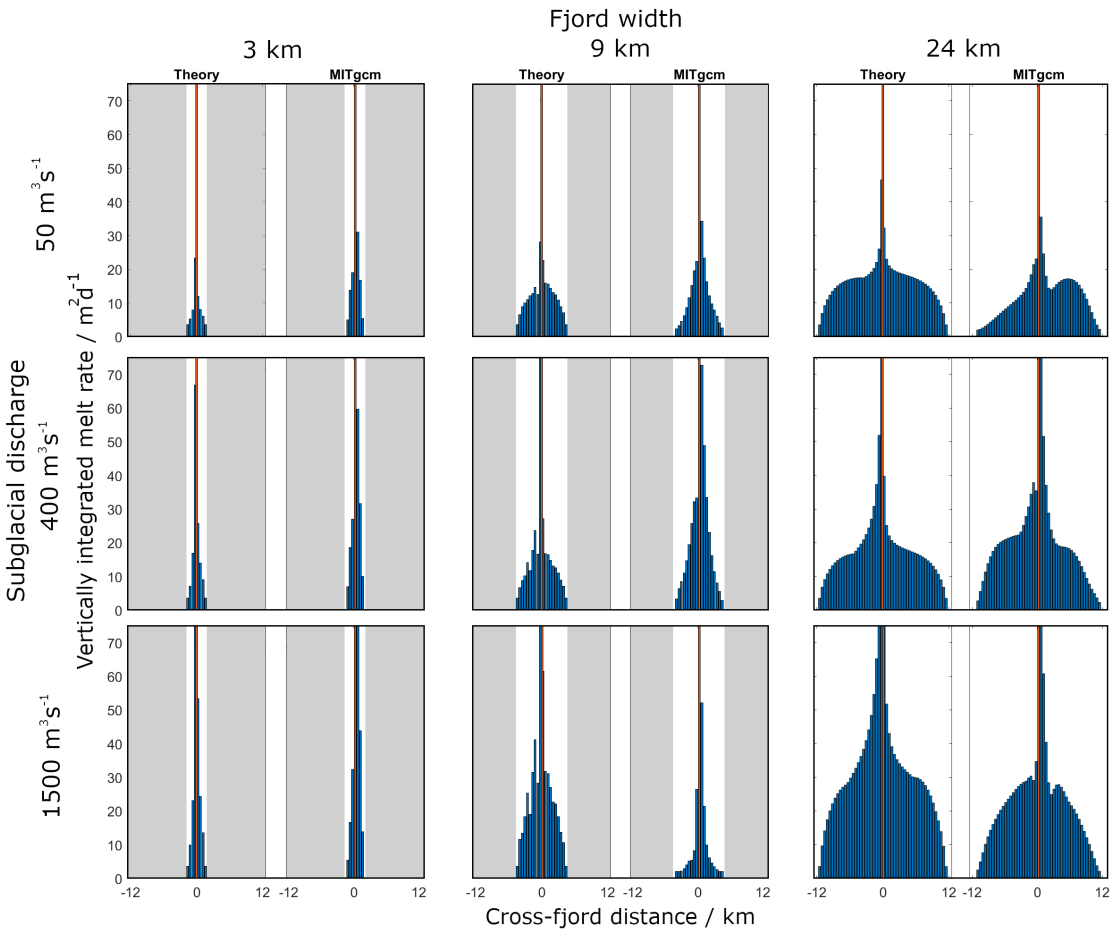

Figure 2.16: Plot of vertically-integrated melt rates predicted by theory and in MITgcm output, over a representative range of fjord widths and subglacial discharges. From top to bottom (rows), $Q_{sg} = 50,\ 400,\ 1500$ m^{3}s^{-1}. From left to right (columns), $B = 3,\ 9,\ 24$ km. MITgcm model output is averaged over the third week after model initialization, motivated by the typical timescales over which Q_{sg} changes in summer months. The red bar in the centre of all panels denotes the plume location, where the melt rates are significantly larger than across the rest of the ice and off the present scale. We truncate the y-axis to show the horizontal structure in the melt rates across the rest of the ice face away from the plume.

discharge changes (e.g. Chauché et al. 2014). Note that the local plume-driven melt rates are substantially larger than the melt rate driven by horizontal circulation, and values at the centre of the fjord thus lie off the scale necessary to see the horizontal structure across the rest of the ice face. Such plume-driven melt is compared with theory in Figure 2.13. Over the rest of the ice face, however, we recover a reasonable prediction for the vertically-integrated melt rates, both in terms of magnitude and cross-fjord structure. Encouragingly, this suggests biases in predicting cross-fjord

flow to the left of the plume in wide fjords have only modest impact on melt rates.

It is important to note that the simulation output displays some time-dependent behaviour in terms of the cross-fjord structure of the depth-integrated melt rates. This time dependence impacts the precise horizontal structure of the vertically-integrated melt rates from MITgcm simulation output, with variations on the order of $10\,\mathrm{m^2\,d^{-1}}$ in each bin over a monthly timescale. The scale of these variations is qualitatively illustrated by the difference in structure between MITgcm simulation outputs in the $B = 24\,\mathrm{km}$ cases in Figure 2.16. This reflects the complex flow structure which develops close to the ice, where growth and change in the size and location of the recirculation region impacts the melt profile. As in the previous discussion of the prediction of cross-fjord velocities at the plume outflow depth, capturing this time-dependent behaviour dramatically increases the complexity, and is likely not possible using the framework or approach used here.

We find that the freshwater flux due to the component of ice face melt associated with cross-fjord velocities at the ice face is found to be $2 - 10$ times larger than that of ice in direct contact with the plume, despite the significantly larger local melt rates of ice in contact with the plume. This is consistent with previous observations (e.g. Sutherland et al. 2019) that predictions of total melt rates based on plume theory alone significantly underestimate the observed freshwater flux due to melting. This highlights the importance of the inclusion of melting due to horizontal fjord-scale circulation in predicting the melt rates of marine-terminating glaciers. The phenomenological theory developed here provides reasonable agreement with computational model output, and provides a simple, computationally light prediction of submarine melting due to cross-fjord velocities resulting from the larger fjord-scale circulation.

2.4 Summary

Circulation in Greenland's proglacial fjords is controlled by a variety of interacting processes. Here, we have considered a circulation regime dominated by subglacial discharge, and developed scalings for the vertical structure of the circulation at the

fjord mouth, and the cross-fjord structure of vertically-integrated melt rates at the ice face. These are properties of key importance for parameterizing the interaction of the ice sheet, subglacial discharge, and the ocean.

For fjords without bathymetric sills, the vertical profile of cross-fjord-integrated, along-fjord velocity remains constant along the entire length of the fjord, echoing the plume dominated signal at the ice face even 100 km away at the fjord mouth. We extend previous scaling laws (Slater et al. 2016) for the height-of-rise of subglacial discharge driven turbulent plumes to account for a two-layer stratification typical of Greenlandic fjords. This forms the basis of predictions for the vertical structure of along- and cross-fjord velocities within the fjord, without requiring the solution of the full set of coupled partial differential equations describing the properties of the plume. These scalings allow for a computationally light prediction of the vertical structure of the estuarine-circulation exchange with the wider ocean.

We find that the horizontal plume outflow leads to a recirculation gyre near to the ice face, transitioning to a boundary current outflow downstream, consistent with some previous computational and observational studies (Carroll et al. 2017; Slater et al. 2018). We have developed a phenomenological theory for the cross-fjord velocity profile at the plume outflow depth at the ice face. This is used in combination with scalings for the vertical structure of the flow, to reconstruct an approximation to the full 2D spatial profile of cross-fjord velocities at the ice face. We extend previous scalings for the melt of ice in direct contact with turbulent plumes. Together, these allow predictions of the vertically-integrated melt rates across the entire ice face which compare favourably with computational model outputs, across a geophysically relevant range of subglacial discharge and fjord widths.

2.4.1 Implications for fjord parameterizations - ocean model coupling

The scalings for the vertical structure of the along-fjord velocity at the fjord mouth derived in this chapter have implications for parameterised treatments of ice-ocean coupling in fjords. One approach to parameterizing this fjord mediated exchange

could consider a plume and ice face in direct contact with the ocean, with some delay to account for the propagation time of signals down the length of the fjord. However, the solution of a full plume model at each fjord location at each timestep may be too computationally intensive to be useful as a parameterization, and so the simple dynamically-based scaling laws developed here offer a promising alternative.

A clear first point of improvement versus prevailing approaches is that we have developed a method to calculate the depth at which freshwater is expected to enter the ocean. In prevailing models, any freshwater discharge is injected into surface grid cells (e.g. Storkey et al. 2018). Building on previous theoretical work (Slater et al. 2016), we have derived a scaling law for the depth at which the outflow at the fjord mouth occurs, as a function of subglacial discharge and ambient ocean properties within the fjord. This uses an approximation of the ambient stratification as a layer of linearly varying density overlying a deeper layer of uniform density. This echoes a typical summertime ocean stratification around Greenland, and the approximate scaling law produces good agreement with outflow depths modelled using MITgcm simulations with a realistic stratification.

2.4.2 Implications for fjord parameterizations - ice model coupling

The phenomenological model of fjord circulation and plume theory also provide information about ice melting rates. Ice models used in global Earth system models often use grid points with a horizontal row of vertically-integrated ice grid cells in each fjord. Because some modern ice sheet models exploit adaptive mesh refinement in the horizontal (e.g. Cornford et al. 2016), it is desirable to provide a melt rate approximation which is independent of model resolution.

We produce a vertically-integrated melt profile across the ice face which compares well to time-averaged MITgcm simulation output over a geophysically relevant timescale. Whilst there are discrepancies between the predicted cross-fjord velocity on the left-hand side of the plume (looking towards the ice), the impact on the resultant melt rate profile is relatively modest, potentially due to the dependence

of melt on the magnitude of velocities rather than the sign. This shows that a simple scaling based approach could be used as a computationally efficient method to approximate melt rate profiles over a range of parameter space relevant to Greenland's fjords.

2.4.3 Limitations and future work

It is important to note that our approach makes several simplifying assumptions. Firstly, throughout this chapter we assumed a rectangular fjord cross-section with no variation of bathymetry. More complex cross-fjord geometry is likely to impact the precise circulation structure within the fjord. The cross-fjord velocities at the ice face are likely to be topographically steered in cases with non-vertical sidewalls near to the ice or appreciable bathymetry. However, the near-ice recirculation region is set up by the plume (as in open ocean settings) and so the resultant velocity structure is likely to retain some anticyclonic component near to the ice. The steady-state cross-fjord-integrated freshwater fluxes are controlled by plume dynamics at the ice face independent of any topographic steering, and so should not be affected significantly unless there is strong modification of the stratification near to the ice.

Model parameters for turbulence at the ice face for both the plume, and the ice in general, are not well constrained. These parameters include the entrainment parameter α, salinity and temperature transfer coefficients Γ_S and Γ_T, and the drag coefficient C_D. We have employed parameter values self-consistently between MITgcm simulations and theory. However, uncertainties in these parameters propagate into any comparison of melt rates and outflow depths with observations. The relative success of an inviscid theory based on potential vorticity in capturing the order of magnitude of the horizontal circulation suggests that uncertainties in isopycnal and diapycnal sub-grid scale mixing in the fjord are less significant in this setting.

We neglect the presence of topographic sills at the fjord mouth, which are common in Greenland's fjords. Global salt and volume flux budgets are set by plume dynamics; however, shallow sills may inhibit exchange between fjords and

waters on the shelf outside and result in significant modifications to fjord circulation. This is revisited in Chapter 4.

Furthermore, we neglect the impact of surface forcing, namely the injection of surface meltwater due to runoff from the ice sheet, and the melting of icebergs within the fjord, as well as atmospheric effects such as heat fluxes and wind stress. However, near-surface modification of the stratification as a result of these processes would not impact plume-driven dynamics provided these effects are confined to depths above the plume outflow.

We neglected cases with multiple discharge plumes at the ice face. In principle, the addition of multiple non-interacting discharge plumes fed by equal subglacial discharge (such that the outflow depths are the same) is a straightforward algebraic modification to the ice melt rate prediction developed here. Difficulty may arise in cases where several plumes outflow at different depth levels in this framework, as the current picture does not consider the impact of multiple 'outflow depths'; this requires further investigation.

Additionally, understanding and theoretically capturing any time-dependent, transient behaviour in velocity profiles and melt rates dramatically increases the complexity of this approach. In particular, the time-dependent response of the stratification within the fjord to changes on the coast will impact the velocity structure at the ice face, as the plume adjusts to a different ambient density profile and drives a new fjord-scale circulation. The interaction between time-dependent plume forcing, fjord stratification, changes to stratification at the fjord mouth, and the resultant impact of this on melt rates at the glacial terminus, are left for future work. As a first approximation, the steady-state theory developed here might be applied in a quasi-steady way when the spin-up of circulation within the fjord is of a shorter timescale than the changes in subglacial discharge forcing. Typical spin up timescales for our MITgcm simulations are $\mathcal{O}$(1-2) weeks, suggesting that this steady-state approach is likely to be good on seasonal timescales, but may become less accurate for fjords with forcing conditions which change on timescales shorter than this; for example, in fjords dominated by intermediary circulation.

Also, a treatment of the horizontal flow structure which employs the alternative approach outlined in §2.3.3.2 may provide a more physically motivated solution for the horizontal flow field in the outflow layer, and hence the cross-fjord velocities at the ice face. This approach relaxed the assumption that the outflow layer thickness is constant in the horizontal, and conserves potential vorticity rather than relative vorticity in the outflow layer. The Rossby radius of deformation appears as a natural length scale in the resultant modified Helmholtz equation, where the phenomenological theory of §2.3.3.1 imposes the deformation radius as the relevant length scale. Seeking solutions to Equation 2.35 would be an interesting line of future inquiry with regards to improvements on the treatment based on Equation 2.17 employed in this thesis.

Appendix

A2.1 Simple scaling analysis

To develop insight into how the flow within fjords depends on the physical dimensions and bathymetry, we consider an anisotropic nondimensionalization of the equations of motion for a shallow and narrow fjord with depth H, width B and length L satisfying $L >> B >> H$. We write:

$$\underline{u} = U\hat{\underline{u}} + V\hat{\underline{v}} + W\hat{\underline{w}},$$

$$\underline{x} = L\hat{\underline{x}} + B\hat{\underline{y}} + H\hat{\underline{z}},$$

$$t = \frac{L}{U}\hat{t} \tag{A2.1}$$

and the angular velocity vector for the Earth's rotation $\underline{\Omega} = \Omega\hat{\underline{\Omega}}$, where hatted quantities are dimensionless and U, V, W are characteristic velocity scales. The distance and velocity in the along-fjord direction are x and u, with y and v the cross fjord components, and z and w the vertical components. The last equation for t corresponds to an advective timescale. Taking rotation into account, the Navier-Stokes equation is:

$$\frac{\partial \underline{u}}{\partial t} + (\underline{u}\cdot\nabla)\,\underline{u} + 2\underline{\Omega}\times\underline{u} = -\frac{1}{\rho}\nabla p - g'\underline{\hat{z}} + \nu_{_H}\nabla^2_{_H}\underline{u} + \nu_{_V}\frac{\partial^2}{\partial z^2}\underline{u}, \tag{A2.2}$$

with $g' = g\frac{\Delta\rho}{\rho}$ and pressure p. Strong vertical stratification may inhibit mixing in the vertical as compared to the horizontal. Thus, we split the viscosity into vertical and horizontal components ν_V and ν_H, respectively, where the viscosities are interpreted as turbulent eddy viscosities. Applying the dimensional scalings to the incompressibility equation $\nabla\cdot\underline{u}$ yields:

$$\frac{U}{L}\frac{\partial\underline{\hat{u}}}{\partial\hat{x}} + \frac{V}{B}\frac{\partial\underline{\hat{v}}}{\partial\hat{y}} + \frac{W}{H}\frac{\partial\underline{\hat{w}}}{\partial\hat{z}} = 0. \tag{A2.3}$$

From this we can make some scaling arguments, in order to simplify the nondimensionalization.

If $V/B \gg W/H,\ U/L$, then the equation reduces to $\underline{\hat{v}}(y) = const$. Given the impermeable boundary conditions on the fjord sides, this implies that there is

no cross-fjord velocity in this limit, violating the initial assumption that V/B is large. Similarly, the W/H term cannot dominate, given the zero vertical velocity requirement at the fjord bottom. In principle, given that there is often some prescribed along-fjord flow due to the influx of freshwater from melt at the ice face, this logic may not hold for the U/L term. If all three terms in Equation A2.3 are of approximately the same magnitude, nondimensionalization of the Navier-Stokes equation can be greatly simplified by replacing velocity ratios with aspect ratios, such that:

$$\frac{U}{V} \sim \frac{L}{B}, \qquad \frac{U}{W} \sim \frac{L}{H}, \qquad \frac{V}{W} \sim \frac{B}{H}. \tag{A2.4}$$

If Equation A2.4 holds, or alternatively if $U/L \gg V/B,\ W/H$, then scaling the advection term $\underline{u} \cdot \nabla \sim \frac{U}{L}(\hat{\underline{u}} \cdot \hat{\nabla}))$, provides an upper bound for the relative size of this term. As a sanity check, we can consider values typical of Greenland's proglacial fjords. Outside of the nonhydrostatic plume region close to the ice face, typical values are approximately given by (Straneo et al. 2013; Sutherland et al. 2014; Slater et al. 2016; Carroll et al. 2017; Spall et al. 2017; Jackson et al. 2018):

$$\begin{array}{cc} U \lesssim 1\,\mathrm{ms}^{-1}, & V \sim 0.1\,\mathrm{ms}^{-1}, \\ W \sim 0.01\,\mathrm{ms}^{-1}, & L \sim 100\,\mathrm{km}, \\ B \sim 10\,\mathrm{km}, & H \sim 1\,\mathrm{km}, \\ \nu_H \sim 100\,\mathrm{m}^2\mathrm{s}^{-1}, & \nu_V \sim 1\,\mathrm{m}^2\mathrm{s}^{-1}. \end{array}$$

From these values, there may be some modest scale separation which contradicts Equation A2.4, varying between fjords. However, the three terms in Equation A2.3, are reasonably similar in magnitude, for the purposes of this nondimensionalization. We define dimensionless numbers relevant to the flow structure; the Rossby number Ro, and the horizontal and vertical Reynolds numbers Re_H and Re_V, respectively, as:

$$Ro = \frac{U}{2\Omega L} \quad \sim \quad 10^{-1}$$

$$Re_{_H} = \frac{UL}{\nu_H} \quad \sim \quad 10^2$$

$$Re_{_V} = \frac{WH}{\nu_V} \quad \sim \quad 10^2$$

Multiplying the $\hat{x}$ component of the Navier-Stokes Equation A2.2 by $\frac{L}{U^2}$, leaving the pressure p unscaled, and replacing velocity ratios with the corresponding aspect ratios from Equation A2.4, yields:

$$\frac{\partial \hat{u}}{\partial \hat{t}} + \hat{u}\frac{\partial \hat{u}}{\partial \hat{x}} + \hat{v}\frac{\partial \hat{u}}{\partial \hat{y}} + \hat{w}\frac{\partial \hat{u}}{\partial \hat{z}} + \frac{1}{Ro}\cdot\frac{B}{L}\left(\underline{\hat{\Omega}}\times\underline{\hat{v}}\right)_x + \frac{1}{Ro}\cdot\frac{H}{L}\left(\underline{\hat{\Omega}}\times\underline{\hat{w}}\right)_x$$
$$= -\frac{1}{\rho U^2}\frac{\partial p}{\partial \hat{x}} + \frac{1}{Re_{_H}}\frac{\partial^2 \hat{u}}{\partial \hat{x}^2} + \frac{1}{Re_{_H}}\cdot\frac{L^2}{B^2}\frac{\partial^2 \hat{u}}{\partial \hat{y}^2} + \frac{1}{Re_{_V}}\frac{\partial^2 \hat{u}}{\partial \hat{z}^2}. \tag{A2.5}$$

Using the scaling values, the $\hat{x}$ component of the Navier-Stokes equation cannot be straightforwardly simplified. As Re_V, $Re_H \gg 1$, only the $\frac{\partial^2 \hat{u}}{\partial \hat{y}^2}$ viscous term is non-negligible. However, the rotational terms are $\mathcal{O}(1)$ and $\mathcal{O}(0.1)$, respectively. Thus, both of these terms may be significant. Continuing this treatment to the y component, we find:

$$\frac{\partial \hat{v}}{\partial \hat{t}} + \hat{u}\frac{\partial \hat{v}}{\partial \hat{x}} + \hat{v}\frac{\partial \hat{v}}{\partial \hat{y}} + \hat{w}\frac{\partial \hat{v}}{\partial \hat{z}} + \frac{1}{Ro}\cdot\frac{L}{B}\left(\underline{\hat{\Omega}}\times\underline{\hat{u}}\right)_y + \frac{1}{Ro}\cdot\frac{H}{B}\left(\underline{\hat{\Omega}}\times\underline{\hat{w}}\right)_y$$
$$= -\frac{L}{\rho BUV}\frac{\partial p}{\partial \hat{y}} + \frac{1}{Re_{_H}}\frac{\partial^2 \hat{v}}{\partial \hat{x}^2} + \frac{1}{Re_{_H}}\cdot\frac{L^2}{B^2}\frac{\partial^2 \hat{v}}{\partial \hat{y}^2} + \frac{1}{Re_{_V}}\frac{\partial^2 \hat{v}}{\partial \hat{z}^2}, \tag{A2.6}$$

The scale values predict that the $\left(\underline{\hat{\Omega}}\times\underline{\hat{u}}\right)_y \sim 10^7$ term dominates, with all other terms at most $\mathcal{O}(1)$. This large term must be balanced by the pressure term, and so to leading order the equation reduces to geostrophic balance in the cross-fjord direction:

$$\frac{1}{Ro}\left(\underline{\hat{\Omega}}\times\underline{\hat{u}}\right)_y \approx -\frac{1}{\rho UV}\frac{\partial p}{\partial \hat{y}} \tag{A2.7}$$

Finally, considering the z component:

$$\frac{\partial \hat{w}}{\partial \hat{t}} + \hat{u}\frac{\partial \hat{w}}{\partial \hat{x}} + \hat{v}\frac{\partial \hat{w}}{\partial \hat{y}} + \hat{w}\frac{\partial \hat{w}}{\partial \hat{z}} + \frac{1}{Ro}\cdot\frac{L}{H}\left(\underline{\hat{\Omega}}\times\underline{\hat{u}}\right)_z + \frac{1}{Ro}\cdot\frac{B}{H}\left(\underline{\hat{\Omega}}\times\underline{\hat{v}}\right)_z$$
$$= -\frac{L}{\rho HUW}\frac{\partial p}{\partial \hat{z}} - \frac{g'L}{UW} + \frac{1}{Re_{_H}}\frac{\partial^2 \hat{w}}{\partial \hat{x}^2} + \frac{1}{Re_{_H}}\cdot\frac{L^2}{B^2}\frac{\partial^2 \hat{w}}{\partial \hat{y}^2} + \frac{1}{Re_{_V}}\frac{\partial^2 \hat{w}}{\partial \hat{z}^2}, \tag{A2.8}$$

which reduces approximately to hydrostatic balance:

$$\frac{1}{H}\frac{\partial p}{\partial \hat{z}} \approx -\rho g'. \tag{A2.9}$$

Altogether, the Navier-Stokes equation reduces to a 'semi-geostrophic' limit, where geostrophy applies in one horizontal direction only, governing the along-fjord flow and hydrostatic balance applies in the vertical. Similar equations apply in the case of atmospheric front formation (e.g. Hoskins 1975), suggesting an interesting parallel between aspects of atmospheric and proglacial fjord circulation.

A2.2 Coefficients for the phenomenological theory for cross-fjord velocity

The solution for $\psi'(x, y)$ is given by:

$$\psi' = \sum_{n=1}^{\infty} \left(A_n e^{\frac{2\pi n x}{B}} + B_n e^{-\frac{2\pi n x}{B}}\right) \sin\frac{2\pi n y}{B} + \left(\alpha_n e^{\frac{(2n+1)\pi x}{B}} + \beta_n e^{-\frac{(2n+1)\pi x}{B}}\right) \cos\frac{(2n+1)\pi y}{B}, \tag{A2.10}$$

where the full form of the coefficients $A_n,\ B_n,\ \alpha_n$, and β_n are:

$$A_n = \frac{S - U e^{\frac{2\pi n l}{B}}}{1 - e^{\frac{4\pi n l}{B}}}, \tag{A2.11a}$$

$$B_n = \frac{U e^{\frac{2\pi n l}{B}} - S e^{\frac{4\pi n l}{B}}}{1 - e^{\frac{4\pi n l}{B}}}, \tag{A2.11b}$$

$$\alpha_n = \frac{T - V e^{\frac{(2n+1)\pi l}{B}}}{1 - e^{\frac{2(2n+1)\pi l}{B}}}, \tag{A2.11c}$$

$$\beta_n = \frac{V e^{\frac{(2n+1)\pi l}{B}} - T e^{\frac{2(2n+1)\pi l}{B}}}{1 - e^{\frac{2(2n+1)\pi l}{B}}}, \tag{A2.11d}$$

and

$$S = -\frac{\Delta\psi}{\pi n} \tag{A2.12a}$$

$$T = \frac{4\omega B^2}{(2n-1)^3\pi^3}\cos\pi n \tag{A2.12b}$$

$$U = -\frac{\Delta\psi}{2b\pi^2 n^2}\left(B\sin\frac{\pi n(2b-B)}{B}\right) \tag{A2.12c}$$

$$V = -\frac{2\Delta\psi}{b(2n-1)^2\pi^2}\left(B\sin\frac{\pi n(2b-B)-\pi b}{B}\right) + \frac{4\omega B^2}{(2n-1)^3\pi^3}\cos\pi n$$

3

Box-model parameterization of subglacial-discharge-driven circulation in Greenland's proglacial fjords

3.1 Introduction

The exchange of heat and meltwater between the Greenland Ice Sheet and the ocean is mediated by several hundred fjords around Greenland's coastline. The circulation within Greenland's fjords is thought to be controlled by several processes. In this thesis, we have focused on the subglacial-discharge-driven estuarine circulation, whereby the injection of freshwater at the grounding line of a marine-terminating glacier generates a buoyant plume at the ice face, in turn generating a fjord-scale circulation (e.g. Cowton et al. 2015; Carroll et al. 2017).

Recall from Chapter 1 that fjords around the coast of Greenland are narrow, typically $\mathcal{O}(10\,\mathrm{km})$ wide. As such, current generation Earth system models typically run at resolutions too coarse to resolve the circulation within these fjords directly. Therefore, the development of a parameterization scheme representing the impact of fjord circulation on the ocean forced component of the melting of the Greenland Ice Sheet is essential for reliable long term projections of ice sheet stability and global climate. The complexity and range of processes which contribute to circulation

within fjords, as well the current lack of predictive understanding of the relationship between submarine melting and iceberg fracture, mean that it is impractical to include all processes in a first parameterization. However, it would be beneficial if any parameterization scheme were able to allow for future additions as simple characterizations of these other processes are developed.

Currently, no parameterization scheme exists which represents the impact of fjord-scale circulation on the ocean forced melt of the Greenland Ice Sheet, although related problems have been considered. Gillibrand et al. (2013) developed a box model of seasonal exchange in inlets on the coast of Scotland, which acts as a simple characterization of the time evolution of water and flow properties given topographically restricted exchange. However, the freshwater forcing considered here leads to significant differences in flow structure and time evolution of water properties in Greenland's fjords, such that the box model developed for Scottish inlets cannot be readily applied. In contrast to Scottish inlets, the injection of freshwater at the ice face within Greenlandic fjords drives a significant estuarine circulation, with the potential for outflows to occur in the sub-surface.

In an alternative approach, some attempt has been made to relate subglacial discharge and ocean temperature to submarine melting and glacial terminus position around Greenland's coastline. Slater et al. (2019) parameterize glacial terminus position as a linear function of the subglacial discharge and ocean thermal forcing, and calibrate and test predictions using datasets of glacial retreat, ocean temperatures and subglacial discharge over several decades. However, their model is intended as a statistical prediction over a large ensemble of outlet glaciers, and the linear relationship between subglacial discharge, ocean thermal forcing and glacial retreat neglects the impact of fjord-scale circulation entirely.

In Chapter 2, we derived theoretical scalings for the vertical structure of this fjord-scale circulation in an idealised, flat-bottomed fjord. We also presented a phenomenologically derived prediction for the horizontal flow structure and the vertically-integrated melt rate at the ice face. In this chapter, we construct a simple box model which builds on these earlier results to predict the time evolution of

fjord waters and vertically-integrated melt rates at the ice face, given time series of ocean stratification and subglacial discharge flux, and fjord dimensions. This box model is intended to be computationally light, such that the implementation as a parameterization in Earth system models is computationally feasible for each glacier-fjord system around Greenland's coastline.

Figure 3.1 schematically illustrates the anticipated structure of inputs to and outputs from a fjord parameterization scheme within an Earth system model. The typical resolution of ice and ocean model components of current generation Earth system models constrain the number and structure of grid points available for a fjord parameterization scheme to use for both input and output. Ice model components typically solve for vertically-integrated ice properties, sometimes with sufficient horizontal resolution to require several grid cells in the cross-fjord direction to represent the calving front of a marine-terminating glacier. Ocean model components, on the other hand, have horizontal resolutions such that the stratification at the mouth of a fjord is represented by a single vertical column of grid cells (e.g. Williams et al. 2018). As previously stated, our box model is intended to represent the fjord circulation in a subglacial-discharge-driven estuarine regime, building upon previous results in this thesis. The box model takes inputs of freshwater flux from subglacial discharge calculated by an ice model forced by an atmosphere model, along with ocean salinity and temperature stratification from an ocean model, outputting a parameterized melt rate to the ice model, and vertical velocity structure, as well as heat and salt fluxes, to the ocean model.

In this chapter, we first describe key assumptions made in the development of the box model and describe the model algorithm (§3.2). Next (§3.3), we investigate several illustrative experiments whereby permutations of realistic and idealised subglacial discharge fluxes and ocean forcing conditions are employed to diagnose the behaviour and limitations of the box model. For the realistic forcing, we take ocean salinity and temperature from the NEMO ocean model component of a pre-industrial control run (not historical) of the HADGEM3-GC3.1-LL global coupled Earth system model (Williams et al. 2018; Menary et al. 2018). Subglacial

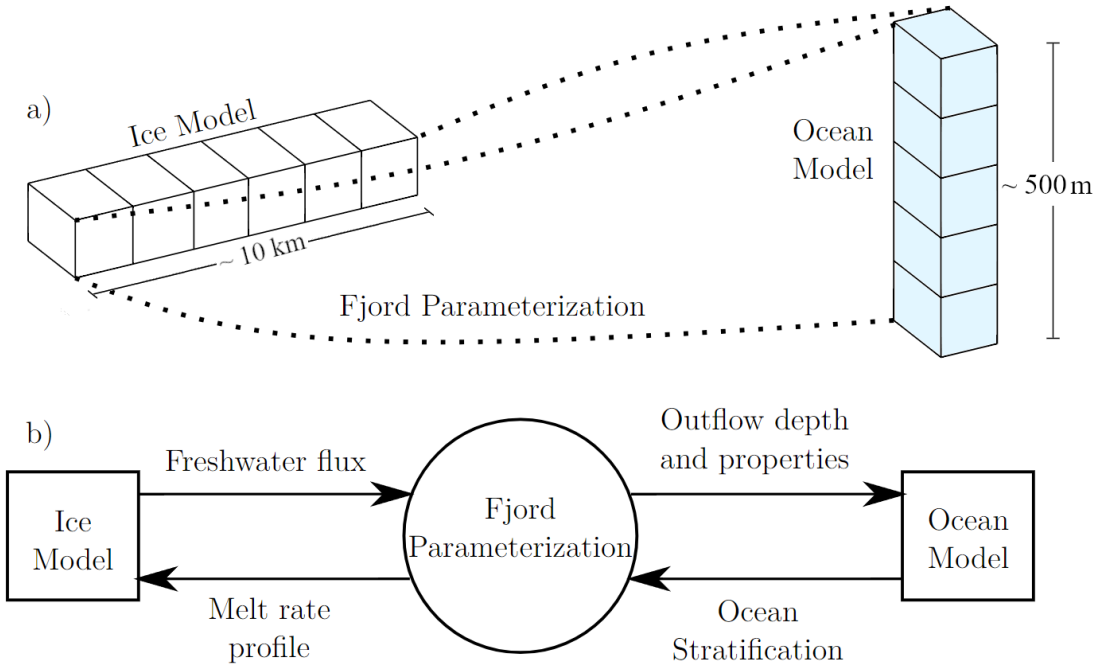

Figure 3.1: a) Schematic of the available ice and ocean model grid cell structure of Earth system models adjacent to a fjord which are the target of the box-model parameterization. b) The key input and output variables required to be passed between the ice and ocean models by a parameterization scheme.

discharge is derived from the atmospherically forced melting of the Greenland Ice Sheet, calculated via the JULES land-surface component. Topographically steered freshwater from surface melt is assumed to percolate down through the ice to become subglacial discharge at the glacial terminus. In §3.4 we compare box-model results to output from MITgcm simulations with the same subglacial discharge and ocean forcing conditions. We summarise key conclusions in §3.5. Potential avenues for future work are discussed in §3.6, including several possible additions to the box model, to account for a wider range of fjord circulation forcing conditions and processes.

3.2 Methods

3.2.1 Box-model assumptions

As previously discussed, the parameter space of relevance to Greenland's fjords is vast and multidimensional. Accurate, high-resolution representation of the

bathymetry of every fjord on the coastline of Greenland, as well as a full treatment of the oceanic stratification, may require prohibitively expensive computational models even in a circulation regime driven by a single process. Progress towards a simple, practical parameterization scheme that captures the leading order response therefore requires several simplifying approximations.

In this chapter, we employ the scaling laws and predictions developed in Chapter 2 to determine the vertical structure and volume fluxes of the box model at each time step, as well as the melt rates supplied to the ice model component. Key assumptions involved in the derivation of these scalings are summarised below and carry over into the work in this chapter.

Vertical flow structure:

- The fjord contains a single, central freshwater point source at the grounding line, generating a single half-conical buoyant plume. An off-centered plume source should not change the cross-fjord-integrated flow dynamics to leading order; however, it would impact the spatial pattern of melt at the ice face.
- The stratification within the fjord is controlled primarily by salinity.
- Both the fjord and oceanic stratifications can be approximated as a layer of linearly varying salinity and temperature overlying a layer of constant salinity and temperature.
- The volume flux of freshwater due to submarine melt is small compared to the subglacial discharge over a geophysically relevant range of forcing conditions, consistent with predictions based on plume theory.

Vertically-integrated melt profiles:

- The outflow layer thickness is constant in the horizontal, such that conservation of potential vorticity is equivalent to conservation of relative vorticity in the outflow layer.

- The relative vorticity of the outflow is set by vortex stretching in the plume as it rises through the unstratified lower layer only.
- The anticyclonic vortex at outflow depth is constrained in along-fjord extent to the smaller of the fjord width or Rossby radius of deformation.
- Flow downstream of the recirculation region occurs as a boundary current, with cross-fjord extent given by the smaller of the fjord width or Rossby radius of deformation.

Furthermore, in constructing the box model itself we introduce additional simplifying assumptions:

- The pycnocline depth within the fjord responds instantaneously to changes in the pycnocline depth in the ocean, although the salinities in the fjord and ocean can differ, conserving salt.
- The along-fjord volume fluxes respond instantaneously along the entire length of the fjord and are predicted by the plume scalings.
- There is a rigid lid, rather than a dynamic free surface with changing water depth.
- Volume fluxes in each layer are uniform in the vertical, for the set of layers introduced below.

The physical constants and parameters used in the box model are summarised in Table 3.1

3.2.2 Box-model structure

The cross-fjord-integrated circulation generated by buoyant plumes can be broken down into several vertical layers, given the previous assumptions (see Figure 3.2). Consider cases with non-zero subglacial discharge; moving upwards from the ocean bed, the deepest layer consists of inflow over a range of depths with constant

Symbol	Name	Value	Units
α	Entrainment parameter	0.2	
$\bar{\rho}$	Reference density	1024	$\mathrm{kg\,m^{-3}}$
c_i	Heat capacity of ice	2000	$\mathrm{J\,kg^{-1}\,°C^{-1}}$
$\mathcal{L}$	Latent heat of fusion of ice	3.35×10^5	$\mathrm{J\,kg^{-1}}$
c_w	Heat capacity of water	3974	$\mathrm{J\,kg^{-1}\,°C^{-1}}$
Γ_T	Thermal turbulent transfer coefficient	2.2×10^{-2}	
Γ_S	Salt turbulent transfer coefficient	6.2×10^{-4}	
C_d	Drag coefficient	3.5×10^{-3}	
λ_1	Freezing point slope	-5.73×10^{-2}	$\mathrm{°C\,PSU^{-1}}$
λ_2	Freezing point offset	8.32×10^{-2}	°C
λ_3	Freezing point depth	7.61×10^{-4}	$\mathrm{°C\,m^{-1}}$
g	Gravitational acceleration	9.81	$\mathrm{m\,s^{-2}}$
B	Fjord width	3–24	km
L	Fjord length	100	km
u_{bg}	Background velocity	0.01	$\mathrm{m\,s^{-1}}$
f	Coriolis parameter	1.2×10^{-4}	$\mathrm{rad\,s^{-1}}$
Δt	Box-model timestep	1×10^5	s

Table 3.1: Parameter values employed in the box model (taken from Cowton et al. (2015)), used in calculating the vertical structure of the overturning circulation and the melt rate profile at the ice face. Values of fjord width, length, background velocity, Coriolis parameter, and box-model timestep are choices made for the work in this chapter.

ambient salinity. Above this is a layer of inflow over depths in which the ambient stratification varies linearly. Overlying this is the plume outflow layer. When the outflow is not predicted to occur at the surface, a stagnant layer sits above the outflow layer. At the very surface, we introduce a shallow mixed layer. This is intended to allow for the future addition of other processes driving fjord-scale circulation and is currently not dynamically active.

The approximation of a piecewise linear stratification with two sections (an

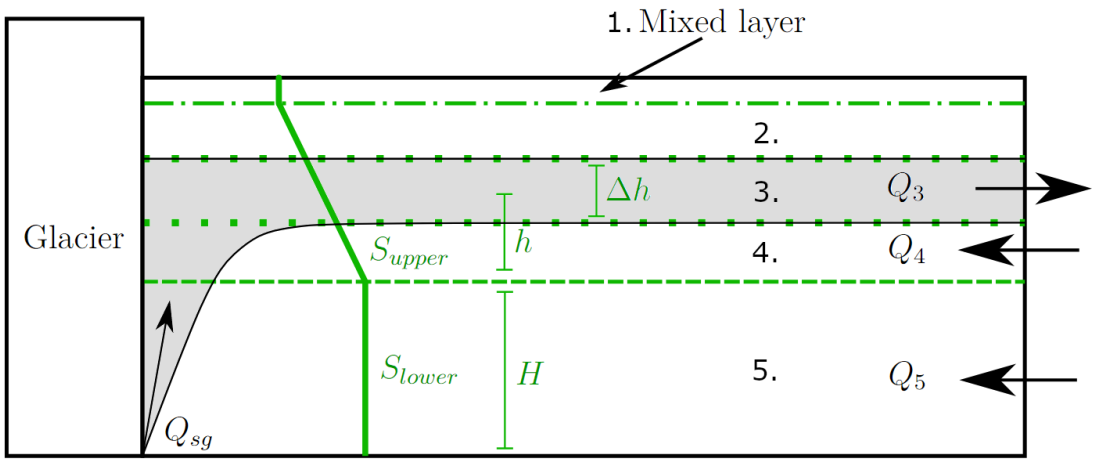

Figure 3.2: Overview of the box and layer structure. The fjord contains two vertically stacked boxes (separated by the dashed line), with an 'upper' stratified box and 'lower' unstratified box. The upper box is subdivided into up to 4 layers by dotted lines with thicknesses h_i. Moving downwards from the surface, these are: 1. a mixed layer (above the dotted and dashed line, initially treated as inactive); 2. a stagnant layer above the plume outflow layer; 3. the plume outflow layer; 4. inflow below the outflow layer, within the upper box; 5. inflow in the lower box. The plume (and associated horizontal outflow) is shaded light grey.

unstratified lower section and a linearly stratified upper section) in both the fjord and the ocean means that one practical choice for the box-model structure is that of two vertically stacked grid boxes, with box thicknesses in the fjord model varying in accordance with the ocean stratification. In this setup, the upper grid box is always of linearly varying salinity, and the lower grid box is always of constant salinity. The aforementioned inflow-outflow structure generated by the plume further subdivides the surface box into several layers, depending on the predicted outflow layer depth and thickness. Furthermore, the changing thicknesses of fjord grid boxes from one timestep to another leads to overlaps between the box and layer structure. Therefore, to reduce ambiguity in terminology we introduce the following terms:

- **Boxes**: Either 'upper' or 'lower' and hold the final salinity profile at the end of a timestep, with the 'upper' box having a linearly varying salinity and the 'lower' box having a constant salinity. The boxes within the fjord at the end of a given timestep are always the same thickness as the boxes in the ocean stratification at that same timestep, although the salinities can differ.

- **Layers**: Subdivisions of the upper box at the previous timestep, labelled with subscripts 'F, i' or 'O, i' where F refers to quantities within the fjord, O to quantities within the ocean, and i labels the i-th layer from the surface. The thicknesses and volume fluxes within these layers are found via plume scalings using the results from Chapter 2. The salinities within these layers are found using the (constant) salinity gradient of the upper box and the height within this box. Within a layer, the volume flux is assumed to be constant in the vertical.

- **Regions**: Between timesteps, the heights of the layer interfaces may move. It is helpful to define 'regions' which subdivide layers temporarily, based on the overlaps between the layer structure of the previous timestep and the box structure at the current timestep. The regions which form between two timesteps depend on the amount and direction of movement of the box interface in the ocean stratification between those two timesteps. Quantities within regions are denoted by subscripts 'F, Ri' or 'O, Ri' where again, F is in the fjord, O in the ocean and here Ri stands for Region i, counted downwards from the shallowest region to the deepest. Salt and heat fluxes are calculated in regions, and then combined into the relevant boxes.

3.2.2.1 Scalings

The volume fluxes and layer structure are determined using scaling laws developed in Chapter 2, relying on the assumptions previously discussed. The key scalings are the height of rise of the plume outflow into the halocline (corresponding to the upper box) h, and the outflow layer thickness Δh. This height of rise is measured from the interface which divides the upper and lower boxes. For cases where $h \leq \Delta h/2$, the outflow layer is of thickness Δh, sits at the bottom of the upper box, and there is no inflow layer in this box for this flow state. Where h is predicted to lie at depths within $\Delta h/2$ of the very surface, the outflow will be treated as occurring at the very surface with thickness Δh and with no stagnant layer above it. For outflow depth predictions between these two extremes, the thicknesses of the inflow

layer below the outflow, and the stagnant layer above are both non-zero. From Equation 2.15 and Equation 2.16, the scalings for these quantities are:

$$h = \frac{5S_2}{3\pi\alpha H_0^{5/3}} \left(\frac{\partial S_1}{\partial z}\right)^{-1} \left(\frac{9\alpha g_0'}{5\pi}\right)^{-1/3} Q_{sg}^{2/3}, \tag{3.1}$$

$$\Delta h = \Gamma_1 (Q_{sg} g_0')^{1/4} N^{-3/4}, \tag{3.2}$$

where Q_{sg} is the subglacial discharge flux, S_2 is the (constant) lower box salinity, $S_1(z)$ is the upper box salinity, N is the buoyancy frequency in the surface box, calculated using $N^2 = -g\beta\partial S_1/\partial z$ for haline contraction coefficient β and gravitational acceleration g, α is the plume entrainment coefficient and g_0' is the reduced gravity at the grounding line. Following the approach in Chapter 2 we set the dimensionless prefactor $\Gamma_1 = 1$, although this could be used as a tuning parameter. Recall that $H_0^{5/3} = (H + z_0)^{5/3} - z_0^{5/3}$, where H is the lower box thickness and

$$z_0 = \frac{5}{6\alpha} \left(\frac{32\alpha Q_{sg}^2}{5\pi^2 g_0'}\right)^{1/5},$$

from Equation 2.6. The volume fluxes in each layer are again given by scaling laws developed in Chapter 2. Referring to Figure 3.2, these are:

$$Q_5 = \frac{3\pi\alpha H_0^{5/3}}{5} \left(\frac{9\alpha g_0'}{5\pi}\right)^{1/3} Q_{sg}^{1/3}, \tag{3.3}$$

$$Q_4 = \pi\alpha (Q_{sg} g_0')^{1/2} N^{-1/2} h, \tag{3.4}$$

$$Q_3 = Q_4 + Q_5 + Q_{sg} + \dot{M}. \tag{3.5}$$

Here $\dot{M}$ is the meltwater volume flux due to submarine melting of the glacial terminus, Q_3 is the volume flux of the plume outflow at the level of neutral buoyancy, and Q_4 and Q_5 are fluxes into the plume due to entrainment. Q_1 and Q_2 are zero by assumption. We assume that this meltwater leaves the fjord at the same depth as the subglacial discharge, although in principle this can be different.

More accurate characterization of the depth at which submarine meltwater from outside of the plume enters the wider ocean is left for future work.

Together, these scalings allow for the construction of the box and layer structure illustrated in Figure 3.2 for a given fjord stratification. In §3.2.2.3, we discuss the method by which we construct the idealised oceanic stratification given the realistic oceanic stratification at a given timestep, with the lower box thickness for the fjord box model moving to match that of the ocean at the current timestep, once the salt fluxes have been calculated. This approximation to the stratification is crucial in order to apply the previously derived scalings for a piecewise linear stratification, although is a source of further approximation. It should be noted that the salt fluxes into each layer are controlled by the salinity and volume flux flowing into and out of each layer at either end of the fjord. The assumptions that the volume flux is constant in each layer, and that the outflow occurs with the salinity corresponding to the ambient fjord salinity at that depth, mean that the outflow layer does not contribute to changing the salinity in the surface box. The time evolution of the stratification within the fjord itself is discussed in more detail from §3.2.3 - 3.2.4 onwards.

3.2.2.2 Melt rate calculation

The melt rate at the ice face is calculated using the approach developed in Chapter 2. We use the phenomenologically motivated cross-fjord velocity at the ice face, and convert the predicted velocity profiles to melt rates using the 'three-equation formulation' (Holland et al. 1999), and the stratification in the fjord at that time step:

$$\begin{aligned} \dot{m}\left[c_i\left(T_b - T_i\right) + \mathcal{L}\right] &= \Gamma_T C_d^{1/2} u c_w \left(T_F - T_b\right), \\ \dot{m} S_b &= \Gamma_S C_d^{1/2} u \left(S_F - S_b\right), \\ T_b &= \lambda_1 S_b + \lambda_2 + \lambda_3 z, \end{aligned} \tag{3.6}$$

where $\dot{m}$ is the melt rate as a function of cross-fjord position and depth, T is temperature and S is salinity. Terms with subscript b refer to properties at the ice-ocean interface and terms with subscript F refer to the fjord box-model stratification. Constants $C_d,\ \Gamma_S,\ \Gamma_T,\ c_i,\ c_w,\ \lambda_1,\ \lambda_2$ and λ_3 are defined in Chapter 2, and take

the values in Table 3.1. The prediction for the velocity u is split into 4 zones across the ice face (see Figure 2.15).

Between the outflow layer and the surface (purple) the velocity is given solely by a uniform small background velocity $u_{bg} = 0.01\,\mathrm{m\,s^{-1}}$, accounting for unresolved fine-scale turbulent mixing as a result of processes such as buoyant meltwater flow or background waves. This background velocity acts as a minimum velocity over the entire ice face. Where the cross-fjord velocity anywhere at the ice face is predicted to be smaller than u_{bg}, the velocity is set to u_{bg}. This leads to a background melt rate even at times when the subglacial discharge is zero. In the outflow layer (green), the cross-fjord velocity is predicted using the streamfunction method developed in Chapter 2, assuming the formation of an anticyclonic vortex at the plume outflow depth. In the inflow region (white), we assume that cross-ice velocities are radial fluid velocities into the plume due to entrainment. Where the plume is in direct contact with the ice (yellow) and thus there are enhanced melt rates due to the large vertical velocities within the plume, we employ the scalings in Equation 2.37, building upon Slater et al. (2016).

3.2.2.3 Approximation to the ocean stratification

To use the scalings for plume outflow developed in Chapter 2, we require an algorithm which approximates the ocean stratification supplied by the ocean model at each time step with a layer of linearly varying density overlying a layer of constant density. This must allow for the systematic determination of an effective pycnocline depth of the ocean stratification, and thus the lower box thickness H at each time step. Occasionally, the fjord may be deeper than the depth of the neighbouring shelf that is resolved in an ocean model, such that there are depths where stratification input is unavailable. In such cases, the deepest available ocean value is projected down to fjord depth, consistent with the assumption of negligible stratification at depth.

Typically, the ocean component within an Earth system model uses vertical resolution on a telescopic grid, from tens of metres near the surface to hundreds of metres at depth. To avoid the fitting routine generating discrete jumps in H

comparable to the distance between consecutive points on the ocean grid, the ocean stratification is interpolated onto a higher resolution grid prior to the generation of the idealised stratification. In this chapter, we cautiously choose a vertical resolution of 1 m, although there may be potential to optimise computational speed in future by using a coarser resolution.

To approximate the stratification, the routine steps through each grid point in the ocean salinity profile in turn. For each test grid point, the initial approximation for the lower layer salinity is taken as the mean of the ocean salinity below that grid point. Then, a least-squares fitting routine generates a linear fit above the test grid point, constrained such that the salinity at the test grid point is continuous between the lower and upper sections of the approximated stratification. The error between the approximated and real stratification is then calculated. The fit associated with the smallest error across all test grid points is taken to be the final approximation to the salinity, and the corresponding test grid point is taken to be the depth of the interface between the upper and lower boxes, with H given by the lower box thickness. To approximate the vertical variation in temperature, the routine uses the box thicknesses generated by the salinity fitting routine, taking the mean value of the temperature in the lower box and a linear fit in the upper box, again constrained to be continuous at the box interface.

Examination of NEMO ocean model data from Greenland's coastline reveals large seasonal variation in the surface $\mathcal{O}(50\,\mathrm{m})$, which can have a large impact on the linear approximation to the salinity in the surface box (Figure 3.3). Dynamically, the salinity in this surface layer can only impact the outflow depth of a buoyant plume if the plume penetrates all the way up to this depth. Recall, however, that for plume outflow depths predicted to lie anywhere within Δh of the ocean surface, the outflow layer must simply sit at the ocean surface. Given that the outflow layer does not contribute to changing the salinity in the surface box, and the typical range of outflow layer thicknesses predicted by the scaling law suggested for $\Delta h \sim \mathcal{O}$(10-100m), the error associated with ignoring this variable layer is likely to be small. Therefore, we ignore data from the top 50 m when fitting the approximation to the

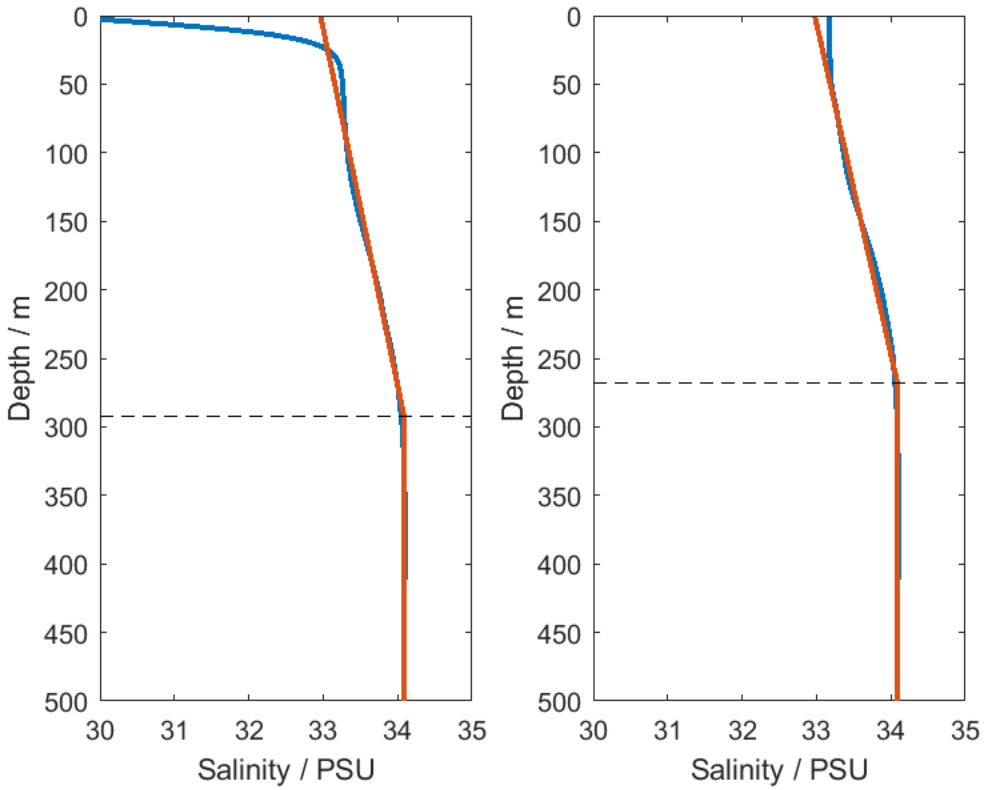

Figure 3.3: *Blue lines*: Salinity profiles from NEMO ocean model output in the nearest ocean grid cell to Jakobshavn, West Greenland taken in a) summer and b) winter, showing the large seasonal variability in the top $\mathcal{O}(50\,\mathrm{m})$. *Red lines*: The approximated salinity profile finding the box interface depth minimizing the error, given the assumption of a linearly varying layer overlying a layer of constant salinity. *Dashed lines*: The box interface depth estimate in each case.

ocean stratification at a given timestep, unless otherwise stated. Potential avenues for a more systematic determination of the most appropriate depth range to neglect are left for future work. It should be noted that this choice to neglect the top 50 m allows for a much more accurate fit over a dynamically active range of depths further below the surface in most test cases we examined.

3.2.3 Algorithm overview

In this section, we give an overview of the algorithm governing the time evolution of the fjord box model. The box model takes fjord dimensions, subglacial discharge and ocean stratification in salinity and temperature at each time step, and returns the volume flux and range of depths over which outflow occurs, as well as a vertically-

integrated melt rate profile at the ice face. At each time step (after initialization), the box model follows the algorithm below.

1. Initialise fjord box model. This sets initial values for the fjord stratification and flow structure given fjord width, length, depth and subglacial discharge flux.

2. Calculate approximation to ocean stratification at the current time step, as discussed in §3.2.2.3.

3. Set the box sizes in the fjord at the current timestep to match that of the current ocean stratification.

4. Calculate the overlap regions of the new ocean boxes and previous fjord layers and choose between three cases.

1. Upper box deepens.
2. Upper box shallows but the box interface remains below the outflow layer from the previous timestep.
3. Upper box shallows into or above outflow layer from the previous timestep.

5. Calculate the salt fluxes into the boxes within the fjord at the current timestep. Use horizontal volume fluxes, layer sizes and salinity within the fjord from the previous timestep, and approximated ocean salinity from the current timestep.

6. Calculate the new lower box salinity, and the salinity gradient within the upper box given the total salt in the upper box and constraining the stratification to be continuous at the box interface.

7. Use the new fjord stratification in the scalings for the volume flux and layer structure for the next timestep. Calculate the ice face melt rates. Advance in time.

Return to step **2**.

3.2.4 Box and layer structure between timesteps

The movement of the ocean pycnocline from one timestep to the next creates overlap regions between the box structure at the current time step, and the box structure at the previous timestep. There are three possible cases, treated individually:

1. The box interface deepens from one timestep to the next.
2. The box interface shallows, but remains below the outflow layer in the fjord from the previous timestep.
3. The box interface shallows into or above the outflow layer in the fjord from the previous timestep.

The box model defaults to case 1 if the pycnocline does not move between two timesteps, such that the only modification to the salinity in the fjord is due to salt fluxes between the fjord and ocean in each layer. We now step through the equations which form the basis of the box model in each of these three cases. Note that whilst the following numerical scheme is described in terms of the salinity in the fjord and the ocean, the stratification in temperature within the fjord is updated using an identical scheme.

3.2.4.1 Box interface deepens (or remains stationary)

Regions

In the case that the bottom of the pycnocline in the ocean stratification deepens from one timestep to the next, the bottom of the new ocean pycnocline will be below the bottom of the fjord pycnocline from the previous timestep. The overlap between the ocean boxes at the current timestep and the fjord layer structure from the previous timestep produces three regions in which salinity is changing due to a salt flux (see Figure 3.4).

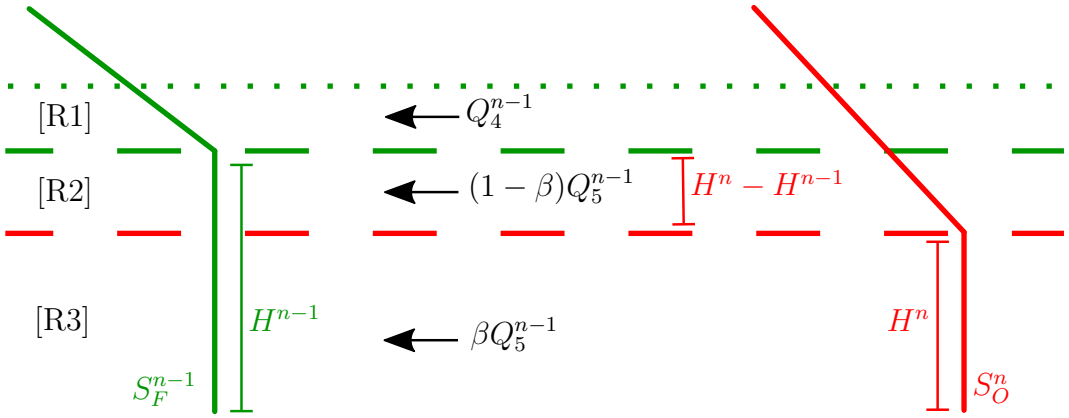

Figure 3.4: When the bottom of the ocean pycnocline deepens from one timestep to the next, ocean and fjord boxes and layers between the two timesteps overlap, and form 3 overlap regions. *Dotted green line*: the bottom of the plume outflow layer at the previous timestep. *Solid green line*: the fjord stratification in salinity at the previous timestep, given the box structure at the previous timestep. *Dashed green line*: Fjord box interface depth at the previous timestep. *Solid red line*: the approximation to the ocean stratification in salinity at the current timestep. *Dashed red line*: Ocean box interface depth at the current timestep. **[R1]** – region 1, within the fjord surface box from the previous timestep, but below the outflow layer. **[R2]** – region 2, between the box interface depth in the fjord from the previous timestep, and the ocean box interface depth at the current timestep. **[R3]** – region 3, below the ocean box interface depth at the current timestep, effectively the entire lower box at the current timestep. $\beta = H^n/H^{n-1}$ gives the fraction of the fjord lower box from the previous timestep which overlaps with the ocean lower box at the current timestep.

The salt flux in regions 1 and 2 contributes to the salinity in the upper box within the fjord at the current timestep. The salt flux within region 3 contributes to the salinity in the lower box within the fjord at the current timestep.

Salt flux calculation - lower box

Assuming the volume fluxes are constant in the vertical within each layer, the volume flux in region 3 is simply scaled by the thickness of this region relative to the full depth of the lower box at the previous timestep, such that

$$S^n_{F,R3} - S^{n-1}_{F,R3} = \frac{\Delta t}{BLH^n}\left(S^n_{O,R3} - S^{n-1}_{F,R3}\right)\beta Q_5^{n-1} \equiv \Delta S^n_{R3}, \tag{3.7}$$

where $\beta = H^n/H^{n-1}$, $S^i_{F,Rj}$ is the mean salinity in region j within the fjord at timestep i, $S^i_{O,Rj}$ is the mean salinity in region j within the ocean at timestep i,

B is the fjord width, L is the fjord length, Δt the timestep size and Q_5^{n-1} is the volume flux in the lower box from the previous timestep. BLH^n represents the volume of region 3 at timestep n. This directly yields the salinity of the lower box within the fjord at the current timestep, $S^n_{lower} = S^n_{F,R3}$.

Salt flux calculation - upper box

For a deepening ocean pycnocline, the salinity in the upper box within the fjord at the current timestep is impacted by the salt fluxes in overlap regions 1 and 2.

The change in mean salinity in region 1 is found from the difference between salt fluxes in and out of this region:

$$S^n_{F,R1} - S^{n-1}_{F,R1} = \frac{\Delta t}{BLh_4^{n-1}} \left(S^n_{O,R1} - S^{n-1}_{F,R1} \right) Q_4^{n-1} \equiv \Delta S^n_{R1}, \tag{3.8}$$

where Q_4^{n-1} is the volume flux in this region, which corresponds to that of layer 4 from the previous timestep.

The mean salinity within region 1 within the fjord at the previous timestep is calculated using the upper box salinity gradient from the previous timestep. Given the constant salinity gradient, the mean salinity within this region is given by

$$S^{n-1}_{F,R1} = \frac{h_4^{n-1}}{2} \frac{\partial S^{n-1}_{upper}}{\partial z} + S^{n-1}_{lower}. \tag{3.9}$$

with a similar calculation for the ocean stratification over the same depth range.

Recall that we assume that the volume flux is constant in the vertical within a layer. Then the remaining fraction of the total flux within layer 5 that enters region 2 from the ocean, and departs into the plume, is $(1-\beta)Q_5^{n-1}$, where $\beta = H^n/H^{n-1}$. Together, the change in salinity in this layer of volume $BL(H^{n-1} - H^n)$ is

$$S^n_{F,R2} - S^{n-1}_{F,R2} = \frac{\Delta t}{BL(H^{n-1} - H^n)} \left(S^n_{O,R2} - S^{n-1}_{F,R2} \right) (1-\beta) Q_5^{n-1} = \Delta S^n_{R2}. \tag{3.10}$$

The total amount of salt in the upper box is given by the amount of salt that is encompassed by the new upper box, given the old fjord salinity profile, plus the total change in salt in regions 1 and 2:

$$\mathcal{S}^n_{tot} = BL\left[\int_{H^n}^{D} S_F^{n-1}\, dz + h_4^{n-1}\Delta S^n_{R1} + (H^{n-1} - H^n)\Delta S^n_{R2}\right], \tag{3.11}$$

where $z = D$ is the ocean surface. We enforce a linear salinity profile in the upper box and continuity of salinity at the interface between boxes, and this allows the calculation of the new salinity gradient in the upper box via

$$\mathcal{S}^n_{tot} = BL\int_{H^n}^{D} \frac{\partial S^n_{upper}}{\partial z}(z - H^n) + S^n_{lower}\, dz \tag{3.12}$$

$$\implies \frac{\partial S^n_{upper}}{\partial z} = 2\left(\frac{\mathcal{S}^n_{tot}}{BL(D - H^n)^2} - \frac{S^n_{lower}}{D - H^n}\right). \tag{3.13}$$

Thus we have the lower box salinity and the upper box salinity gradient in the fjord at the current timestep. These are used in scalings to determine the depth of each layer interface, ready for the next timestep. It should be noted that if the pycnocline does not move, then the contribution $\Delta S^n_{R2} = 0$ for region 2, and the upper box salinity is affected only by ΔS_{R1}. To avoid singularities in this case, this change in salinity is calculated at the same time as the integral is performed for $\mathcal{S}_{tot}$ such that at no point are any terms divided by $H^{n-1} - H^n$.

3.2.4.2 Box interface shallows but remains below previous outflow layer

Regions

In the case that the ocean pycnocline shallows from one timestep to the next, the new ocean box interface can either sit below the previous outflow layer but above the previous fjord box interface, or it can rise to sit within (or above) the outflow layer at the previous timestep. In the first case, the overlaps between the ocean boxes at the new timestep and the fjord layer structure from the previous timestep produces three regions in which salinity is changing due to a salt flux (see Figure 3.5).

In this case, the salt flux in region 1 contributes to the salinity in the upper box within the fjord from the current timestep. The salt flux within regions 2 and 3 contributes to the salinity in the lower box within the fjord at the current timestep.

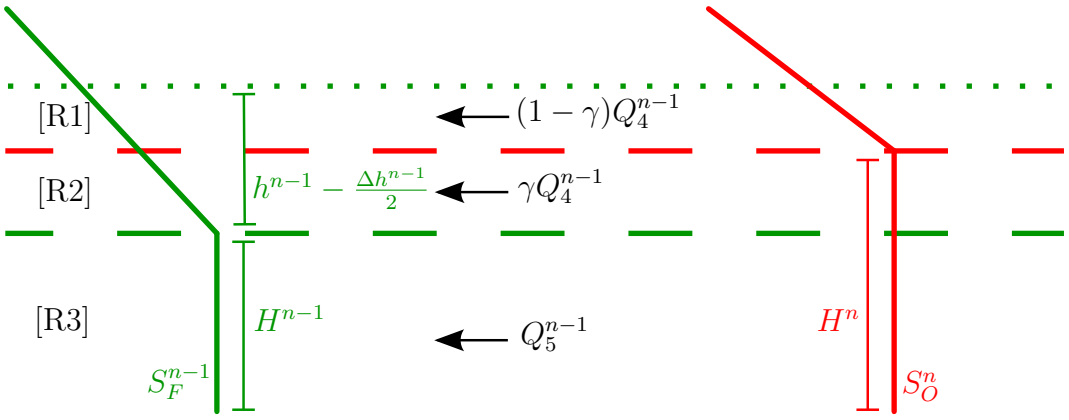

Figure 3.5: When the ocean pycnocline shallows from one timestep to the next, ocean and fjord boxes and layers between the two timesteps overlap, and form 3 overlap regions. *Dotted green line*: the bottom of the plume outflow layer at the previous timestep. *Solid green line*: the fjord stratification in salinity at the previous timestep, given the box structure at the previous timestep. *Dashed green line*: Fjord box interface depth at the previous timestep. *Solid red line*: the approximation to the ocean stratification in salinity at the current timestep. *Dashed red line*: Ocean box interface depth at the current timestep. **[R1]** – region 1, within the ocean surface box at the current timestep, but below the outflow layer from the previous timestep. **[R2]** – region 2, between the box interface depth in the fjord from the previous timestep and the ocean box interface depth at the current timestep. **[R3]** – region 3, below the fjord box interface depth at the previous timestep. $\gamma = (H^n - H^{n-1})/h_4^{n-1}$ is the fraction of layer 3 which overlaps with the ocean lower box at the current timestep.

Salt flux calculation - lower box

The volume flux in region 3 is the full flux in the lower box at the previous timestep. Therefore the change in salinity in region 3 is given by

$$S_{F,R3}^n - S_{F,R3}^{n-1} = \frac{\Delta t}{BLH^{n-1}} \left(S_{O,R3}^n - S_{F,R3}^{n-1}\right) Q_5^{n-1} \equiv \Delta S_{R3}^n. \tag{3.14}$$

In region 2

$$S_{F,R2}^n - S_{F,R2}^{n-1} = \frac{\Delta t}{BL(H^n - H^{n-1})} \left(S_{O,R2}^n - S_{F,R2}^{n-1}\right) \gamma Q_4^{n-1} \equiv \Delta S_{R2}^n, \tag{3.15}$$

where a fraction $\gamma = (H^n - H^{n-1})/h_4^{n-1}$ of the total flux Q_4^{n-1} from layer 4 flows into this region. Exploiting the linear stratification, the average salinity $S_{F,R2}^{n-1}$ in region 2 is found via

$$S^{n-1}_{F,R2} = \frac{\partial S^{n-1}_{upper}}{\partial z}\frac{(H^n - H^{n-1})}{2} + S^{n-1}_{lower}. \tag{3.16}$$

The change in salinity in regions 2 and 3 contributes to setting the new lower box salinity. This average can be calculated by weighting the salinities by the depth of each region:

$$S^n_{lower} = \frac{S^n_{F,R3}H^{n-1} + S^n_{F,R2}(H^n - H^{n-1})}{H^n}. \tag{3.17}$$

Salt flux calculation - upper box

The change in salinity in region 1 is the only contribution to changing the upper layer salinity, and occurs due to the remaining fraction of the volume flux $(1-\gamma)Q_4$ from layer 4,

$$S^n_{F,R1} - S^{n-1}_{F,R1} = \frac{\Delta t}{BL(h^{n-1}_4 - H^n + H^{n-1})}\left(S^n_{O,R1} - S^{n-1}_{F,R1}\right)(1-\gamma)Q^{n-1}_4 \equiv \Delta S^n_{R1}, \tag{3.18}$$

where $S^{n-1}_{F,R1}$ is found by averaging the linear salinity stratification over region 1

$$S^{n-1}_{F,R1} = \frac{\partial S^{n-1}_{upper}}{\partial z}\frac{(h^{n-1}_4 + H^n - H^{n-1})}{2} + S^{n-1}_{lower}. \tag{3.19}$$

The total salinity from the old stratification that is above the depth of the new box interface is calculated and added to the change in salinity ΔS^n_{R1} due to the salt flux, to give the new total amount of salt in the upper box

$$\mathcal{S}^n_{tot} = BL\left[\int_{H^n}^{D} S^{n-1}_F\, dz + (h^{n-1}_4 - H^n + H^{n-1})\Delta S^n_{R1}\right]. \tag{3.20}$$

Given that we enforce a linear salinity profile in the upper layer and continuity in the salinity at the interface between boxes, this allows the calculation of a salinity gradient in the upper box as in Equation 3.12 and Equation 3.13. Thus we have the lower box salinity and the upper box salinity gradient in the fjord at

the current timestep. These are used in scalings to determine the layer structure, ready for the next timestep.

3.2.4.3 Box interface shallows into or above previous outflow layer

Here only two regions have an evolving salt flux (see Figure 3.6). Region 1 is comprised of the outflow layer at the previous timestep and thus does not contribute to modifying the salinity in the surface box, because the plume outflows with the same salinity as the fjord at that depth. Regions 2 and 3 impact the lower box only. The salinity gradient in the upper box therefore changes in response to the new lower box salinity and box interface depth but does not have an associated salt flux driven by the estuarine circulation.

Salt flux calculation - lower box

The change in salinity in region 2 is given by

$$S^n_{F,R2} - S^{n-1}_{F,R2} = \frac{\Delta t}{BLh^{n-1}_4}\left(S^n_{O,R2} - S^{n-1}_{F,R2}\right)Q^{n-1}_4 \equiv \Delta S^n_{R2}, \tag{3.21}$$

where BLh^{n-1}_4 is the volume flux into this region, and the depth-averaged salinity

$$S^{n-1}_{F,R2} = \frac{\partial S^{n-1}_{upper}}{\partial z}\frac{h^{n-1}_4}{2} + S^{n-1}_{lower}. \tag{3.22}$$

$S_{O,R2}$ is calculated similarly from the ocean stratification. The change in salinity in region 3 is given by

$$S^n_{F,R3} - S^{n-1}_{F,R3} = \frac{\Delta t}{BLH^{n-1}}\left(S^n_{O,R3} - S^{n-1}_{F,R3}\right)Q^{n-1}_5 \equiv \Delta S^n_{R3}, \tag{3.23}$$

The salinity in the lower box at timestep n is calculated by conserving salt

$$S^n_{lower} = \frac{S^n_{F,R2}h^{n-1}_4 + S^n_{F,R3}H^{n-1} + S^{n-1}_{F,R1}(H^n - H^{n-1} - h^{n-1}_4)}{H^n}, \tag{3.24}$$

where here we calculate the mean salinity within the fjord in the new lower box, given the stratification within the fjord at the previous timestep.

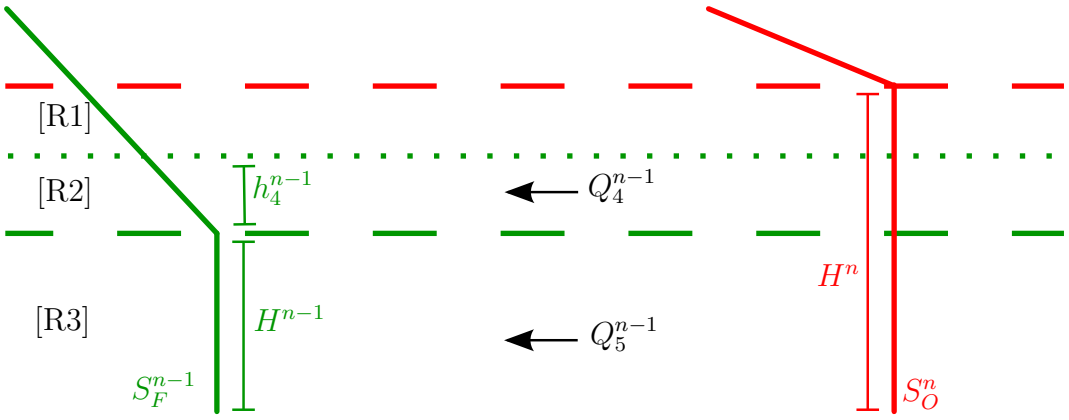

Figure 3.6: When the ocean box interface depth moves into or above the previous timestep outflow layer, three regions form. *Dotted green line*: the bottom of the plume outflow layer at the previous timestep. *Solid green line*: the fjord stratification in salinity at the previous timestep, given the box structure at the previous timestep. *Dashed green line*: Fjord box interface depth at the previous timestep. *Solid red line*: the approximation to the ocean stratification in salinity at the current timestep. *Dashed red line*: Ocean box interface depth at the current timestep. **[R1]** – region 1, within in and above the previous timestep outflow layer. **[R2]** – region 2, between the previous timestep box interface depth in the fjord and the previous timestep outflow layer. **[R3]** – region 3, below the previous timestep fjord box interface depth.

Salt flux calculation - upper box

In the upper box, we again conserve salt and enforce continuity in the salinity profile within the fjord at the box interface. Given that all the exchange of salt occurs below the new upper box in this scenario, the total amount of salt in the upper box is constant, given by

$$\mathcal{S}_{tot}^n = BL \int_{H^n}^{D} S_F^{n-1}\, dz. \tag{3.25}$$

Again, given the assumptions of linearity and continuity, we can find the new surface box salinity gradient via Equation 3.12 and Equation 3.13. In all cases, S_{lower}^n and $\frac{\partial S_{upper}^n}{\partial z}$ are then used in the melt rate and plume scaling calculations, setting the layer structure for the start of the next timestep. Together, this allows the time evolution of the stratification within the fjord to be calculated for all possible movements of the ocean pycnocline.

In the next section, we discuss several illustrative experiments designed to explore the behaviour of the box model over a range of forcing conditions, both

realistic and idealised.

3.3 Results

In this section, we examine the behaviour of the box model over a range of forcing conditions, with both realistic and idealised inputs. The key inputs of interest (given fjord width, length and depth) are the subglacial discharge and ocean stratification. To investigate the behaviour over a geophysically relevant range of parameter space, we run each model configuration with a fjord width ranging from 3 km to 24 km and subglacial discharge flux that is constant in time (in idealised cases), ranging from $50\,\mathrm{m^3\,s^{-1}}$ to $1500\,\mathrm{m^3\,s^{-1}}$. The larger fjord width is likely outside of the range expected in the real world; however, it is intended to test model behaviour even under extremal forcing conditions. The key diagnostic outputs considered are the fjord upper box salinity gradient, lower box salinity and thickness, plume outflow depth, and total submarine melt rate.

Initially, we hold the fjord depth fixed at 500 m. However, we discuss model output over a range of fjord depths in §3.3.1.2. We anticipate that varying fjord length is likely to have a smaller impact on results than varying fjord width, due to the results in Chapter 2 which suggest that the cross-fjord-integrated along-fjord velocity structure is the same along the length of the fjord in steady state, and thus restrict our primary investigation to the impact of changing fjord widths. In the first instance, model behaviour is illustrated using idealised forcing conditions for both subglacial discharge and ocean stratification.

3.3.1 Idealised Subglacial Discharge and Idealised Ocean Stratification

We first investigate the behaviour of the box model given idealised subglacial discharge and ocean stratification forcing conditions, holding temperature at 1 °C everywhere. In §3.3.1.1 we test the box model given subglacial discharge which is constant in time, and an ocean stratification in salinity which is also constant in time, with the fjord initialised with a different stratification in salinity to that

of the ocean. Next, we investigate the impact of varying fjord depth on the time evolution of the stratification within fjords in §3.3.1.2. Then, in §3.3.1.3 we again hold the subglacial discharge constant, but vary the ocean stratification in salinity sinusoidally between two profiles.

3.3.1.1 Constant subglacial discharge, constant ocean stratification

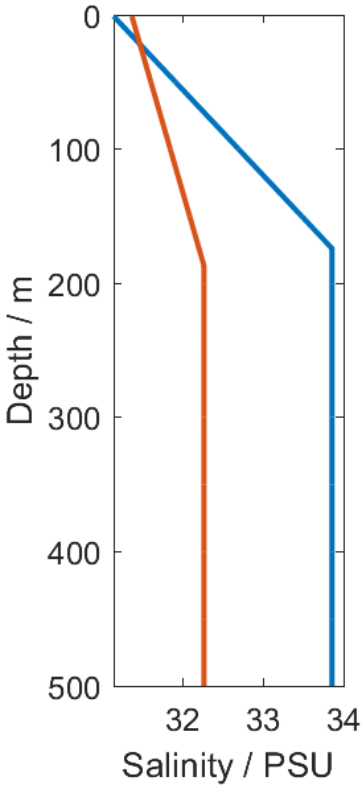

Figure 3.7: Salinity profiles $S_1(z)$ (red) and $S_2(z)$ (blue).

In this section, we test the box model for any spurious behaviour, such as drifts in box properties when the fjord should be in steady state, and we investigate model adjustment timescales over a range of parameter space. We run model configurations in cases with idealised ocean stratification for 20 years model time, to examine this steady state. The ocean stratification in salinity $S_1(z)$ and the subglacial discharge are held constant in time and the fjord initialised with a significantly different salinity profile $S_2(z)$ (see Figure 3.7). The volume flux generated by the plume scalings results in a salt flux, causing fjord properties to adjust towards those of the ocean. The fjord is initialised with a more saline lower box, and stronger stratification in the surface box, relative to the ocean. Both the ocean and fjord in-situ temperature profiles are held at a constant 1°C at all depths, such that any impact on melt rate is due solely to the changing flow structure and salinity profile.

Figure 3.8 shows time series of the total freshwater flux due to melting of the ice face, fjord stratification properties in salinity, plume outflow depth, and the (constant) lower box thickness of both the ocean and the fjord (constrained to be equal). The lower box salinity and upper box salinity gradient (shown in blue) tend

towards the oceanic values (shown in red), with an exponential decay, reflecting the fact that the salt flux depends itself on the salinity difference between the fjord and the ocean. Interestingly, the melt rate varies much more linearly initially, before tending to a steady-state value. A small change in the total melt rate results from the change in salinity within the fjord, which impacts the vertical structure of the flow as well as the strength of the cross-fjord velocities at the ice face, from theoretical predictions developed in Chapter 2. The plume outflow depth quickly tends to the surface as the fjord upper box salinity gradient decreases, with a sharp transition resulting from the clipping of the plume height of rise once it reaches the surface.

The e-folding adjustment timescale in fjord stratification properties is shown in Figure 3.9, for simulations over a range of subglacial discharge and fjord width. The lower box salinity responds more slowly than the upper box salinity gradient, in general, consistent with the lower box having a larger volume to replenish. The slowest response occurs for the widest fjords and lowest subglacial discharge, reflecting the longer flushing timescale associated with a larger fjord volume and smaller exchange with the ocean. The e-folding timescale in all cases is at least $\mathcal{O}(100)$ days, up to multiple years. Thus, the fjord stratification has a significant memory of previous ocean conditions, and there is a significant lag in the time taken for the ice face to see changes in ocean conditions. This behaviour suggests that there may be significant differences in seasonal response between different fjords, which we explore in the next section.

Investigation of log-log plots of the e-folding timescales against fjord width suggests that the timescale increases linearly with fjord width for both the lower and upper boxes, reflecting the linear increase in the volume of the boxes with fjord width. Plots of e-folding timescale against subglacial discharge show different behaviour for the salinity in each box (Figure 3.10). Performing a linear fit for each fjord width suggests that, in the lower box, there is a simple power law relationship between the e-folding timescale τ_e and subglacial discharge, such that

$$\tau_e = kQ_{sg}^{-0.4\pm0.02} \tag{3.26}$$

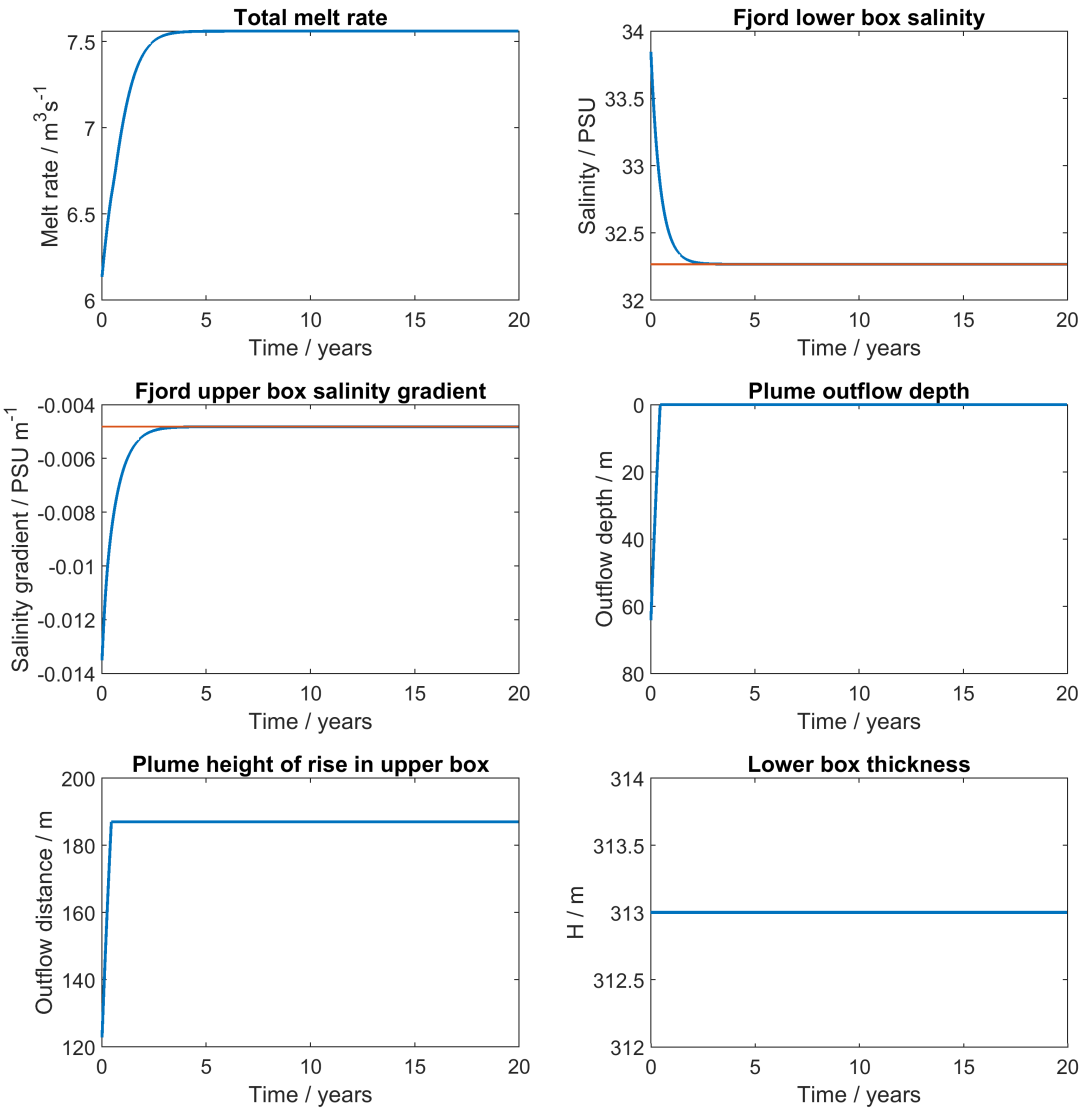

Figure 3.8: Box-model output time series for a configuration with subglacial discharge $Q_{sg} = 750\,\mathrm{m^3\,s^{-1}}$, and fjord width $B = 9\,\mathrm{km}$. Red lines in the top right and middle left panels give the lower box salinity and upper box salinity gradient of the idealised ocean stratification, which are held constant. Blue lines show fjord properties in all panels.

where k is a constant of proportionality linearly dependent on fjord width, and the exponent is the average over the best fit value for all fjord widths.

We can derive an analytic prediction for the relationship between the e-folding timescale in the lower box and subglacial discharge. The salinity in the lower box in the fjord $S_{F,lower}$ changes according to

$$\frac{\partial S_{F,lower}}{\partial t} = \frac{Q_5}{LBH}(S_{O,lower} - S_{F,lower}). \tag{3.27}$$

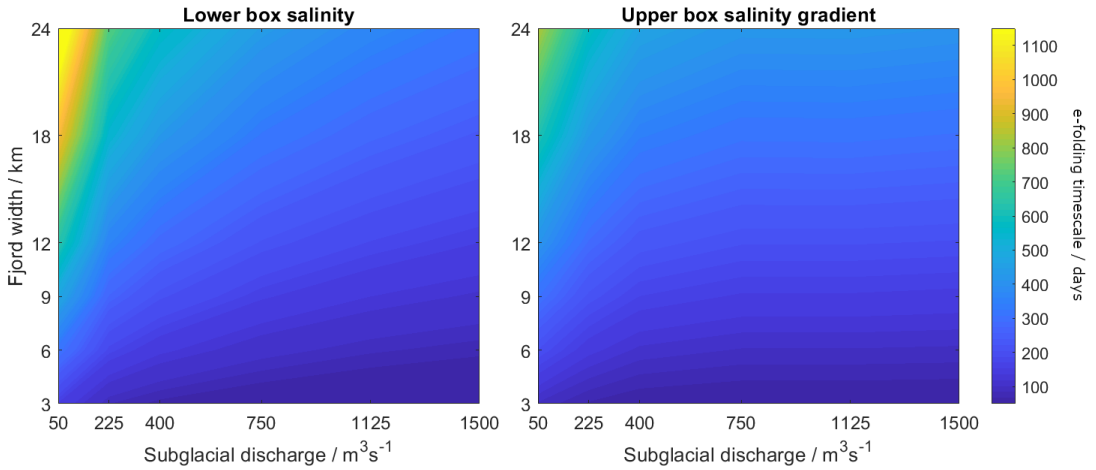

Figure 3.9: Contour plots of the e-folding adjustment timescale (days) in lower box salinity (left) and upper box salinity gradient (right) over a range of subglacial discharge flux and fjord width.

for fjord length L, width B, lower box thickness H, ocean lower box salinity $S_{O,lower}$, and the volume flux into the lower box Q_5 given by Equation 3.3. Assuming that the change in salinity in the lower box is small, Q_5 is constant. Under this assumption, solving for $S_{F,lower}$ yields

$$S_{F,lower} = (S_{F,init} - S_{O,lower}) \exp\left(-\frac{Q_5}{LBH}t\right) + S_{O,lower}, \tag{3.28}$$

where $S_{F,init}$ is the initial lower box salinity in the fjord. Therefore, the prediction for the e-folding timescale is

$$\tau_p = \frac{LBH}{Q_5}. \tag{3.29}$$

The dependence of Q_5 on Q_{sg} is also impacted by the dependence of z_0 on Q_{sg}, via $H_0^{5/3} = (H+z_0)^{5/3} - z_0^{5/3}$. Thus, the dependence of τ_p on Q_{sg} is not a straightforward power law. Given that the change in salinity in the lower box is small, using a lower box salinity $S_{F,lower} = 0.5 \cdot (S_{F,init} + S_{O,lower}) = 33.25\,\text{PSU}$ when calculating g_0' allows for numerical evaluation of Equation 3.29. This yields $\tau_p \sim Q_{sg}^{-0.381}$, with the exponent of Q_{sg} within the confidence interval found in Equation 3.26. The prediction of Equation 3.29 as a function of subglacial discharge is shown in Figure 3.10(a) for each fjord width and yields a very similar quality of fit to the data.

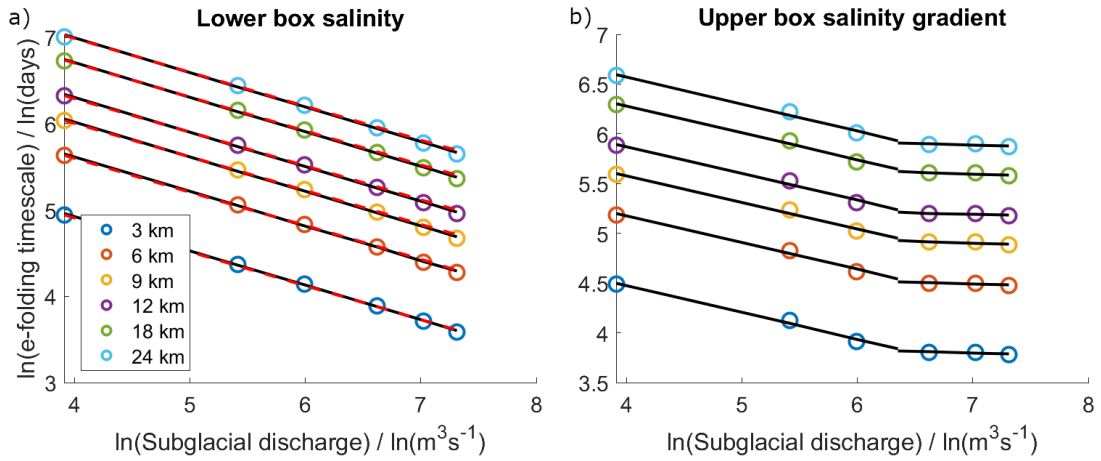

Figure 3.10: a) Plot of ln(e-folding timescale) against ln(subglacial discharge) for each fjord width (markers) for the lower box salinity. *Black, solid lines*: linear fits performed over the full range of subglacial discharge. *Red, dashed lines*: theoretical prediction using Equation 3.29.
b) Plot of ln(e-folding timescale) against ln(subglacial discharge) for each fjord width (markers) for the upper box salinity gradient. *Black, solid lines*: Linear fits performed separately over each half of the range of subglacial discharge.

For the upper box, the behaviour separates into two regimes, with a different power law providing the best fit over each half of the range of subglacial discharge. For $Q_{sg} = 50 - 400\,\mathrm{m^3 s^{-1}}$, the exponent of Q_{sg} in the e-folding timescale goes as -0.27 ± 0.002, whereas over the second half of the range ($Q_{sg} = 750 - 1500\,\mathrm{m^3 s^{-1}}$) the best fit exponent is found to be -0.033 ± 0.002. In both cases, the sign of the exponent reflects the increased volume flux acting to refresh the water in the upper box with increased subglacial discharge. This regime change occurs approximately where the plume reaches the surface of the upper box and $h \to D - H$ in the flux scaling Equation 2.9. As the plume cannot rise above the ocean surface, the dependence of h on Q_{sg} no longer impacts the volume flux where $h \geq D - H$. This highlights the importance of plume outflow depth not only for the accurate representation of the depth at which freshwater enters the ocean but also for the time evolution of the fjord stratification itself.

The approach of Equation 3.27 is not straightforwardly applicable to the change in salinity in the upper box for the ocean forcing in Figure 3.8. The volume flux into the upper box driven by the plume depends on the salinity gradient in this box (see Equation 2.9), which changes significantly. Therefore, analytic prediction of

e-folding timescales for each fjord width using a similar expression to Equation 3.29 (with $Q_5 \rightarrow Q_4$) yields a functional dependence on subglacial discharge which is significantly different to that displayed by the box model in Figure 3.10(b).

3.3.1.2 Varying fjord depth

We now briefly discuss the impact of changing fjord depth on the behaviour of the box model. Variation in fjord depth differs from variation in fjord width. Whilst both the width and depth impact the volume of water in the fjord to replenish, changing fjord depth also changes the thickness of each box relative to the total depth. Given that the ocean stratification is set by far-field ocean processes, and to aid comparison with previous results, we consider the same idealised ocean forcing as in §3.3.1.1 and vary depth alone. We run model configurations over a range of subglacial discharge ($Q_{sg} = 50 - 1500\,\mathrm{m^3\,s^{-1}}$) and fjord depths ($D = 400 - 900\,\mathrm{m}$) holding fjord width at 9 km in all cases.

We hold ocean stratification constant in time and investigate the steady-state solution as the fjord stratification tends to that of the ocean, as in §3.3.1.1. The model displays similar functional behaviour over time to that shown in Figure 3.8. Comparing the e-folding timescales in fjord stratification properties, namely lower box salinity and upper box salinity gradient, reveals some potentially interesting behaviour. Figure 3.11 shows a different structure in the timescale of response of the two boxes in the fjord, over the range of parameter space.

As expected, the longest timescale responses in lower box salinity are associated with low subglacial discharge as this has a lower flushing rate. The response in the upper box salinity gradient is slowest for shallower fjords and low subglacial discharge, with long multi-year response timescales for shallow fjords across the whole range of subglacial discharge considered. For the salinity gradient response in the upper box, this is likely due to the fact that, for deeper fjords, the plume rises through a thicker layer of constant density, and so entrains a larger volume of ambient water. This then generates a more vigorous exchange flow in the surface layer, which decreases the time taken for this layer to adjust to the ocean properties

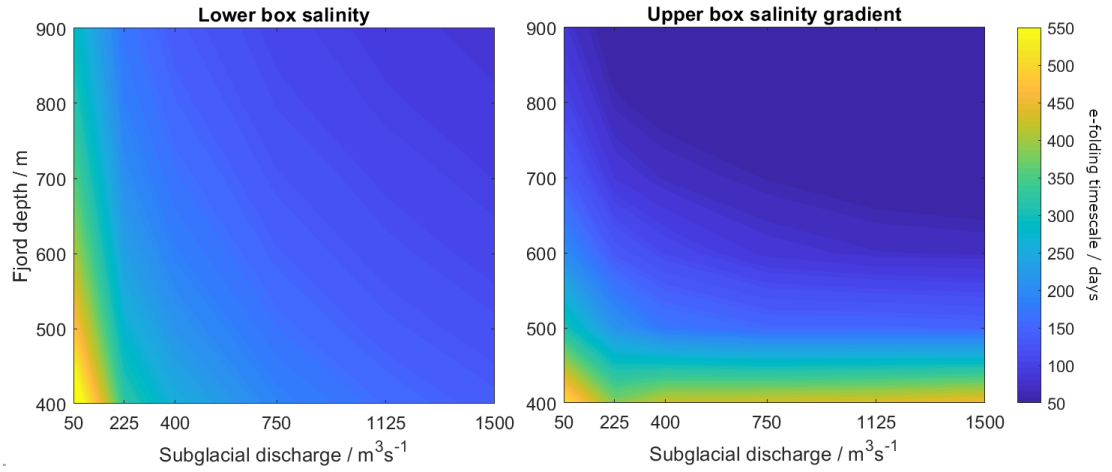

Figure 3.11: Contour plots of the e-folding timescale (days) in lower box salinity (left) and upper box salinity gradient (right) over a range of subglacial discharge flux and fjord depths.

at the same depth. The increased volume flux due to entrainment in the lower layer is seemingly not enough to account for the increased total volume in the lower box in the box model. Thus, the adjustment timescale in the lower box is longest for low subglacial discharge, and varies most strongly with subglacial discharge over a geophysically relevant range of parameter space.

Along with the response observed for differing fjord widths, the above sensitivity to fjord depth may offer a partial explanation for the observation that neighbouring fjords which see almost identical ocean forcing conditions can display wildly different behaviours in terms of melt and iceberg calving rates (Bartholomaus et al. 2016). Indeed, it may be possible that the response of any individual fjord itself changes over time. As glacial termini retreat, the effective depth of a given fjord may change on decadal timescales. Thus, the relative depth of the effective lower layer in salinity may change, changing subglacial discharge plume behaviour and modifying the outflow depth and properties of the fjord-scale estuarine circulation which the plume generates.

3.3.1.3 Constant subglacial discharge, oscillatory ocean stratification

We next introduce oscillatory behaviour in the ocean stratification to simulate an idealised seasonal cycle and run configurations over a range of different subglacial

discharges and fjord widths. We use plume-driven exchange rates using the scalings of Equation 2.7 and Equation 2.9 only and do not account for circulation driven by horizontal density gradients.

Figure 3.12 shows time series of box-model properties for a configuration with subglacial discharge $Q_{sg} = 750\,\mathrm{m^3\,s^{-1}}$, and fjord width $B = 9\,\mathrm{km}$. The red lines in the top right panel (fjord lower box salinity) and middle left panels (fjord upper box salinity gradient) show the corresponding ocean forcing condition time series at the fjord mouth, which varies between two vertical profiles in salinity, via

$$S_{ocean}(z,t) = \frac{S_1(z) + S_2(z)}{2} + \frac{S_1(z) - S_2(z)}{2} \cos\left(\frac{2\pi t}{1\text{ year}}\right), \tag{3.30}$$

with a constant temperature of 1°C at all depths. The fjord is initialised with the mean temperature and salinity over a full cycle of ocean forcing conditions. S_1 and S_2 are given by the red and blue profiles in Figure 3.7, respectively.

The fjord response oscillates about the mean of the ocean seasonal cycle for both the lower box salinity, and upper box salinity gradient, with an amplitude set by the ratio of the volume flux exchange driven by the plume and the total volume of water in the fjord. As a result, for constant subglacial discharge, the seasonal cycle in plume outflow depth is larger for narrow fjords, due to the larger amplitude oscillations in the strength of the salinity gradient in the surface layer. For wider fjords, or lower values of subglacial discharge, the plume outflow depth time series displays a correspondingly smaller amplitude response over a seasonal cycle.

The ratio of the amplitude of variations in the salinity gradient in the fjord in response to the ocean forcing is shown in Figure 3.13, over a range of subglacial discharge and fjord widths. For both the lower box salinity (Figure 3.13a) and the upper box salinity gradient (Figure 3.13b), the largest amplitude oscillations occur for small fjord widths, due to the reduced volume of each box. Neglecting the lowest subglacial discharge case, there is a slight increase in amplitude as subglacial discharge increases; however, the largest variation occurs with fjord width. This may represent another factor contributing to the observation of different responses

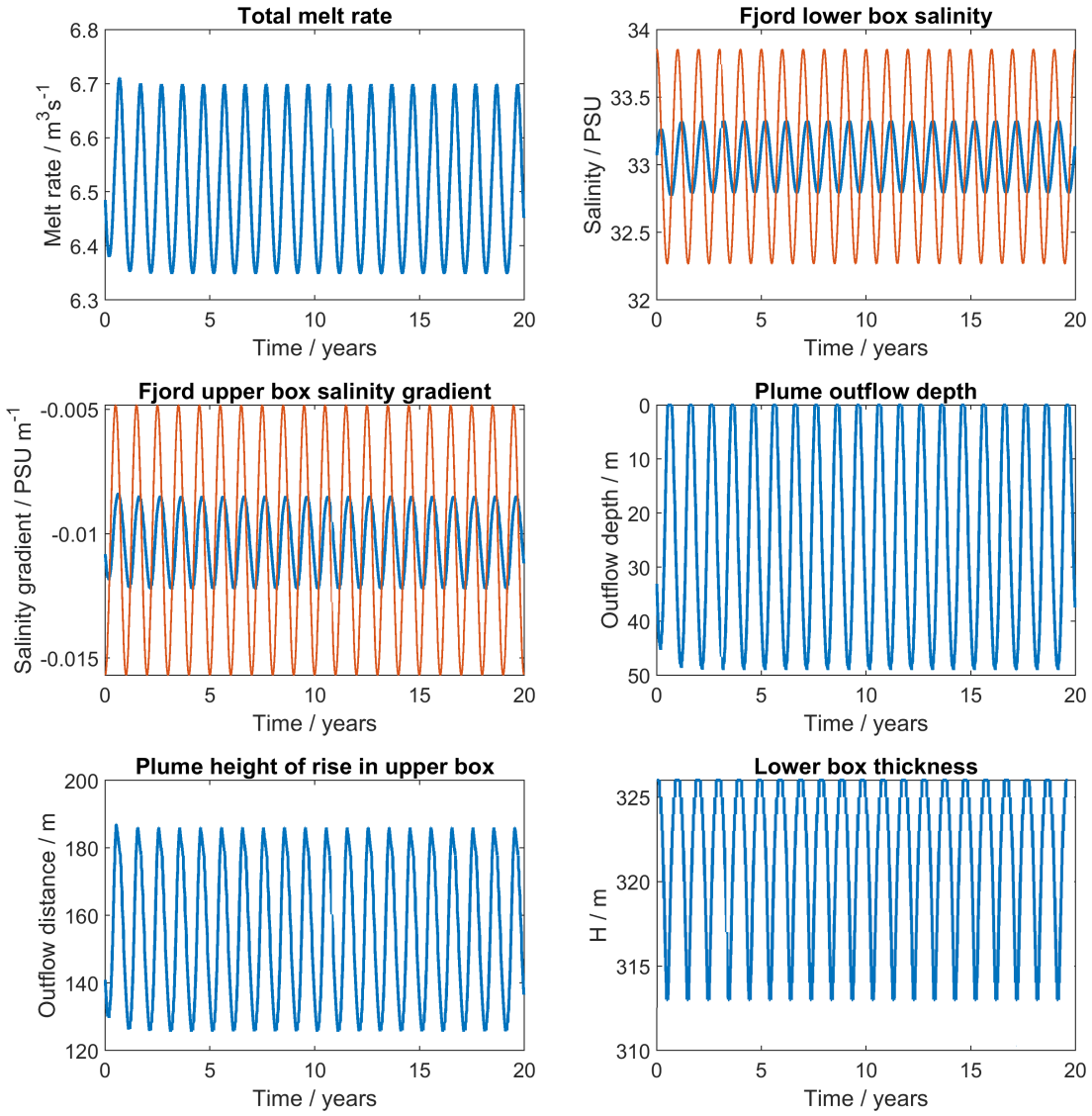

Figure 3.12: Time series of total submarine melt rate, lower box salinity, upper box salinity gradient, predicted plume outflow depth, plume height of rise in the upper box, and lower box thickness, for a configuration with constant subglacial discharge $Q_{sg} = 750\,\mathrm{m^3\,s^{-1}}$, fjord width $B = 9\,\mathrm{km}$, fjord length $L = 100\,\mathrm{km}$ and fjord depth $D = 500\,\mathrm{m}$. Red lines in the top right and middle left panels give the time series of the lower box salinity and upper box salinity gradient in the ocean at the fjord mouth, respectively. Blue lines indicate fjord properties in all panels.

in neighbouring fjords (Bartholomaus et al. 2016), with small changes in fjord width producing large differences in salinity profiles.

The fjord response under this combination of forcing conditions also displays a phase lag relative to the ocean stratification, which varies with subglacial discharge and fjord width. Figure 3.14 displays this phase lag in days, for both the lower

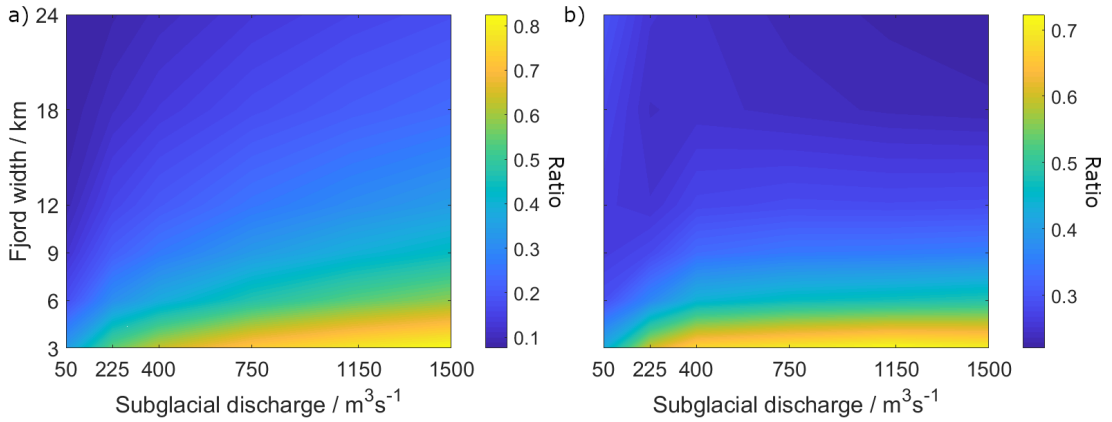

Figure 3.13: a) Ratio of the amplitude of the lower box salinity in the fjord to the amplitude of the salinity in the lower box in the ocean, from box-model output over a range of fjord widths and subglacial discharge fluxes.
b) Ratio of the amplitude of the upper box salinity gradient response in the fjord to the amplitude of the salinity gradient in the upper box in the ocean, from box-model output over a range of fjord widths and subglacial discharge fluxes.

box salinity (Figure 3.14a) and upper box salinity gradient (Figure 3.14b) in the fjord. Interestingly, the model displays a phase lag of 20-85 days over the range of fjord width and subglacial discharge considered here, which is comparable to the duration of the summer melt season.

The phase lag of the salinity of the lower box within the fjord relative to that of the ocean is largest for wide fjords and low subglacial discharge (Figure 3.14a). For wider fjords, the increased volume of the lower box means that an increased volume of fluid must be replenished by the volume flux driven by the plume. As this volume flux is independent of fjord width, the timescale of the response in fjord lower box salinity is larger for wide fjords. The phase lag decreases with increasing subglacial discharge, due to the increased volume flux into the lower box.

For the upper box salinity gradient, as subglacial discharge increases, the fjord width corresponding to this peak phase lag increases sharply for low values of subglacial discharge, and more slowly at higher values (Figure 3.14b). The salinity gradient response within the fjord is set by a combination of the salt flux driven by the estuarine overturning circulation, and the movement of the pycnocline within the fjord. The volume of water which is encompassed by the movement of the interface between boxes can be larger than the volume exchanged by the estuarine

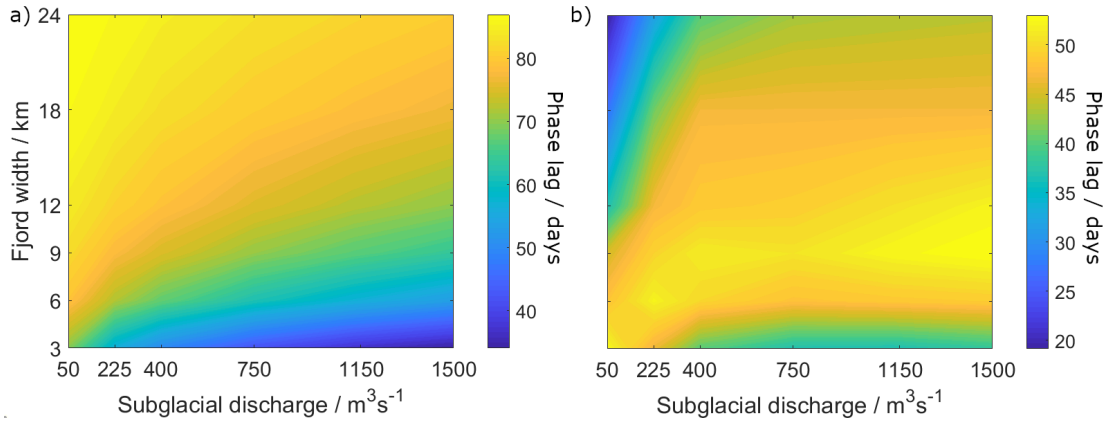

Figure 3.14: a) Phase lag (days) of the oscillatory response in the fjord lower box salinity relative to the ocean, from box-model output over a range of subglacial discharge and fjord widths.
b) Phase lag (days) of the oscillatory response in the fjord upper box salinity gradient relative to the ocean, from box model over a range of subglacial discharge and fjord widths.

circulation over a given timestep when subglacial discharge is sufficiently low. In this case, the assumption that the fjord pycnocline moves instantaneously to match that of the ocean at each time step brings the fjord response closer in phase to that of the ocean. For higher subglacial discharge, the change in salinity gradient in the surface box within the fjord is controlled instead by the overturning circulation. For very narrow fjords, and high subglacial discharge, this again has the effect of reducing the phase lag in the fjord response, as a comparatively large fraction of the fjord water is renewed in each time step by the estuarine circulation.

Analytic predictions for the salinity in the fjord lower box can be derived following a similar approach to Equation 3.27. Assuming that the lower box thickness H is constant, the salinity in the lower box in the ocean has a time-dependent form

$$S_{O,lower}(t) = \overline{S} + \frac{\Delta S}{2}\cos(\omega_o t), \tag{3.31}$$

where $\overline{S} = [S_1(z) + S_2(z)]/2$ for $z < H$, $\Delta S = S_1(z) - S_2(z)$ for $z < H$, and $\omega_o = 2\pi/\tau_o$ with $\tau_o = 1\,\text{year}$. For variations in the salinity of the lower box in the fjord which are small relative to the mean salinity, the volume flux into the lower box driven

by the plume Q_5 (Equation 3.3) can be considered as approximately constant in time. The solution of Equation 3.27 with the definition of $S_{O,lower}$ from Equation 3.31 is

$$S_{F,lower} = \left[S_{F,init} - \overline{S} - \frac{\gamma^2 \Delta S}{2(\omega_o^2 + \gamma^2)}\right] \mathrm{e}^{-\gamma t} + \overline{S} + \frac{\gamma^2 \Delta S}{2(\omega_o^2 + \gamma^2)} \cos(\omega_o t) + \frac{\gamma \omega_o \Delta S}{2(\omega_o^2 + \gamma^2)} \sin(\omega_o t), \tag{3.32}$$

where $\gamma = Q_5/LBH$ and $S_{F,init}$ is the initial salinity in the fjord lower box. At long times, this solution becomes

$$S_{F,lower}(t \to \infty) = \overline{S} + \frac{\gamma \Delta S}{2(\omega_o^2 + \gamma^2)^{1/2}} \cos\left(\omega_o t + \tan^{-1}\left[\frac{\gamma}{\omega_o}\right] - \frac{\pi}{2}\right). \tag{3.33}$$

This allows for the analytic prediction of the amplitude and phase lag of the lower box salinity in the fjord relative to that of the ocean. The percentage difference between the amplitude of oscillations in the lower box salinity from box-model output and the amplitude of the theoretical response in the fjord from Equation 3.33 is shown in Figure 3.15(a). The largest departure from theory occurs for low subglacial discharge, where the difference in amplitude is as large as $\sim 20\%$. This is likely due to the larger relative impact of changes in lower box thickness on lower box salinity for low subglacial discharge, where we neglected changes in lower box thickness in deriving Equation 3.33. However, changes in box thickness have less impact over most of the parameter space, and the theory is accurate to within $\sim 10\%$ of the box-model output. The percentage difference between the phase lag relative to the ocean forcing predicted in Equation 3.33 and the phase lag from box-model output is shown in Figure 3.15(b). The predicted phase lag is within 5% of the corresponding phase lag in the lower-box salinity diagnosed from box-model output over the range of subglacial discharge and fjord widths considered. Thus,

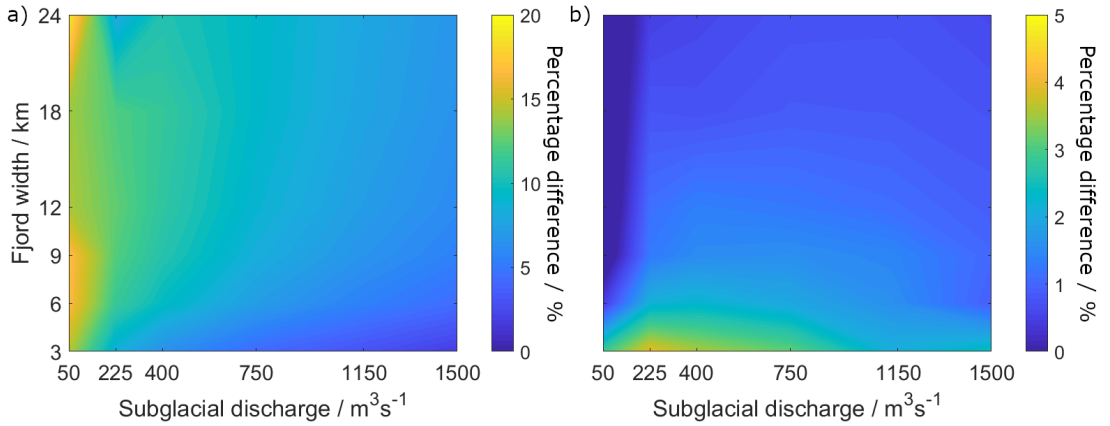

Figure 3.15: Percentage difference between a) amplitude of oscillations, b) phase lag of the oscillatory response in lower box salinity in the fjord from box-model output and the predictions of Equation 3.33, over a range of fjord widths and subglacial discharge fluxes.

Equation 3.33 provides a reasonable theoretical prediction of the behaviour of the lower box salinity in the box model at long times.

The time-averaged submarine melt rate is shown as a function of subglacial discharge and fjord width in Figure 3.16. The melt increases with subglacial discharge, as a more vigorous circulation is predicted close to the ice face, and the vertical velocities in the plume increase. Melt rates also increase with fjord width, as there is a larger surface area of the glacial terminus available for melting. Over most of the range of parameter space shown here, the assumption that the amount of submarine meltwater is small relative to the subglacial discharge holds, although this assumption is worse for low subglacial discharge, and wider fjords. The more geophysically motivated range of fjord widths ($B = 3 - 12$km) predicts a submarine meltwater flux at most 34% that of the subglacial discharge, with the upper bound reached for the $Q_{sg} = 50\,\mathrm{m^3\,s^{-1}}$, $B = 24\,\mathrm{km}$ case. Increasing subglacial discharge quickly improves the validity of this assumption. Again, more accurate treatment of the injection of submarine meltwater would add significant complication and is left for future work, likely requiring the inclusion of a smaller secondary outflow layer in the vertical structure of along-fjord velocity.

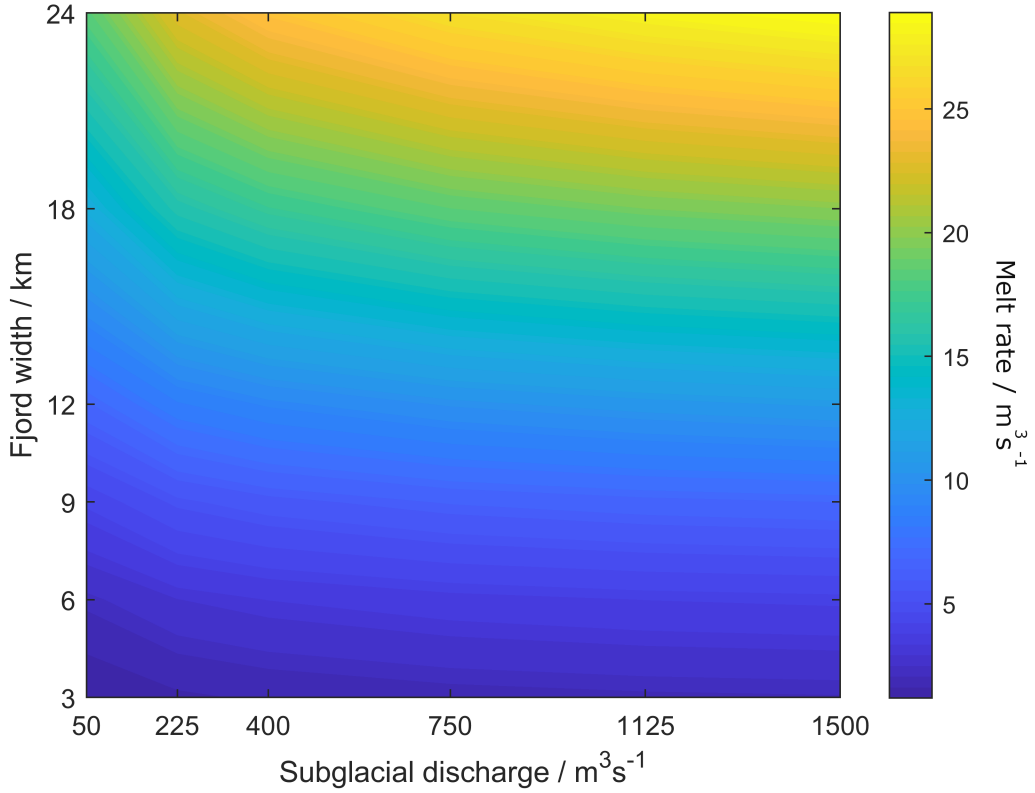

Figure 3.16: Time-averaged total submarine melt rate ($m^3\,s^{-1}$) as a function of subglacial discharge and fjord width, for constant subglacial discharge and sinusoidal ocean forcing. For a proglacial fjord with width $B = 24\,km$ and depth $D = 500\,m$, a melt rate of $29\,m^3\,s^{-1}$ corresponds to $0.21\,m\,d^{-1}$ of glacial retreat.

3.3.2 Realistic Subglacial Discharge and Idealised Ocean Stratification

We now investigate model behaviour under realistic subglacial discharge forcing that varies seasonally and interannually. This is intended to ensure that the box model does not display spurious behaviour given large, realistic changes in subglacial discharge. Subglacial discharge is taken from the JULES land-surface component of a HADGEM3-GC3.1-LL pre-industrial control run; this Earth system model includes a representation of Greenland's ice sheet as well as coupled atmosphere and ocean models at low resolution (Williams et al. 2018; Kuhlbrodt et al. 2018; Menary et al. 2018). Meltwater due to atmospheric forcing is assumed to entirely flow out below the ice sheet as subglacial runoff, with topographic channelling steering the meltwater towards the ocean. This section is intended to investigate

realistic changes in subglacial discharge to ensure that the box model does not display spurious behaviour.

3.3.2.1 Constant ocean stratification

We initially consider a case with the ocean stratification held constant over time, and the fjord box model initialised with a more saline lower layer and stronger stratification in the surface layer, identically to the profiles shown in Figure 3.7. The in-situ temperature is held at 1°C everywhere in the fjord and the ocean at all times. We run model configurations with fjord widths ranging from $3 - 24\,\mathrm{km}$. The subglacial discharge time series used here is taken from the maximum subsurface runoff source within a 3×3 grid cell stencil of 62°N, 48.5°W in the HADGEM3 output.

The estuarine circulation generated by the subglacial discharge plume again causes the fjord properties to adjust to those of the ocean over time (Figure 3.17). In contrast to the results in §3.3.1.1, the seasonal cycle in subglacial discharge generates a slightly staggered structure in the adjustment in lower box salinity and upper box salinity gradient and a longer adjustment timescale. However, the adjustment remains broadly similar to that in §3.3.1.1.

The seasonal cycle in subglacial discharge has a strong impact on both the melt rate and plume outflow depth. For this ocean stratification, the magnitude of the peak subglacial discharge flux in each seasonal cycle is sufficient for the plume to penetrate to the fjord surface every year apart from the first year, where fjord properties retain a sufficiently strong stratification to prevent the plume from surfacing. As such, the interannual variability is lost, as the plume height of rise is clipped at the ocean surface. However, the strong seasonality results in a height of rise for the discharge plume in the surface layer which can occur anywhere between the box interface depth and the surface, depending on the time of year. This demonstrates that the prevailing approach to glacial meltwater addition in Earth system models neglects significant variability in the true outflow depth of estuarine circulation from Greenland's fjords by injecting freshwater at the surface of the ocean model component.

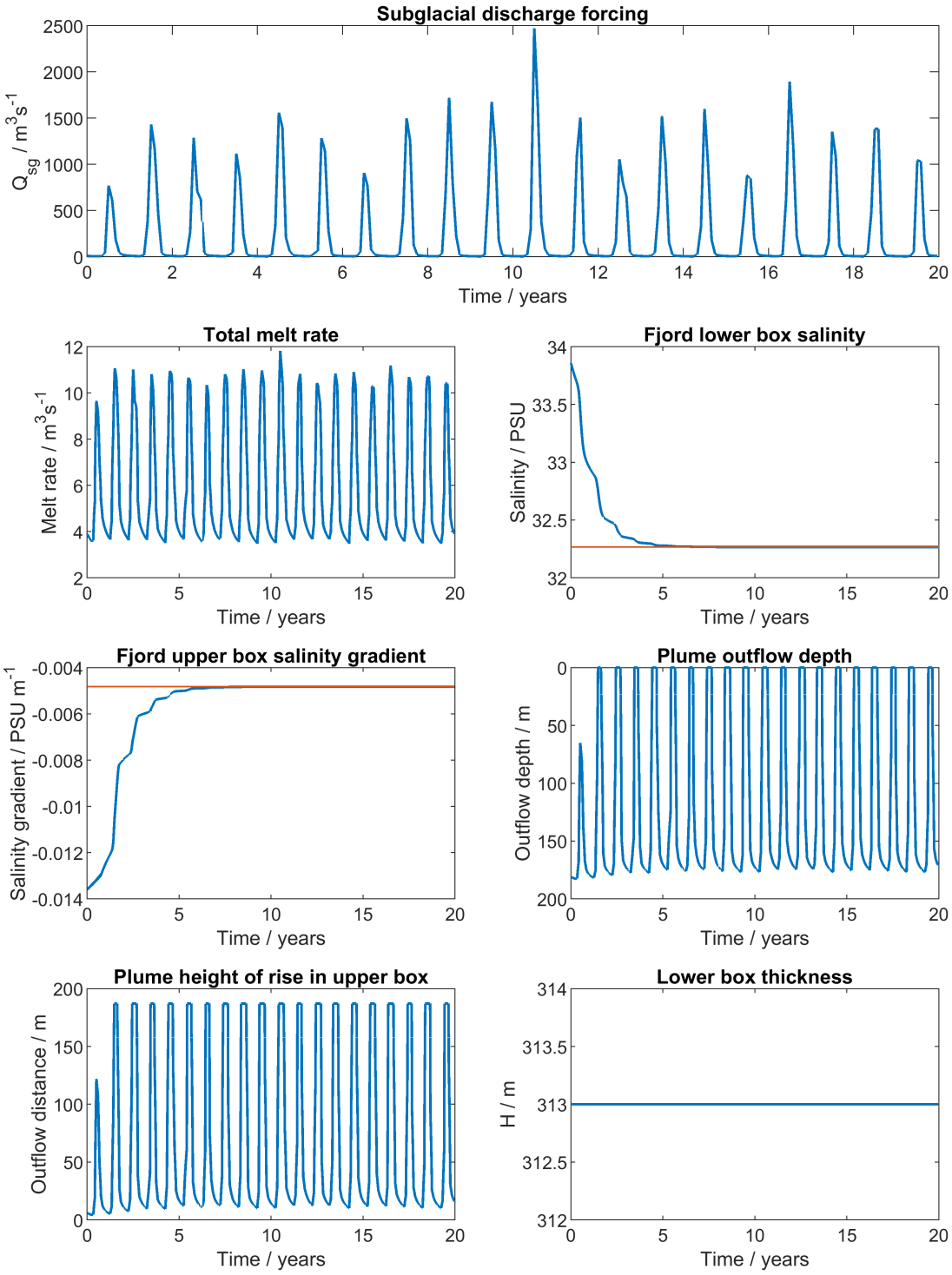

Figure 3.17: Subglacial discharge forcing and box-model output time series for a configuration with subglacial discharge taken from the ice sheet component of a HADGEM3-GC3.1-LL pre-industrial control run, and ocean stratification held constant (red). Fjord width $B = 9\,\text{km}$, length $L = 100\,\text{km}$ and depth $D = 500\,\text{m}$.

Comparison of the peaks in the melt rate time series to those in the subglacial discharge forcing show a close correspondence between the two, such that the interannual variability in peaks in the forcing can also be seen in the melt response. For example, the largest peak in the subglacial discharge forcing at $t \approx 10.5$ years corresponds to the peak in melting at precisely the same time, across the range of fjord widths considered here. This is consistent with results in §2.3.4 which show that the melt driven by both the plume and the recirculation increase with subglacial discharge. Total melt rate varies from $\sim 3.5 - 12\,\mathrm{m^3 s^{-1}}$, corresponding to predicted glacial terminus retreat rates of $\sim 0.02 - 0.1\,\mathrm{km yr^{-1}}$. Whilst it is not sensible to compare predicted retreat rates to observation directly given the simplified ocean forcing used here, the predicted order of magnitude is nevertheless reasonable (e.g. Murray et al. 2015).

Even in periods of time with extremely low subglacial discharge, there remains a non-trivial background melt rate, at around 33% of the maximum melt rate (for any given fjord width). The inclusion of a small background velocity in the calculation of the melt rates at the ice face, and the constant temperature profile above the melting temperature, combine to result in a melt rate that remains non-trivial even when the subglacial discharge plume is weak.

3.3.2.2 Oscillatory ocean stratification

We now retain the subglacial discharge time series used in §3.3.2.1, and force the box model with an oscillating ocean stratification, as in §3.3.1.3. Again, we investigate model configurations with fjord widths from 3 to 24 km and use a vertically uniform in-situ temperature of 1°C.

Figure 3.18 shows that the seasonality in subglacial discharge leads to a different mean state in the fjord box salinities when compared to previously discussed configurations with a constant Q_{sg} (Figure 3.12). Rather than oscillating about the annual mean lower box salinity and upper box salinity gradient of the ocean, the fact that subglacial discharge shuts down in winter months pushes the fjord response closer to the 'summer' ocean values on average. This suggests that the

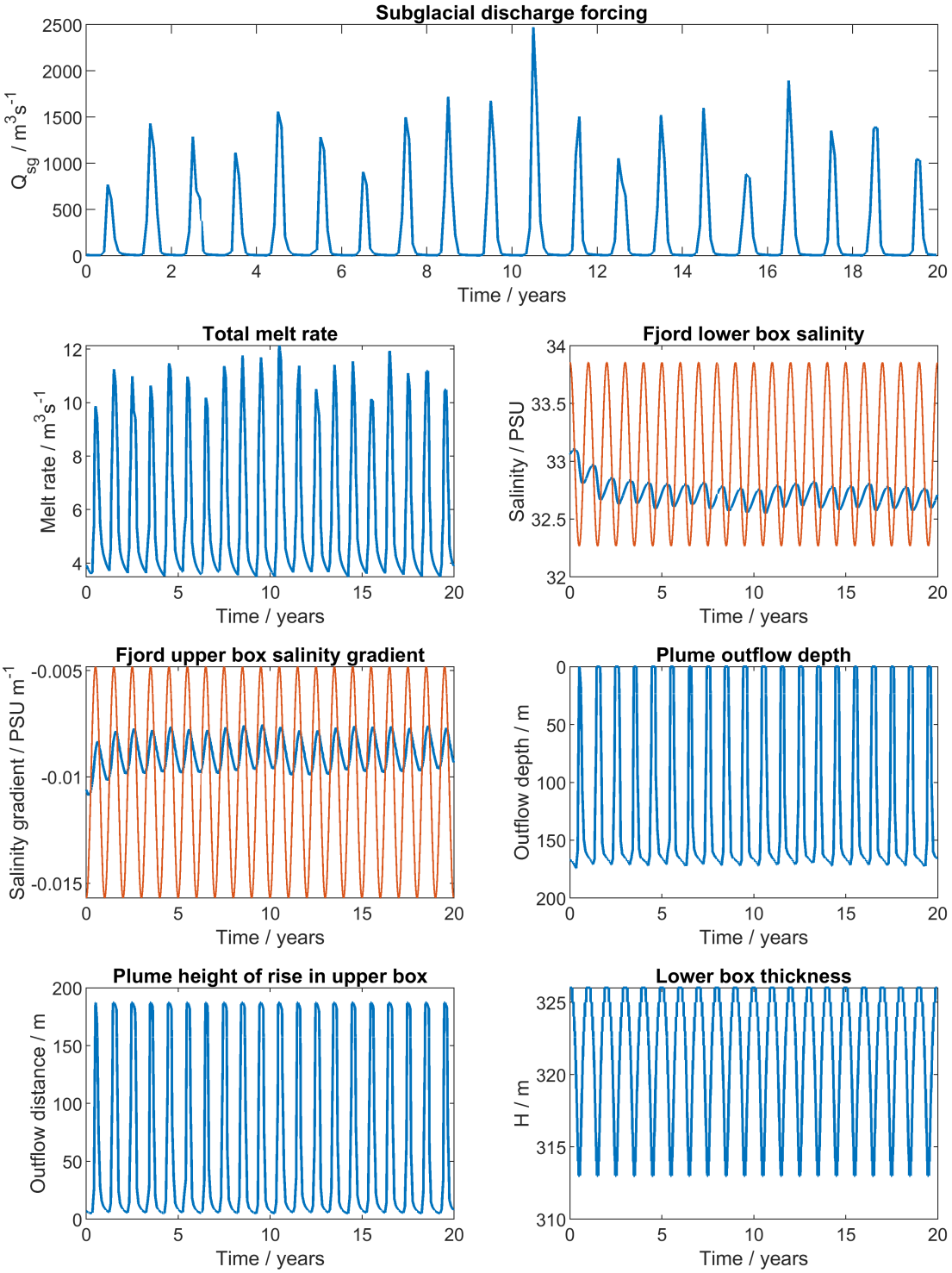

Figure 3.18: Time series of subglacial discharge forcing and box-model output for a configuration with subglacial discharge taken from the ice sheet component of a HADGEM3-GC3.1-LL pre-industrial control run, and ocean stratification oscillating sinusoidally between two states (red). Fjord width $B = 9\,\text{km}$, length $L = 100\,\text{km}$ and depth $D = 500\,\text{m}$.

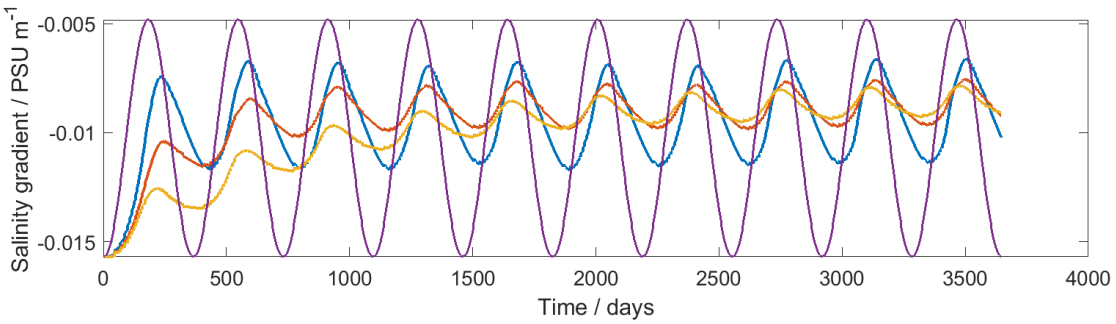

Figure 3.19: Fjord upper box salinity gradient for fjords with widths 3 km (blue), 9 km (red), and 24 km (yellow), with the ocean upper box salinity gradient in purple. The corresponding subglacial discharge time series is shown in Figure 3.18.

ocean properties seen by the ice face, as mediated by the fjord circulation, skew towards summer properties over an annual cycle. Indeed, it can be seen that the peak in subglacial discharge at $t \approx 10.5$ years corresponds with the minimum value in fjord lower box salinity, and one of the smallest values in upper box salinity gradient. Both correspond with the fjord stratification most closely matching the 'summer' ocean properties. This may represent a positive feedback mechanism on melt rates. As global mean temperatures increase and increased melt over inland regions of the Greenland Ice Sheet generates increased subglacial discharge in summer months, generating a more vigorous fjord circulation, seasonality in Q_{sg} may push fjord properties even further towards summertime ocean properties on average, increasing the heat available for submarine melting.

The fjord width has some impact on the response of the fjord stratification to oscillating ocean stratifications, although the overall picture remains the same. Figure 3.19 shows the fjord upper box salinity gradient for three different fjord widths, and the corresponding ocean salinity gradient forcing. Increasing fjord width increases the volume of fluid to renew and hence the timescale for mean fjord properties to reach their steady-state values, consistent with previous results. Narrower fjords show increased recovery towards the wintertime ocean properties, due to the smaller volume of water in the upper box which must be replenished by the estuarine circulation, which has the same volume transport in all cases.

3.3.3 Realistic Subglacial Discharge and Realistic Ocean Stratification

3.3.3.1 Southwest Greenland

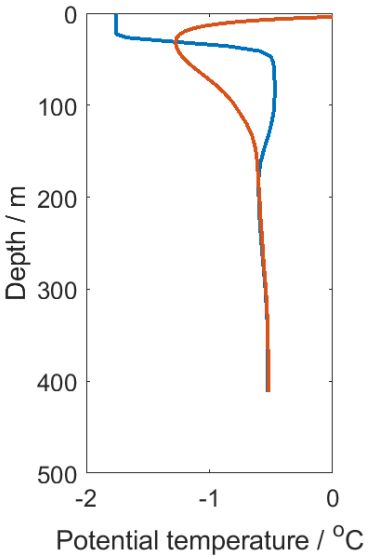

Figure 3.20: Example profiles of potential temperature on the coast of west Greenland taken from NEMO output in a pre-industrial HADGEM3-GC3.1-LL control run, used in the ocean forcing of the box model. January values are shown in blue, July in red. Profiles are taken from the first year of HADGEM3 output at 62°N, 48.5°W.

We now investigate model behaviour given realistic forcing conditions in both subglacial discharge and ocean stratification. Ocean temperature and salinity are taken from the NEMO ocean model component of the HADGEM3-GC3.1-LL Earth system model, from a pre-industrial control run. Vertical profiles are taken from the coast of southwest Greenland, at 62°N, 48.5°W. Example summer and winter profiles of potential temperature are shown in Figure 3.20. We run a box-model configuration with fjord width $B = 9\,\text{km}$ and depth $D = 500\,\text{m}$, to illustrate the general behaviour of the box model with forcing conditions which could be provided by an Earth system model. For this case study, we initially ignore only the top 25 m of the ocean stratification when calculating the approximation using the routine in §3.2.2.3.

Figure 3.21 shows the total ice face melt rate, lower box salinity, upper box salinity gradient, plume outflow depth, outflow distance above the pycnocline, and lower box thickness over a 25 year period. The melt rate and plume outflow depths display seasonal behaviour, with maximum melt and shallowest outflow occurring every summer. The lower box salinity and upper box salinity gradient, as well as the lower box thickness, display several sharp spikes in the period from $\sim$ 19 years to the end of the time series. Whilst these are seemingly not reflected strongly in the melt rates and plume outflow depths, which are the key outputs that the

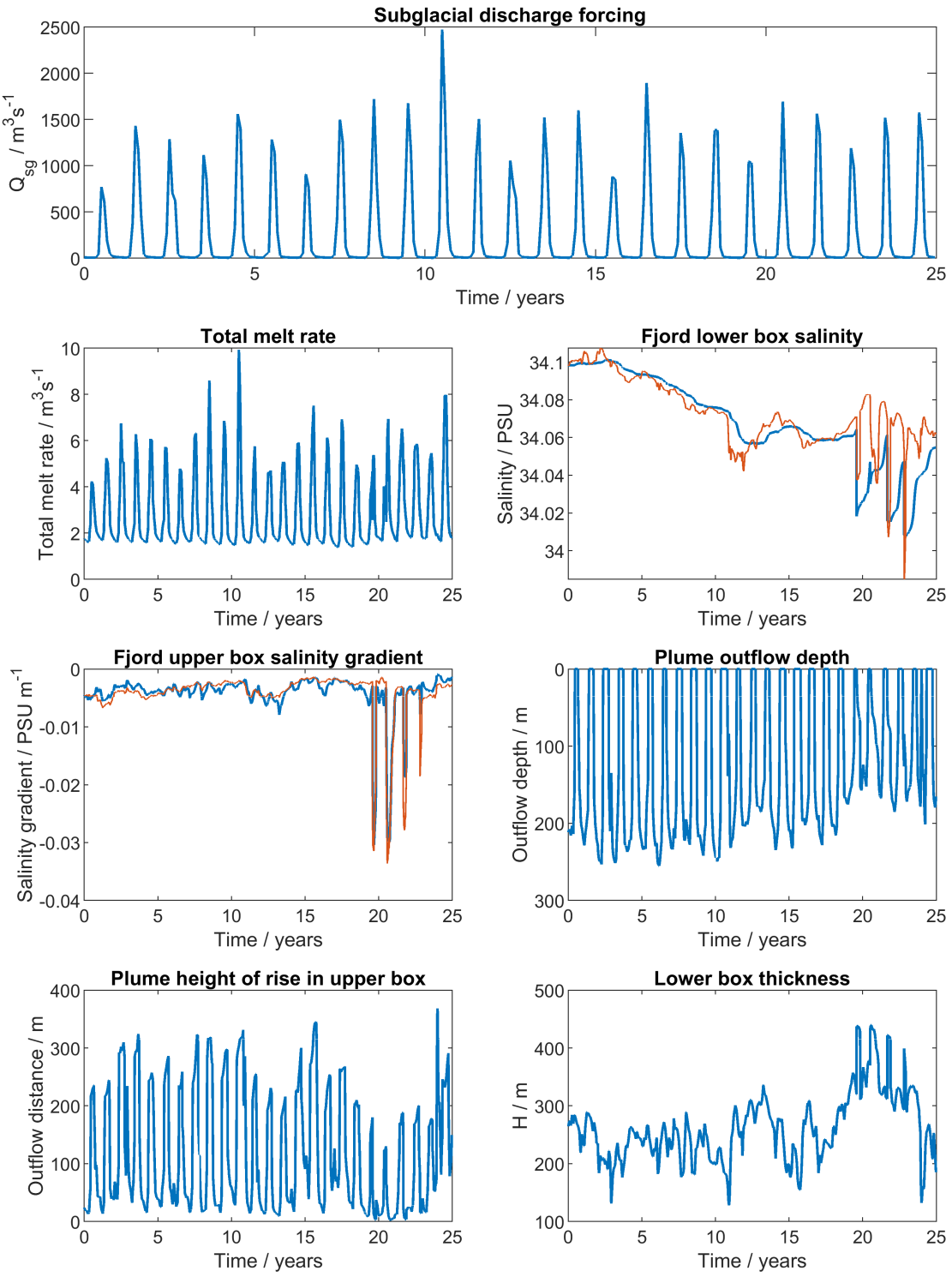

Figure 3.21: Box-model time series outputs for a configuration with subglacial discharge and ocean stratification taken from 62°N, 48.5°W, southwest Greenland, in the ice sheet and ocean components of a HADGEM3-GC3.1-LL pre-industrial control run. Fjord width $B = 9\,\text{km}$, length $L = 100\,\text{km}$ and depth $D = 500\,\text{m}$. The ocean lower box salinity and upper box salinity gradient are shown in red.

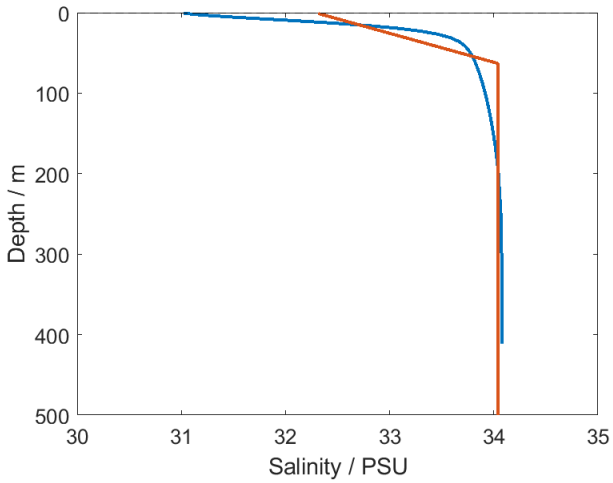

Figure 3.22: Ocean model salinity profile (blue) and approximation using the fitting routine described in §3.2.2.3 (red), with the fitting routine ignoring only the top 25 m in the ocean stratification, corresponding with the first large spike in fjord upper layer salinity gradient seen at $t \approx 19$ years in Figure 3.21.

parameterization would provide to ice and ocean model components of an Earth system model, it is nevertheless important to understand this behaviour.

Investigation of the ocean salinity at the times at which the rapid changes in fjord salinity occur reveals a potential area for future model improvement. Figure 3.22 shows the ocean salinity profile with depth and the approximation used by the box model at $t = 7148$ days (~ 19 years), corresponding with the first of the spikes. Comparison of Figure 3.22 with the profiles in Figure 3.3 reveals that the fitting routine occasionally detects the strong stratification occurring due to the seasonal cycle at the ocean surface, rather than stratification deeper in the pycnocline. This causes the box interface in the approximation to the ocean stratification to jump towards the surface, and the salinity gradient in the surface box to strengthen significantly.

In such cases, the plume outflow remains forced to occur in the surface box and may jump towards the surface. However, the corresponding increase in the surface box salinity gradient restricts the height of rise in this box such that the outflow will occur at the bottom of the surface box over a geophysically relevant range of subglacial discharge. Furthermore, the increase in lower layer thickness itself reduces the prediction for the height of rise in the surface box. This somewhat counteracts the

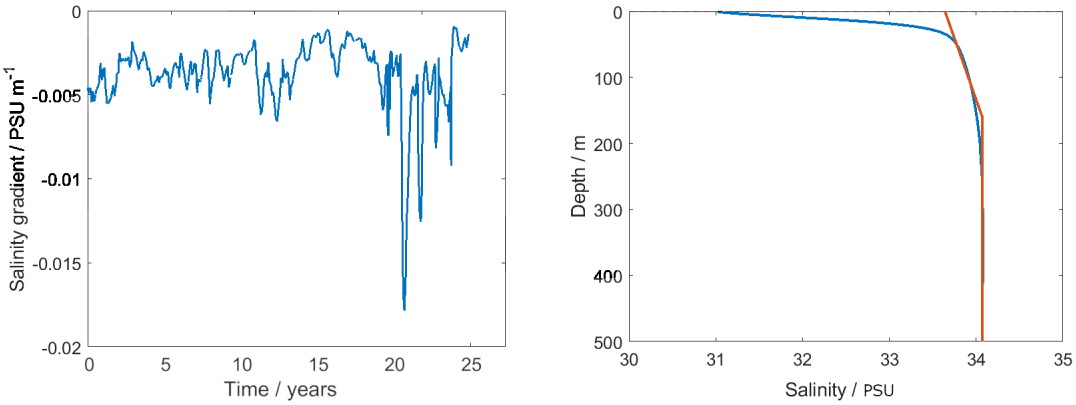

Figure 3.23: *Left*: Fjord upper box salinity gradient for a fjord with width $B = 9\,\mathrm{km}$, length $L = 100\,\mathrm{km}$ and depth $D = 500\,\mathrm{m}$, with a stratification fitting routine which now ignores the top 75 m of the ocean salinity stratification. *Right*: Ocean model salinity profile (blue) and approximation using a fitting routine which now ignores the top 75 m of the ocean salinity stratification (red) at $t \approx 19$ years (as in Figure 3.22).

upwards movement of the pycnocline base due to the increase in lower layer thickness itself and may explain why the signal is not seen as clearly in plume outflow depth.

A more careful selection of the range of depths over which to perform the fitting routine generating the approximation to the ocean stratification at each time step reduces this behaviour. Figure 3.23 shows the salinity gradient time series for an identical model configuration to those in Figure 3.21, with a fitting routine which now ignores the upper 75 m of the ocean stratification in the stratification fitting routine. The large spikes in salinity gradient are reduced by around a factor of 2. A systematic method for choosing the most appropriate depth range encompassing the surface seasonal cycle, to be ignored by the fitting routine, is theoretically simple to develop. For example, a routine could first fit the full ocean data, then calculate the disparity between the gradient in salinity at the surface in the ocean data and the approximation, ignore ocean data which has a difference in gradient above some threshold, and fit again. Any such routine will, however, increase the computational cost of the box model. The level of acceptable trade-off between improving the fit and increased computational cost is likely dependent on the precise usage of the box model, and thus we leave the implementation of this alternative for future work as the need arises.

3.3.3.2 Nares Strait, northwest Greenland

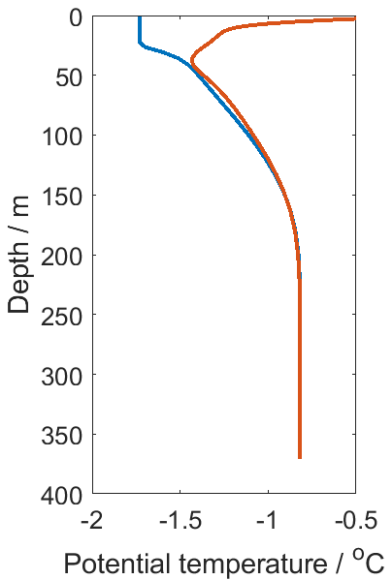

Figure 3.24: Example profiles of potential temperature on the coast of southeast Greenland from NEMO output in a pre-industrial HADGEM3-GC3.1-LL control run, used in the ocean forcing of the box model. January values are shown in blue, July in red. Profiles are taken from the first year of HADGEM3 output, at 81°N, 65.5°W.

We now use forcing conditions taken from Nares Strait (81°N, 65.5°W). For consistency, we retain the same fjord dimensions, with width $B = 9\,\mathrm{km}$, length $L = 100\,\mathrm{km}$ and depth $D = 500\,\mathrm{m}$. Example summertime and wintertime temperature profiles for this region taken from the first year of HADGEM3 output are shown in Figure 3.24. Total submarine melt rate, fjord lower box salinity, upper box salinity gradient, plume outflow depth and lower box thickness are shown in Figure 3.25, along with the subglacial discharge forcing time series.

In this case, the fitting routine generating the approximation to the oceanic stratification does not cause large discontinuities in box-model outputs, and the lower box salinity and upper box salinity gradient display much smoother behaviour than in §3.3.3.1, the seasonal cycle in upper box salinity gradient notwithstanding. Interestingly, the salinity gradient in the upper box is sufficiently strong to prevent the surface emergence of the subglacial discharge plume, which remains subsurface at all times, consistent with observations at Petermann Fjord (e.g. Johnson et al. 2011), although the associated glacier terminates in an ice shelf rather than a vertical cliff. Indeed, the mean salinity gradient is far larger than that seen in western Greenland (§3.3.3.1). Also, the variation in upper box salinity gradient is much larger than that in §3.3.3.1 (neglecting the large jumps or discontinuities), with an amplitude of around $0.01\,\mathrm{PSU\,m^{-1}}$ due to the larger seasonal variability in the ocean salinity gradient.

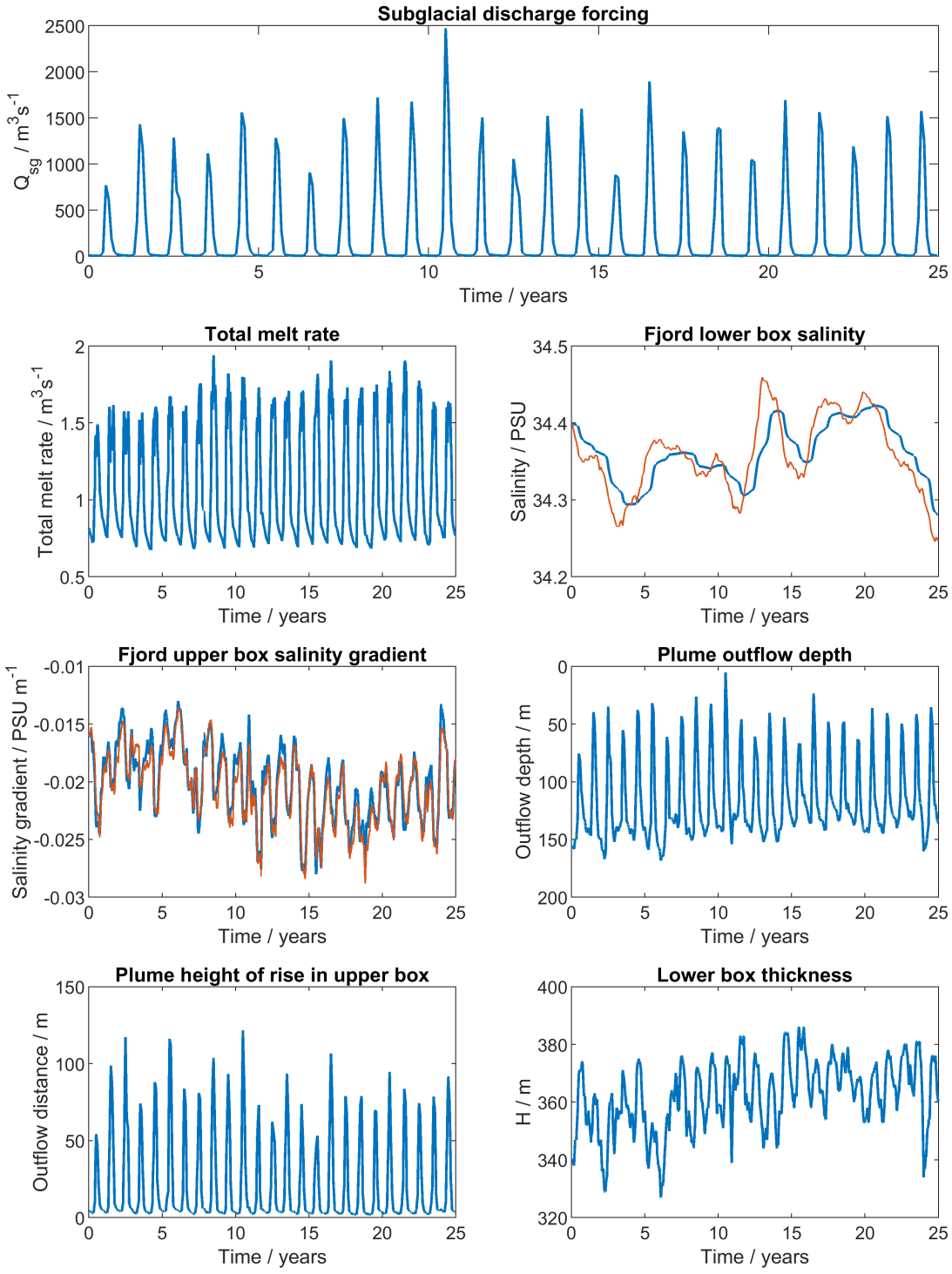

Figure 3.25: Box-model time series outputs for a configuration with subglacial discharge and ocean stratification taken from Nares Strait (81°N, 65.5°W) in a HADGEM3-GC3.1-LL pre-industrial control run. Fjord width $B = 9\,\text{km}$, length $L = 100\,\text{km}$ and depth $D = 500\,\text{m}$. The ocean lower box salinity and upper box salinity gradient are shown in red.

The variability in the approximated ocean lower box thickness is much less than in the previous case study, again even when ignoring the large discontinuities. The unstratified layer thickness varies by less than 40 m over the full model run. At the ice, the box model predicts extremely low melt rates at all times, with a small seasonal cycle as the subglacial discharge transitions between summer and winter states. This is reflective of the very low ocean temperatures in the (pre-industrial) forcing data throughout the entire model run. Comparison of melt rates in Figure 3.25 for Nares Strait and Figure 3.21 for southwest Greenland shows the large differences in melt rates possible around Greenland's coastline given realistic forcing conditions.

3.3.3.3 Southeast Greenland

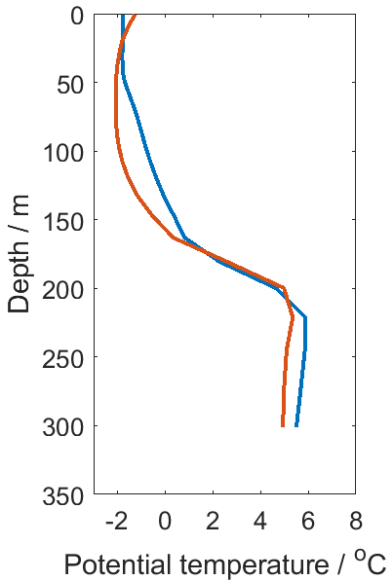

Figure 3.26: Example profiles of potential temperature on the coast of southeast Greenland from NEMO output in a pre-industrial HADGEM3-GC3.1-LL control run, used in the ocean forcing of the box model. January values are shown in blue, July in red. Profiles are taken from the first year of the HADGEM3 model data, at 65°N, 35°W.

Finally, we investigate the behaviour of the fjord box model given forcing conditions taken from southeast Greenland (65°N, 35°W). This region contains Helheim Glacier, one of Greenland's largest outlet glaciers in terms of mass loss, with ocean forcing conditions considered here to be those at the mouth of Sermilik Fjord (in this pre-industrial setting). Example summertime and wintertime temperature profiles for this region taken from the first year of HADGEM3 output are shown in Figure 3.26. Again, we run the model with fjord dimensions $B = 9\,\text{km}$, $L = 100\,\text{km}$ and $D = 500\,\text{m}$.

The box-model outputs are shown in Figure 3.27. As in §3.3.3.2, the box model does not display the spurious spikes in upper box salinity gradient or lower box salinity associated with the routine which approximates the stratification flipping to a solution with a shallow surface box, as a result of seasonal fluctuations

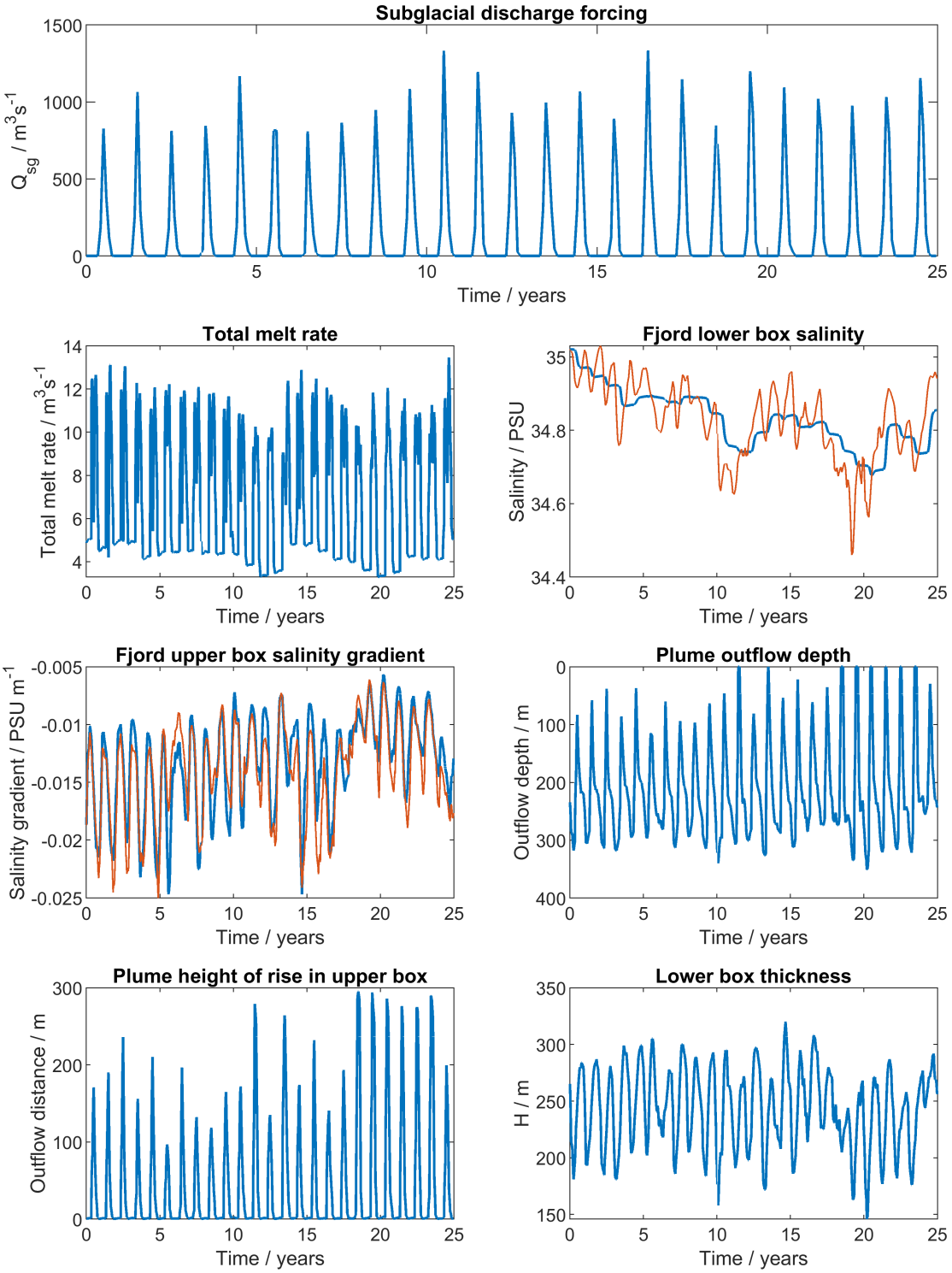

Figure 3.27: Box-model time series outputs for a configuration with subglacial discharge and ocean stratification taken from southeastern Greenland (65°N, 35°W) in a HADGEM3-GC3.1-LL pre-industrial control run. Fjord width $B = 9\,\text{km}$, length $L = 100\,\text{km}$ and depth $D = 500\,\text{m}$. The approximated ocean lower box salinity and upper box salinity gradient time series are shown in red.

at the surface. Interestingly, the plume terminates in the subsurface for much of the model run, penetrating all the way to the surface when the salinity gradient becomes small, particularly from $t \approx 19$ years onward. The melt rates predicted here are around an order of magnitude larger than those for the Nares Strait case study in §3.3.3.2, despite the significantly lower peak subglacial discharge, highlighting the impact of warmer ocean conditions on the submarine melting.

3.4 Comparison to MITgcm simulation

As initial validation of the box model, we compare the observed box-model behaviour to MITgcm simulations under the same forcing conditions. We employ an idealised fjord model in MITgcm, configured as in §2.2.1, with a vertically uniform temperature profile. In §3.4.1, we employ a time-dependent salinity variation for ocean forcing along with constant subglacial discharge and compare the resultant time series of fjord stratification and total melt rate between the MITgcm simulation and box-model outputs. In §3.4.2, we compare melt-rate predictions from the MITgcm simulations and the box model for an ocean stratification in salinity which remains constant in time, for several vertically uniform ambient temperature profiles.

3.4.1 Time-varying ocean forcing

In this section, we modify the sponge region (where $x \geq 100\,\text{km}$) in the MITgcm configuration from Chapter 2 to restore to a time-dependent stratification in salinity given by Equation 3.30, where again S_1 and S_2 are the red and blue profiles in Figure 3.7. The temperature is initialised at 1 °C everywhere, and the sponge region restores temperature to a constant 1 °C. The vertical resolution of the MITgcm simulations is 25 m. This is larger than the movement of the pycnocline predicted by the box model. Therefore, we consider the upper 175 m and lower 325 m in the MITgcm simulation as equivalent to the upper and lower boxes of the box model, and we consider no change in these depth ranges over time when analyzing MITgcm simulation output.

The finite restoration timescale in the sponge region, and the fact that there is a linear ramp up in restoring strength from zero at $x = 100\,\mathrm{km}$, means that the stratification at $x = 100\,\mathrm{km}$ in the MITgcm simulation is not precisely identical to ocean conditions in the box model. However, qualitative comparison of the behaviour of properties in the fjord over time is useful for initial validation of the box model. To mitigate the impact of the finite restoring strength, we decrease the restoring timescale in the sponge by a factor of 50 versus values considered in Chapter 2, such that the salinity and temperature in the sponge decay towards the target profiles more rapidly than simulations in Chapter 2. This does, however, decrease the effectiveness of the sponge region in damping waves, which may reflect back into the fjord.

Figure 3.28 shows the total melt rate, salinity gradient over the upper 175 m, and mean salinity over the lower 325 m from MITgcm simulation output over 2.5 years. Box-model output from a configuration with identical ocean stratification time series, subglacial discharge, and fjord dimensions is shown in black. In this section and §3.4.2, the drag coefficient used in the calculation of melt in the box model is set to $C_d = 2.5 \times 10^{-3}$ for consistency with the MITgcm simulation. Note that the magnitude of changes in both lower box salinity and upper box salinity gradient in the ocean stratification considered here are significantly larger than those of the realistic forcing from HADGEM3 output considered in §3.3.3, to illustrate the response to very strong forcing.

The amplitude of variations of the total melt rate from the MITgcm simulation is significantly larger than that predicted by the box model, and displays more complex behaviour. The time-averaged melt rate is also significantly higher than the box-model prediction, by $\sim 50\%$. Given the additional density-driven flow in the MITgcm simulation resulting from differences in salinity between the fjord and sponge region, the velocities at the ice face are larger than those of previous simulations (such as those considered in Chapter 2) where the stratification is held constant. Thus, the melt rates are somewhat larger than those predicted by the box model.

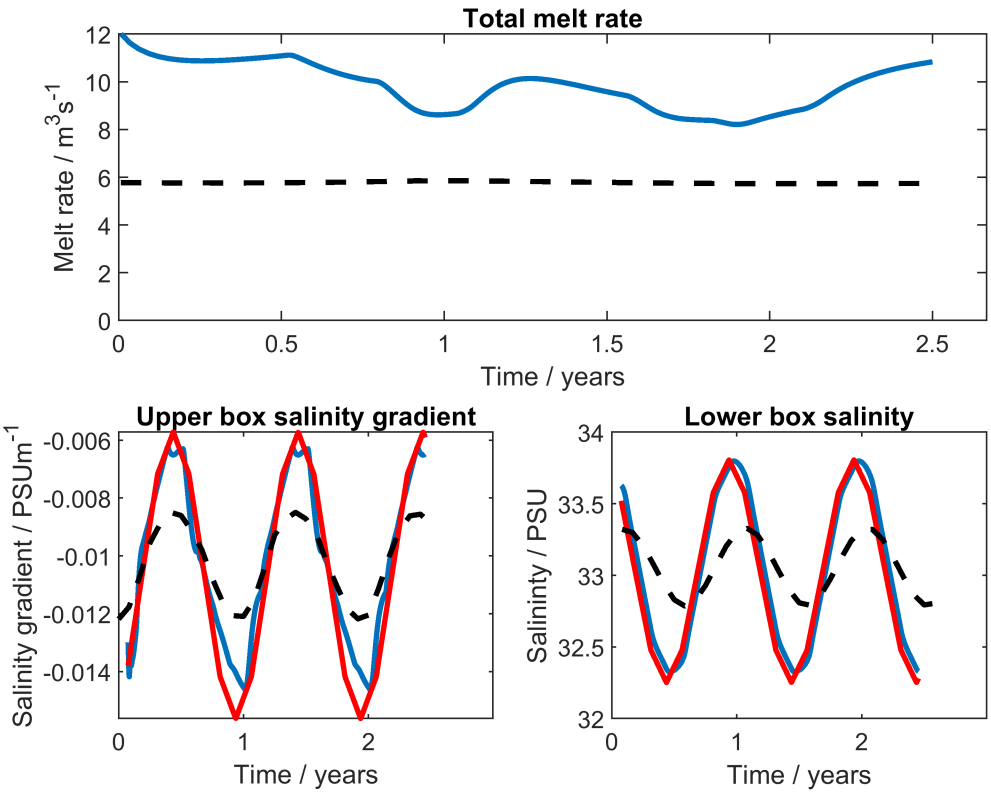

Figure 3.28: Time series of fjord properties from MITgcm simulation output with subglacial discharge $Q_{sg} = 750\,\mathrm{m^3\,s^{-1}}$ and fjord width $B = 9\,\mathrm{km}$. The salinity gradient in the upper 175 m (blue, bottom left panel) and salinity in the lower 325 m (blue, bottom right panel) are the mean values over the fjord length and width. The corresponding quantities averaged over the sponge region are shown in red. *Black, dashed lines*: Box-model output corresponding to the same ocean forcing, subglacial discharge, and fjord dimensions as in the MITgcm simulation.

The stratification within the fjord tracks changes on the shelf much more quickly in the MITgcm simulation than in our box model; the lag in the fjord response is significantly shorter in the MITgcm simulation than in the box model, and also the amplitude of variation in salinity in the lower 350 m and salinity gradient in the upper 175 m is significantly larger than that observed in box-model output. Potentially, this is a direct result of flow driven by horizontal density gradients between the fjord and the shelf in the MITgcm simulation, in a similar manner to wind-driven intermediary circulation, which we have not currently implemented in the box model.

Considering density-driven flows between the shelf and the fjord as gravity currents driven by a horizontal gradient in salinity (e.g. Turner 1973), we can

(very roughly) estimate the magnitude of the density-driven volume flux. We assume a constant difference in salinity between the fjord and the ocean of $\sim 1\,\mathrm{PSU}$. Assuming uniform volume flux over the fjord cross-section, the Froude number of density-driven flow over the full fjord depth is

$$Fr = \frac{u}{\sqrt{g'D}} = \frac{Q}{BD\sqrt{g'D}} \tag{3.34}$$

where $Q = uBD$ is the volume flux, B the fjord width, D the fjord depth, and $g' = g\beta\Delta S/\bar{\rho}$ the reduced gravity associated with the horizontal salinity difference ΔS, with β the haline contraction coefficient and $\overline{\rho}$ a reference density. Given that the flow is driven by horizontal density gradients, we expect that the Froude number $Fr \approx 1$ (see Turner 1973). For a horizontal difference in salinity $\Delta S \sim 1\,\mathrm{PSU}$, this leads to $Q \approx 1.5 \times 10^5\,\mathrm{m^3\,s^{-1}}$, which is $\mathcal{O}(10)$ times larger than the predicted volume flux due to the subglacial-discharge-driven estuarine circulation. This volume flux would flush the entire fjord in ~ 30 days. This provides an *a posteriori* validation of our assumption that the fjord and ocean differ in salinity by approximately 1 PSU, which is approximately true over this timescale given the period of ocean forcing. The magnitude of the density-driven flows therefore likely explains the faster response of the stratification in the fjord to the forcing observed in MITgcm simulations. This highlights the need to include density-driven horizontal flows including tides and wind-driven intermediary circulation into the box model, which is left for future work.

Density-driven flow clearly dominates over the estuarine flow for large amplitude oscillations in the ocean forcing. Given the magnitude of salinity changes in the realistic ocean time series in §3.3.3, and for a fairer comparison to the box model, we now consider a case with a smaller density-driven flow. Figure 3.29 shows the total melt rate, salinity gradient over the upper 175 m, and mean salinity over the lower 325 m from MITgcm simulation output for a simulation with the amplitude of oscillations in the ocean forcing reduced by a factor of ~ 3. Box-model output from a configuration with identical ocean stratification time series, subglacial discharge, and fjord dimensions is shown in black.

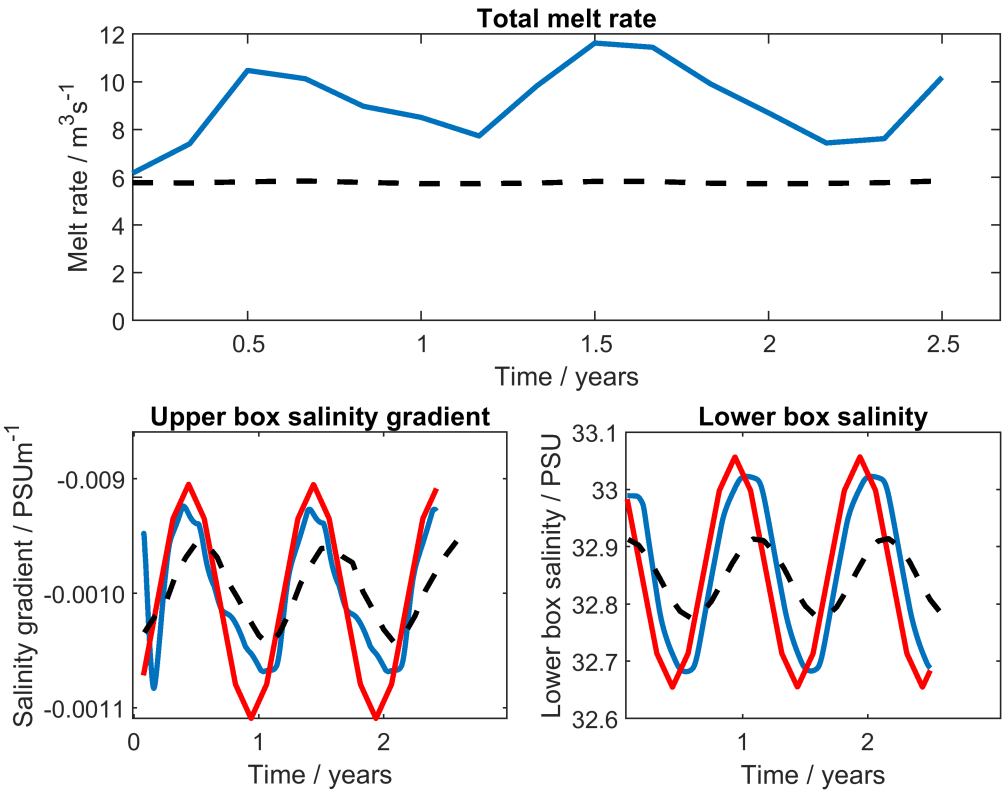

Figure 3.29: Time series of fjord properties from MITgcm simulation output with subglacial discharge $Q_{sg} = 750\,\mathrm{m^3\,s^{-1}}$ and fjord width $B = 9\,\mathrm{km}$, for simulations with smaller amplitude oscillations in the ocean forcing. The salinity gradient in the upper 175 m (blue, bottom left panel) and salinity in the lower 325 m (blue, bottom right panel) are the mean values over the fjord length and width. The corresponding quantities averaged over the sponge region are shown in red. *Black, dashed lines*: Box-model output corresponding to the same ocean forcing, subglacial discharge, and fjord dimensions as in the MITgcm simulation.

It can be seen that the simulated salinity in the fjord less closely matches that of the ocean, and is brought closer to the prediction of the box model. Furthermore, the melt rate time series displays a clearer seasonal cycle, although the magnitude of the deviation from the mean remains similar to that in Figure 3.28. The reduced density-driven flow also reduces cross-fjord velocities at the ice face, such that the melt rate calculated by the box model is closer to that of the MITgcm simulation, although the box-model prediction remains a significant underestimate. In the next section, we investigate the total melt rate in both MITgcm and box-model simulations for cases where the ocean stratification is held constant in time, with

vertically uniform temperature.

3.4.2 Constant ocean forcing

We now compare the total melt rate between MITgcm simulation and box-model outputs over a range of ambient ocean temperatures T_a which are vertically uniform and constant in time, for $T_a = -1,\ 1,\ 2,\ 3$ and $4\,^{\circ}\mathrm{C}$. The ambient salinity profile is given by $S_1(z)$ (Figure 3.7, red line). The horizontal resolution of the MITgcm simulation is 500 m, and velocities are calculated on an Arakawa C-grid. Therefore, for closer comparison between cross-fjord velocities in the box model and MITgcm simulation, in this section, we take the predicted cross-fjord velocity 250 m from the ice face when calculating melt rates in the box model.

Figure 3.30 shows the total melt rates predicted by the box model (dashed line) and taken from MITgcm simulations (markers) for a fjord with width $B = 9\,\mathrm{km}$ and depth $D = 500\,\mathrm{m}$, forced by a constant subglacial discharge $Q_{sg} = 750\,\mathrm{m^3\,s^{-1}}$. In this case, there is no density-driven flow driven by a time-varying ocean forcing in the MITgcm simulation, and the melt rate prediction of the box model is very close to that of the MITgcm simulation. The box-model prediction is closer for lower ambient temperatures, where the prediction for the highest ambient temperature considered here differs from that of the MITgcm simulation by $\sim 10\%$. Nevertheless, the box model predicts the melt rate in the MITgcm simulation to good accuracy where density-driven flows can be neglected.

Whilst the density-driven flows between the shelf and the fjord may dominate in setting the stratification within the fjord, it is important to note that the subglacial-discharge-driven response considered in this thesis remains important in setting the vertical structure of the background flow state within the fjord. The plume scalings derived in Chapter 2 are applied in a quasi-steady way given the fjord stratification, independently of the processes which set the stratification. Thus, the plume should follow the same scaling laws even where the stratification is set by density-driven flows rather than the estuarine circulation itself. Furthermore, wind-driven intermediary circulation is typically short-lived, with the net impact

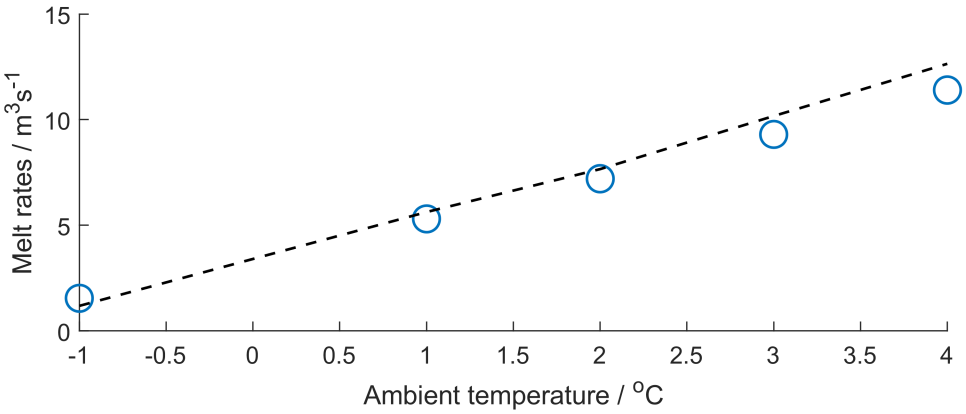

Figure 3.30: *Markers*: Total melt rate from MITgcm simulation output with subglacial discharge $Q_{sg} = 750\,\mathrm{m^3\,s^{-1}}$, fjord width $B = 9\,\mathrm{km}$ and depth $D = 500\,\mathrm{m}$, for simulations with differing vertically uniform ambient temperatures. *Black, dashed line*: Box-model output corresponding to the same ocean stratification, subglacial discharge, and fjord dimensions as in the MITgcm simulation.

on the stratification in the fjord given by the residual over a large amplitude cycle (see §1.2.1.3). It is therefore crucial to understand the estuarine circulation driven by subglacial discharge before attempts to characterize flows due to time-varying ocean forcing. Nevertheless, characterization of density-driven flow resulting from wind-driven intermediary circulation, tides, seasonal cycles or other time-varying ocean forcings, as well as further validation of the box model, is a high priority for future work.

3.5 Summary

In this chapter, we have created a simple, idealised box model of estuarine circulation driven by subglacial discharge within Greenland's proglacial fjords. This is intended to form the basis of a parameterization scheme representing the impact of ocean forcing on the melting of the Greenland Ice Sheet in Earth system models. To allow the box model to be computationally light, the fjord velocity structure is generated using scaling laws for the vertical structure of cross-fjord-integrated along-fjord velocity, and the melt rate is calculated using a phenomenologically based theory, both of which are discussed in more detail in Chapter 2. The use

of scalings in this way removes the need to solve coupled differential equations describing the plume dynamics at each time step.

The box model is composed of two vertically stacked boxes, the lower assumed to be of vertically uniform salinity and temperature, and the upper box allowing for some linear variation of salinity and temperature with depth, with profiles continuous at the box interface. We use an approximation for the ocean stratification, using a least-squares fitting method to generate the idealised piece-wise linear ocean T and S profiles. The upper box is subdivided into several layers, controlled by the vertical structure in along-fjord velocity predicted by the scalings. Volume fluxes in each layer are also provided by scaling laws and assumed constant along the entire length of the fjord.

We have investigated the behaviour of the box model given a combination of idealised and realistic forcings, over a geophysically relevant range of fjord depths and widths, in order to develop understanding of the leading order response in Greenland's fjords. We have shown that, even with identical subglacial discharge and ocean stratification, fjords of differing widths and/or depths can display different behaviour in terms of melt rates, and stratification. In an estuarine circulation regime, wider fjords adjust more slowly to ocean forcing conditions and display less temporal variability given variable ocean conditions. The surface layer of deeper fjords responds more quickly to changing ocean conditions, as the increase in deep water entrained into the plume generates a more vigorous circulation. The adjustment timescale in the deep layer, however, is more strongly dependent on subglacial discharge flux than fjord depth over geophysically relevant ranges.

The box model response to a realistic, seasonally varying subglacial discharge flux suggests that fjord conditions may tend towards summertime ocean conditions for cases where the plume-driven circulation dominates, such that the annual mean properties within the fjord skew towards the summertime properties of the ocean, rather than matching the annual mean ocean properties. This has implications for submarine melt rates and glacial stability. In §3.4, results from MITgcm simulation for time-varying ocean forcing suggest that density-driven flow may enhance the

exchange between the fjord and ocean in some settings, such that the fjord tracks changes on the shelf more rapidly than via plume-driven circulation alone. The inclusion of density-driven flow is therefore a high priority for future work.

3.6 Limitations, alternative approximations and future work

Progress in characterizing the flow response to changing subglacial discharge and conditions at the fjord mouth in a subglacial-discharge-driven estuarine circulation regime required a significant number of approximations. Fundamentally, the box model depends on the approximation that the ocean stratification can be represented as a layer of linearly varying salinity overlying a layer of constant density. In this chapter, we have presented an example of the strong seasonality at the surface in ocean data causing large jumps in the approximation to the ocean stratification (Figure 3.22). The fitting method described in §3.2.2.3 will always produce an approximation of the required form. However, there may be cases where this structure does not describe the observed ocean stratification in salinity, in which case the approximation will be poor. This could be mitigated by the addition of further layers in the theoretical treatment, although the complexity quickly increases to the point that a simple scaling solution becomes intractable.

It may be possible to add a surface mixed layer more straightforwardly. If the plume outflow depth is predicted to lie below the mixed layer, then the mixed layer has no impact on the salt flux into or out of the fjord. If the plume reaches the mixed layer without reaching neutral buoyancy, then it will penetrate through the entire mixed layer of uniform density and outflow at the surface. Such a mixed layer could also be useful for the inclusion of other freshwater sources within the fjord, such as surface runoff or iceberg melt.

The assumption that the pycnocline in the fjord box model responds instantly to that of the ocean is a potential avenue for improvement. It may be possible to build in some time-dependent response of the box interface depth within the fjord, with some physically motivated decay or lag timescale. Furthermore, the assumption

that the volume flux set by plume scalings responds instantaneously along the entire length of the fjord is increasingly inaccurate as fjord length increases. MITgcm model output suggests that the spin-up time of a 100 km long, 10 km wide and 500 m deep fjord is $\sim$ 10 days, approximately one box-model time step for the results presented in this chapter. For times shorter than this, the assumption of an instantaneous response becomes increasingly invalid.

In terms of future work, it may be possible to make several additions to the box model relatively simply. Firstly, the addition of any passive tracer would be trivial, as it would evolve according to the same principles as salinity and temperature. This would provide a framework for a study of the evolution of biogeochemical or mineral tracers in Greenland's fjords, with implications for biodiversity and habitat health (e.g. Meire et al. 2017). Furthermore, the two-layer structure of the box model may allow for the inclusion of katabatic wind events based on the theory of Farmer (1976) and Spall et al. (2017), discussed in §1.2.1.4. As a first approximation, this could simply be treated as an additional volume flux in each layer, with magnitude depending on the wind stress, summed linearly with the estuarine volume fluxes considered here. Intermediary circulation, where density differences between the fjord and the shelf due to barrier wind stress on the coast can be a driver of rapid change within fjords, is potentially more complex to include due to the short timescale over which events occur; although some volume flux scalings exist (see §1.2.1.3).

Quantitative comparison of the box model to MITgcm simulations with comparable forcing is an important next step to validate box-model results. Care must be taken to ensure that the forcing conditions at the location considered to be the fjord mouth in each model are the same. Rather than choosing the ocean salinity and temperature time series and then using these time series in MITgcm simulations and the box model independently, it would be instructive to take the salinity and temperature profiles from MITgcm simulations and use these to force the box model. This would ensure greater comparability in what is considered the ocean stratification in each model. Comparison with the MITgcm simulation in

§3.4 suggested that density-driven flows between the shelf and the fjord can be significant, and cause the stratification to track changes in the forcing rapidly. This highlights the importance of the inclusion of some density-driven component in the volume fluxes predicted by the box model. As a first-order estimate, it may be possible to sum the volume flux contribution of the density gradient-driven and subglacial-discharge-driven components linearly, although further work is required to determine if neglecting interactions is justified.

4

Subglacial-discharge-driven estuarine circulation over sills

4.1 Introduction

A large number of Greenland's fjords contain a bathymetric sill between the ice face and the wider ocean (Straneo et al. 2015). These sills are typically located at the furthest historical extent of the glacier which carved the fjord, where debris carried by the glacier was deposited prior to an inland retreat of the glacial terminus (e.g. Shoemaker 1986). Sills within fjords are reminiscent of bathymetric constrictions in other geophysical settings. Indeed, much of the exchange between oceanic basins occurs over ridges and sills (e.g. Lane-Serff et al. 2000). In general, sills act as restrictions on the depths and volume fluxes of exchange flows (e.g. Armi 1986). Thus, building understanding of the effect of sills in proglacial fjord settings is of great importance to the accurate representation of exchange flows within proglacial fjords.

As discussed in Chapter 2, estuarine circulation in Greenland's proglacial fjords is driven by the injection of fresh meltwater at the glacial grounding line. This generates a buoyant plume, with outflow in a stratified upper layer, and inflow below this. Thus, the vertical structure of the along-fjord flow generated near to the ice face is approximately three-layer: an inflow layer at depth, where the plume is entraining ambient fjord water; outflow above this, where the plume reaches

the level of neutral buoyancy; and a layer above the outflow layer, with no net volume flux. In some cases, the plume outflow penetrates all the way to the ocean surface, such that the flow can be approximated as two-layer. For fjords with widths on the order of the Rossby radius of deformation R_d, the estuarine circulation develops significant cross-fjord structure. While this does not impact the cross-ford integrated along-fjord transport in fjords without sills, the impact of rotation is likely to be important in setting the flow structure over sills.

In this chapter, we employ computational models of idealised fjords with sills of two canonical depths: one 'shallow' and within the stratified upper layer, and the other 'deep' and below the stratified upper layer. Rather than varying sill depth beyond these two cases, we instead consider variations of subglacial discharge, which has the effect of increasing or decreasing the vertical distance between the level of neutral buoyancy of the plume and the top of the sill. We aim to investigate the impact of sills on the flow structures discussed in Chapter 2, and discuss potential steps for the inclusion of sills in the box model developed in Chapter 3. In this chapter, §4.2 describes the computational model setup. In §4.3 we present computational results over a representative range of subglacial discharge and fjord widths for two canonical sill depths. Next, §4.4 discusses the implications of results from §4.3 for a parameterization scheme, as well as an outline of initial theoretical explorations attempting to capture and model the computational results. Finally, we provide a summary (§4.5) and a discussion of limitations and potential avenues for future work (§4.6).

4.2 Idealised fjord model

In this chapter, we use the Massachusetts Institute of Technology general circulation model (MITgcm, Marshall et al. 1997; Adcroft et al. 2004) in a similar configuration to that in Chapter 2. In particular, we retain the same parameter values, boundary conditions and plume turbulence parameterizations. We introduce a bathymetric sill at $x = 100\,\mathrm{km}$, with two canonical depths (one sill of depth 150 m and one

of 350 m) investigated separately. In this chapter, we employ a uniform grid in the vertical, with a resolution of 25 m.

In principle, the addition of a sill adds several further parameters to the parameter space of relevance to proglacial fjords. For example, the height, the along-fjord extent, and the functional form of the along-fjord variation of the sill (such as Gaussian, sheer vertical or realistic bathymetry taken from real-world observations) all have potential relevance to the precise flow structure which develops over and near to the sill. To restrict this parameter space, we choose a sheer vertical sill with along-fjord extent of a single grid-cell. This is intended to mitigate the impact of changes in sill shape which would occur as a result of changes in sill amplitude for sills with more complex bathymetry. Furthermore, we make the observation that the key dynamical constraint is the relative depth of the estuarine outflow driven by the subglacial discharge plume compared to the top of the sill, rather than the depth of the sill directly. As such, we restrict our investigation to two canonical sill depths; one 'deep', and one 'shallow' relative to the stratified surface layer (and so possible plume outflow depths). We instead vary the magnitude of subglacial discharge, which in turn varies the relative depth between the plume outflow and the top of the sill for each sill depth.

To prevent the reflection of waves from the open boundary, a sponge region in the outer portion of the domain relaxes salinity and temperature to the initial ambient stratification as described in Figure 4.1. The restoring timescale in the region of constant strength is the approximate time taken for the plume outflow to travel the along-fjord distance of this region in benchmarking runs with no sponge region. This time scale ranges from $\mathcal{O}(1 \times 10^6)$ to $\mathcal{O}(1 \times 10^7)$ seconds, inversely proportional to subglacial discharge. To allow for some investigation of the flow structure which develops beyond the sill, the sponge region starts at $x = 125$ km, with the restoring timescale increasing linearly between $x = 125$ and 150 km, and held at a constant maximum value from $x = 150$ km to the open boundary at $x = 200$ km. For ease of discussion, note that we refer to locations

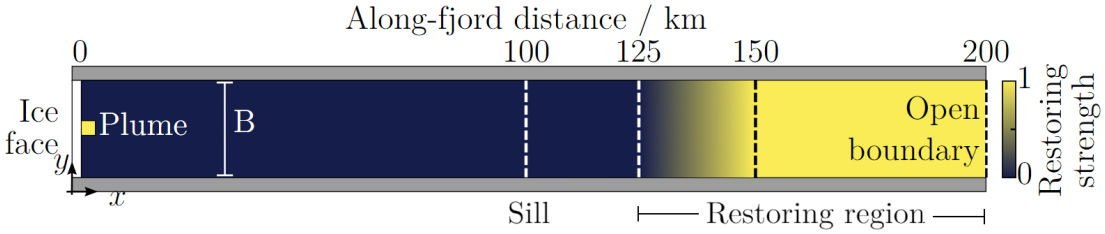

Figure 4.1: Plan view of the MITgcm model configuration. A subglacial discharge plume is parameterized using the ICEPLUME package (Cowton et al. 2015), adjacent to a thermodynamically active ice face at $x = 0$. The fjord is bounded by impermeable vertical walls at $y = \pm B/2$ for a fjord of width B. A vertical bathymetric sill of depth 150 m (shallow case) or 350 m (deep case) is introduced at $x = 100$ km across the entire width of the fjord, with an along-fjord extent of one grid cell. To prevent waves from reflecting off the open boundary and back into the fjord itself, the salinity and temperature are restored to the initial ambient stratification in the outer portion of the domain. Between 125 km and 150 km the restoring strength increases linearly, reaching a constant maximum value between 150 km and 200 km.

where $x > 100$ km beyond the sill as 'on the shelf', although we recognise that in our computational domain, these points are still within a channel.

4.3 Results

We now investigate the impact of the addition of a sill on the subglacial-discharge-driven estuarine circulation in fjords. As discussed in §4.2, idealised MITgcm simulations are used over a geophysically relevant range of subglacial discharge and fjord widths. In particular, we focus on along-fjord flow properties, to inform how the impact of bathymetric sills might be included in the box model developed in Chapter 3. In the next section (§4.3.1), we investigate output from MITgcm simulations with a 350 m deep sill, over a range of fjord widths and subglacial discharge flux, with a focus on the extent to which results in chapters 2 and 3 carry over to fjords with deep sills. §4.3.2 continues this investigation to MITgcm simulations of fjords with shallow (150 m deep) sills.

4.3.1 Deep Sill

Initially, we investigate the impact on the fjord-scale flow structure set up by the subglacial discharge plume for a deep sill, entirely contained within the unstratified

lower layer. The stratification is that of Figure 2.2, as in the base cases in Chapter 2, to aid comparison. In this case, the sill is a sheer vertical wall 350 m deep, rising 150 m from the bottom of a 500 m fjord. We run MITgcm model simulations with fjord widths $B = 3,\ 6,\ 9,\ 12$ and 24 km and subglacial discharge $Q_{sg} = 50,\ 225,\ 400,\ 750$ and $1500\,\mathrm{m^3 s^{-1}}$.

Guided by the box-model structure, we first investigate the steady-state cross-fjord integrated along-fjord velocity which develops within the fjord. Figure 4.2 shows the 3-month time-mean cross-fjord integrated structure as a function of depth and along-fjord distance for a 9 km wide fjord and different subglacial discharge fluxes. In each case, the outflow shows no significant vertical deflection by the sill. That is to say, the range of depths over which outflow occurs remains the same along the entire length of the fjord and beyond the sill, with negligible vertical deviation. As for no-sill cases discussed in Chapter 2, the vertical structure of cross-fjord-integrated along-fjord velocity is the same for each fjord width at any fixed subglacial discharge.

The inflow shows more significant variation along the length of the fjord and out onto the shelf. Close to the ice, the entire water column below the outflow flows towards the ice face as the rising plume entrains ambient water, across the entire range of parameter space. Within the main body of the fjord, the inflowing volume flux decreases in magnitude from the ice to the sill at most depths, suggesting a slow downwelling of inflowing shelf water as it flows towards the ice face. This downwelling must occur as a consequence of mass conservation, balancing the entrainment into the plume and upwelling within the plume. On the shelf, inflow appears to come entirely from the range of depths above sill depth. This is of potential significance to the salt and heat flux into the fjord, particularly where the temperature and salinity on the shelf change between depths below and above the sill. In this case study, the initial vertical profiles in temperature and salinity used in model simulations do not vary significantly below sill depth, such that the difference in salt flux between simulation outputs of a deep sill configuration and a corresponding configuration without a sill is negligible.

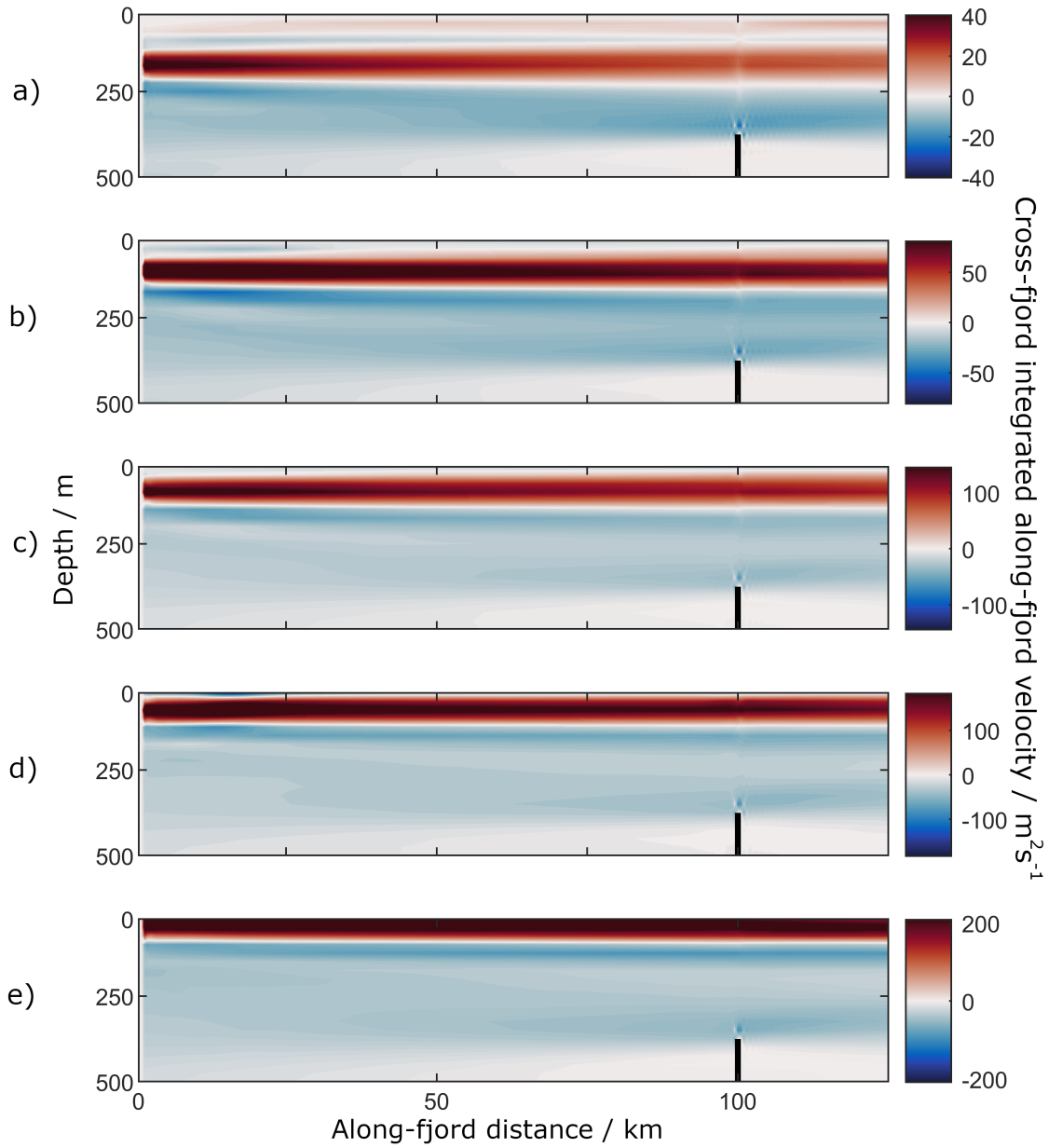

Figure 4.2: 3-month time-mean, cross-fjord-integrated, along-fjord volume transport per unit depth (m^2s^{-1}) as a function of fjord depth and along-fjord distance from the ice face, from MITgcm simulations with fjord width $B = 9\,km$, forced with subglacial discharge Q_{sg} of a) 50, b) 225, c) 400, d) 750 and e) $1500\,m^3s^{-1}$. The sill is denoted by the black line at $x = 100\,km$. Red denotes flow away from the ice face at $x = 0\,km$, and blue denotes flow towards the ice face.

Figure 4.3 illustrates the variation of the along-fjord flow over the sill with depth and cross-fjord distance, for several combinations of fjord width and subglacial discharge. As in cases without a sill in Chapter 2, the flow over the sill is increasingly horizontally sheared as fjord width increases relative to the first baroclinic Rossby

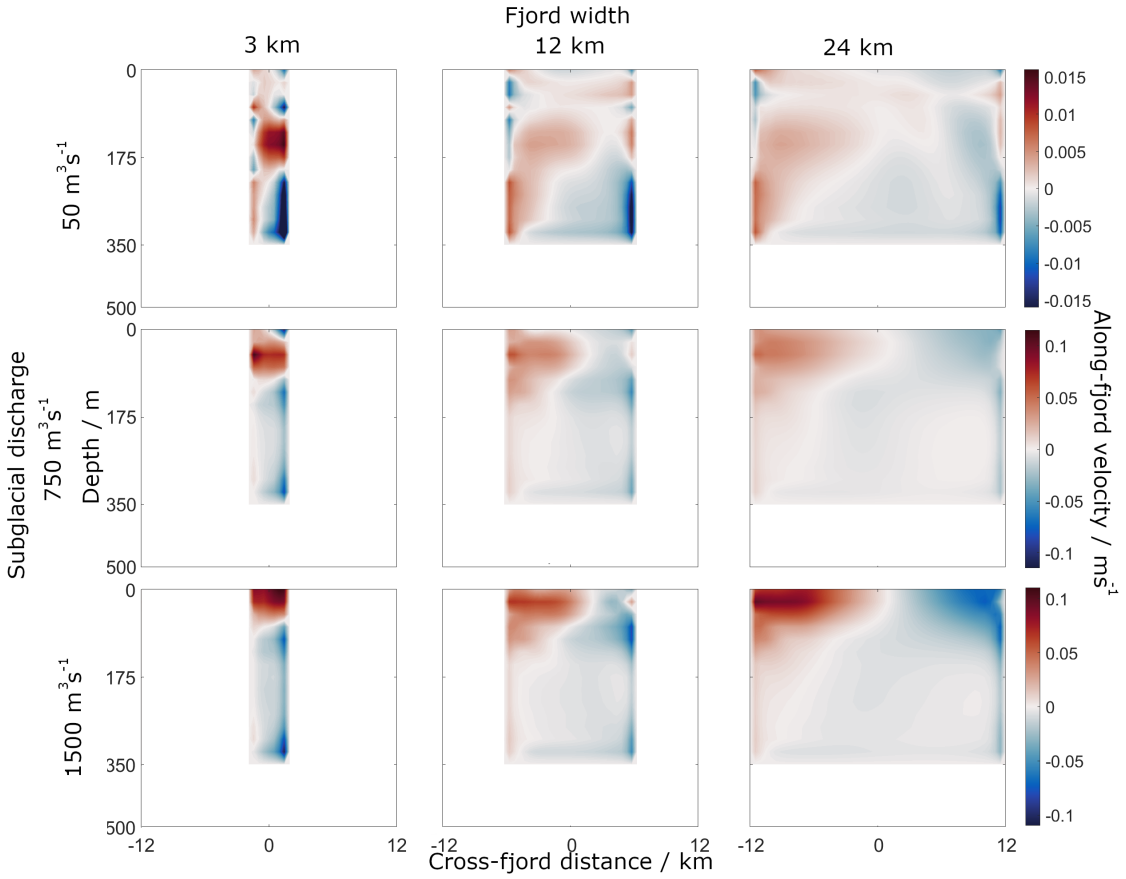

Figure 4.3: 3-month time-mean along-fjord velocity (ms^{-1}) over a 350 m deep sill at $x = 100$ km, from MITgcm simulation output for combinations of fjord widths $B = 3,\ 12,\ 24$ km and subglacial discharge fluxes $Q_{sg} = 50,\ 750,\ 1500\,\mathrm{m}^3\mathrm{s}^{-1}$. Red denotes flow away from the ice face, which is located at $x = 0$ km, and blue denotes flow towards the ice face.

radius of deformation $R_d \sim 10$ km. Weak outflow occurs at depth on the left-hand side of the fjord (looking towards the ice face) for wide fjords. This contrasts with fjords without sills, where the left-hand side at depth is typically inflow (e.g. see Figure 2.4). Alone, this feature is of little dynamical relevance for our box-model parameterization scheme, which has only one grid cell in the cross-fjord direction. In §4.4.3, we discuss the influence of this horizontally sheared flow on the heat and salt exchanges over the sill, finding that the impact of deep sills is negligible. However, greater understanding of this cross-fjord structure may be important if a representation of fjords with a higher horizontal resolution is required.

In terms of the development of a scheme for the inclusion of sills in the box model of Chapter 3, these results suggest that deep sills should not impact the

fjord circulation or stratification significantly when compared with fjords without a sill. As mentioned previously, the designation of a sill as 'deep' is relative to the natural range of plume outflow depths over a geophysically relevant range of parameter space. To determine some quantitative measure of how the flow structure is impacted by the outflow depth relative to sill depth, we now investigate the impact of a bathymetric sill which penetrates all the way through the relatively unstratified lower layer. As a result, the natural outflow depth for subglacial discharge plumes (particularly those generated by weak subglacial discharge) is expected to sit close to the top of the sill, and the sill can be said to be 'shallow'.

4.3.2 Shallow Sill

In the previous section, we discussed the impact of a deep sill which terminates within the relatively unstratified lower layer, with a focus on the along-fjord velocity structure. We found that there is no vertical deflection of the estuarine-circulation outflow layer driven by the plume, in a cross-fjord integrated sense. There is some flow acceleration in the inflow near to the top of the sill as a result of the reduced cross-sectional area of the fjord over the sill, and some apparent blocking of the inflow below sill depth beyond the sill. However, the stratification in temperature and salinity of the inflow remains that of the unstratified lower layer, and thus there is little impact on the salinity and temperature within the fjord. In the next section, we investigate the impact of a shallow sill which penetrates through to the bottom of the stratified upper layer.

4.3.2.1 Velocity structure

We now investigate MITgcm simulation output for fjords with a 150 m deep sill, which penetrates into the stratified upper layer. The influence of the sill on the vertical structure of the cross-fjord integrated along-fjord flow can clearly be seen, particularly for values of subglacial discharge where the range of depths for the plume outflow includes the top of the sill. Figure 4.4 shows the cross-fjord integrated along-fjord velocity for a 9 km wide fjord, with relatively low values of

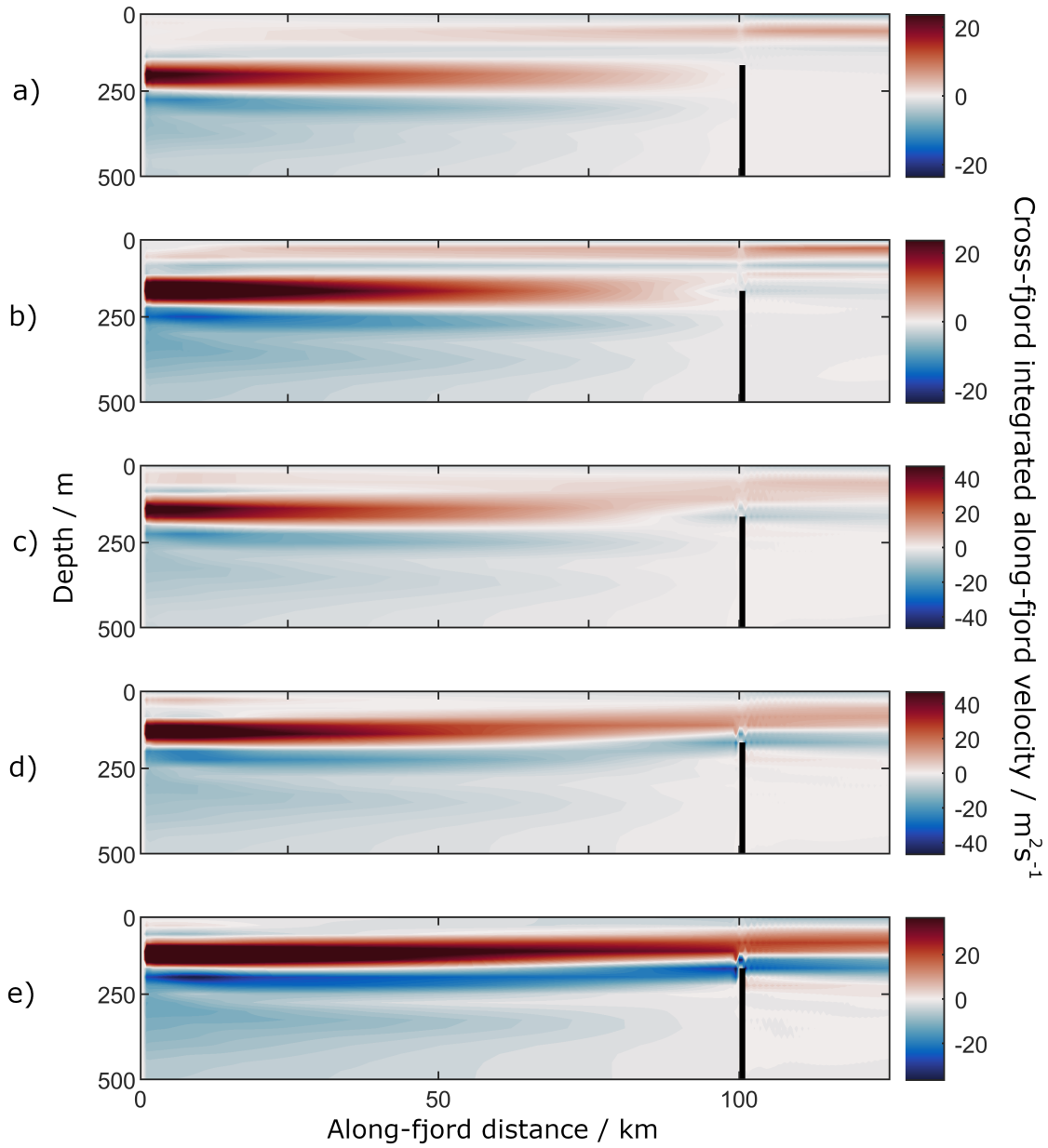

Figure 4.4: 3-month time-mean, cross-fjord integrated, along-fjord transport per unit depth (m^2s^{-1}) from MITgcm simulations with fjord width $B = 9\,km$, forced with 'low' subglacial discharge Q_{sg} of a) 25, b) 50, c) 75, d) 100 and e) $125\,m^3s^{-1}$, such that the top of the sill lies within the natural plume outflow depth range. The sill is denoted by the black line at $x = 100\,km$. Red denotes flow away from the ice face (at $x = 0\,km$), and blue denotes flow towards the ice face.

subglacial discharge $Q_{sg} = 25,\ 50,\ 75,\ 100$ and $125\,m^3s^{-1}$. For the lowest two values of subglacial discharge, the plume outflow at the ice face is almost entirely disconnected from the outflow layer on the shelf in this cross-fjord integrated metric. For $Q_{sg} = 75m^3s^{-1}$, the plume outflow is connected between the interior and exterior

of the fjord; however, there is significant vertical deflection over the sill, occurring over an along-fjord extent $\mathcal{O}(R_d)$ upstream of the sill.

For higher subglacial discharge, the natural outflow depth at the level of neutral buoyancy of the plume moves closer to the ocean surface, and therefore further above the top of the sill (see Figure 4.5). There is a smaller vertical deflection of the outflow between the fjord and the shelf. Interestingly, for subglacial discharge larger than $225\,\mathrm{m^3\,s^{-1}}$, this deflection appears to occur as a sharp transitional step over the sill, rather than a slow change with some significant along-fjord extent. Potentially, this is evidence of the generation of a feature akin to a hydraulic jump (e.g. Gill 1977). There is an acceleration of inflowing water constrained by the plume entrainment, and the depth range at the sill over which the inflow can occur. This may be sufficient to cause a transition from sub-critical flow, with a Froude number $Fr < 1$ to supercritical flow with $Fr > 1$ (assuming a suitable definition of Froude number for this system based on the flow speed versus the gravity wave speed).

The inflow throughout the domain also displays interesting behaviour across the range of parameter space spanned by simulation output. For very low subglacial discharge, there is evidence of inflow towards the ice face beyond the sill in cross-fjord integrated output, although this inflow is significantly weaker than the recirculation between the ice face and the sill. At the ice face, and within the fjord at depth, the entrainment into the rising plume still imposes a volume flux constraint towards the ice with an outflow at some level of neutral buoyancy. Therefore, the plume generates a near closed overturning circulation within the fjord, with a small outflow with net volume flux of the total freshwater injected due to subglacial discharge and melting, which must leave the fjord close to the surface above sill depth due to mass conservation. This outflow generates a double overturning cell-like structure within much of the fjord, with a weakening surface cell for increasing Q_{sg} as the primary plume-driven outflow is less strongly blocked by the sill. The injection of a volume flux at the ice face means that the circulation cannot be entirely closed within the fjord, as the increase in the volume of water between the ice

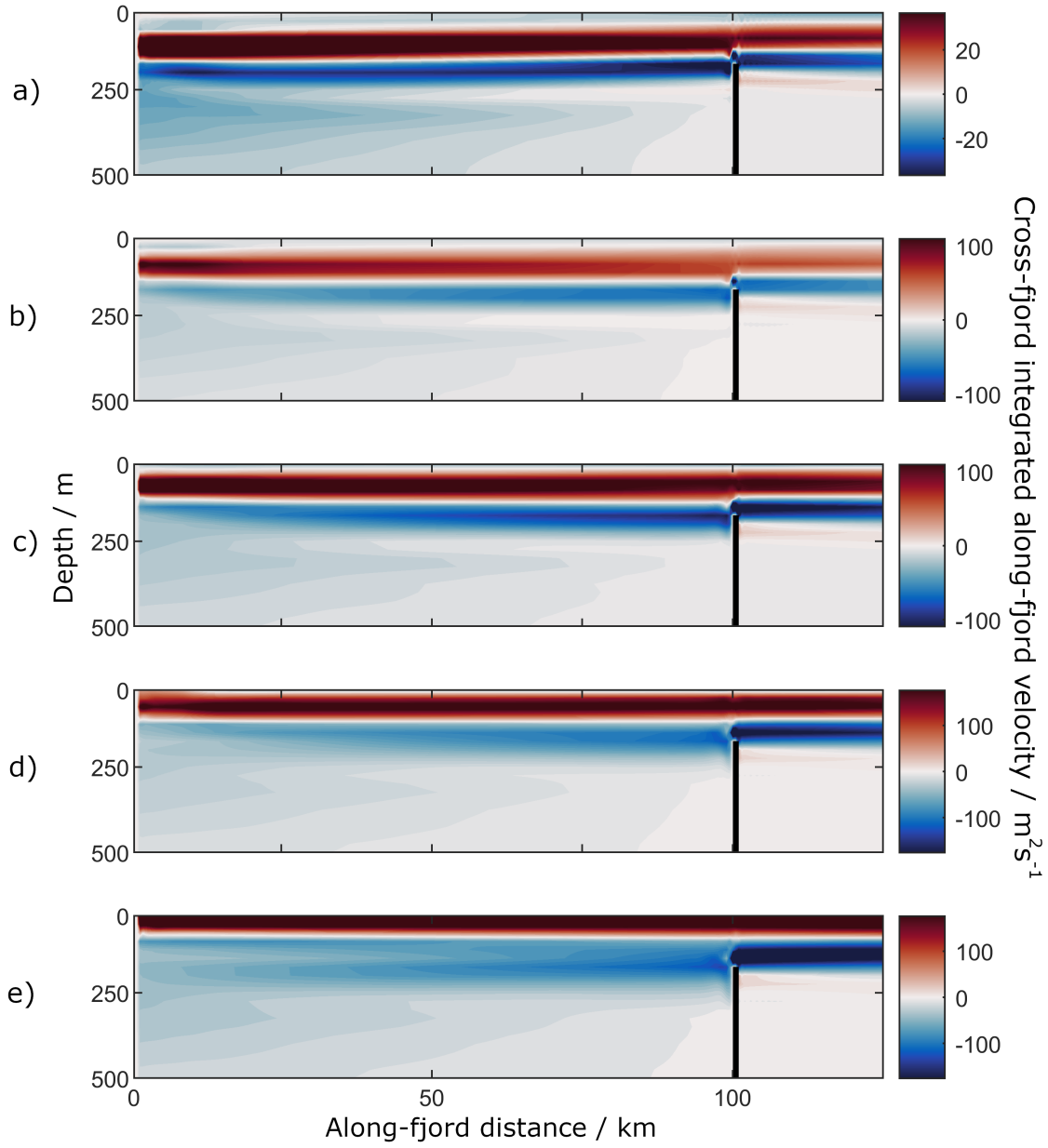

Figure 4.5: 3-month time-mean, cross-fjord integrated along-fjord transport per unit depth (m^2s^{-1}) from MITgcm simulations with fjord width $B = 9\,km$, forced with 'high' subglacial discharge Q_{sg} of a) 150, b) 225, c) 400, d) 750 and e) $1500\,m^3s^{-1}$. The sill is denoted by the black line at $x = 100\,km$. Red denotes flow away from the ice face (at $x = 0\,km$), and blue denotes flow towards the ice face.

and the sill would generate a horizontal pressure gradient between the fjord and the shelf, driving a net flow out onto the shelf.

For higher subglacial discharge ($Q_{sg} = 150 - 1500\,m^3\,s^{-1}$), simulation output suggests that fjord water is replenished at depth by water from the shelf. However, the inflow in the shelf region occurs almost entirely at depths above the top of the

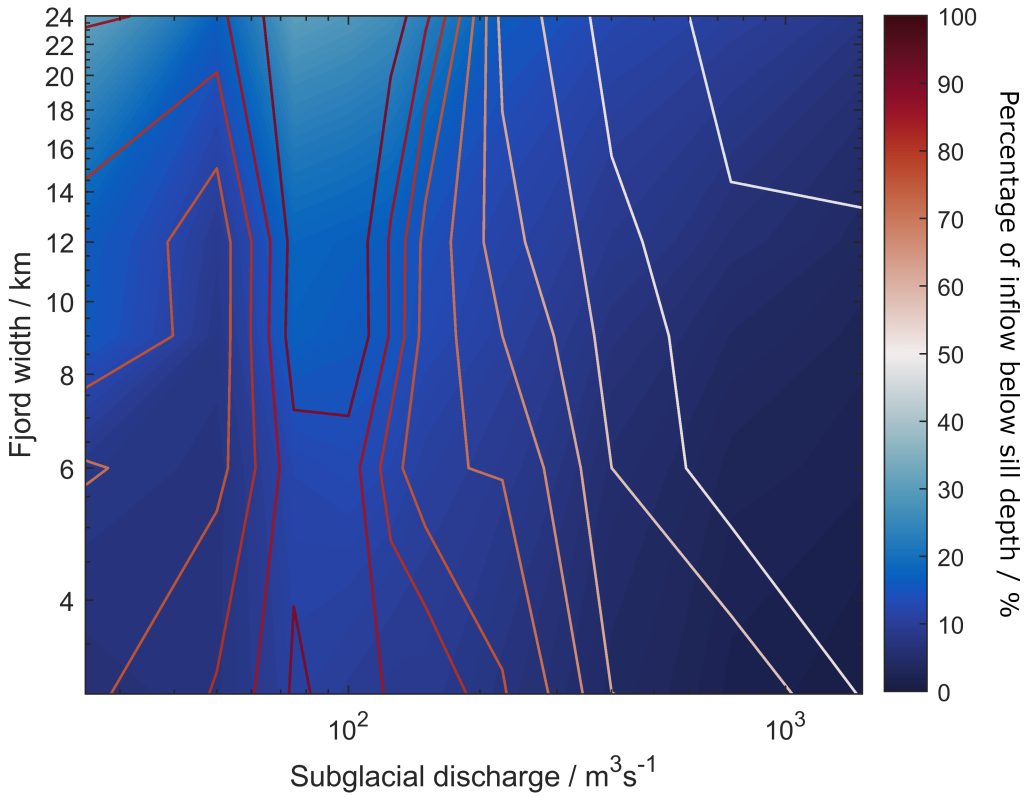

Figure 4.6: Percentage of the total volume flux (%) of the cross-fjord integrated flow towards the ice face occuring below the sill; within the fjord at $x = 90\,\text{km}$ (contour lines), and outside the fjord at $x = 110\,\text{km}$ (filled contour), from MITgcm simulation output over a range of configurations with differing subglacial discharge and fjord widths. Note that both axes are logarithmic.

sill, with very little cross-fjord integrated volume flux into the fjord originating below sill depth. Figure 4.6 shows the percentage of the total cross-fjord integrated flow towards the ice face which occurs below sill depth, both within the fjord and on the shelf, over the range of fjord width and subglacial discharge considered here. This percentage P is calculated via

$$P(x) = 100\% \times \int_{-B/2}^{B/2} \int_{0}^{h_S} u(x,y,z)\theta(-u)\,\mathrm{d}z\mathrm{d}y \Big/ \int_{-B/2}^{B/2} \int_{0}^{D} u(x,y,z)\theta(-u)\,\mathrm{d}z\mathrm{d}y \quad (4.1)$$

where here z increases upwards from the fjord bottom at $z = 0$, h_S is the height of the sill, D is the total fjord depth and θ is a Heaviside step function filter such that only inflow with $u < 0$ contributes to the integrals. We evaluate $P(x)$

at two along-fjord locations; within the fjord at $x = 90\,\mathrm{km}$, and on the other side of the sill at $x = 110\,\mathrm{km}$.

It can be seen that within the fjord, at least half of the flow towards the ice face occurs below sill depth across this range of parameter space. For the shelf flow, this value is no higher than 20% and is under 10% over most of the parameter space. As the subglacial discharge increases, the clearance of the plume outflow increases over the sill. This results in an increase in the percentage of total inflow occurring above sill depth (and therefore a decrease below sill depth) within the fjord with subglacial discharge, as shown by the contour line overlay in Figure 4.6. This increase with subglacial discharge is not seen on the shelf outside (Figure 4.6, colour background). For the purposes of a box-model parameterization scheme, this means that the heat and salt fluxes into the fjord are determined primarily by the ocean stratification above sill depth, rather than their values over the full depth on the shelf. This has implications for the time evolution of the stratification within the fjord and, by extension, the melt rates across the ice face. We discuss this further in §4.4.2.

Figure 4.7 shows the along-fjord velocity over the sill from MITgcm simulation output for several combinations of fjord width ($B = 3,\ 12,\ 24\,\mathrm{km}$) and subglacial discharge ($Q_{sg} = 50,\ 400,\ 750$ and $1500\,\mathrm{m^3 s^{-1}}$). As before, the horizontal shear increases as fjord width increases. For fjord widths larger than 9 km, and subglacial discharge larger than $100\,\mathrm{m^3 s^{-1}}$, the flow over the sill is horizontally sheared at all depths, with outflow on the left-hand wall looking into the fjords. These correspond to cases where the outflow is connected along the entire length of the domain (as in panels 3, 4 and 5 in Figure 4.4 and all panels in Figure 4.5). For subglacial discharge lower than $100\,\mathrm{m^3\,s^{-1}}$, the flow structure over the sill displays a more complex structure. The peak outflow occurs on the right-hand wall (looking into the fjord) and the spatial pattern of inflow and outflow is less regularly structured, with both boundaries displaying two flow reversals with depth.

Figure 4.8 shows a metric for the ratio of vertical to horizontal exchange flow over the sill (with larger numbers indicating increased vertical shear). We calculate the vertical exchange flow by first horizontally integrating the along-fjord velocity at a

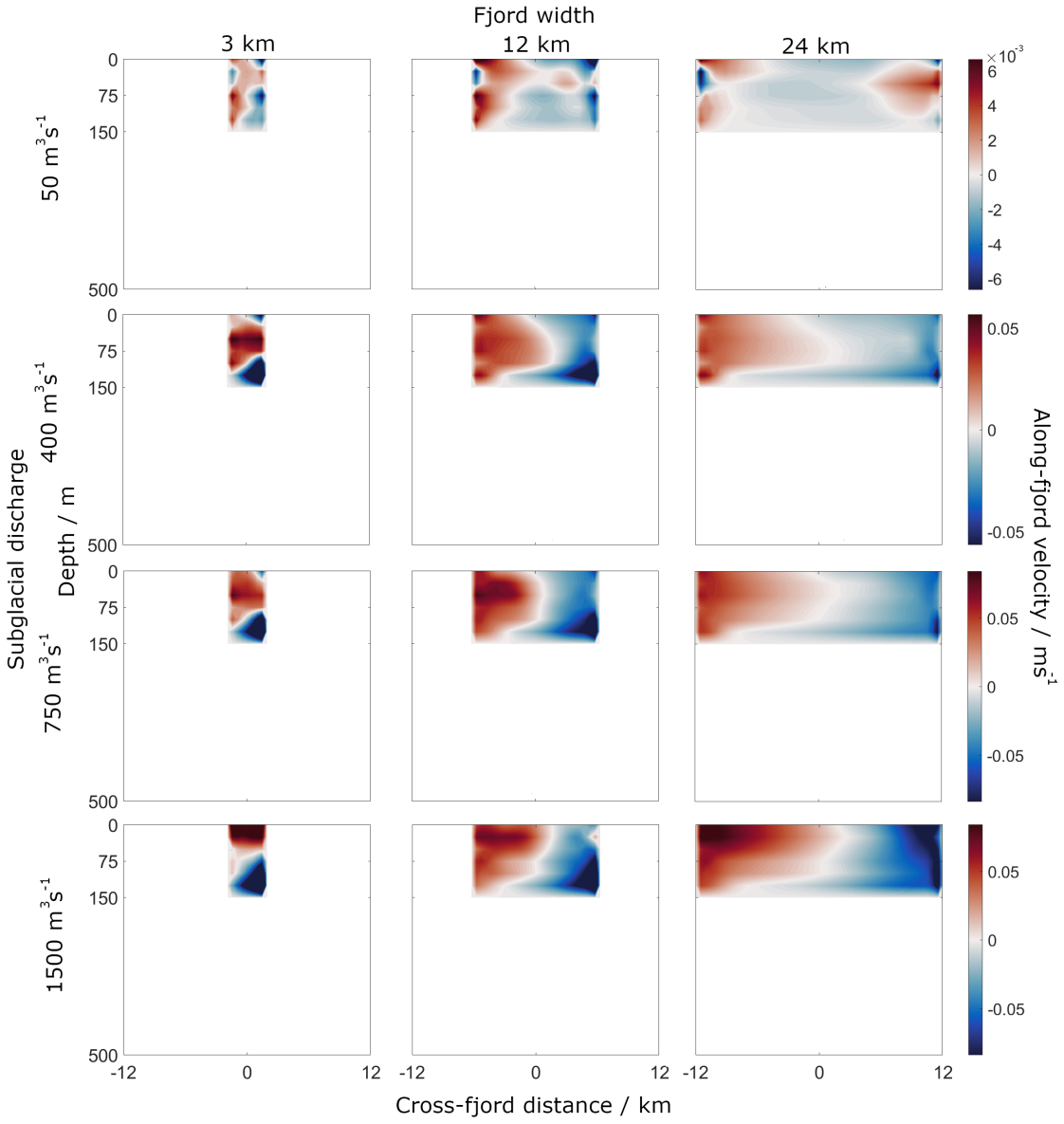

Figure 4.7: 3-month time mean along-fjord velocity (ms^{-1}) over a 150 m deep sill at $x = 100$ km, from MITgcm simulation output for combinations of fjord widths $B = 3,\ 12,\ 24$ km and subglacial discharge fluxes $Q_{sg} = 50,\ 400,\ 750,\ 1500\,\mathrm{m}^3\mathrm{s}^{-1}$. Red denotes flow away from the ice face at $x = 0$ km, and blue denotes flow towards the ice face.

transect over the sill, then taking the absolute magnitude of the resulting 1D profile and integrating again to find the total vertical exchange flux, then taking the ratio of the vertical flux to the horizontal flux for each simulation. The horizontal exchange flux is found via a similar procedure with the order of vertical and horizontal integration reversed. It can be seen that the flow over the sill is increasingly

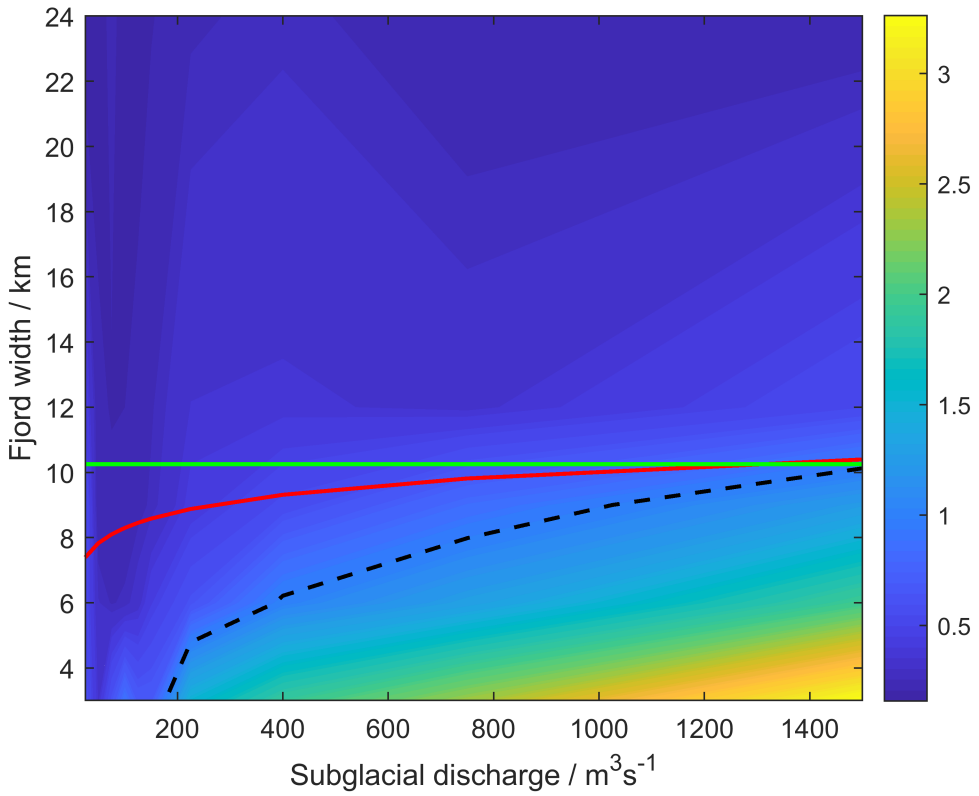

Figure 4.8: *Contour:* Metric showing the ratio of the total vertical exchange volume flux to the total horizontal exchange flux over the sill as a function of fjord width and subglacial discharge for a shallow (150 m deep) sill. The metric is calculated using a method described in the text. Values greater than 1 indicate a more vertical shear, where less than 1 indicates a more horizontal shear. Equal horizontal and vertical shear is indicated by the dashed line. *Red line:* Estimate of the Rossby radius of deformation using $R_d = (g' Q_{out}/f^3)^{1/4}$, where Q_{out} is the total outflow volume flux using the sum of Equation 2.7 and Equation 2.9 and $g' = g(\partial\rho/\partial z)(D - h_S)/\bar{\rho}$. *Green line:* Estimate of the Rossby radius of deformation using $R_d = N(D - h_S)/f$, where N is the depth-averaged buoyancy frequency above the sill.

vertically sheared with decreasing fjord width, given sufficient subglacial discharge for the estuarine outflow to flow over the sill ($Q_{sg} > 150\,\mathrm{m^3\,s^{-1}}$). Plotting two estimates for the Rossby radius of deformation R_d suggests that the flow is (broadly) more vertically sheared for widths less than R_d, and more horizontally sheared where $B > R_d$. The first estimate of the deformation radius uses $R_d = (g' Q_{out}/f^3)^{1/4}$, where Q_{out} is the total outflow volume flux using Equation 2.7 and Equation 2.9 and $g' = g(\partial\rho/\partial z)(D - h_S)/\bar{\rho}$, with $\partial\rho/\partial z$ taken over the upper 150 m in the initial stratification (Figure 4.8, red line). The second estimate uses $R_d = N(D - h_S)/f$,

where N is the depth-averaged buoyancy frequency above the sill. This provides a first-order method to estimate the horizontal versus vertical structure over the sill.

Close to the sill within the fjord, the flow structure is remarkably consistent across the range of fjord width and subglacial discharge considered in this study. Figure 4.9 shows the along-fjord velocity as a function of depth and cross-fjord location at a transect 10 km from the sill at $x = 90$ km. The spatial pattern of inflow and outflow is that of a checkerboard, with strong outflow in upper layers on the left-hand boundary (looking into the fjord), strong inflow on the right-hand boundary, and a weaker reversal at depth, potentially geostrophically driven due to isopycnal gradients. This pattern breaks down near to the surface in narrow fjords, where the outflow remains connected to both sidewalls over the range of subglacial discharge for which the sill does not block the outflow (i.e. $Q_{sg} \gtrsim 100\,\mathrm{m^3\,s^{-1}}$). As subglacial discharge increases, the peak outflow moves towards the surface as the plume intrudes higher into the stratification, such that there is increased vertical shear. As fjord width increases, the regions of peak inflow velocity also move towards the surface with increasing subglacial discharge. Interestingly, plume-driven outflow seems to occur over almost exactly half of the total fjord depth for all but the narrowest fjords. This is in contrast to the structure seen in both simulations of fjords without sills (e.g. Figure 2.4) and in the cross-fjord integrated structure in simulation output of silled fjords (Figure 4.5), where the outflow occurs over a much narrower range of depths in the stratified upper layer.

Beyond the sill at $x = 110$ km, Figure 4.10 shows that the observed flow structures display different behaviour over the range of subglacial discharge considered here. Where the plume outflow in Figure 4.4 and Figure 4.5 is connected along the entire length of the domain, the flow in the shelf region occurs primarily above sill depth, with the outflow displaying a boundary current structure. Again, for narrow fjords the velocity structure is more vertically sheared, where fjords with widths $B \gtrsim R_d \sim 10$ km display horizontally sheared exchange, with inflow on the right-hand boundary looking into the fjord. Where the sill blocks the outflow (for low subglacial discharge, $Q_{sg} \lesssim 100\,\mathrm{m^3\,s^{-1}}$), the flow on the shelf is very different in

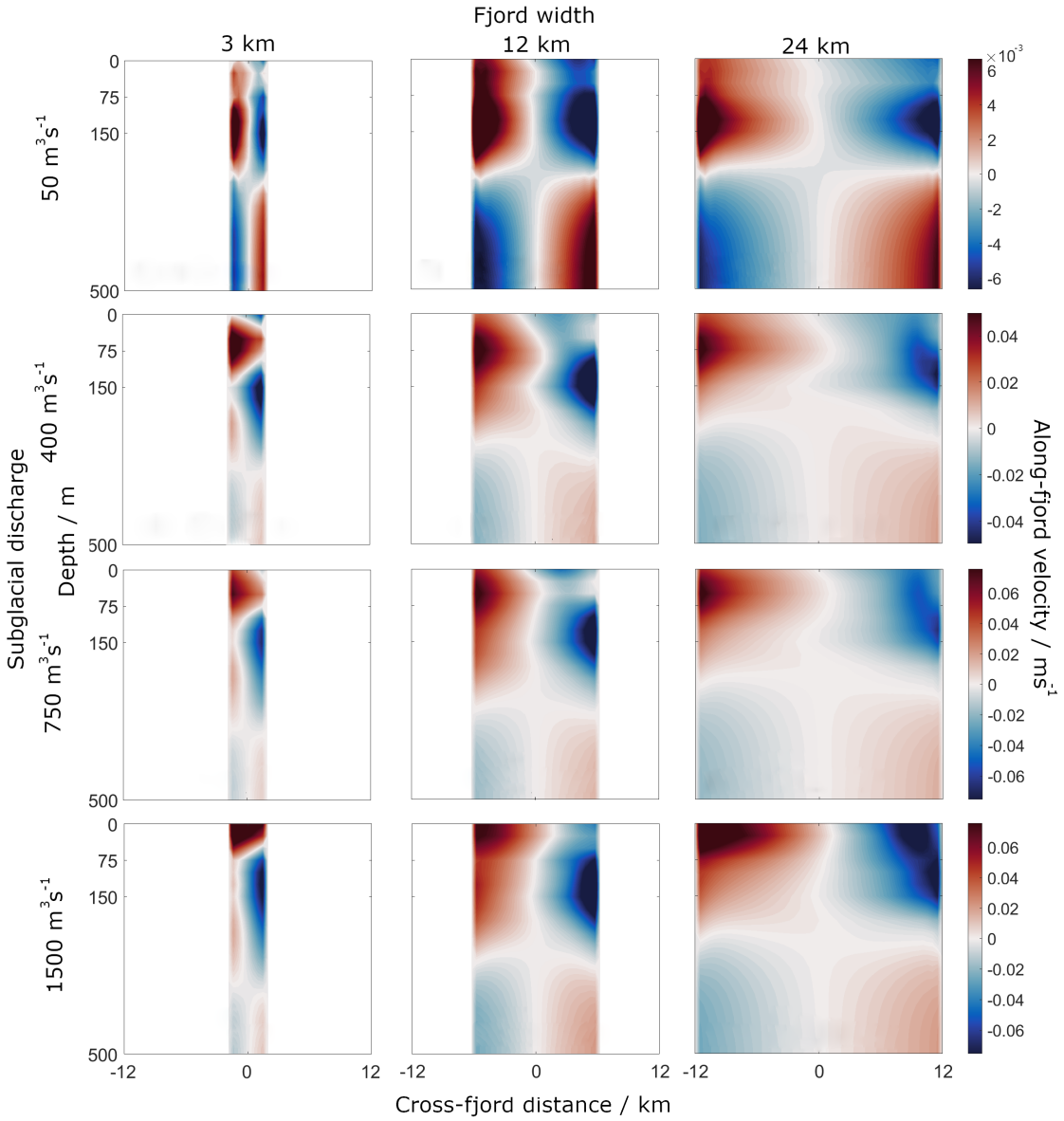

Figure 4.9: 3-month time mean along-fjord velocity (ms^{-1}) in the fjord at $x = 90\,\mathrm{km}$, from MITgcm simulation outputs for combinations of fjord widths $B = 3,\ 12,\ 24\,\mathrm{km}$ and subglacial discharge fluxes $Q_{sg} = 50,\ 400,\ 750,\ 1500\,\mathrm{m}^3\mathrm{s}^{-1}$. Red denotes flow away from the ice face at $x = 0\,\mathrm{km}$, and blue denotes flow towards the ice face.

structure. Again, in this regime, the outflow occurs on the right-hand boundary, with inflow on the left, and the flow structure is less easily interpretable. Some grid-scale structure is observable in the along-fjord flow beyond the sill, for each fjord width. These structures are consistent over time, however, suggesting that they are not the result of numerical instability. Further investigation of the flow in this regime is necessary to understand these structures.

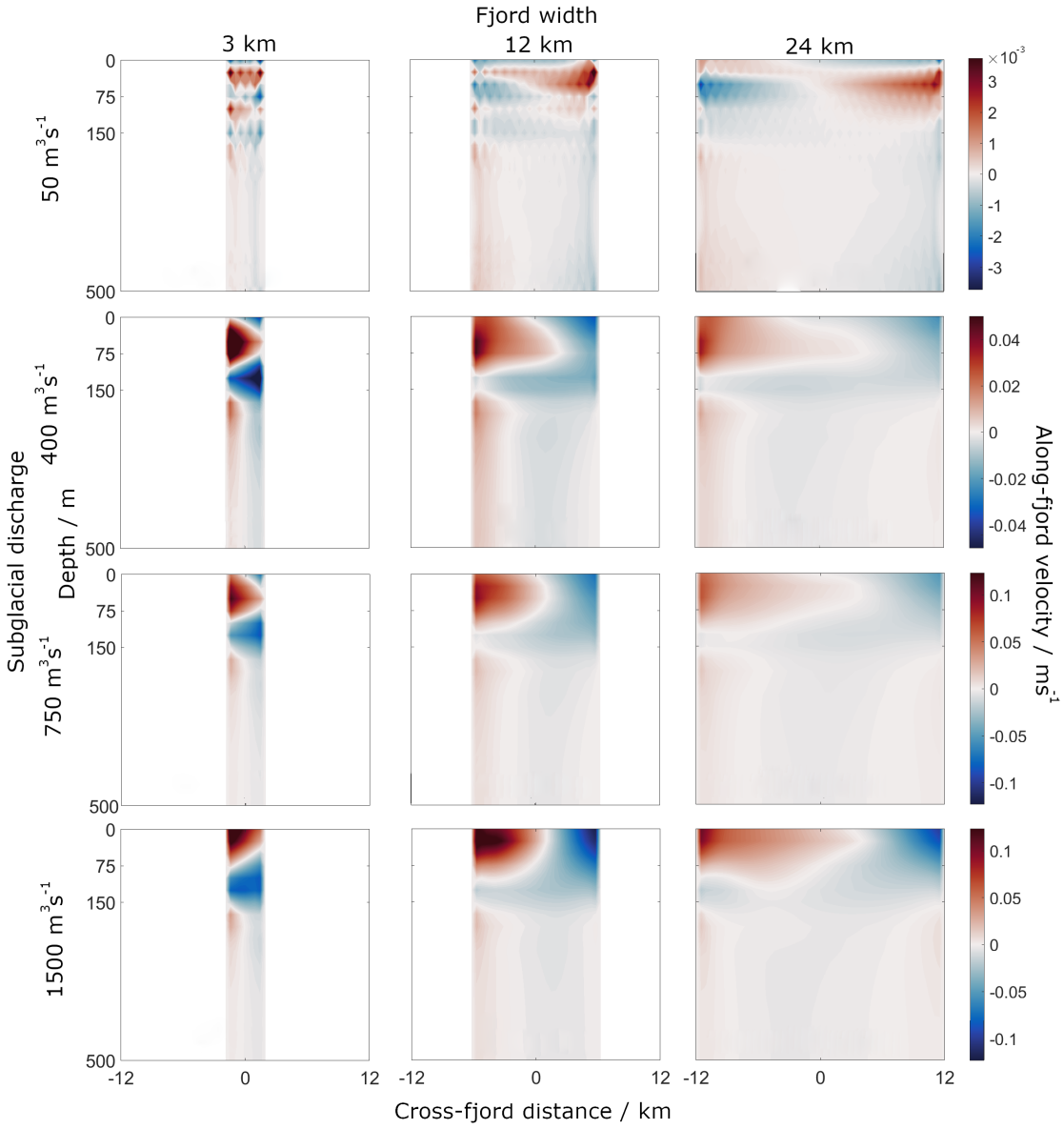

Figure 4.10: 3-month time-mean, along-fjord velocity (ms^{-1}) in the shelf region at $x = 110\,\mathrm{km}$, from MITgcm simulation output for combinations of fjord widths $B = 3,\ 12,\ 24\,\mathrm{km}$ and subglacial discharge fluxes $Q_{sg} = 50,\ 400,\ 750,\ 1500\,\mathrm{m}^3\mathrm{s}^{-1}$. Red denotes flow away from the ice face at $x = 0\,\mathrm{km}$, and blue denotes flow towards the ice face.

4.3.2.2 Salinity

Given that water below sill depth within the fjord is replenished by inflow over the sill, it is important to characterize the properties of the inflowing water. In particular, the density stratification within the fjord is strongly controlled by the salinity, in turn impacting the dynamics of the subglacial discharge plume, velocity

structure, and the melt rate across the ice face. The velocity structures shown in §4.3.2.1 suggest that inflow from the shelf region into the fjord originates entirely above sill depth. To test this, we calculate the percentage difference between the mean salinity of the inflow over the sill in steady state, to the mean salinity over the same inflowing depth and width ranges in the far field.

This difference is calculated by first forming a mask M for inflow grid cells over the sill at $x = 100\,\text{km}$ using the along-fjord velocities (as a function of depth and cross-fjord distance) from MITgcm simulation output, for each combination of subglacial discharge and fjord width. Grid cells with along-fjord velocity $u < 0$ correspond to $M = 1$, and grid cells with $u \geq 0$ to $M = 0$. Then, we compute the mean salinity in grid cells with $M = 1$ using the steady-state salinity in each grid cell over the sill, as well as the far-field (or equivalently the initial) salinity. The percentage difference between these two mean salinities is at most 0.11%. In contrast, the mean salinity of water below sill depth differs from the mean salinity above sill depth by $\mathcal{O}(10\%)$, thus, if inflow into the fjord was originating below sill depth we would expect to see far larger differences in salinity, by up to two orders of magnitude. This supports the hypothesis that the salinity of the inflow into the fjord is determined above sill depth, also supported by investigation of the velocity structure in §4.3.2.1.

As a consequence, the water in the fjord below sill depth is replenished by water with lower salinity than the initial (or far-field) salinity below sill depth. This suggests that the salinity at depth within the fjord should decrease over time. Figure 4.11 shows the difference between the mean salinity below sill depth within the fjord 6 months after model initialization and the initial mean value below sill depth. Across the range of fjord widths and subglacial discharge considered here, the mean salinity decreases within the fjord below sill depth, as expected. For low subglacial discharge, it can be seen that the mean salinity changes relatively little for all fjord widths. This corresponds to a range of subglacial discharge flux where the plume outflow is not able to rise over the sill and forms a (near) closed

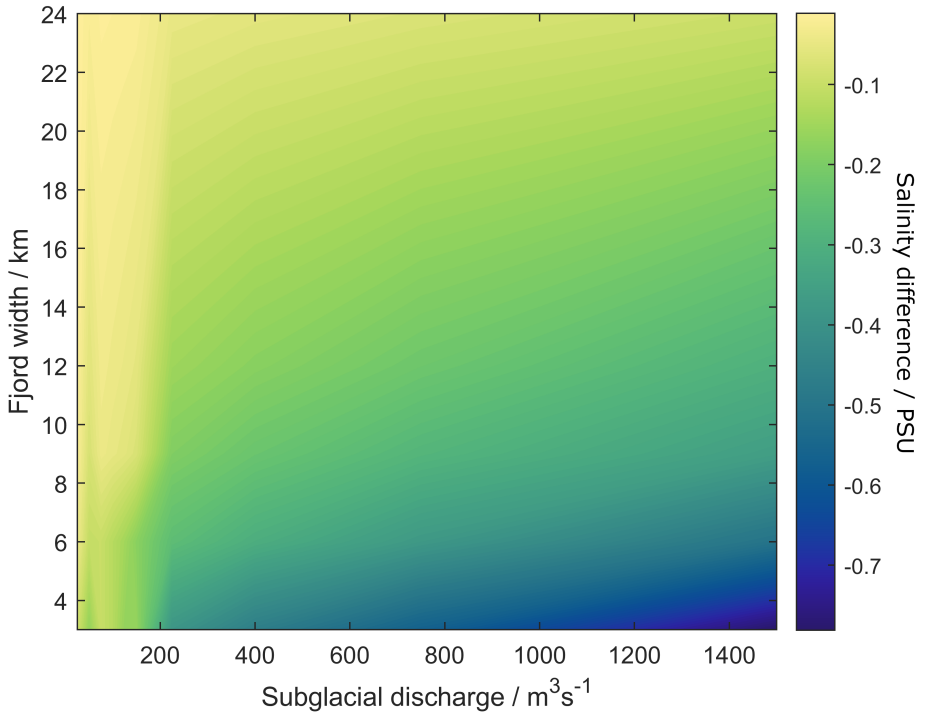

Figure 4.11: Mean difference in salinity (PSU) below sill depth within the fjord between model initialization and steady-state conditions after 6 months model time, from MITgcm simulation output. Negative values indicate a mean freshening below sill depth, consistent with replenishment via shelf waters from above sill depth.

overturning cell. As a result, there is little inflow from the shelf region which is able to modify the salinity at depth within the fjord.

4.4 Implications for parameterization of fjord circulation

Overall, the MITgcm simulations reveal that the presence of a bathymetric sill adds significant complication to the flow structure and exchange fluxes of heat and salt between the fjord and the wider ocean, with implications for melt rates at the ice face, and glacier and ice sheet stability as a whole. We have seen that there is large asymmetry in the flow structure on either side of the sill for sills with crests that sit near to the natural outflow depth of the plume. This is visible in both contour plots of along-fjord velocity taken at transects at along-fjord locations on either side of the sill (Figure 4.9, Figure 4.10), and in the variation of cross-fjord

integrated transport along the length of the fjord (Figure 4.4, Figure 4.5). For low subglacial discharge, the natural depth range of the outflow layer at the ice face encompasses the depth of the sill crest. In these cases, little of the exchange flux set up by the plume at the ice face continues over the sill, and a near-closed overturning cell is set up within the fjord.

In both shallow and deep sill cases, the MITgcm results suggest that sills can cause blocking of inflow from below sill depth in the shelf region. However, this blocking alone is not sufficient to impact the stratification within the fjord, or melt rates at the ice face. Instead, the difference between the sill depth and the depth of the lower layer in the far-field ocean stratification determines the extent to which this blocking is important. The constriction on the flow imparted by the sill leads to an acceleration of the inflow in a boundary layer over the sill. Provided that this accelerated inflow layer remains within the lower, unstratified section of the far-field ocean stratification, then the sill seems to have negligible impact. This is because the waters flowing in over the sill still approximately match the properties of waters at depth behind the sill in the fjord.

Figure 4.12 shows the depth at which cross-fjord integrated peak outflow over the sill occurs across the range of subglacial discharge and fjord widths, for both sill depths, from MITgcm simulation output. The outflow depth scaling Equation 2.15 works reasonably well, except where the predicted plume outflow depth is close to sill depth. To very first order, the minimum observed inflow layer thickness over the sill is comparable in magnitude to that of the outflow layer, for which we have a scaling Equation 2.16, although there is little physical justification as to why the lower layer should follow this scaling. Note that examination of the corresponding metric outside of the fjord shows that the outflow depth in each simulation remains the same throughout the region outside of the sill, and is identical to the peak outflow depth over the sill. For the purposes of a parameterization scheme, this suggests that the appropriate outflow depth provided by a parameterization to the ocean component of an Earth system model is the outflow depth over the sill.

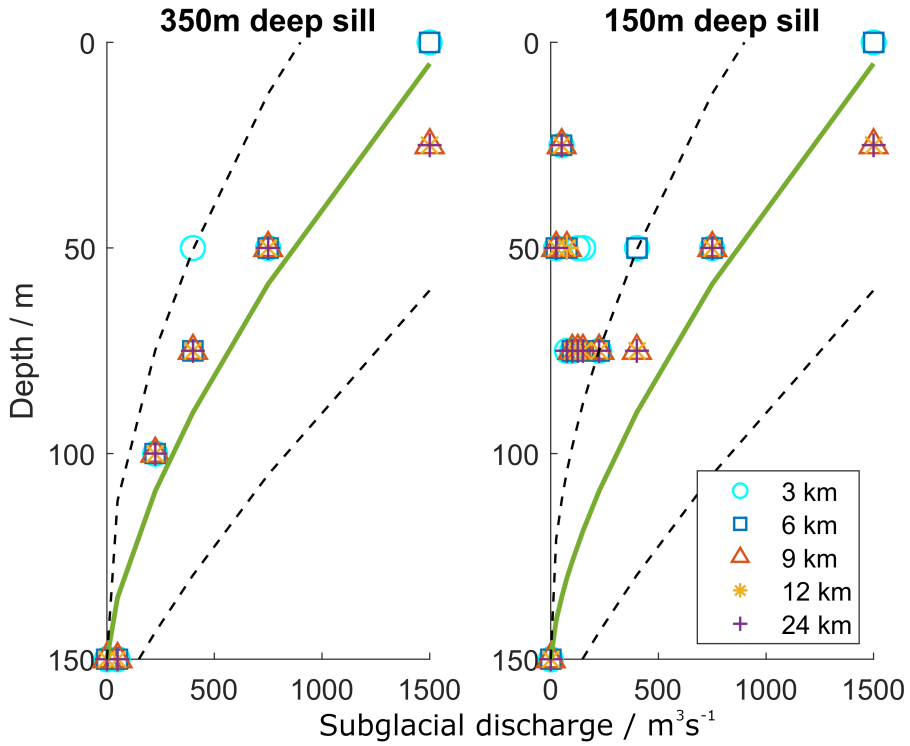

Figure 4.12: Depth at which the peak cross-fjord-integrated outflow occurs over the sill for a range of subglacial discharge and fjord widths, from MITgcm simulation output. *Left:* Peak outflow depths from MITgcm simulations with a 350 m deep sill. *Right:* Peak outflow depth from MITgcm simulations with a shallow 150 m deep sill. In both panels the green line shows the expected peak outflow depth for a fjord with no sill, using the scaling of Equation 2.15. Note that in many cases markers denoting different fjord widths overlap. Dashed lines show the outflow layer thickness using the scaling of Equation 2.16.

A further commonality between the deep and shallow sill cases is the complexity of the along-fjord velocity structure taken at transects close to the sill. Whilst this complexity is increased for the shallow sill case, the flow structure is fundamentally three dimensional in all cases, adding significant complication to efforts to characterize the full flow structure simply. Some of the complexity in the flow may be due to the choice of a vertical wall with little along-fjord extent as the bathymetric form of the sill in each case. Typically, theoretical studies of multi-layer exchange flow over sills using reduced gravity hydraulic models (see §1.2.2.2) are restricted to cases where the bathymetry varies slowly in the along-channel direction relative to the Rossby radius of deformation, such that cross-channel velocities can be assumed to be negligible. This assumption of slow along-channel

variations in the bathymetry may or may not apply to individual Greenlandic sills, however, given that the mechanism by which sills typically form (the deposition of debris at the furthest historical extent of the glacier) should be independent of the local value of the Coriolis parameter.

These results suggest that sills can have a significant impact on the exchange flux between fjords and the wider ocean in an estuarine circulation regime driven by subglacial discharge. As such, it is of critical importance to characterize and capture the relationship between several key length scales, the strength of the subglacial discharge forcing, and the stratification, to represent the impact of sills in a sub-grid scale parameterization scheme. These length scales are; the fjord width, the natural level of neutral buoyancy or plume outflow depth and the thickness of the plume outflow layer (both of which are dependent on the strength of the stratification in the upper layer), the outflow layer depth and thickness downstream of the sill, the thicknesses of the unstratified lower layer and the stratified upper layer, the thickness of the layer of accelerated inflow over the sill crest (as seen in the deep sill case), and the depth of the sill crest itself. In the next section, we discuss a potential theoretical framework which could be used to build a prediction of these key length scales, although the full solution is beyond the scope of this thesis.

4.4.1 Hydraulic model

As discussed in §1.2.2.2, multi-layer exchange flows over bathymetric sills are ubiquitous in the ocean. Hydraulic models, based on the shallow water equations, have found great utility in characterizing and understanding these sorts of flows, across a range of physical settings. Flows with a single active layer are particularly well studied. The addition of further layers adds complication, both conceptually and algebraically. The addition of the effects of rotation further increases the complexity of hydraulic models, by allowing for cross-channel as well as along-channel variations in the flow.

In our case, the flow structures exhibited in our MITgcm simulation outputs suggest that a minimum number of 3 layers are required for a hydraulic model to

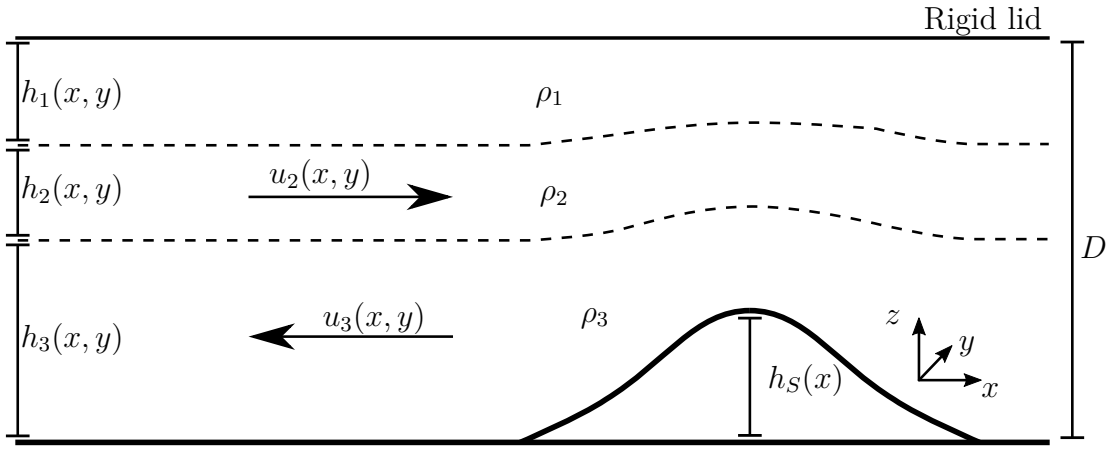

Figure 4.13: Schematic diagram of three layer exchange flow over a sill under the rigid lid assumption. The surface layer is assumed to have zero volume flux, with the middle layer outflowing and the bottom layer inflowing, as in plume-driven estuarine circulation. Note that there is also cross-fjord variation in the layer thicknesses, leading to multiple flow configurations over the sill (see Figure A4.1 in the Appendix).

capture the flow structure, with a surface layer of zero net volume flux overlying a middle outflow layer and a bottom inflow layer, with volume fluxes set by plume dynamics at the ice face (see Figure 4.13). This itself neglects the potentially significant vertical structure in the bottom inflow layer, both in terms of the velocity profile and the stratification. Furthermore, the significant cross-fjord structure in our simulation outputs suggests that any hydraulic model intended to capture the leading order impact of a bathymetric sill must include Coriolis effects. For sufficiently high subglacial discharge flux, the plume penetrates through the stratified surface layer and outflows at the ocean surface. In this case, the flow may be considered to consist of two layers. Application of two-layer hydraulic models to the estuarine circulation over the sill (e.g. Dalziel 1991) may therefore provide a reasonable prediction of the flow over a limited range of parameter space. Investigation of the applicability of two-layer hydraulic models is left for future work.

As an initial investigation, we build a three-layer hydraulic model including rotation, which we summarise here (further details of the calculation can be found in Appendix A4.1). We assume a rectangular cross-section of the channel and a rigid lid, such that the maximum channel depth $D = h_1(x,y) + h_2(x,y) + h_3(x,y) + h_S(x)$,

with x the along-fjord coordinate, y the cross-fjord coordinate, h_i the thickness of layer i, and the bathymetry $h_S(x)$ describes the sill depth and location (Figure 4.13). The Bernoulli functions in each layer are conserved along the length of the fjord and over the sill (see Appendix, Equation A4.1–Equation A4.3). Taking the difference between the Bernoulli function in consecutive layers yields two expressions:

$$B_{12} = \frac{1}{2}\left(u_1^2 - u_2^2\right) - g_1'(h_2 + h_3 + h_S), \tag{4.2}$$

$$B_{23} = \frac{1}{2}\left(u_2^2 - u_3^2\right) - g_2'(h_3 + h_S). \tag{4.3}$$

where $g_i' = g(\rho_{i+1} - \rho_i)/\bar{\rho}$ are reduced gravities across layer interfaces and $\bar{\rho}$ is the Boussinesq reference density. These expressions should allow the tracing of solutions from a known state in the fjord, as set by the plume dynamics, to a state over the sill.

In multi-layer flows, the flow has several possible configurations over the sill with regards to permutations of the intersection of each layer interface with the sidewalls, the bathymetry, the surface, and the other layer interface. For two-layer flows where there is one layer interface (e.g. Timmermans et al. 2005), there are three possible configurations which must be treated individually; the layer interface intersects either both sidewalls, intersects one sidewall and either the surface or the bathymetry, or intersects neither sidewall. In our three-layer case, solving for all possible flow configurations over the sill adds ten or more combinations of intersections. Solving the problem generally for all flow conditions over the sill is therefore well beyond the scope of this thesis.

As an initial investigation, we briefly discuss only the case where both layer interfaces intersect the sidewalls (see Appendix, Figure A4.1). Assuming that the along-fjord flow in each layer is geostrophic (Equation A4.6, Equation A4.7 and Equation A4.8), and assuming that the potential vorticity in each layer is zero (Equation A4.11), and that the volume flux in each layer is constant along the length of the channel, yields further expressions relating the layer thicknesses and velocities to known conditions, again as set by plume dynamics. The volume flux in each layer is:

$$Q_i = \int_{-\frac{B}{2}}^{\frac{B}{2}} u_i h_i \, \mathrm{d}y. \tag{4.4}$$

We set the volume flux in the surface layer $Q_1 = 0$. The volume fluxes in layers 2 and 3 are driven by the plume at the ice face, such that $Q_2 = -Q_3 - Q_{sg} \approx Q$. In principal, we now have a set of 6 equations (Equation 4.2, Equation 4.3, Equation 4.4 and the rigid lid condition $D = h_1 + h_2 + h_3 + h_S$) in 6 unknowns (three u_i's and three h_i's). The upstream conditions set by the plume dynamics provide the values of Q, B_{12} and B_{23}. Solving these equations numerically, however, has not yielded meaningful results. Taking parameter values for Q, B_{12} and B_{23} for non-zero rotation produces solutions with negative layer thicknesses and along-fjord velocities which are several orders of magnitude too large.

Possibly, the flow structure over the sill does not have a solution with both layer interfaces intersecting the sidewalls only, but instead enters one of the other regimes with layer interfaces outcropping at the surface or intersecting the bathymetry. Indeed, we have seen that almost all contour plots of the along-fjord flow over the sill from MITgcm simulation reveal significant horizontal shear, corresponding to the intersection of layer interfaces with the top and bottom boundaries rather than the fjord sidewalls. Furthermore, solution of the full problem following the functional approach of Gill (1977) quickly yields expressions which are extremely algebraically involved, to the point that they are not practically useful.

It is possible that this approach is not readily applicable to silled fjords, given the strong constraint that the layers are immiscible, and the fact that the fjord forms a finite, closed channel rather than an infinite basin or reservoir. In particular, we have seen from MITgcm simulation output that the flow in the shelf region is potentially best described as 4-layer, with inflow above sill depth which fills the fjord below sill depth, and stagnant water on the shelf below sill depth. This contrasts with the 3-layer structure within the fjord. Furthermore, this hydraulic model allows no change to the density in the lower layer, such that the freshening within the fjord below sill depth observed as a result of the inflow structure on the

shelf cannot be captured, although some quasi-steady treatment could allow this effect to be included in a numerical scheme or parameterization.

4.4.2 Submarine melt rates

As previously discussed, the presence of a sill restricts inflow in the shelf region to occur above sill depth, over the range of subglacial discharge for which the plume-driven estuarine circulation is able to outflow over the sill. As a result, the water which replenishes the region below sill depth within the fjord has properties which correspond to those above sill depth outside of the fjord, rather than below sill depth. This has implications for the heat content within proglacial fjords, and thus the melt rates at glacial termini. MITgcm simulation output suggests that deep sills, which do not restrict the inflow of deep water from the far-field into the fjord, have little impact on the melt rates. We therefore restrict our attention to MITgcm simulation output for the shallow sill cases. The change in salinity and temperature below sill depth discussed in § 4.3.2.2 suggests that initialising a model of a fjord with a shallow sill with the same stratification as the ambient ocean is physically unrealistic. However, this section is intended to investigate the melt rate in a fjord with a shallow sill, relative to the melt rate in an otherwise geometrically identical fjord without a sill. As such, we investigate the melt rate in the fjord after a 6-month spin-up period, to allow the fjord stratification in salinity and temperature below sill depth to reach a more realistic profile.

Figure 4.14(a) shows the spatial mean in-situ temperature difference below sill depth within the fjord ($x = 0-100\,\mathrm{km}$), between fjords with a shallow 150m-deep sill and fjords with no sill, at the end of a 6-month simulation in MITgcm. Overall, there is a relative cooling of water below sill depth for fjords with a shallow sill, consistent with the cooler waters above sill depth in the far-field stratification assumed here (see Figure 2.2). This cooling is most pronounced for narrow fjords, consistent with their smaller total volume below sill depth and thus faster flushing timescales. Interestingly, there seems to be only small variation with subglacial discharge above $Q_{sg} \sim 200\,\mathrm{m^3 s^{-1}}$, where the plume is able to outflow over the sill. Below this

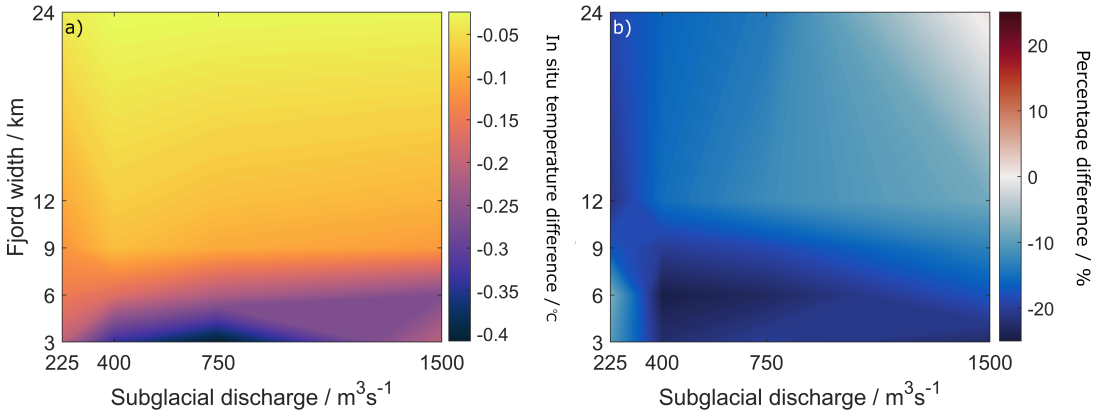

Figure 4.14: a) Spatial-mean temperature difference below sill depth (°C) between fjords with shallow (150 m deep) sills and fjords with no sill over a range of subglacial discharge and fjord width, after 6 months.
b) Percentage difference in the total melt rate at the ice face between fjords with shallow (150 m deep) sills and fjords with no sill over a range of subglacial discharge and fjord width. Melt rates are from MITgcm simulation output, averaged over 5.5 months after a 2-week spin-up period.

subglacial discharge, where inflow from the far-field does not replenish water below sill depth (not shown), there is a small decrease in the mean temperature $\mathcal{O}(0.05\,°\mathrm{C})$. It may be expected that an overall cooling occurs as a result of the heat lost in order to melt ice at the glacial terminus and the injection of subglacial discharge.

The scaling for entrainment into the plume in a layer of constant salinity from Chapter 2 (Equation 2.7) gives the rate at which the water below sill depth is replenished by inflow originating above sill depth. This allows an order of magnitude estimate of the expected mean temperature change below sill depth, within the fjord. For subglacial discharge $Q_{sg} \sim 750\,\mathrm{m^3 s^{-1}}$ this yields an inflow volume flux $Q_{in} \sim 1 \times 10^4\,\mathrm{m^3 s^{-1}}$. For a 9 km wide, 100 km long fjord, the total volume of water below a 150 m deep sill $V = 3.15 \times 10^{11}\,\mathrm{m^3}$. This yields a flushing timescale of below-sill water $t_f \sim 400$ days. Over the range of subglacial discharge $Q_{sg} = 25 - 1500\,\mathrm{m^3\,s^{-1}}$, fjords with widths $B = 9 - 24$ km have flushing timescales $t_f = 300 - 1200$ days. The change in mean temperature below sill depth T within the fjord is given by

$$\frac{\partial T}{\partial t} = \frac{Q_{in}}{V}(T_S - T)$$

$$\implies T(t) = (T_0 - T_S)\mathrm{e}^{-Q_{in}/Vt} + T_S \tag{4.5}$$

where T_S is the depth-averaged temperature above sill depth in the far-field and T_0 the initial mean temperature below sill depth and we note that Q_{in} and V are independent of time. After 6 months, we therefore would expect a temperature change of $\Delta T \sim -0.5\,°\mathrm{C}$. This is a factor of around 3 times larger than that seen in MITgcm simulation output for the same parameter values but is of a reasonable order of magnitude.

Figure 4.14(b) shows the percentage difference in the total melt rate at the glacial terminus between fjords with 150 m sills and fjords with no sills from MITgcm simulation output, across a range of subglacial discharge and fjord widths for which the plume-driven-estuarine circulation is able to outflow over the sill. Melt rates are averaged over 5.5 months, 2 weeks after model initialization to neglect initial spin up. It can be seen that across the entire range of parameter space, and consistent with the overall cooling observed in Figure 4.14(a), the total submarine melt rate decreases for the shallow silled fjords relative to fjords with no sill. This decrease in melt rates for silled fjords is consistent with observations of proglacial fjord systems in Greenland (e.g. Jakobsson et al. 2020). Considering only computational simulations of plume-driven melt, Jakobsson et al. (2020) find that melt rates for Ryder Glacier are 15% lower when temperatures at depth in the fjord match those above sill depth beyond the sill, rather than below sill depth beyond the sill. This difference is of a similar order of magnitude to that found in our MITgcm simulations, where we additionally consider melt across the entire ice face.

For wide fjords and high subglacial discharge, the difference in melt rates between silled and sill-less fjords is close to zero. The total volume of water within the fjord increases with increased fjord width. This leads to a smaller change in the mean temperatures, and thus decreased difference in melt rates relative to the no-sill cases. However, the decrease in the difference between the total submarine melt rates with increasing subglacial discharge is interesting, given that this corresponds to a decreased flushing timescale. Potentially, as the plume outflow occurs higher above the sill for increasing subglacial discharge, a larger fraction of the melting

occurs above sill depth, and the total melt rate is therefore relatively unaffected by the change in temperatures below sill depth.

4.4.3 Impact of horizontally sheared exchange over the sill

We now investigate the impact of the horizontally sheared flow which develops over the sill on the heat and salt fluxes into the fjord, from MITgcm simulation output. For a quantity C (where C is either the salinity S or temperature T), we denote vertical averages over z via $[C]$ and horizontal averages over y via $\langle C \rangle$. We define a spatial mean flux at each depth $F_m(C, z) = \langle u \rangle \langle C \rangle$ and an eddy flux at each depth $F_e(C, z) = \langle uC \rangle - \langle u \rangle \langle C \rangle$, where $u(y, z)$ is the baroclinic component of the along-fjord velocity over the sill. The vertical average of F_m and F_e yields a single metric for the spatial mean and eddy fluxes into the fjord, respectively. Note that this is equivalent to taking Reynolds-averaged fluxes at each depth level, with the velocity and salinity or temperature over the sill split into mean and fluctuating components such that $u = \langle u \rangle + u'$ and $C = \langle C \rangle + C'$, where primed quantities are fluctuations from the spatial mean. In this framework, the eddy flux at each depth is equivalently written as $F_e(C, z) = \langle u'C' \rangle$.

As there is a net volume flux resulting from the subglacial discharge and melt at the ice face, taking the full velocity when calculating transports over the sill leads to a mean heat transport which depends on the choice of reference temperature (see e.g. Schauer et al. 2009). Therefore, the baroclinic component of the along-fjord velocity over the sill is determined by subtracting the barotropic velocity over the sill from the total velocity $u_{tot}(y, z)$. This allows for the calculation of the mean and eddy heat fluxes through a vertical plane over the sill, with no net volume transport.

Figure 4.15(a) shows the ratio of eddy to mean fluxes of heat over the sill, from MITgcm simulations of fjords with shallow (150 m) sills, over a range of subglacial discharge and fjord widths. This ratio is calculated by first taking the vertical average of the eddy flux of heat at each depth $[F_e(T, z)]$ and the mean flux of heat at each depth $[F_m(T, z)]$, then taking the logarithm (base 10) of the absolute magnitude of $[F_e(T, z)] / [F_m(T, z)]$. Note that values of this metric larger than 0

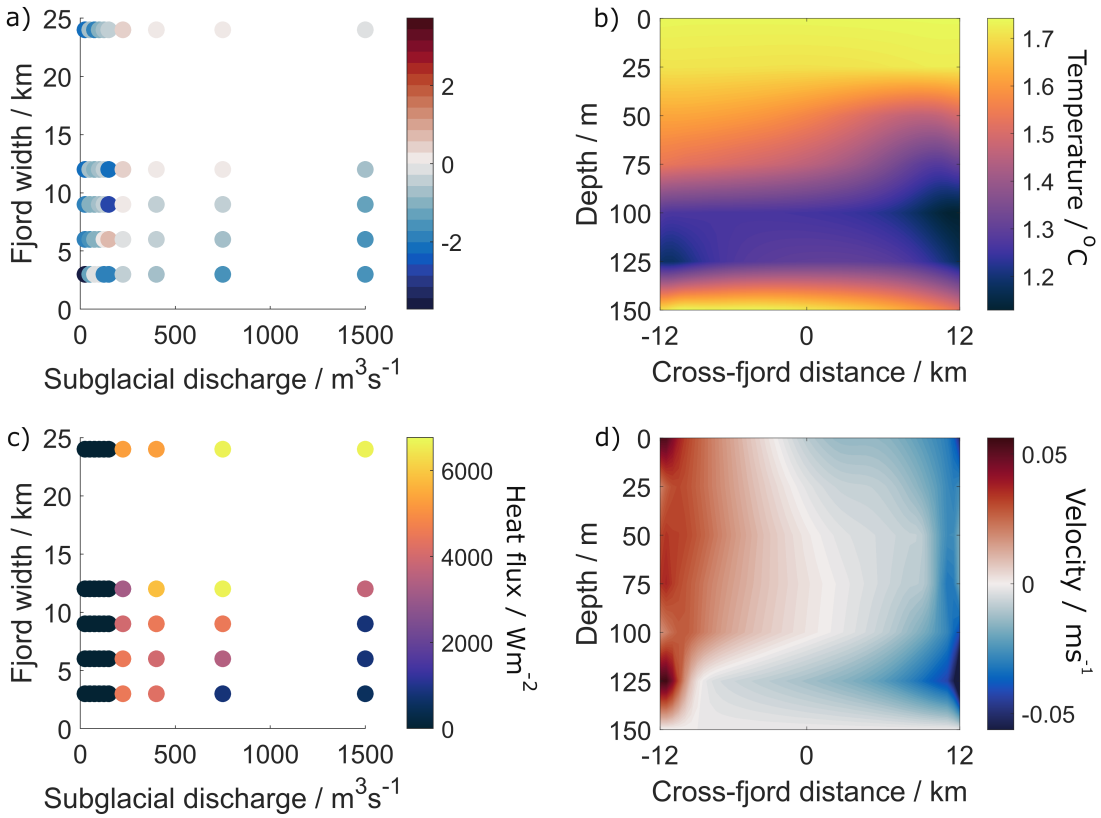

Figure 4.15: a) Logarithm (base 10) of the absolute magnitude of the ratio of the vertically-averaged eddy flux of heat to the vertically-averaged mean flux of heat ($\log_{10}(|[F_e(T,z)]\,/[F_m(T,z)]\,|)$, from MITgcm simulation outputs for fjords with shallow sills, over a range of fjord widths and subglacial discharge fluxes.
b) 3-month time-mean potential temperature as a function of depth and cross-fjord distance over the sill, from an MITgcm simulation of a fjord with width $B = 24\,\mathrm{km}$ driven by subglacial discharge $Q_{sg} = 400\,\mathrm{m^3 s^{-1}}$.
c) Eddy component of the heat flux over the sill ($\mathrm{Wm^{-2}}$), for simulations over a range of fjord widths and subglacial discharge fluxes.
d) 3-month time-mean along-fjord velocity as a function of depth and cross-fjord distance over the sill, from an MITgcm simulation of a fjord with width $B = 24\,\mathrm{km}$ driven by subglacial discharge $Q_{sg} = 400\,\mathrm{m^3 s^{-1}}$. Time-averaging is taken after a 3-month spin up period.

imply that the eddy flux is larger than the mean, and vice versa for values less than 0. For values of subglacial discharge where the plume outflows above sill depth, Figure 4.15(a) suggests that the eddy heat flux remains small for very narrow fjords. Furthermore, this remains the case for high subglacial discharge and all but the widest fjords. This corresponds to outflow having sufficient vertical distance above the sill crest for a significant vertical shear to develop, or the fjord width $B \lesssim R_d$, such that rotational steering and horizontal shear is less significant. For wide fjords and intermediate values of subglacial discharge, the eddy component is similar in magnitude to the mean. For low subglacial discharge, where the plume outflows at or just below the sill crest, the ratio of eddy to mean heat fluxes displays no clear systematic structure, although for some combinations of subglacial discharge and fjord width the eddy flux dominates.

Figure 4.15(b) shows the potential temperature over the (shallow) sill for a fjord with width $B = 24\,\mathrm{km}$ and subglacial discharge $Q_{sg} = 400\,\mathrm{m^3 s^{-1}}$. Moderate cross-fjord variation in temperature can be seen, due to the difference in temperature between the plume outflow and the ambient stratification. For fjords narrower than the deformation radius, the eddy heat flux is more than two orders of magnitude smaller than the mean. For wider fjords, the eddy heat flux increases (Figure 4.15c), becoming similar in magnitude to the mean heat flux as a result of the strong horizontal shear in along-fjord velocity which develops in wide fjords (Figure 4.15d), coupled with the variation in temperature across the fjord (c.f. Figure 4.15b). The total heat flux therefore changes by a factor of $\mathcal{O}(1)$ for fjords with widths $B \gtrsim R_d$ and outflow with small vertical separation above the sill. As such, parameterization of the exchange of heat between the ocean and fjords with shallow sills requires consideration of the cross-fjord structure in both along-fjord velocity and temperature over shallow sills. This increases the complexity required to include the impact of sills into a dynamically based box model of fjord circulation. Note that for low subglacial discharge, both eddy and mean fluxes are small, leading to increased variability in Figure 4.15(a).

For shallow sills, the eddy component of the salt flux into the fjord is larger than the corresponding flux in fjords with deep sills, at the same fjord width and subglacial discharge flux. However, this component remains an order of magnitude smaller than the mean flux across all fjord widths and subglacial discharge volume fluxes, ranging from 1-10% of the mean flux (from additional analysis not plotted here). This is consistent with our assumption that the level of neutral buoyancy of the plume is controlled primarily by salinity, and that vertical velocities outside of the plume are small, such that the impact of the flow on salinity at each depth level above sill depth should be negligible. That is to say, if the horizontal recirculation is primarily along isopycnals, then the inflow and outflow occur with approximately the same salinity, leading to negligible eddy salt flux.

We similarly find that in MITgcm simulations of fjords with deep sills, the eddy flux $[F_e]$ is negligible compared to the mean flux $[F_m]$ for both salt and heat, for all fjord widths and subglacial discharge volume fluxes. In terms of the heat flux, this is consistent with the negligible impact of deep sills on submarine melt rates at the ice face discussed in §4.4.2. Recall from §4.3.1 that modification of the flow over a deep sill relative to fjords without sills occurs entirely within the unstratified lower layer. Thus, the impact of deep sills on the heat and salt fluxes into the fjord is negligible.

In the context of the box-model structure employed in Chapter 3, one modification allowing the inclusion of the eddy heat flux may be the addition of a further box in the cross-fjord direction, such that the fjord is represented as a 2×2 grid, with a single grid-cell in the along-fjord direction. This would allow the inclusion of cross-fjord gradients in velocity and temperature, such that an eddy component may be computed. Alternatively, it may be possible to retain the two-box structure employed in Chapter 3 and instead derive a theoretical prediction for the eddy component of heat flux over the sill which could be included as an additional term in the volume flux into each box, with some dynamically motivated transfer function. This approach provides an interesting avenue for future work which would minimize modification to the box model.

4.5 Summary

The presence of bathymetric sills provides key constraints on exchanges between the fjord and wider ocean driven by estuarine circulation. If the inflow in the shelf region occurs entirely above sill depth, any changes in the heat content in the ocean below sill depth are not able to propagate into silled fjords. Thus, water below sill depth within these fjords is fresher and cooler than water at the equivalent depth on the shelf outside, consistent with observations of silled fjords (e.g. Johnson et al. 2011; Gladish et al. 2015). For deep sills, the modification to the velocity structure relative to fjords without sills occurs within the unstratified lower layer. Thus, the impact of the sill on the salinity and temperature at depth within the fjord will be small. However, for shallower sills with depths close to the bottom of the stratified upper layer, blocking of deep shelf waters by the sill has a non-negligible impact on the stratification within the fjord, as deep water in the fjord is replenished by water originating above sill depth beyond the sill.

As a result of this blocking of the inflow of warm, deep water, our MITgcm simulations suggest that fjords with shallow sills have significantly decreased submarine melt rates compared to similar fjords with no sill. Whilst the precise value depends upon subglacial discharge forcing and fjord width, we find a decrease of up to 25% in the total submarine melt rate at glacial termini due to the presence of a shallow sill, consistent with previous studies (e.g. Jakobsson et al. 2020). This difference may have implications for the stability of marine-terminating glaciers around Greenland's coastline, and for the long term evolution of the Greenland Ice Sheet as a whole, although the impact may ultimately be small compared to other uncertainties.

The results presented in this chapter have several implications for the inclusion of sills into a box-model parameterization of proglacial fjords. Firstly, the impact of sills on submarine melt rates highlights the necessity of the inclusion of sills into any parameterization of fjord scale circulation intended for use in Earth system models. The observation that inflow into the fjord originates from above sill depth

outside of the fjord suggests a first-order method to include the impact of sills, with the properties of inflowing water approximately given by those at the sill crest.

We find that scalings developed for the outflow depth of the plume in Chapter 2 remain applicable provided the plume outflow depth is sufficiently far above the sill. However, this picture is complicated where the plume outflow at the ice face is close to the sill depth. In all cases, the depth of the peak cross-fjord averaged outflow velocity is the same both over the sill and throughout the region beyond the sill, suggesting that the outflow depth over the sill is the appropriate outflow depth to provide to the ocean component of an Earth system model. Some estimate for the distance of the deflection of the outflow over the sill versus the level of neutral buoyancy of the plume at the ice face as a function of fjord width, subglacial discharge, and sill depth is required to include even a simple representation of sills into a parameterization scheme.

We find that for shallow sills, the velocity structure over the sill is more vertically sheared than horizontally sheared for fjords with widths $B < R_d$. The flow is more horizontally sheared for fjords wider than R_d. Hence, the ratio of fjord width to an estimate of the deformation radius $R_d = (g'Q_{out}/f^3)^{1/4}$ provides a first-order prediction of the relative size of the vertical and horizontal shear in the velocity structure over the sill. We find that the salt flux associated with the horizontally sheared component of the along-fjord flow over the sill is small compared to the mean salt flux, for both deep and shallow sills. At most, the horizontally sheared component comprises 10% of the mean for shallow sills and is at most two orders of magnitude smaller for deep sills.

The eddy component of the heat flux is similarly negligible for deep sills. For shallow sills, however, the eddy heat flux is of the same magnitude as the mean flux where there are both intermediate values of subglacial discharge, and fjord widths $B \gtrsim R_d$. Significant modification of the box-model structure developed in Chapter 3 may be required to account for cross-fjord gradients in temperature and along-fjord velocity which give rise to the large eddy component in these wide fjords. One approach may be the addition of a second grid cell in each box in the cross-fjord

direction, such that the fjord is represented by two stacked boxes, each with two cross-fjord grid cells. Alternatively, theoretical predictions of the magnitude of the eddy heat flux could be developed such that the box structure discussed in Chapter 3 could remain unmodified, although no progress has been made as of yet.

4.6 Limitations and future work

The parameter space of relevance to subglacial-discharge-driven circulation within proglacial fjords is vast. Adding bathymetric sills further adds several new parameters to this parameter space. As such, a number of simplifying choices and approximations were made to allow for tractable investigation of the key impacts of sills. Firstly, the choice to model the sill as a sheer vertical wall with minimal along-fjord extent may impact model results by driving strong cross-fjord velocities and sharp changes in upwelling with along- and cross-fjord position close to the sill. This choice was made to minimise the number of simulations necessary to capture the impact of varying sill shape and along-fjord extent. Future work should investigate the impact of different choices to ensure that the interpretations discussed in this chapter still hold.

Also, the choice to investigate only two sill depths (defined relative to the stratification) may not span the entire space of possible flow structures given geophysically relevant forcing conditions. We assumed that the key dynamical length scale is likely to be the vertical distance between the level of neutral buoyancy of the plume, and the sill crest, rather than the sill height directly. Whilst we have seen that the cross-fjord integrated along-fjord flow is only deflected vertically where this distance is small, it is possible that a strong outflow resulting from high subglacial discharge which sits close to the sill crest could generate a different flow structure, for example, with inflow in the region outside of the fjord below sill depth, with sufficient energy to flow up and over the sill and into the fjord.

In terms of theoretical modelling of the velocity structure, previous hydraulic model approaches typically applied to channel flow over bathymetric constrictions (e.g. Gill 1977, Timmermans et al. 2005) are seemingly not straightforwardly

applicable to this type of flow. Firstly, the number of possible flow configurations over the sill given a representative number of layers in the model adds significant algebraic complexity when extending previous work, where typically hydraulic models deal with only two layers when including Coriolis effects (e.g. Dalziel 1991). The velocity over the sill in MITgcm simulation output is fundamentally 3-dimensional, with strong horizontal shear, such that simplified theories which neglect the impact of rotation (e.g. Smeed 2000) are not likely to provide an accurate prediction of the volume, heat, and salt exchange between the fjord and the wider ocean. Secondly, the time evolution of the salinity at depth within the fjord cannot be captured given the steady-state assumptions in the theoretical model, although it may be possible to apply the framework in a quasi-steady sense.

The highest priority next step is to determine the minimum thickness of the inflow layer over the sill, either via scaling argument or via some more complex theoretical or empirically derived model. Then, the depth at which the cross-fjord integrated outflow occurs on the shelf can be predicted, as well as the salt flux into the fjord given the depth range over which inflow can occur. This would allow at least a first-order method of inclusion of sills into the box model developed in Chapter 3. The development of a full theoretical model based on the hydraulic model approach of §4.4.1 provides one potential avenue for future investigation. Indeed, such a model may have applicability to a range of geophysical problems concerning three-layer flows (e.g. Smeed 2000), and would not be restricted to circulation within fjords.

Appendix

A4.1 Hydraulic model

As an initial investigation, we develop the theoretical model following a similar approach to those of Dalziel (1991) and Smeed (2000). Following the scaling arguments in Appendix A2.1 we include rotation. However, cross-fjord velocities are considered to be small, such that the influence of rotation is to permit cross-fjord structure. We assume that the fluid is hydrostatic, steady, inviscid and make the Boussinesq approximation. The flow is considered to consist of three layers (see Figure 4.13), and we assume a rigid lid. From the surface, these are:

1. A surface layer which can have non-zero along-fjord velocities, but no net volume flux. This layer may be of zero thickness, dependent on the predicted plume outflow depth.

2. An outflow layer, with volume flux and thickness given by the scalings in Chapter 2.

3. An inflow layer from the bottom of the outflow layer down to the bathymetry, with volume flux given by the total incoming volume flux due to entrainment predicted in Chapter 2.

We assume a rectangular channel cross-section and rigid lid, such that the channel depth $D(x) = h_1(x,y) + h_2(x,y) + h_3(x,y) + h_S(x)$, with x the along-fjord coordinate, y the cross-fjord coordinate, h_i the thickness of layer i, and the bathymetry $h_S(x)$ describing the sill depth and location.

Assuming cross-fjord velocities are negligible, the x component of the momentum equations in each layer is

$$\frac{\partial}{\partial x}\left(\frac{1}{2}u_1^2 + \frac{p_0}{\bar{\rho}} + \frac{g}{\bar{\rho}}\left[\rho_1(h_1+h_2+h_3+h_S)\right]\right) = \frac{\partial B_1}{\partial x} = 0, \tag{A4.1}$$

$$\frac{\partial}{\partial x}\left(\frac{1}{2}u_2^2 + \frac{p_0}{\bar{\rho}} + \frac{g}{\bar{\rho}}\left[\rho_1 h_1 + \rho_2(h_2+h_3+h_S)\right]\right) = \frac{\partial B_2}{\partial x} = 0, \tag{A4.2}$$

$$\frac{\partial}{\partial x}\left(\frac{1}{2}u_3^2+\frac{p_0}{\bar{\rho}}+\frac{g}{\bar{\rho}}\left[\rho_1 h_1+\rho_2 h_2+\rho_3\left(h_3+h_S\right)\right]\right)=\frac{\partial B_3}{\partial x}=0, \tag{A4.3}$$

where $u_i(x,y)$ is the velocity in each layer, p_0 is the pressure at the surface on the rigid lid, ρ_i is the density in layer i, and $\bar{\rho}$ is the reference density arising via the Boussinesq approximation. Integrating each equation and defining $B_{12} = B_1 - B_2$, and $B_{23} = B_2 - B_3$ yields

$$B_{12}=\frac{1}{2}\left(u_1^2-u_2^2\right)+\frac{g}{\bar{\rho}}(\rho_1-\rho_2)(h_2+h_3+h_S), \tag{A4.4}$$

$$B_{23}=\frac{1}{2}\left(u_2^2-u_3^2\right)+\frac{g}{\bar{\rho}}(\rho_2-\rho_3)(h_3+h_S). \tag{A4.5}$$

We also define reduced gravities

$$g_i'=g\frac{\rho_{i+1}-\rho_i}{\bar{\rho}}.$$

To account for the effects of rotation (still assuming that cross-fjord velocities are negligible), we start from the y component of the momentum equations:

$$fu_1=-\frac{1}{\bar{\rho}}\frac{\partial}{\partial y}\left(g\rho_1[h_1+h_2+h_3+h_S]+p_0\right), \tag{A4.6}$$

$$fu_2=-\frac{1}{\bar{\rho}}\frac{\partial}{\partial y}\left(g\rho_1 h_1+g\rho_2[h_2+h_3+h_S]+p_0\right), \tag{A4.7}$$

$$fu_3=-\frac{1}{\bar{\rho}}\frac{\partial}{\partial y}\left(g\rho_1 h_1+g\rho_2 h_2+g\rho_3[h_3+h_S]+p_0\right). \tag{A4.8}$$

Taking the differences between Equation A4.6 and Equation A4.7; and Equation A4.7 and Equation A4.8, yields the thermal wind relations,

$$f(u_1-u_2)=-g_1'\frac{\partial h_1}{\partial y}, \tag{A4.9}$$

$$f(u_2-u_3)=g_2'\frac{\partial h_3}{\partial y}. \tag{A4.10}$$

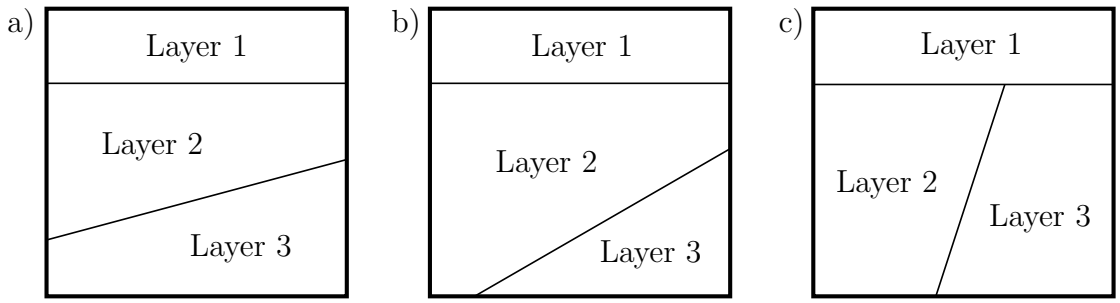

Figure A4.1: Observed layer structures over the sill (including cases where layer 1 has zero thickness), showing a) doubly attached, b) singly attached, and c) unattached interfaces between layers 2 and 3.

We further require an approximation for the potential vorticity in each layer. A common approach taken in previous work is the assumption of zero potential vorticity in each layer, which greatly simplifies the mathematics. Typically, this is equivalent to the assumption that the depths of the basins either side of the sill go to infinity, such that layer thicknesses either side of the sill are very large. Here, the basin depth cannot be assumed to go to infinity, however, for simplicity we retain this assumption. The assumptions of zero potential vorticity in each layer and negligible cross-fjord velocities means that the potential vorticity equation in each layer reduces to:

$$\frac{f - \frac{\partial u_i}{\partial y}}{h_i} = 0$$

$$\implies \frac{\partial u_i}{\partial y} = f. \tag{A4.11}$$

Following the approach in Dalziel (1991), we must consider the layer structure over the sill. Simulation outputs outlined in §4.3 seemingly display 'detached' interfaces between layers 1 and 2, such that this interface intersects both the surface and bathymetry. In principle, many more flow configurations are possible, with permutations of each layer interface being doubly, singly, or not attached. While these flow configurations are interesting, we restrict our attention to the simplest theoretical case of doubly attached layer interfaces, and leave investigation of the other cases to future work.

Fully attached layer interface

In the case that both layer interfaces intersect the fjord sidewalls at the sill, we construct expressions for the layer thicknesses and velocities in terms of the value at $y = 0$ (denoted by overbars). Velocities in each layer are constructed by integrating Equation A4.11;

$$u_i(x, y) = fy + \bar{u}_i(x). \tag{A4.12}$$

Expressions for the layer thicknesses are found by substitution of Equation A4.12 into Equation A4.9 and Equation A4.10, integrating each equation, and the use of the rigid lid condition, such that

$$h_1(x, y) = \frac{fy}{g_1'} (\bar{u_2} - \bar{u_1}) + \bar{h_1}(x) \tag{A4.13}$$

$$h_2(x, y) = D(x) - h_S(x) - h_1(x, y) - h_3(x, y) \tag{A4.14}$$

$$h_3(x, y) = \frac{fy}{g_2'} (\bar{u_3} - \bar{u_2}) + \bar{h_1}(x) \tag{A4.15}$$

The volume flux in each layer is constant along the length of the channel. Thus, we can find layer velocities in terms of layer thicknesses by integrating the volume flux in each layer:

$$Q_i = \int_{-\frac{B}{2}}^{\frac{B}{2}} u_i h_i \, \mathrm{d}y \tag{A4.16}$$

By construction, the volume flux in the surface layer $Q_1 = 0$. The volume fluxes in layers 2 and 3 are driven by the plume at the ice face, such that $Q_2 = -Q_3 - Q_{sg} \approx Q$.

This gives us 6 equations in 6 variables; two from the differences between Bernoulli functions Equation A4.4 and Equation A4.5, three from the volume flux constraints relating $u_i's$ and $h_i's$ (Equation A4.16), and one rigid lid condition, with variables the three layer thicknesses h_i and layer velocities u_i.

5
Conclusions and future work

The interaction between the Greenland Ice Sheet and the wider ocean is mediated by circulation within several hundred fjords around Greenland's coastline. Circulation within these fjords is controlled by a variety of processes, as reviewed in Chapter 1. Current generation Earth system models operate at horizontal resolutions too coarse to directly include interactions between the Greenland Ice Sheet, fjord-scale circulation, and the ocean. This represents a fundamental limitation in the ability of Earth system models to predict the long-term stability of the Greenland Ice Sheet, as well as the impact of the freshwater flux from submarine melting on the ocean, and global climate. As such, the development of a sub-grid scale parameterization of circulation within Greenland's fjords is of crucial importance in reducing uncertainty in long-term climate predictions. This thesis took initial steps towards this goal by building physical understanding and an approximate description of selected forcing processes.

This thesis investigated fjord circulation in an estuarine regime driven by subglacial discharge and has taken the first steps in the development of a sub-grid scale parameterization scheme for use in Earth system models. Subglacial-discharge-driven estuarine circulation within fjords is fundamentally three-dimensional, and it is challenging to fully represent the flow structures which develop over a geophysically relevant range of forcing conditions and fjord geometries, and their impact on melting

at the ice face. Furthermore, the parameter space of relevance to Greenland's proglacial fjords is vast. Therefore, approximations and simplifications were required to make progress.

Attention was primarily focused on understanding aspects of fjord circulation which could be taken as inputs by the ice and ocean model components of current generation Earth system models. Theoretical predictions were developed for the vertical structure of cross-fjord-integrated along-fjord velocities at the fjord mouth, and the horizontal structure of vertically-integrated melt rates at the ice face. These developments are then used as the foundation for a simple box-model parameterization of subglacial-discharge-driven circulation. Finally, the impact of bathymetric sills on the fjord-scale circulation was investigated, to determine the necessary next steps to include the effect of sills in a parameterization scheme.

This chapter collects key conclusions and discusses the broader significance of the work in this thesis. The key research questions and results illustrated in each chapter are summarised in §5.1. Then, §5.2 discusses the broader context and implications of the work in this thesis. Finally, §5.3 outlines limitations of the work, outstanding research questions, and potential avenues for future work.

5.1 Chapter summaries

5.1.1 Chapter 2

Chapter 2 aimed to understand and characterize fjord circulation in a regime driven by subglacial discharge, for fjords without bathymetric sills. There was a focus on the impact of changing the fjord width and the magnitude of subglacial discharge on the vertical structure of the fjord circulation. Simple scaling laws describing the structure of the circulation given fjord geometry and subglacial discharge flux were developed, which could be used as the basis for a computationally light and efficient parameterization scheme. Furthermore, the impact of fjord circulation on melt rates across the ice face was investigated over a range of fjord widths and subglacial discharge fluxes.

To build understanding, idealised computational models of fjords in the MITgcm ocean circulation model were employed. These models consisted of flat-bottomed channels with vertical flat sidewalls, with a thermodynamically active vertical ice face at one end, and an open boundary at the other. A single, central source of subglacial discharge at the grounding line fed a turbulent plume, which rose buoyantly up the ice face. Stratifications in salinity and temperature based on observations of fjords around the coastline of Greenland were used as initial conditions throughout the computational domain. Broadly, the stratification in salinity typically consists of a layer of linearly varying salinity, overlying a layer of approximately constant salinity. This yields a corresponding piecewise linear stratification of density. The steady-state fjord-scale flow structures which developed as a result of subglacial discharge forcing were investigated over a range of fjord widths and subglacial discharge fluxes.

A key observation was that the vertical structure in the cross-fjord-integrated along-fjord velocity was broadly consistent along the entire length of the fjord, independent of fjord width. At the ice face, this vertical structure is set by the behaviour of the buoyant plume which arises due to the injection of subglacial discharge at the grounding line. Therefore, scaling laws for the vertical structure of the outward flux away from the ice face apply along the length of the fjord, and crucially at the fjord mouth, where the fjord circulation interacts with the wider ocean.

Work from previous literature for flow with uniform stratification was combined with an integral constraint on the salt flux to derive scaling laws for the outflow depth of turbulent plumes and the outflow layer thickness accounting for the two-layer stratification typical of Greenlandic fjords. The prediction of the plume outflow depth was found to be robust over the range of fjord width and subglacial discharge flux considered, and for different stratification strengths in the upper layer within the fjord. This allowed for the prediction of the range of depths over which the estuarine circulation outflows into the ocean from Greenland's fjords, which is a key element of any parameterization scheme representing fjords within Earth system models.

Investigation of the horizontal structure of cross-fjord flow at the ice face revealed interesting dynamics. At the outflow depth of the plume, an anticyclonic

recirculation region was found to develop close to the ice face, with sufficient strength to impact the melt rates across the ice face. A phenomenological theory was developed to predict cross-fjord velocities at the plume outflow depth, based on the combination of this fjord-scale circulation, as well as the radial cross-fjord velocities resulting from the injection of fluid by the horizontal plume outflow. This theory captured cross-fjord velocities at the outflow depth with partial success. Velocities to the right of the plume (looking towards the ice face) were very similar between theory and simulation over much of the parameter space. To the left of the plume, a sign reversal in the cross-fjord velocities was observed in simulation output linked to a cyclonic corner eddy, which our theory was unable to capture.

Combination of the predictions for the vertical structure of the horizontal flow within the fjord, as well as predictions for the horizontal flow at each depth and vertical plume flow, allowed for the construction of a 2D map of the spatial pattern of melt across the entire ice face using standard turbulence parameterizations for the heat and salt flux. It was found that the vertically-integrated, horizontal profiles of melt at the ice face compared well between our theoretical predictions and simulation output. The predicted melt rates (which depend on the magnitude of the cross-fjord velocity of the fjord circulation at the ice) are of the correct order of magnitude even in the region impacted by the cyclonic corner eddy, despite the less satisfactory comparison for the direction and structure of the flow. Such predictions of the melt rates at glacial termini are of key importance in the development of a parameterization scheme.

5.1.2 Chapter 3

Chapter 3 took the first steps in building a new parameterization scheme of circulation in Greenland's fjords, in the form of an idealised box model. As the Greenland Ice Sheet interacts with the ocean via several hundred fjords around the coastline, any parameterization scheme intended to represent each fjord individually within an Earth system model must be computationally light, to make the use of such a scheme computationally feasible.

The model developed in Chapter 3 consisted of two vertically stacked boxes, of time-varying thickness; a lower box, with constant salinity and temperature, and an upper box that is linearly stratified in salinity and temperature. The approximation of the stratification in this way allowed the use of the scaling laws developed in Chapter 2 to set the volume fluxes in each box and the melt rates at the ice face. This reduces the computational cost of the model compared to, say, solving the full set of coupled differential equations describing the vertical variation of plume properties at each time step, and then using these solutions to set the volume fluxes in each box, although the routine which fits an approximation to the ocean stratification could be optimised by using a coarser vertical resolution. The box model constrains the stratification within the fjord to evolve in a manner consistent with integral heat and salt budgets.

The behaviour of the model was investigated over a range of realistic and idealised forcing conditions. Idealised forcings consisting of constant subglacial discharge and ocean stratification were used as validation of the box model, ensuring that the model behaved sensibly given these simple conditions, and to understand the timescales of adjustment. The complexity of forcing conditions was increased, using combinations of time series of ocean stratification that were either oscillatory or realistic, combined with time series of subglacial discharge that were either constant or realistic. Realistic forcings for the far-field ocean were taken from the NEMO ocean model and for subglacial discharge from the JULES land components of pre-industrial control runs of the HADGEM3-GC3.1-LL Earth system model.

The box-model results for circulation driven purely by subglacial discharge suggested that fjords of differing widths and depths display different behaviour in terms of the time evolution of stratification and melt rates, given identical forcing conditions. The model suggests that the increased volume of water in wider fjords means that the stratification within the fjord responds more slowly to changes in the ocean stratification, given that the volume fluxes are independent of fjord width. Increasing fjord depth while keeping the thickness of the stratified layer constant leads to a slower response in the unstratified lower layer in the fjord. However, the

increased entrainment into the plume due to the increased distance through which the plume rises in the unstratified lower layer leads to a more vigorous exchange flow in the stratified surface layer, in turn leading to a more rapid response to the ocean stratification in the surface layer for deeper fjords. This sensitivity to changes in fjord width and depth is conceptually consistent with real-world observations that neighbouring fjords subjected to similar forcing conditions can display very different behaviour (Bartholomaus et al. 2016), although there may of course be other factors at play in other settings, such as ice dynamics.

The model response to realistic, seasonally varying subglacial discharge suggests that the stratification within fjords skews towards summertime ocean conditions, as higher subglacial discharge in summer months drives increased replenishment of fjord water by the summertime ocean stratification. This has implications for melt rates at the ice, which are dominated by the summer subglacial discharge and temperature. Model results further show that the outflow depth of the estuarine circulation within fjords displays significant seasonal variability given realistic fjord-mouth forcing conditions, with outflow occurring anywhere from the bottom to the top of the stratified surface layer over a seasonal cycle. This highlights the importance of accurate representation of the depth at which freshwater enters the ocean, as well as revealing the scale of the inaccuracy when simply adding freshwater into the surface grid cell in the ocean component of Earth system models, with outflow anywhere from the surface to depths of $\mathcal{O}(200\,\mathrm{m})$ over a seasonal cycle in subglacial discharge. However, MITgcm simulations suggest that baroclinic exchange flows driven by density gradients between the fjord and ocean may dominate exchange fluxes in some settings. Characterization and inclusion of these density-driven flows is a high priority for future work.

5.1.3 Chapter 4

In Chapter 4, the impact of bathymetric sills on fjord circulation in a subglacial-discharge-driven regime was investigated, using idealised computational modelling. Again, the focus was on understanding aspects of fjord circulation which are of

relevance to a parameterization scheme for use in Earth system models. The addition of a bathymetric sill adds several further parameters to the parameter space of relevance to subglacial-discharge-driven circulation within fjords. To restrict the parameter space, only two sill depths were considered and instead subglacial discharge and fjord width were varied. Variation in subglacial discharge changes the vertical distance between the sill crest and the plume outflow depth, which is the dynamically relevant length scale.

As in the investigation of fjords without sills in Chapter 2, it was found that the vertical structure of the cross-fjord-integrated along-fjord velocities is the same between different fjord widths, at the same value of subglacial discharge. In contrast with sill-less fjords, however, the inflow replenishing water at depth within the fjord originates entirely above sill depth and downwells within the fjord, rather than originating at greater depth and flowing horizontally. For fjords with shallow sills, this leads to a freshening of water below sill depth within the fjord, relative to water at the corresponding depth in the far-field ocean. There is a similar modification to temperatures at depth within the fjord towards the temperature of waters above sill depth beyond the sill. As a result, submarine melt rates in fjords with shallow sills differ significantly ($\sim 25\%$) from those without sills. This highlights the importance of the inclusion of sills in a parameterization of fjord circulation.

We found that the salt and heat fluxes associated with the horizontally sheared component of the flow over the sill are negligible for deep sills. For shallow sills, however, the eddy heat flux is of the same magnitude as the mean flux for intermediate values of subglacial discharge, and fjord widths approximately equal to or larger than the Rossby radius of deformation. Modification to the box-model structure developed in Chapter 3 may be required to account for the large eddy component in wide fjords. One approach may be the addition of a second grid cell in each box in the cross-fjord direction, such that the fjord is represented by two stacked boxes each with two cross-fjord grid cells. Alternatively, theoretical predictions of the magnitude of the eddy heat flux could be developed such that the box structure discussed in Chapter 3 could remain unmodified.

Initial attempts to develop a theoretical prediction of the flow structure over the sill using hydraulic control theory were unsuccessful. The most applicable hydraulic model to the circulation structures seen in simulation outputs should contain three layers and include the effects of rotation. Currently, no previous work has developed such a model. An initial framework for tackling this problem was proposed, which suggests the need to solve for cases involving different combinations of isopycnal intersections with the fjord sidewalls, ocean surface, ocean bed, and other isopycnals, as well as transitions between these cases. This interesting but complex problem is left for future work.

5.2 Context

The work in this thesis has focused on understanding fjord circulation in an estuarine regime driven by subglacial discharge. Previous plume scaling laws were extended to stratifications of relevance to Greenlandic fjords, developing a simple theoretical prediction of the vertical structure of along-fjord flow. These previous scaling laws for the height of rise of a plume in a linearly stratified layer contain unknown dimensionless constants of proportionality, which must be determined empirically (Slater et al. 2016). Here, a testable prediction of the plume height of rise without any unknown constants was developed by exploiting an additional constraint on the net salt flux, which compares well to computational model output.

In principle, this result may be used in several ways. In this thesis, the plume scalings were used to predict the flow structure at the fjord mouth for fjords without sills, and formed the basis of the box-model parameterization in Chapter 3. The scalings could also be applied to interpret real-world observations. For example, measurements of the outflow depth and stratification within fjords may allow an estimation of the subglacial discharge forcing at the ice face, by solving Equation 2.15 for Q_{sg}, assuming the presence of a single plume, similar to the approach taken in De Andrés et al. (2020). In contrast to De Andrés et al. (2020), the work in this thesis removes the requirement to fit an unknown dimensionless constant relating the plume height of rise to the subglacial discharge and also

accounts for an approximation to the full two-layer stratification. Theoretical scalings for plume outflow depth may also be useful in terms of predicting the distribution of biogeochemical nutrients within the fjord. Subglacial discharge contains sediment carried from beneath the ice sheet (Delaney et al. 2020). As the plume rises and entrains ambient water, it also entrains nutrient-rich sediment, which then outflows at the level of neutral buoyancy (Meire et al. 2017; Kanna et al. 2018). The extent to which biogeochemical nutrients sit within the photic zone within the fjord has important consequences for ecological health (Howarth 1988), and prediction of the plume outflow depth may be used to infer the depth range over which nutrients are injected.

Furthermore, it may be possible to extend plume scalings to other settings, either oceanographic or otherwise. Interactions between the plume and the ice face were neglected here, both in terms of drag, and the injection of buoyancy due to plume-induced melting. The wall acted only as a geometric constraint on the surface area of the rising plume over which entrainment could occur, restricting our treatment to half-conical plumes. In principle, this assumption could be relaxed by modifying Equation 2.7 and Equation 2.9, accounting for the entraining surface area of plumes with different geometries, but retaining consideration of the integral salt or buoyancy flux. This would allow the work in this thesis to find applicability to line plumes at marine-terminating glaciers, or plumes in the open ocean such as those which arise due to thermal vents (e.g. Speer et al. 1995), for example.

The key approximations in terms of the ambient density profile are that; (i) density is controlled by a single parameter, and that (ii) the vertical profile of density is well described as a layer of linearly varying density overlying a layer of constant density. Therefore, the scalings developed in this thesis could equally apply to plumes rising in a thermally stratified environment, in regions where this is the strongest control on the ambient density profile. For such an application the integral constraints on the salt flux considered in Chapter 2 are instead modified to consider the heat flux. This may be useful in some civil engineering settings, such as the impact of a localised heat source on airflow in buildings (Linden 1999).

The prediction of the spatial pattern of melt across the entire ice face compared well to computational model output, and highlighted the impact of fjord circulation on the submarine melting of marine-terminating glaciers, with implications for glacial retreat and ice sheet stability. Previous work in the literature has parameterized glacial melt rates empirically in terms of subglacial discharge and thermal forcing (e.g. Slater et al. 2019). However, no previous study recreates a 2D melt pattern at the ice face via theoretical prediction of cross-fjord velocities resulting from fjord-scale circulation (note that some studies have calculated this melt numerically for isolated case studies, e.g. Carroll et al. 2017, Slater et al. 2018). The total submarine melt rates induced by this horizontal circulation at the ice are $2-10$ times larger than the melting of ice in direct contact with the plume. This is consistent with (albeit limited) observations of marine-terminating glaciers (Slater et al. 2018; Sutherland et al. 2019) where melt rates exceed those predicted by buoyant plume theory, and highlights the importance of the prediction of submarine melt rates across the entire ice face in any fjord parameterization scheme.

The box model developed in Chapter 3 could form the initial basis of a sub-grid scale parameterization scheme to capture the effect of subglacial-discharge-driven flow without significant further additions, neglecting the impact of sills. It allows for parameterization of the impact on submarine melting of changing ocean conditions and melting over inland regions of the ice sheet that can be provided as input to an ice sheet model. The parameterization and the corresponding exchanges of heat, salt, and mass also predicts the depth at which freshwater from melting of the ice sheet enters the wider ocean that can be provided as input into an ocean model. This is an important step toward a full parameterization of the impact of fjord circulation on the ocean forced melt of the Greenland Ice Sheet.

The addition of passive tracers to the box model would be trivial, evolving using an identical framework to temperature in the current box-model formulation. These tracers could model the distribution and concentration of nutrients with depth within the fjord. This would allow for interaction of the box model with some additional biogeochemical model of the fjord ecosystem.

Looking forward, the box model developed here could form the basis of a more complex scheme that includes the impacts of other processes, such as katabatic wind events, or intermediary circulation. The addition of the impact of bathymetric sills is a high priority. The inclusion of further physics requires the development of some simple theoretical framework describing the flow structure within the fjord, as the representation of a forcing process by any complex real-time numerical simulation is likely to render a parameterization scheme computationally infeasible. The inclusion of other processes is discussed in the next section.

Validation and testing of the box model would require comparison to observations of fjord circulation in a regime dominated by subglacial discharge. It may be possible that other processes which influence fjord-scale circulation are sufficiently commonplace that measurement of fjords solely in this circulation regime is challenging. Clearly, the inclusion of other forcing processes is vital to the accurate prediction of the impact of fjord circulation on the GrIS.

In the first instance, measurement of the vertical profile of salinity and the cross-fjord-integrated along-fjord velocity, both several kilometers from the ice face, and at the fjord mouth, along with the magnitude of subglacial discharge, would allow for the validation of predictions for the velocity structure developed in Chapter 2. Some observations of this nature exist (e.g. Inall et al. 2014; Sutherland et al. 2019). Previous studies have collected cross-fjord transects of the velocity structure within proglacial fjords (e.g. Sutherland et al. 2014, Fraser et al. 2018), or with depth at individual locations (e.g. Sutherland et al. 2012), as well as observations of subglacial discharge plumes (e.g. Mortensen et al. 2020; Everett et al. 2021), suggesting that collection of the relevant data is feasible. Validation of the method to calculate melt at the ice face developed in this thesis would require measurements of cross-fjord velocities across the entire ice face, as well as the strength of subglacial discharge forcing, and the total freshwater flux into the fjord at the ice face. The measurement of cross-fjord velocities at the ice face is particularly challenging, given the necessity of measurement close to the ice, although some observations do exist (e.g. Stevens et al. 2016; Slater et al. 2018).

5.3 Limitations and future work

Limitations and suggestions for future work specific to each chapter can be found at the end of the corresponding chapter. This section discusses the limitations of the approaches taken throughout work in this thesis as a whole.

In all simulations, the flow structure of fjord circulation was found to be fundamentally three-dimensional for the considered regime dominated by the injection of subglacial discharge at the grounding line. As such, significant simplifications and approximations were made in order to make progress in characterizing and understanding the first-order controls on the flow. First, the computational model consists of a rectangular fjord cross-section with no bathymetry. The extent to which this captures the physical essence of flow in Greenlandic fjords may be questioned. However, whilst the bathymetry of some fjords has been measured (e.g. An et al. 2019), there is currently no quantitative characterization of fjord geometries and bathymetries for all fjords around the coastline of Greenland. Hence, it is not clear how to generalise a choice of 'realistic' bathymetry to all fjords. This may provide an interesting avenue for future work; statistically quantifying bathymetric properties including fjord widths, depths, and sidewall geometries to provide a framework to build representative fjord bathymetries for use in computational models. Nonetheless, progress in understanding the circulation within idealised fjords should prove useful for understanding the circulation in fjords with more complex geometries.

It was further assumed that the stratification in salinity is well approximated by a layer of linearly varying salinity overlying a layer of constant salinity. The extent to which this is a good approximation at all times for fjords around the coastline of Greenland is not quantified. The realistic ocean time series from the HADGEM3-GC3.1-LL model employed in Chapter 3 suggest that this approximation is often reasonable, with the fitting routine usually converging. However, cases where the approximation breaks down were observed, particularly at times with significant surface mixed layer depths. Future work could include the impact of a surface mixed layer on plume outflow properties, and circulation within fjords. In principle, the addition of a surface mixed layer as an extension to the work in this thesis would

be straightforward, as a mixed layer has no impact on the dynamics of plumes which terminate below this layer, and any plume which reaches the bottom of a surface mixed layer must penetrate all the way through to the surface. Icebergs and sea ice impact the near-surface stratification in both salinity and temperature and are thought to be a large source of freshwater injected into the fjord, with some larger icebergs also acting as a source of freshwater at significant depth within the fjord (e.g. Davison et al. 2020). Thus, the inclusion of a surface mixed layer should also include some treatment of ice at the ocean surface.

The addition of multiple discharge plumes at the ice face to the work in Chapter 2 is trivial, provided that each plume is fed by equal subglacial discharge, and is sufficiently far from adjacent plumes that they can be considered to be non-interacting. Work is required to determine the impact of the interaction on the fjord-scale circulation for interacting plumes, or those with differing subglacial discharge forcing and therefore different levels of neutral buoyancy.

As previously discussed, the circulation within fjords is controlled by a variety of processes. Improvement in the accuracy of a parameterization scheme of fjord circulation requires the inclusion of more processes than the subglacial-discharge-driven circulation considered in this thesis. Perhaps the most readily included process is katabatic winds, which has a well-developed theory considering a two-layer stratification that yields exchange fluxes in each layer (see §1.2.1.4 and Farmer (1976); Spall et al. (2017)). However, work is required to build a box model of fjord circulation driven by katabatic winds in combination with subglacial discharge. As these winds typically occur in winter, when the subglacial discharge and related estuarine circulation is weak, it may be possible that the interaction between the two is not geophysically relevant. Thus, investigation of the potentially complex interaction between katabatic winds and estuarine circulation may not be necessary in the context of the development of a simple parameterization scheme and one might simply be able to apply the exchange flux scalings of Farmer (1976) and Spall et al. (2017).

Intermediary circulation is thought to be a significant driver of water mass exchanges between fjords and the wider ocean (see §1.2.1.3). The nature of this process means that much of the impact on the stratification within the fjord and melting at the ice face is the result of the residual of changes over a large amplitude cycle. The focus on subglacial-discharge-driven estuarine circulation in this thesis provides increased understanding of the mean flow state within fjords around which the shelf-wind-induced variations occur. Thus, a sensible avenue of future work is to attempt to characterize the impact of intermediary circulation, with the intention of inclusion into the box model developed in Chapter 3. In principle, scalings for exchange fluxes associated with intermediary circulation discussed in §1.2.1.3 could be included in the box model. One first-order approach could neglect interactions between circulation driven by intermediary circulation and that driven by subglacial discharge, and sum the volume fluxes in each layer linearly.

The highest priority next step is to determine quantitative predictions of the impact of bathymetric sills. The addition of sills, particularly shallow sills, has significant implications for the stratification within fjords and melt rates at the ice face, as the inflow into the fjord due to entrainment into the plume at the ice face originates above sill depth on the shelf outside. Thus, the lack of inclusion of sills in the box model developed in Chapter 3 is a fundamental limitation. In particular, characterizing the relationship between the stratification within the fjord, the sill depth, and the horizontal outflow depth of the plume, is vital to the accurate parameterization of circulation in Greenland's fjords, although results in Chapter 4 suggest that the scalings for the plume outflow derived in Chapter 2 remain reasonable where the outflow occurs above sill depth at the ice face. The hydraulic model approach discussed in Chapter 4 is promising, although the development of such a model proved beyond the scope of this thesis. Future work characterizing the impact of sills should revisit this approach.

Estuarine circulation driven by subglacial discharge in proglacial fjords gives rise to fundamentally 3-dimensional flow structures. The flow has many interesting and complex features, across length scales ranging from the full fjord length down to turbulent scales at the ice face. Full understanding and theoretical characterization of all aspects of the flow is challenging, although flow at all scales has relevance to interactions between the fjord, ice at the glacial terminus, and the ocean outside of the fjord. The multi-scale nature of the flow provides a fascinating and rich opportunity to combine and build upon many existing concepts within fluid dynamics, while the characterization of flow within fjords is of great importance to a variety of scientific fields. Not least, the representation of fjord circulation and ice interactions within Earth system models is crucial to accurate long-term projections of climate change and sea level rise, of enormous scientific and humanitarian importance. Increased physical understanding is essential to the fidelitous parameterization of fjord circulation within these models, particularly given that processes driving circulation are predicted to change as global temperature increases.

In this thesis, we have taken a dynamically motivated approach; building physical insight into the structure of the fjord-scale flow, as well as melt rates at the ice face, in an estuarine circulation regime. We have developed a simple and computationally light method by which estuarine circulation driven by subglacial discharge may be represented as a sub-grid scale parameterization within Earth system models, based on theoretical scaling laws. However, many questions remain, and significant work must be undertaken before progress towards full understanding of the impacts of fjord circulation over all relevant forcing conditions is achieved.

References

Adcroft, A., C. Hill, J.-M. Campin, J. Marshall, and P. Heimbach (2004). "Overview of the formulation and numerics of the MIT GCM". In: pp. 139–150.

Alley, R. B., S. Anandakrishnan, K. Christianson, H. J. Horgan, A. Muto, B. R. Parizek, D. Pollard, and R. T. Walker (2015). "Oceanic Forcing of Ice-Sheet Retreat: West Antarctica and More". In: *Annual Review of Earth and Planetary Sciences* 43.1, pp. 207–231. DOI: 10.1146/annurev-earth-060614-105344.

An, L., E. Rignot, N. Chauche, D. M. Holland, D. Holland, M. Jakobsson, E. Kane, M. Wood, I. Klaucke, M. Morlighem, I. Velicogna, W. Weinrebe, and J. K. Willis (2019). "Bathymetry of Southeast Greenland From Oceans Melting Greenland (OMG) Data". In: *Geophysical Research Letters* 46.20, pp. 11197–11205. DOI: 10.1029/2019GL083953.

Antipov, Y. A. and A. S. Fokas (2005). "The modified Helmholtz equation in a semi-strip". In: *Mathematical Proceedings of the Cambridge Philosophical Society* 138.2, pp. 339–365. DOI: 10.1017/S0305004104008205.

Armi, L. (1986). "The hydraulics of two flowing layers with different densities". In: *Journal of Fluid Mechanics* 163, pp. 27–58. DOI: 10.1017/S0022112086002197.

Arneborg, L., C. P. Erlandsson, B. Liljebladh, and A. Stigebrandt (2004). "The rate of inflow and mixing during deep-water renewal in a sill fjord". In: *Limnology and Oceanography* 49.3, pp. 768–777. DOI: 10.4319/lo.2004.49.3.0768.

Bamber, J., R. L. Layberry, and S. P. Gogineni (2001). "A new ice thickness and bed data set for the Greenland ice sheet: 1. Measurement, data reduction, and errors". In: *Journal of Geophysical Research: Atmospheres* 106.D24, pp. 33773–33780. DOI: 10.1029/2001JD900054.

Bamber, J., M. van den Broeke, J. Ettema, J. Lenaerts, and E. Rignot (2012). "Recent large increases in freshwater fluxes from Greenland into the North Atlantic". In: *Geophysical Research Letters* 39.19. DOI: 10.1029/2012GL052552.

Bartholomaus, T. C., L. A. Stearns, D. A. Sutherland, E. L. Shroyer, J. D. Nash, R. T. Walker, G. Catania, D. Felikson, D. Carroll, M. J. Fried, and et al. (2016). "Contrasts in the response of adjacent fjords and glaciers to ice-sheet surface melt in West Greenland". In: *Annals of Glaciology* 57.73, pp. 25–38. DOI: 10.1017/aog.2016.19.

Biswas, S. and J. C. Kalita (2016). "Moffatt vortices in the lid-driven cavity flow". In: *Journal of Physics: Conference Series* 759, p. 012081. DOI: 10.1088/1742-6596/759/1/012081.

Blau, M. T., J. V. Turton, T. Sauter, and T. Mölg (2021). "Surface mass balance and energy balance of the 79N Glacier (Nioghalvfjerdsfjorden, NE Greenland) modeled by linking COSIPY and Polar WRF". In: *Journal of Glaciology* 67.266, pp. 1093–1107. DOI: 10.1017/jog.2021.56.

Böning, C. W., E. Behrens, A. Biastoch, K. Getzlaff, and J. L. Bamber (2016). "Emerging impact of Greenland meltwater on deepwater formation in the North Atlantic Ocean". In: *Nature Geoscience* 9.7, pp. 523–527. DOI: 10.1038/ngeo2740.

Bormans, M. and C. Garrett (1989). "The Effects of Nonrectangular Cross Section, Friction, and Barotropic Fluctuations on the Exchange through the Strait of Gibraltar". In: *Journal of Physical Oceanography* 19.10, pp. 1543–1557. DOI: 10.1175/1520-0485(1989)019<1543:TEONCS>2.0.CO;2.

Broeke, M. R. van den, E. M. Enderlin, I. M. Howat, P. Kuipers Munneke, B. P. Y. Noël, W. J. van de Berg, E. van Meijgaard, and B. Wouters (2016). "On the recent contribution of the Greenland ice sheet to sea level change". In: *The Cryosphere* 10.5, pp. 1933–1946. DOI: 10.5194/tc-10-1933-2016.

Broeke, M. R. van den and H. Gallée (1996). "Observation and simulation of barrier winds at the western margin of the Greenland ice sheet". In: *Quarterly Journal of the Royal Meteorological Society* 122.534, pp. 1365–1383. DOI: 10.1002/qj.49712253407.

Carroll, D., D. A. Sutherland, E. L. Shroyer, J. D. Nash, G. A. Catania, and L. A. Stearns (2017). "Subglacial discharge-driven renewal of tidewater glacier fjords". In: *Journal of Geophysical Research: Oceans* 122.8, pp. 6611–6629. DOI: 10.1002/2017JC012962.

Cenedese, C. and V. M. Gatto (2016). "Impact of a Localized Source of Subglacial Discharge on the Heat Flux and Submarine Melting of a Tidewater Glacier: A Laboratory Study". In: *Journal of Physical Oceanography* 46.10, pp. 3155–3163. DOI: 10.1175/JPO-D-16-0123.1.

Chauché, N., A. Hubbard, J.-C. Gascard, J. E. Box, R. Bates, M. Koppes, A. Sole, P. Christoffersen, and H. Patton (2014). "Ice–ocean interaction and calving front morphology at two west Greenland tidewater outlet glaciers". In: *The Cryosphere* 8.4, pp. 1457–1468. DOI: 10.5194/tc-8-1457-2014.

Church, J., P. Clark, A. Cazenave, J. Gregory, S. Jevrejeva, A. Levermann, M. Merrifield, G. Milne, R. Nerem, P. Nunn, A. Payne, W. Pfeffer, D. Stammer, and A. Unnikrishnan (2013). "Sea Level Change". In: *Climate Change 2013: The Physical Science Basis. Contribution of Working Group I to the Fifth Assessment Report of the Intergovernmental Panel on Climate Change*. Ed. by T. Stocker, D. Qin, G.-K. Plattner, M. Tignor, S. Allen, J. Boschung, A. Nauels, Y. Xia, V. Bex, and P. Midgley. Cambridge, United Kingdom and New York, NY, USA: Cambridge University Press. Chap. 13, pp. 1137–1216. DOI: 10.1017/CBO9781107415324.026.

Cornford, S. L., D. F. Martin, V. Lee, A. J. Payne, and E. G. Ng (2016). "Adaptive mesh refinement versus subgrid friction interpolation in simulations of Antarctic ice dynamics". In: *Annals of Glaciology* 57.73, pp. 1–9. DOI: 10.1017/aog.2016.13.

Cowton, T., D. Slater, A. Sole, D. Goldberg, and P. Nienow (2015). "Modeling the impact of glacial runoff on fjord circulation and submarine melt rate using a new subgrid-scale parameterization for glacial plumes". In: *Journal of Geophysical Research: Oceans* 120.2, pp. 796–812. DOI: 10.1002/2014JC010324.

Dalziel, S. B. (1991). "Two-layer hydraulics: a functional approach". In: *Journal of Fluid Mechanics* 223, pp. 135–163. DOI: 10.1017/S0022112091001374.

Davison, B. J., T. R. Cowton, F. R. Cottier, and A. J. Sole (2020). "Iceberg melting substantially modifies oceanic heat flux towards a major Greenlandic tidewater glacier". In: *Nature Communications* 11.1, p. 5983. DOI: 10.1038/s41467-020-19805-7.

De Andrés, E., D. A. Slater, F. Straneo, J. Otero, S. Das, and F. Navarro (2020). "Surface emergence of glacial plumes determined by fjord stratification". In: *The Cryosphere* 14.6, pp. 1951–1969. DOI: 10.5194/tc-14-1951-2020.

Delaney, I. and S. Adhikari (2020). "Increased Subglacial Sediment Discharge in a Warming Climate: Consideration of Ice Dynamics, Glacial Erosion, and Fluvial Sediment Transport". In: *Geophysical Research Letters* 47.7. e2019GL085672 10.1029/2019GL085672, e2019GL085672. DOI: 10.1029/2019GL085672.

Engqvist, A. (1996). "Self-similar multi-layer exchange flow through a contraction". In: *Journal of Fluid Mechanics* 328, pp. 49–66. DOI: 10.1017/S0022112096008646.

Everett, A., T. Murray, N. Selmes, D. Holland, and D. Reeve (2021). "The Impacts of a Subglacial Discharge Plume on Calving, Submarine Melting, and Mélange Mass Loss at Helheim Glacier, South East Greenland". English (US). In: *Journal of Geophysical Research: Earth Surface* 126.3. DOI: 10.1029/2020JF005910.

Farmer, D. M. (1976). "The Influence of Wind on the Surface Layer of a Stratified Inlet: Part II. Analysis". In: *Journal of Physical Oceanography* 6.6, pp. 941–952. DOI: 10.1175/1520-0485(1976)006<0941:TIOWOT>2.0.CO;2.

Farmer, D. M. and H. J. Freeland (1983). "The physical oceanography of fjords". In: *Progress in Oceanography* 12.2, pp. 147–219. DOI: 10.1016/0079-6611(83)90004-6.

Fenty, I., J. K. Willis, A. Khazendar, S. Dinardo, R. Forsberg, I. Fukumori, D. Holland, M. Jakobsson, D. Moller, J. Morison, A. Münchow, E. Rignot, M. Schodlok, A. F. Thompson, K. Tinto, Lamont-Doherty, M. Rutherford, and N. Trenholm (2016). "Oceans Melting Greenland: Early Results from NASA's Ocean-Ice Mission in Greenland". In: *Oceanography* 29. DOI: 10.5670/oceanog.2016.100.

Fettweis, X., J. E. Box, C. Agosta, C. Amory, C. Kittel, C. Lang, D. van As, H. Machguth, and H. Gallée (2017). "Reconstructions of the 1900–2015 Greenland ice sheet surface mass balance using the regional climate MAR model". In: *The Cryosphere* 11.2, pp. 1015–1033. DOI: 10.5194/tc-11-1015-2017.

Fox-Kemper, B., H. Hewitt, C. Xiao, G. Aðalgeirsdóttir, S. Drijfhout, T. Edwards, N. Golledge, M. Hemer, R. Kopp, G. Krinner, A. Mix, D. Notz, S. Nowicki, I. Nurhati, L. Ruiz, J. Sallée, A. Slangen, and Y. Yu (2021). "Ocean, Cryosphere and Sea Level Change". In: *Climate Change 2021: The Physical Science Basis. Contribution of Working Group I to the Sixth Assessment Report of the Intergovernmental Panel on Climate Change*. Ed. by V. Masson-Delmotte, P. Zhai, A. Pirani, S. Connors, C. Péan, S. Berger, N. Caud, Y. Chen, L. Goldfarb, M. Gomis, M. Huang, K. Leitzell, E. Lonnoy, J. Matthews, T. Maycock, T. Waterfield, O. Yelekçi, R. Yu, and B. Zhou. Cambridge, United Kingdom and New York, NY, USA: Cambridge University Press. DOI: 10.1017/9781009157896.011.

Fraser, N. J. and M. E. Inall (2018). "Influence of Barrier Wind Forcing on Heat Delivery Toward the Greenland Ice Sheet". In: *Journal of Geophysical Research: Oceans* 123.4, pp. 2513–2538. DOI: 10.1002/2017JC013464.

Fujiwara, T., L. Sanford, K. Nakatsuji, and Y. Sugiyama (1997). "Anti-cyclonic circulation driven by the estuarine circulation in a gulf type ROFI". In: *Journal of Marine Systems* 12.1, pp. 83–99. DOI: 10.1016/S0924-7963(96)00090-5.

Fyke, J., O. Sergienko, M. Löfverström, S. Price, and J. T. M. Lenaerts (2018). "An Overview of Interactions and Feedbacks Between Ice Sheets and the Earth System". In: *Reviews of Geophysics* 56.2, pp. 361–408. DOI: 10.1029/2018RG000600.

Gill, A. E. (1977). "The hydraulics of rotating-channel flow". In: *Journal of Fluid Mechanics* 80.4, pp. 641–671. DOI: 10.1017/S0022112077002407.

Gillibrand, P., M. Inall, E. Portilla, and P. Tett (2013). "A box model of the seasonal exchange and mixing in Regions of Restricted Exchange: Application to two contrasting Scottish inlets". English. In: *Environmental Modelling Software* 43, pp. 144–159. DOI: 10.1016/j.envsoft.2013.02.008.

Gladish, C. V., D. M. Holland, A. Rosing-Asvid, J. W. Behrens, and J. Boje (2015). "Oceanic Boundary Conditions for Jakobshavn Glacier. Part I: Variability and Renewal of Ilulissat Icefjord Waters, 2001–14". In: *Journal of Physical Oceanography* 45.1, pp. 3–32. DOI: 10.1175/JPO-D-14-0044.1.

Harden, B. E., I. A. Renfrew, and G. N. Petersen (2011). "A Climatology of Wintertime Barrier Winds off Southeast Greenland". In: *Journal of Climate* 24.17, pp. 4701–4717. DOI: 10.1175/2011JCLI4113.1.

Helfrich, K. R. (1995). "Time-Dependent Two-Layer Hydraulic Exchange Flows". In: *Journal of Physical Oceanography* 25.3, pp. 359–373. DOI: 10.1175/1520-0485(1995)025<0359:TDTLHE>2.0.CO;2.

Hewitt, I. J. (2011). "Modelling distributed and channelized subglacial drainage: the spacing of channels". In: *Journal of Glaciology* 57.202, pp. 302–314. DOI: 10.3189/002214311796405951.

Hoegh-Guldberg, O., R. Cai, E. Poloczanska, P. Brewer, S. Sundby, K. Hilmi, V. Fabry, and S. Jung (2014). "The Ocean". In: *Climate Change 2014: Impacts, Adaptation, and Vulnerability. Part B: Regional Aspects. Contribution of Working Group II to the Fifth Assessment Report of the Intergovernmental Panel on Climate Change*. Cambridge, United Kingdom and New York, NY, USA: Cambridge University Press., pp. 1655–1731.

Hogg, N. G. (1983). "Hydraulie Control and Flow Separation in a Multi-Layered Fluid with Applications to the Vema Channel". In: *Journal of Physical Oceanography* 13.4, pp. 695–708. DOI: 10.1175/1520-0485(1983)013<0695:HCAFSI>2.0.CO;2.

Holland, D. M. and A. Jenkins (1999). "Modeling Thermodynamic Ice–Ocean Interactions at the Base of an Ice Shelf". In: *Journal of Physical Oceanography* 29.8, pp. 1787–1800. DOI: 10.1175/1520-0485(1999)029<1787:MTIOIA>2.0.CO;2.

Holland, D. M., R. H. Thomas, B. de Young, M. H. Ribergaard, and B. Lyberth (2008). "Acceleration of Jakobshavn Isbræ triggered by warm subsurface ocean waters". In: *Nature Geoscience* 1.10, pp. 659–664. DOI: 10.1038/ngeo316.

Hoskins, B. J. (1975). "The Geostrophic Momentum Approximation and the Semi-Geostrophic Equations". In: *Journal of Atmospheric Sciences* 32.2, pp. 233–242. DOI: 10.1175/1520-0469(1975)032<0233:TGMAAT>2.0.CO;2.

Howarth, R. W. (1988). "Nutrient limitation of net primary production in marine ecosystems". In: *Annual Review of Ecology and Systematics* 19.1, pp. 89–110. DOI: 10.1146/annurev.es.19.110188.000513.

Inall, M. E., T. Murray, F. R. Cottier, K. Scharrer, T. J. Boyd, K. J. Heywood, and S. L. Bevan (2014). "Oceanic heat delivery via Kangerdlugssuaq Fjord to the south-east Greenland ice sheet". In: *Journal of Geophysical Research: Oceans* 119.2, pp. 631–645. DOI: 10.1002/2013JC009295.

Inall, M. E., F. Nilsen, F. R. Cottier, and R. Daae (2015). "Shelf/fjord exchange driven by coastal-trapped waves in the Arctic". In: *Journal of Geophysical Research: Oceans* 120.12, pp. 8283–8303. DOI: 10.1002/2015JC011277.

Jackson, R. H., J. D. Nash, C. Kienholz, D. A. Sutherland, J. M. Amundson, R. J. Motyka, D. Winters, E. Skyllingstad, and E. C. Pettit (2020). "Meltwater Intrusions Reveal Mechanisms for Rapid Submarine Melt at a Tidewater Glacier". In: *Geophysical Research Letters* 47.2. e2019GL085335 10.1029/2019GL085335, e2019GL085335. DOI: 10.1029/2019GL085335.

Jackson, R. H., S. J. Lentz, and F. Straneo (2018). "The Dynamics of Shelf Forcing in Greenlandic Fjords". In: *Journal of Physical Oceanography* 48.11, pp. 2799–2827. DOI: 10.1175/JPO-D-18-0057.1.

Jackson, R. H. and F. Straneo (2016). "Heat, Salt, and Freshwater Budgets for a Glacial Fjord in Greenland". In: *Journal of Physical Oceanography* 46.9, pp. 2735–2768. DOI: 10.1175/JPO-D-15-0134.1.

Jackson, R. H., F. Straneo, and D. A. Sutherland (2014). "Externally forced fluctuations in ocean temperature at Greenland glaciers in non-summer months". In: *Nature Geoscience* 7.7, pp. 503–508. DOI: 10.1038/ngeo2186.

Jakobsson, M., L. A. Mayer, J. Nilsson, C. Stranne, B. Calder, M. O'Regan, J. W. Farrell, T. M. Cronin, V. Brüchert, J. Chawarski, B. Eriksson, J. Fredriksson, L. Gemery, A. Glueder, F. A. Holmes, K. Jerram, N. Kirchner, A. Mix, J. Muchowski, A. Prakash, B. Reilly, B. Thornton, A. Ulfsbo, E. Weidner, H. Åkesson, T. Handl, E. Ståhl, L.-G. Boze, S. Reed, G. West, and J. Padman (2020). "Ryder Glacier in northwest Greenland is shielded from warm Atlantic water by a bathymetric sill". In: *Communications Earth & Environment* 1.1, p. 45. DOI: 10.1038/s43247-020-00043-0.

Jenkins, A. (2011). "Convection-Driven Melting near the Grounding Lines of Ice Shelves and Tidewater Glaciers". In: *Journal of Physical Oceanography* 41.12, pp. 2279–2294. DOI: 10.1175/JPO-D-11-03.1.

Johnson, H. L., A. Münchow, K. K. Falkner, and H. Melling (2011). "Ocean circulation and properties in Petermann Fjord, Greenland". In: *Journal of Geophysical Research: Oceans* 116.C1. DOI: 10.1029/2010JC006519.

Kanna, N., S. Sugiyama, Y. Ohashi, D. Sakakibara, Y. Fukamachi, and D. Nomura (2018). "Upwelling of Macronutrients and Dissolved Inorganic Carbon by a Subglacial Freshwater Driven Plume in Bowdoin Fjord, Northwestern Greenland". In: *Journal of Geophysical Research: Biogeosciences* 123.5, pp. 1666–1682. DOI: 10.1029/2017JG004248.

Kaye, N. B. and G. R. Hunt (2004). "Time-dependent flows in an emptying filling box". In: *Journal of Fluid Mechanics* 520, pp. 135–156. DOI: 10.1017/S0022112004001156.

Killworth, P. D. (1992). "Flow Properties in Rotating, Stratified Hydraulics". In: *Journal of Physical Oceanography* 22.9, pp. 997–1017. DOI: 10.1175/1520-0485(1992)022<0997:FPIRSH>2.0.CO;2.

Kimura, S., P. R. Holland, A. Jenkins, and M. Piggott (2014). "The Effect of Meltwater Plumes on the Melting of a Vertical Glacier Face". In: *Journal of Physical Oceanography* 44.12, pp. 3099–3117. DOI: 10.1175/JPO-D-13-0219.1.

Klinck, J. M., J. J. O'Brien, and H. Svendsen (1981). "A Simple Model of Fjord and Coastal Circulation Interaction". In: *Journal of Physical Oceanography* 11.12, pp. 1612–1626. DOI: 10.1175/1520-0485(1981)011<1612:ASMOFA>2.0.CO;2.

Knudsen, M. (1900). "Ein hydrographischer Lehrsatz". In: *Annalen der Hydrographie und Maritimen Meteorologie* 28.7. cited By 132, pp. 316–320.

Kopera, M. A., F. X. Giraldo, and W. Maslowski (2018). "Ice-Sheet / Ocean Interaction Model for Greenland Fjords Using High-Order Discontinuous Galerkin Methods". In: DOI: 10.2172/1480068.

Kuhlbrodt, T., C. G. Jones, A. Sellar, D. Storkey, E. Blockley, M. Stringer, R. Hill, T. Graham, J. Ridley, A. Blaker, D. Calvert, D. Copsey, R. Ellis, H. Hewitt, P. Hyder, S. Ineson, J. Mulcahy, A. Siahaan, and J. Walton (2018). "The Low-Resolution Version of HadGEM3 GC3.1: Development and Evaluation for Global Climate". In: *Journal of Advances in Modeling Earth Systems* 10.11, pp. 2865–2888. DOI: 10.1029/2018MS001370.

Laanearu, J. and P. A. Davies (2007). "Hydraulic control of two-layer flow in "quadratic"-type channels". In: *Journal of Hydraulic Research* 45.1, pp. 3–12. DOI: 10.1080/00221686.2007.9521738.

Lane-Serff, G., D. Smeed, and C. Postlethwaite (2000). "Multi-layer hydraulic exchange flows". In: *Journal of Fluid Mechanics* 416, pp. 269–296. DOI: 10.1017/S0022112000008958.

Large, W. G., J. C. McWilliams, and S. C. Doney (1994). "Oceanic vertical mixing: A review and a model with a nonlocal boundary layer parameterization". In: *Reviews of Geophysics* 32.4, pp. 363–403. DOI: 10.1029/94RG01872.

Linden, P. F. (1999). "The fluid mechanics of natural ventilation". In: *Annual Review of Fluid Mechanics* 31.1, pp. 201–238. DOI: 10.1146/annurev.fluid.31.1.201.

Lozier, M. S., F. Li, S. Bacon, F. Bahr, A. S. Bower, S. A. Cunningham, M. F. de Jong, L. de Steur, B. deYoung, J. Fischer, S. F. Gary, B. J. W. Greenan, N. P. Holliday, A. Houk, L. Houpert, M. E. Inall, W. E. Johns, H. L. Johnson, C. Johnson, J. Karstensen, G. Koman, I. A. L. Bras, X. Lin, N. Mackay, D. P. Marshall, H. Mercier, M. Oltmanns, R. S. Pickart, A. L. Ramsey, D. Rayner, F. Straneo, V. Thierry, D. J. Torres, R. G. Williams, C. Wilson, J. Yang, I. Yashayaev, and J. Zhao (2019). "A sea change in our view of overturning in the subpolar North Atlantic". In: *Science* 363.6426, pp. 516–521. DOI: 10.1126/science.aau6592.

Lundesgaard, Ø., B. Powell, M. Merrifield, L. Hahn-Woernle, and P. Winsor (2019). "Response of an Antarctic Peninsula Fjord to Summer Katabatic Wind Events". In: *Journal of Physical Oceanography* 49.6, pp. 1485–1502. DOI: 10.1175/JPO-D-18-0119.1.

Magorrian, S. J. and A. J. Wells (2016). "Turbulent plumes from a glacier terminus melting in a stratified ocean". In: *Journal of Geophysical Research: Oceans* 121.7, pp. 4670–4696. DOI: 10.1002/2015JC011160.

Mankoff, K. D., F. Straneo, C. Cenedese, S. B. Das, C. G. Richards, and H. Singh (2016). "Structure and dynamics of a subglacial discharge plume in a Greenlandic fjord". In: *Journal of Geophysical Research: Oceans* 121.12, pp. 8670–8688. DOI: 10.1002/2016JC011764.

Marshall, J., A. Adcroft, C. Hill, L. Perelman, and C. Heisey (1997). "A finite-volume, incompressible Navier Stokes model for studies of the ocean on parallel computers". In: *Journal of Geophysical Research: Oceans* 102.C3, pp. 5753–5766. DOI: 10.1029/96JC02775.

Meire, L., J. Mortensen, P. Meire, T. Juul-Pedersen, M. K. Sejr, S. Rysgaard, R. Nygaard, P. Huybrechts, and F. J. R. Meysman (2017). "Marine-terminating glaciers sustain high productivity in Greenland fjords". In: *Global Change Biology* 23.12, pp. 5344–5357. DOI: 10.1111/gcb.13801.

Menary, M. B., T. Kuhlbrodt, J. Ridley, M. B. Andrews, O. B. Dimdore-Miles, J. Deshayes, R. Eade, L. Gray, S. Ineson, J. Mignot, C. D. Roberts, J. Robson, R. A. Wood, and P. Xavier (2018). "Preindustrial Control Simulations With HadGEM3-GC3.1 for CMIP6". In: *Journal of Advances in Modeling Earth Systems* 10.12, pp. 3049–3075. DOI: 10.1029/2018MS001495.

Moffatt, H. K. (1964). "Viscous and resistive eddies near a sharp corner". In: *Journal of Fluid Mechanics* 18.1, pp. 1–18. DOI: 10.1017/S0022112064000015.

Moon, T., D. A. Sutherland, D. Carroll, D. Felikson, L. Kehrl, and F. Straneo (2018). "Subsurface iceberg melt key to Greenland fjord freshwater budget". In: *Nature Geoscience* 11.1, pp. 49–54. DOI: 10.1038/s41561-017-0018-z.

Mortensen, J., K. Lennert, J. Bendtsen, and S. Rysgaard (2011). "Heat sources for glacial melt in a sub-Arctic fjord (Godthåbsfjord) in contact with the Greenland Ice Sheet". In: *Journal of Geophysical Research: Oceans* 116.C1. DOI: 10.1029/2010JC006528.

Mortensen, J., S. Rysgaard, J. Bendtsen, K. Lennert, T. Kanzow, H. Lund, and L. Meire (2020). "Subglacial Discharge and Its Down-Fjord Transformation in West Greenland Fjords With an Ice Mélange". In: *Journal of Geophysical Research: Oceans* 125.9. e2020JC016301 2020JC016301, e2020JC016301. DOI: 10.1029/2020JC016301.

Morton, B. R., G. I. Taylor, and J. S. Turner (1956). "Turbulent gravitational convection from maintained and instantaneous sources". In: *Proceedings of the Royal Society of London. Series A. Mathematical and Physical Sciences* 234.1196, pp. 1–23. DOI: 10.1098/rspa.1956.0011.

Motyka, R. J., L. Hunter, K. A. Echelmeyer, and C. Connor (2003). "Submarine melting at the terminus of a temperate tidewater glacier, LeConte Glacier, Alaska, U.S.A." In: *Annals of Glaciology* 36, pp. 57–65. DOI: 10.3189/172756403781816374.

Murray, T., K. Scharrer, N. Selmes, A. D. Booth, T. D. James, S. L. Bevan, J. Bradley, S. Cook, L. C. Llana, Y. Drocourt, L. Dyke, A. Goldsack, A. L. Hughes, A. J. Luckman, and J. McGovern (2015). "Extensive retreat of Greenland tidewater glaciers, 2000–2010". In: *Arctic, Antarctic, and Alpine Research* 47.3, pp. 427–447. DOI: 10.1657/AAAR0014-049.

Oltmanns, M., F. Straneo, G. W. K. Moore, and S. H. Mernild (2014). "Strong Downslope Wind Events in Ammassalik, Southeast Greenland". In: *Journal of Climate* 27.3, pp. 977–993. DOI: 10.1175/JCLI-D-13-00067.1.

Priestley, C. H. B. and F. K. Ball (1955). "Continuous convection from an isolated source of heat". In: *Quarterly Journal of the Royal Meteorological Society* 81.348, pp. 144–157. DOI: 10.1002/qj.49708134803.

Rahmstorf, S., J. Box, G. Feulner, M. Mann, A. Robinson, S. Rutherford, and E. Schaffernicht (2015). "Exceptional twentieth-Century slowdown in Atlantic Ocean overturning circulation". In: *Nature Climate Change* 5. DOI: 10.1038/nclimate2554.

Rignot, E., J. E. Box, E. Burgess, and E. Hanna (2008). "Mass balance of the Greenland ice sheet from 1958 to 2007". In: *Geophysical Research Letters* 35.20. DOI: 10.1029/2008GL035417.

Robinson, A., R. Calov, and A. Ganopolski (2012). "Multistability and critical thresholds of the Greenland ice sheet". In: *Nature Climate Change* 2.6, pp. 429–432. DOI: 10.1038/nclimate1449.

Rysgaard, S., V. Torben, M. Stjernholm, B. Rasmussen, A. Windelin, and S. Kiilsholm (2003). "Physical Conditions, Carbon Transport, and Climate Change Impacts in a Northeast Greenland Fjord". In: *Arctic Antarctic and Alpine Research - ARCT ANTARCT ALP RES* 35, pp. 301–312. DOI: 10.1657/1523-0430(2003)035[0301:PCCTAC]2.0.CO;2.

Schauer, U. and A. Beszczynska-Möller (2009). "Problems with estimation and interpretation of oceanic heat transport – conceptual remarks for the case of Fram Strait in the Arctic Ocean". In: *Ocean Science* 5.4, pp. 487–494. DOI: 10.5194/os-5-487-2009.

Seale, A., P. Christoffersen, R. I. Mugford, and M. O'Leary (2011). "Ocean forcing of the Greenland Ice Sheet: Calving fronts and patterns of retreat identified by automatic satellite monitoring of eastern outlet glaciers". In: *Journal of Geophysical Research: Earth Surface* 116.F3. DOI: 10.1029/2010JF001847.

Shoemaker, E. M. (1986). "The Formation of Fjord Thresholds". In: *Journal of Glaciology* 32.110, pp. 65–71. DOI: 10.3189/S0022143000006894.

Slater, D., D. Carroll, H. Oliver, M. J. Hopwood, F. Straneo, M. Wood, J. K. Willis, and M. Morlighem (2022). "Characteristic Depths, Fluxes, and Timescales for Greenland's Tidewater Glacier Fjords From Subglacial Discharge-Driven Upwelling During Summer". In: *Geophysical Research Letters* 49.10. e2021GL097081 2021GL097081, e2021GL097081. DOI: 10.1029/2021GL097081.

Slater, D., D. N. Goldberg, P. W. Nienow, and T. R. Cowton (2016). "Scalings for Submarine Melting at Tidewater Glaciers from Buoyant Plume Theory". In: *Journal of Physical Oceanography* 46.6, pp. 1839–1855. DOI: 10.1175/JPO-D-15-0132.1.

Slater, D., F. Straneo, S. B. Das, C. G. Richards, T. J. W. Wagner, and P. W. Nienow (2018). "Localized Plumes Drive Front-Wide Ocean Melting of A Greenlandic Tidewater Glacier". In: *Geophysical Research Letters* 45.22, pp. 12, 350–12, 358. DOI: 10.1029/2018GL080763.

Slater, D., F. Straneo, D. Felikson, C. M. Little, H. Goelzer, X. Fettweis, and J. Holte (2019). "Estimating Greenland tidewater glacier retreat driven by submarine melting". In: *The Cryosphere* 13.9, pp. 2489–2509. DOI: 10.5194/tc-13-2489-2019.

Smeed, D. A. (2000). "Hydraulic Control of Three-Layer Exchange Flows: Application to the Bab al Mandab". In: *Journal of Physical Oceanography* 30.10, pp. 2574–2588. DOI: 10.1175/1520-0485(2000)030<2574:HCOTLE>2.0.CO;2.

Smith, R. S. and J. M. Gregory (2009). "A study of the sensitivity of ocean overturning circulation and climate to freshwater input in different regions of the North Atlantic". In: *Geophysical Research Letters* 36.15. DOI: 10.1029/2009GL038607.

Smith, R. S., P. Mathiot, A. Siahaan, V. Lee, S. L. Cornford, J. M. Gregory, A. J. Payne, A. Jenkins, P. R. Holland, J. K. Ridley, and C. G. Jones (2021). "Coupling the U.K. Earth System Model to Dynamic Models of the Greenland and Antarctic Ice Sheets". In: *Journal of Advances in Modeling Earth Systems* 13.10. e2021MS002520 2021MS002520, e2021MS002520. DOI: 10.1029/2021MS002520.

Spall, M. A., R. H. Jackson, and F. Straneo (2017). "Katabatic Wind-Driven Exchange in Fjords". In: *Journal of Geophysical Research: Oceans* 122.10, pp. 8246–8262. DOI: 10.1002/2017JC013026.

Speer, K. G. and K. R. Helfrich (1995). "Hydrothermal plumes: a review of flow and fluxes". In: *Geological Society, London, Special Publications* 87.1, pp. 373–385. DOI: 10.1144/GSL.SP.1995.087.01.29.

Stevens, L. A., F. Straneo, S. B. Das, A. J. Plueddemann, A. L. Kukulya, and M. Morlighem (2016). "Linking glacially modified waters to catchment-scale subglacial discharge using autonomous underwater vehicle observations". In: *The Cryosphere* 10.1, pp. 417–432. DOI: 10.5194/tc-10-417-2016.

Stigebrandt, A. (1990). "On the response of the horizontal mean vertical density distribution in a fjord to low-frequency density fluctuations in the coastal water". In: *Tellus A* 42.5, pp. 605–614. DOI: 10.1034/j.1600-0870.1990.t01-1-00010.x.

Stigebrandt, A. and J. Aure (1990). "De ytre drivkreftenes betydning for vannutskiftningen i fjordene fra Skagerrak til Finnmark". In: *Rapport/Notat Fysisk oseanografi;FO 9003*.

Stigebrandt, A. (2012). "Hydrodynamics and Circulation of Fjords". In: *Encyclopedia of Lakes and Reservoirs*. Ed. by L. Bengtsson, R. W. Herschy, and R. W. Fairbridge. Dordrecht: Springer Netherlands, pp. 327–344. DOI: 10.1007/978-1-4020-4410-6_247.

Stommel, H. and H. G. Farmer (1953). "Control of salinity in an estuary by a transition". In: *J. Mar. Res* 12.1, pp. 13–20. DOI: 10.1357/002224021834614380.

Storkey, D., A. T. Blaker, P. Mathiot, A. Megann, Y. Aksenov, E. W. Blockley, D. Calvert, T. Graham, H. T. Hewitt, P. Hyder, T. Kuhlbrodt, J. G. L. Rae, and B. Sinha (2018). "UK Global Ocean GO6 and GO7: a traceable hierarchy of model resolutions". In: *Geoscientific Model Development* 11.8, pp. 3187–3213. DOI: 10.5194/gmd-11-3187-2018.

Straneo, F. and C. Cenedese (2015). "The Dynamics of Greenland's Glacial Fjords and Their Role in Climate". In: *Annual Review of Marine Science* 7.1. PMID: 25149564, pp. 89–112. DOI: 10.1146/annurev-marine-010213-135133.

Straneo, F., G. S. Hamilton, D. A. Sutherland, L. A. Stearns, F. Davidson, M. O. Hammill, G. B. Stenson, and A. Rosing-Asvid (2010). "Rapid circulation of warm subtropical waters in a major glacial fjord in East Greenland". In: *Nature Geoscience* 3.3, pp. 182–186. DOI: 10.1038/ngeo764.

Straneo, F. and P. Heimbach (2013). "North Atlantic warming and the retreat of Greenland's outlet glaciers". In: *Nature* 504.7478, pp. 36–43. DOI: 10.1038/nature12854.

Straneo, F., D. A. Sutherland, D. Holland, C. Gladish, G. S. Hamilton, H. L. Johnson, E. Rignot, Y. Xu, and M. Koppes (2012). "Characteristics of ocean waters reaching Greenland's glaciers". In: *Annals of Glaciology* 53.60, pp. 202–210. DOI: 10.3189/2012AoG60A059.

Sulak, D., D. Sutherland, E. Enderlin, L. Stearns, and G. Hamilton (2017). "Iceberg properties and distributions in three Greenlandic fjords using satellite imagery". In: *Annals of Glaciology*, pp. 1–15. DOI: 10.1017/aog.2017.5.

Sutherland, D. A., R. H. Jackson, C. Kienholz, J. M. Amundson, W. P. Dryer, D. Duncan, E. F. Eidam, R. J. Motyka, and J. D. Nash (2019). "Direct observations of submarine melt and subsurface geometry at a tidewater glacier". In: *Science* 365.6451, pp. 369–374. DOI: 10.1126/science.aax3528.

Sutherland, D. A., G. E. Roth, G. S. Hamilton, S. H. Mernild, L. A. Stearns, and F. Straneo (2014). "Quantifying flow regimes in a Greenland glacial fjord using iceberg drifters". In: *Geophysical Research Letters* 41.23, pp. 8411–8420. DOI: 10.1002/2014GL062256.

Sutherland, D. A. and F. Straneo (2012). "Estimating ocean heat transports and submarine melt rates in Sermilik Fjord, Greenland, using lowered acoustic Doppler current profiler (LADCP) velocity profiles". In: *Annals of Glaciology* 53.60, pp. 50–58. DOI: 10.3189/2012AoG60A050.

Timmermans, M.-L. E. and L. J. Pratt (2005). "Two-Layer Rotating Exchange Flow between Two Deep Basins: Theory and Application to the Strait of Gibraltar". In: *Journal of Physical Oceanography* 35.9, pp. 1568–1592. DOI: 10.1175/JPO2775.1.

Turner, J. S. (1973). *Buoyancy Effects in Fluids*. Cambridge Monographs on Mechanics. Cambridge University Press. DOI: 10.1017/CBO9780511608827.

Vallis, G. (2006). *Atmospheric and Oceanic Fluid Dynamics*, p. 745. DOI: 10.2277/0521849691.

WCRP Global Sea Level Budget Group (2018). "Global sea-level budget 1993–present". In: *Earth System Science Data* 10.3, pp. 1551–1590. DOI: 10.5194/essd-10-1551-2018.

Williams, K. D., D. Copsey, E. W. Blockley, A. Bodas-Salcedo, D. Calvert, R. Comer, P. Davis, T. Graham, H. T. Hewitt, R. Hill, P. Hyder, S. Ineson, T. C. Johns, A. B. Keen, R. W. Lee, A. Megann, S. F. Milton, J. G. L. Rae, M. J. Roberts, A. A. Scaife, R. Schiemann, D. Storkey, L. Thorpe, I. G. Watterson, D. N. Walters, A. West, R. A. Wood, T. Woollings, and P. K. Xavier (2018). "The Met Office Global Coupled Model 3.0 and 3.1 (GC3.0 and GC3.1) Configurations". In: *Journal of Advances in Modeling Earth Systems* 10.2, pp. 357–380. DOI: 10.1002/2017MS001115.

Woods, A. W. and J. W. M. Bush (1999). "Dimensions and dynamics of megaplumes". In: *Journal of Geophysical Research: Oceans* 104.C9, pp. 20495–20507. DOI: 10.1029/1999JC900063.

Worster, M. G. and H. E. Huppert (1983). "Time-dependent density profiles in a filling box". In: *Journal of Fluid Mechanics* 132, pp. 457–466. DOI: 10.1017/S002211208300172X.

Xu, Y., E. Rignot, D. Menemenlis, and M. Koppes (2012). "Numerical experiments on subaqueous melting of Greenland tidewater glaciers in response to ocean warming and enhanced subglacial discharge". In: *Annals of Glaciology* 53.60, pp. 229–234. DOI: 10.3189/2012AoG60A139.

Yang, Q., T. H. Dixon, P. G. Myers, J. Bonin, D. Chambers, M. R. van den Broeke, M. H. Ribergaard, and J. Mortensen (2016). "Recent increases in Arctic freshwater flux affects Labrador Sea convection and Atlantic overturning circulation". In: *Nature Communications* 7.1, p. 10525. DOI: 10.1038/ncomms10525.